

5111
11-11-11
167873
P-228

Final Technical Report for
NASA Grant NAG 5-1125
The Role of Global Cloud Climatologies in Validating Numerical Models

Principal Investigator:
Harshvardhan
Department of Earth and Atmospheric Sciences
Purdue University
West Lafayette, Indiana 47907-1397

Period of Performance:
April 1, 1989 - March 31, 1993

(NASA-CR-193135) THE ROLE OF
GLOBAL CLOUD CLIMATOLOGIES IN
VALIDATING NUMERICAL MODELS Final
Technical Report, 1 Apr. 1989 - 31
Mar. 1993 (Purdue Univ.) 228 p

N93-27536

Unclass

G3/45 0167873

The Role of Global Cloud Climatologies in Validating Numerical Models

The research covered during the period of the grant primarily involved studies of the hydrological cycle and radiation budget of general circulation models. Extensive use was made of satellite data of cloud cover and the radiation budget at the top of the atmosphere. For ease of presentation, the work has been categorized as follows.

1. Study of the temporal aspects of tropical convective rainfall simulated by a general circulation model.
2. The feasibility of obtaining the longwave radiation budget at the surface from satellite data.
3. Parameterization of atmospheric radiation transport.

The technical report contains documentation of all the results from the research performed under each category separately. Where available the information is from publications. This is supplemented by other documents and reports that have been prepared by us.

Students fully or partially supported by the grant.

Outtara Fatogoma, M.S. 1990
Hui Zhi, M.S. 1990
Kathryn Ginger, M.S. 1993 (expected)
Surabi Menon, M.S. 1994 (expected)

Meetings attended with grant support

1. FIRE Science Team Meeting, Monterey, CA, July 10-14, 1989.
2. Fifth Scientific Assembly of the International Association of Meteorology and Atmospheric Physics, Reading, U.K., July 31 - August 12, 1989.
3. American Geophysical Union Spring Meeting, Baltimore, MD, May 29 - June 1, 1990.
4. Seventh Conference on Atmospheric Radiation of the American Meteorological Society, San Francisco, CA, July 23-27, 1990.
5. American Geophysical Union Spring Meeting, Montreal, Canada, May 11 -16, 1992.
6. Fourth Symposium on Global Change Studies of the American Meteorological Society, Anaheim, CA, January 17-22, 1993.

Technical Report

Section 1

Study of the temporal aspects of tropical convective rainfall simulated
by a general circulation model.

**Sampling Error Estimates of Satellite-Derived Tropical Rainfall Using
General Circulation Model Data**

by

Ouattara Fatogoma

TABLE OF CONTENTS

	Page
LIST OF TABLES	iv
LIST OF FIGURES	v
ABSTRACT	vii
1. INTRODUCTION	1
2. DERIVATION OF SAMPLING ERROR	10
2.1 General formulation	10
2.2 Sunsynchronous polar orbit	16
2.3 Two simultaneous sunsynchronous polar orbits	16
3. SAMPLING CHARACTERISTICS OF A SATELLITE	18
3.1 Orbital dynamics for the sampling error study	18
3.2 Sampling characteristics of the satellites	20
4. RAINFALL DISTRIBUTION IN TIME	22
4.1 Example of rainfall distribution	22
4.2 Autocovariance function	22
4.3 Final note on the derivation of sampling error	23
5. SAMPLING ERROR RESULTS AND DISCUSSIONS	25
6. SUMMARY AND RECOMMENDATIONS	28
LIST OF REFERENCES	129
APPENDIX	130

LIST OF TABLES

Table	Page
1. Orbits parameters for TRMM and NOAA-10	30
2. Rainfall statistics for December, January, and February	31

LIST OF FIGURES

Figure	Page
1. Grid box map	34
2. The visiting time differences from that of a sun-synchronous orbit in minutes .	35
3. Variation of the sampling intervals versus grid box latitude for the TRMM orbit	36
4. Distribution of the monthly area averaged rain rates versus time for different grid box locations in December, January, and February	37
5. Variation of the monthly mean rain rates versus grid box location in December, January, and February	73
6. Variation of the monthly rain rate standard deviations versus grid box locations in December, January, and February	76
7. Variation of the autocovariance functions versus time lag for different grid box locations in December, January, and February	79
8. Variation of the correlation times versus grid box locations in December, January, and February	88
9. Variation of the standard sampling error versus monthly mean rain rates in December for the TRMM, NOAA-10, and two sun synchronous orbits . . .	91
10. Variation of the standard sampling error versus monthly rain stdard deviation in December for the TRMM, NOAA-10, and two sun synchronous orbits .	94
11. Variation of the standard sampling error versus correlation time in december for the TRMM, NOAA-10, and two sun synchronous orbits	97
12. Variation of the standard sampling error versus grid box location in december for the TRMM, NOAA-10, and two sun synchronous orbits	100
13. Same as Figure 9 but in January	103
14. Same as Figure 10.but in January	106
15. Same as Figure 11.but in January	109
16. Same as Figure 12.but in January	112

Figure	Page
17. Same as Figure 9 but in February	115
18. Same as Figure 10 but in February	118
19. Same as Figure 11 but in February	121
20. Same as Figure 12 but in February	124
21. Average standard sampling error for the TRMM, NOAA-10, and the two sun-synchronous orbits in December, January, and February	127
22. Variation of averaged rain rate statistics from December to February	128

ABSTRACT

Fatogoma, Ouattara. M.S., Purdue University, August 1990. Sampling Error Estimates of Satellite-Derived Tropical Rainfall Using General Circulation Model Data. Major Professor: Dr. Harshvardhan.

The purpose of this work is to estimate sampling errors of area-time averaged rain rate due to temporal samplings by satellites. In particular, the proposed low inclination orbit satellite of the Tropical Rainfall Measuring Mission (TRMM; 35° inclination and 350 km altitude), one of the sunsynchronous polar orbiting satellites of NOAA series (98.89° inclination and 833 km altitude) and two simultaneous sunsynchronous polar orbiting satellites, assumed to carry a perfect passive microwave sensor for direct rainfall measurements. This estimate is done by performing a study of the satellite orbits and the autocovariance function of the area-averaged rain rate time series. A model based on an exponential fit of the autocovariance function is used for actual calculations. Varying visiting intervals and total coverage of averaging area on each visit by the satellites are taken into account in the model.

The data are generated by a General Circulation Model (GCM). The model has a diurnal cycle and parameterized convective processes. A special run of the GCM was made at NASA/Goddard Space Flight Center in which the rainfall and precipitable water fields were retained globally for every hour of the run for the whole year.

For the areas chosen (5° by 4° grid boxes located at 130°E, 150°E, 160°W with latitude varying from 22°S to 10°N), on average, the sampling error for the three months (December, January, and February) of the northern hemisphere winter would be of the order of 10% of the monthly mean for a satellite in the TRMM orbit. This error

is almost equivalent (difference less than 1%) to the sampling error produced by a polar-orbiting NOAA-series orbit. Observations with a system of two sunsynchronous polar-orbiting satellites simultaneously would reduce the sampling error from 10% to about 5%.

1. INTRODUCTION

The roles of tropical rainfall are very important in the energy budget of the planet and in affecting planetary waves that control weather patterns over the globe. A significant fraction of the heating of the tropical atmosphere comes from latent heat release in precipitating clouds. As a matter-of-fact, much of the sun's energy does not go into the air directly, but goes into heating land and ocean surfaces. Over the continents, the sun raises the temperature of the land surfaces which are cooled as the air carries away the heat. Over the ocean, particularly in the tropics, much of the sun's energy is used to evaporate water. It is only when this water vapor condenses to form cloud and rain that the sun's energy is deposited in the atmosphere. This energy, in turn, becomes the available energy that drives the winds. Since much of the tropics is covered by ocean, the formation of rain in the tropics is an important step in a process that transforms the energy in incoming solar radiation into kinetic energy which drives the motions of the atmosphere. Heated equatorial air moves towards the poles at high altitudes and is replaced by cooler air flowing towards the equator at lower levels. Because of the vital role of latent heat released in driving general atmospheric circulation, the variability of tropical rainfall is a key in understanding the circulation variability and short term climate changes.

As we can see, tropical regions are the primary source of the earth's weather and atmospheric circulation patterns. Accurate estimates of the amount of rainfall there would greatly improve our understanding of global weather, climate and the dynamics of the earth's atmosphere. However, tropical rainfall is not well monitored because of

its high variability in both space and time, and much of the area is covered by jungle and ocean. Consequently, it is very difficult, even impossible to use conventional ground-based rainfall measuring devices such as rain gauges and radar. Because of this, rainfall observations in the tropics are limited to what can be obtained from occasional ship and air reports, occasional experiments mounted specifically to collect data for a given region such as GATE [GARP Atlantic Tropical Experiment, GARP (Global Atmospheric Research Program)], and extrapolations from land observations which are not easy to verify quantitatively.

Continuous coverage of these large oceanic areas and highly variable rain rates is probably only feasible from space borne sensors which can provide a global data set over both the ocean and the continents. Measurements of cloud-top infrared emission from geostationary operational satellites carrying the Visible and Infrared Spin Scan Radiometer (VISSR) Atmospheric Sounder (VAS), currently furnish the best indirect estimate of rain variability over the tropical region. In addition, passive microwave measurements made by the Electrically Scanning Microwave Radiometer (ESMR) aboard Nimbus-5, the Scanning Multichannel Microwave Radiometer (SMMR) aboard Nimbus-7, and the Special Sensor for Microwave/Imager (SSM/I) aboard U.S. Defense Department Satellites provide valuable information on rainfall rates and distributions. Some of these measurements however have been made from geostationary satellites whose fields of view cover only a portion of the globe, and the estimating technique is based upon empirical procedure with fitted regression coefficients specific to the area and season of calibration. Besides, the estimates of average rain over a month have random errors greater than 50% of the mean. And the microwave measurements are made only from sunsynchronous polar-orbiting satellites. Due to the expected diurnal cycle of precipitation, measurements from sun-synchronous polar orbiting satellites would lead to a bias in the estimation of area-time averaged rainfall because they

revisit, at fixed local times, a given location. The low inclination orbits (LIO) or an observation system based upon two satellite orbits simultaneously would reduce significantly the observing time interval of an area down from twelve to six hours depending on the orbit parameters. Therefore, they could observe precipitation through the diurnal cycle.

The use of satellites in measuring averaged rain rate within a given area during a period of time, introduces two significant sources of errors. Firstly, the error inherent in the method used to determine rain rate at a given instant. Secondly, there is the sampling error associated with the satellite only being able to observe a given area intermittently. The first source of error arises from a number of factors such as the non-homogeneous distribution of rain rates inside a field-of-view, the non-linear relationship between the rain rates and the radiant intensity (those two factors are known as the beam-filling problem) and calibration problems due to the limited information for some atmospheric and surface parameters. This error may in principle be considerably reduced by developing good retrieval algorithms to generate unbiased estimates of rain rate and designing sensor elements which help in calibrating satellite retrievals. Moreover, low-altitude satellites provide a small field of view which helps reduce errors due to the beam-filling problem introduced by the high spatial variability of precipitation.

The second source of error, the sampling error, is due to temporal gaps in the observations induced by the orbit. Consequently, it is determined by the orbit of the satellite and the size of the swath scanned by the satellite as it passes over, and by the statistical characteristics of the observed rainfall. Its size depends on how well sampled the area is during a period of time. It is the dominant contribution to the error in time averages if the beam-filling problem and retrieval error are minimized.

The sampling error problems of tropical rainfall have been studied by many researchers mainly using data from cloud-top infrared temperature profiles and most importantly, the GATE rainfall data. The GATE experiment was conducted in two phases in the summer of 1974. The data were recorded from radars in an array of ships centered at 8.5°N , 23.5°W , off the west coast of Africa (Hudlow and Patterson, 1979). However, sampling errors may be different elsewhere on the globe or during a different season, since rainfall is known to be highly variable in both space and time. Laughlin (1981) examined the time series of area-averaged rain rates and noted that the lagged autocorrelation functions were close to exponential. His results show that for twelve hours repeated observations (Sun-synchronous Polar orbiting satellite) and for flush visits (satellite observes the entire box), the sampling error for monthly rain rate estimated over 2.5° by 2.5° grid box were about 8%. McConnell and North (1987) and Kedem et al. (1987) used a mixed probability distribution method along with an imaginary orbit ensemble to show sampling errors of about 8% and 10%, respectively. Shin and North (1988) used the random field method (Bell, 1987) along with uneven sampling intervals and fractional observations of 5° by 5° grid boxes to estimate the sampling error about 8% to 12%.

We see that there are a number of sampling models. A survey of these sampling models tells us that most of them were developed not a long time ago and checked against the GATE rainfall data set only. The first of them is the poisson process. In this model, it is assumed that the individual field-of-view (FOV) of the satellite are rain fauge, the space-time statistics are homogeneous and stationary in the L Km by L Km averaging box and the averaging interval is 30 days. Moreover, the length and time scales are assumed to be short compared to these dimensions. An averaging box will have the results of N readings over the 30 days. If the probability of rain is P for 1 Km by 1 Km FOV and the average rain rate for pixels is R mm/hr and each FOV represents

a statistically independent observation (that is no FOV's result of whether or not it is raining depends upon the result found in a neighboring FOV) then we have a binomial process with N trials. One of the outcomes, rain is rare (P), hence we can use the poisson statistics approximation to the binomial distribution. The standard error of estimating the probability of rain expressed in percent is $100/(P.N)^{0.5}$. This model underestimates the sampling error since the FOV's are not actually independent. Secondly, we have the Markov model of area average rain rate. This model, designed by Laughlin (1981) is based upon a stochastic model. The time series of area average rain rates is examined and if the lagged autocorrelation functions are reasonably close to exponential, we can construct a first order Markov process using the autocorrelation time corresponding to a particular averaging area (that is fit the autocorrelation functions to an exponential) and proceed to find an analytical expression for the sampling error. This is the model I used in this work against the GCM data. Thirdly, we have the partitioned rates and orbit ensembles model. This model was designed by McConnell and North (1987). First, an imaginary satellite orbit is started and flown over a given area at a time t , it returns 11 hours later and so on throughout the phase. During each flush visit, the individual pixels are collected into different categories (example: no rain, 0-5 mm/hr, 5-10 mm/hr, 10-20 mm/hr, and 20 mm/hr and above). The average rain contributed from each of these categories is then estimated from the single imaginary orbit (realization). Realization number 2 is constructed the same way except that the orbit is started at time t plus one hour. In this way, an ensemble of satellite orbits can be constructed and the results can be compared. If the results differ widely from one orbit to another, it can be inferred for instance that significant storms are missed by the 11 hours gap. This model is so simple and assumption-free that it is very appealing. However, the autocorrelation in the area-wide time series of rain rates is not appreciated. Fourthly, we have the mixed distribution method. This model was

designed by Kedem, Chiu, and North (1987). It involves use of a sparse sampling in space and time on a regular grid. At the end of the phase, the pixel average rates are collected into a histogram of rain rates. These are then fitted to the log normal distribution by a chi-square minimization procedure. After determining the appropriate probability density function (pdf) for the data, the average rain rate is calculated by finding the expectation value of the pdf. One such design of a satellite orbit corresponds to the sampling design of a satellite orbit with flush visits (exactly like McConnell and North above). Finally, we have the simulations with random fields model. It is designed by Bell (1987) following this recipe: first a gaussian random field is constructed in fourier spectral form over a grid. This can be thought of as a kind of turbulent vertical wind field. If the wind exceeds a certain threshold, we agree that it is raining. Such a procedure leads to islands of raining areas. The random variable representing the exceedence over threshold can then be converted to a log normal distribution rain rate. This model is more complete since the fields are constructed (it supplements the non-availability of real data) and evolved in fourier space with conversions by way of fast fourier transforms (a fourier series can describe completely all the harmonics of diurnal cycles). Besides, Bell proved that once it is calibrated to GATE statistics, it imitates very well Laughlin's Markov model and the mixed distribution method. The data used in this study were generated using a General Circulation Model (GCM) that has a diurnal cycle and parameterized convective process (Randall et al., 1989). The precipitation climatology of GCM is presented by Randall et al. (1989). Actually, the data are obtained from a cloud generation process in which the vertical distribution of moisture content is parameterized. Throughout the year, roughly two-thirds of the simulated precipitation falls from cumulus ensembles, primarily in the tropics and the summer hemisphere; and the remaining third from large-scale saturation clouds, mainly in the winter midlatitudes. The geographical distribution of the

simulated precipitation is fairly realistic. The GCM successfully produces the rainbands associated with the Atlantic and Pacific branches of the intertropical convergence zone, and also the heavy precipitation of the south Pacific convergence zone and the equatorial western Pacific. The simulated seasonally varying precipitation maxima for eastern North America, tropical Africa, tropical South America, and the Indian subcontinent are realistically positioned, but somewhat strong. The model physics is updated every hour and usually only daily means are retained for analysis. A special run of the GCM was made at NASA/Goddard Space Flight Center in which the rainfall and precipitable water fields were retained globally for every hour of the run for the whole year.

In the proposed work, I conducted a study of satellite orbits along with the autocovariance function of the area-averaged rain rate time series. This was to estimate sampling errors for different grid boxes of 5° by 4° embedded in three different meridional regions: 150°E , 130°E , and 160°W (Figure 1). Note that the grid boxes at 130°E and 160°W are completely in the ocean. At 150°E we have two grid boxes; one in the ocean, the other over land. The orbit characteristics of three satellite systems were used: the Tropical Rainfall Measuring Mission (TRMM) orbit, one NOAA-series orbit, and the combination of two simultaneous NOAA-series orbits.

TRMM is a joint Japan (Science and Technology Agency of Japan) / United States (NASA) mission which has set out to orbit satellites by 1994 designed to provide direct and quantitative measurements of rainfall data in the tropics (Simpson et al., 1988). The main goal of the mission is to produce a monthly mean time series of average rain rate over 5° by 5° boxes in the tropics. The TRMM orbit is planned to be circular with altitude 350 km and inclination 35° to the equator. This orbit gives extensive coverage in the tropics and allows extraction of the diurnal cycle in climatological rainfall because of its low inclination. The low altitude also ensures a small field of

view facilitating the interpretation of rainfall measurements over small spatial scales. Plans for TRMM include four principal sensors. The two microwave radiometers for rainfall rates over the oceans consist of a conically scanning multichannel instrument of moderate resolution with three dual polarized channels at 19, 37, and 85 GHz to provide a wider range of rainfall intensities, and a single-channel (19 GHz) electrically scanning instrument that provides a higher resolution at the more prevalent rain rates of 10 to 20 mm hr⁻¹. The third sensor is a cross-track scanning precipitation radar, specially developed for TRMM, which will measure rainfall over both land and sea. The radar data are necessary to obtain the vertical distribution of latent heat release, a very important parameter for global climate models. The fourth sensor is the Advanced Very High Resolution Radiometer (AVHRR) now in operation on polar-orbiting environmental satellites, which offers high-resolution channels in the visible and infrared spectral regions. The AVHRR will provide a link between measurements made by the first three TRMM sensors and those made simultaneously by visible and infrared radiometers on geostationary spacecraft.

The mission of the NOAA series is to collect global data on cloud cover, surface conditions such as ice and snow, surface and atmospheric temperature, and atmospheric humidity. It is also used to measure solar particle flux, and its third aim is to collect and relay information from fixed and moving data platforms. Finally, it provides continuous data broadcasts. An attempt is made to maintain two NOAA satellites in orbit at all times, a so-called "afternoon" bird with nominal observing times of 2 P.M. and 2 A.M. at altitude 833 km and "morning" bird with observations at 7 A.M. and 7 P.M. at altitude 870 km. The NOAA series is sun-synchronous with a circular orbit and inclination 98.89°. The satellite orbit of interest in this work is that of the latest "afternoon" bird NOAA-10. The platform has four main sensors: the Advanced Very High Resolution Radiometer (AVHRR/2) composed of five bands; the Tiros

Operational Vertical Sounder (TOVS), a three-sensor atmospheric sounding system composed of the High Resolution Infrared Radiation Sounder (HIRS/2) with a ground resolution of 17.4 km and 20 bands; the Stratospheric Sounding Unit (SSU) with a ground resolution of 147.3 km and three bands; the Microwave Sounding Unit (MSU) with a ground resolution of 105 km and four bands; the Space Environment Monitor (SEM) and the ARGOC Data Collection System (DCS).

I also assumed that the satellite sees the whole grid box when it passes over and the rainfall is homogeneous inside a FOV. The orbit parameters and sampling intervals are obtained by a computer-generated model (Appendix) designed by Thomas Bell¹ based on the theories outlined by D.R. Brooks (1977).

¹ Dr. Thomas L. Bell, NASA/Goddard Space Flight Center, Climate and Radiation Branch, Greenbelt, Maryland 20771.

2. DERIVATION OF SAMPLING ERROR

2.1 General Formulation

As a measure of sampling error, I shall use the root mean squared (rms) difference between the actual area-averaged rain rate averaged over a month and the mean of the satellite observations during that month. The derivation of sampling error follows closely that outlined by Laughlin (1981).

Let $M(T)$ be the true monthly-averaged rain rate,

$$M(T) = \frac{1}{T} \int_0^T X(t) dt, \quad (2-1)$$

where $X(t)$ is an area-averaged rain rate,

$$X(t) = \frac{1}{A} \int_A R(r,t) dr^2, \quad (2-2)$$

where $R(r,t)$ is the rain rate at location r , t is the time since the beginning of the month and T and A are the period (1 month) and area averaged over. In practice, a continuous record of $X(t)$ is seldom available. Assuming spatially homogeneous rainfall statistics (so no weighting scheme is necessary), an estimate of $M(T)$ by the satellite observation would be

$$\hat{M}(T) = \sum_{i=1}^N f_i X_i(i\Delta t) / \sum_{i=1}^N f_i \quad (2-3)$$

where N is the total number of observations, Δt the time difference between two observations (time difference between two consecutive nodes), $T = N \cdot \Delta t$ and $X_i(i\Delta t)$ would be a subarea averaged rain rate for the fraction of f_i .

As a first approximation, $X(i\Delta t)$ is substituted for $X_i(i\Delta t)$ because the rainfall is homogeneous in space and the satellite is expected to see the whole grid box. Then

$$\hat{M}(T) = \sum_{i=1}^N f_i X(i\Delta t) / \sum_{i=1}^N f_i . \quad (2-4)$$

The mean squared error (MSE) is the expected value of the squared difference of the two means.

$$\sigma_e^2 = E[(\hat{M}(T) - M(T))^2] . \quad (2-5)$$

The sampling intervals are not always the same as the satellite rotates owing to orbital precession. Nonetheless, they would be different within only one nodal period. Moreover, ascending and descending nodes can be treated as two individual sampling series which have sampling time difference of Δt_d (visiting time difference between an ascending and descending node or vice versa). Then the estimated mean rain rate from satellite observation can be written as

$$\hat{M}(t) = \frac{1}{\left[\sum_{i=1}^N a_i + \sum_{j=1}^N b_j \right]} \left[\sum_{i=1}^N a_i X(t+i\Delta t) + \sum_{j=1}^N b_j X(t+\Delta t_d + j\Delta t) \right] , \quad (2-6)$$

where a_i and b_j are the fractional coverages of each visit by the ascending and descending nodes, respectively, and t is time since the beginning of the month.

I shall assume that if the satellite passes over a given grid box, it sees the whole box (flush visit). Therefore, $a_i = b_j = 1$ and

$$\hat{M}(t) = \frac{1}{(2N)} \left[\sum_{i=1}^N X(t+i\Delta t) + \sum_{j=1}^N X(t+\Delta t_d + j\Delta t) \right] \quad (2-7)$$

$$\begin{aligned} \text{The MSE } \sigma_e^2 &= E[(M(T) - \hat{M}(T))^2] \\ &= E[M^2(T)] + E[\hat{M}^2(T)] - 2E[\hat{M}(T)M(T)] \end{aligned} \quad (2-8)$$

where

$$E[M^2(T)] = E\left[\frac{1}{T^2} \int_0^T X(t)dt \int_0^T X(s)ds\right] \quad (2-9)$$

$$\begin{aligned} E[\hat{M}^2(T)] &= E\left[\frac{1}{(2N)^2} \left\{ \sum_{i=1}^N X(t+i\Delta t) \right\} + \left\{ \sum_{j=1}^N X(t+\Delta t_d + j\Delta t) \right\} \times \right. \\ &\quad \left. \left\{ \sum_{k=1}^N X(t+k\Delta t) + \sum_{l=1}^N X(t+\Delta t_d + l\Delta t) \right\} \right] \end{aligned} \quad (2-10)$$

$$E[\hat{M}(T)M(T)] = E\left[\frac{1}{(2N) \cdot T} \left\{ \sum_{i=1}^N (t+i\Delta t) + \sum_{j=1}^N X(t+\Delta t_d + j\Delta t) \right\} \cdot \int_0^T X(t)dt\right] \quad (2-11)$$

For a physical time-dependent function Q , its expected value $E(Q)$ may be represented as the limit of a time average of Q ; if the limit exists.

$$E(Q) = \lim_{L \rightarrow \infty} \frac{1}{L} \int_0^L Q(a)da \quad (2-12)$$

with L representing time. Therefore the true mean of $X(t)$ denoted by $E[X(t)] = \bar{X}$ is

$$\bar{X} = \lim_{L \rightarrow \infty} \frac{1}{L} \int_0^L X(t) dt. \quad (2-13)$$

The autocovariance function may be calculated as

$$R(\tau) = \lim_{L \rightarrow \infty} \frac{1}{L} \int_0^L [X(t) - \bar{X}][X(t+\tau) - \bar{X}] dt, \quad (2-14)$$

where τ is the time lag. Expanding the terms in the integrand yields

$$R(\tau) = \lim_{L \rightarrow \infty} \frac{1}{L} \int_0^L [X(t)X(t+\tau) dt - \bar{X}^2]. \quad (2-15)$$

Let us evaluate the expected values of the expressions (2-9), (2-10), and (2-11):

$$E[M^2(T)] = \lim_{L \rightarrow \infty} \left[\frac{1}{L} \int_0^L \frac{1}{T^2} \int_0^T X(t+a) dt \int_0^T X(s+\alpha) ds \right] da, \quad (2-16)$$

and

$$E[M^2(T)] = \frac{1}{T^2} \int_0^T \int_0^T \lim_{L \rightarrow \infty} \left[\frac{1}{L} \int_0^L X(t+a)X(s+\alpha) da \right] dt ds \quad (2-17)$$

Letting $u = t+a$,

$$E[M^2(T)] = \frac{1}{T^2} \int_0^T \int_0^T \lim_{L \rightarrow \infty} \left[\frac{1}{L} \int_0^L X(u)X(u+s-t) du \right] dt ds, \quad (2-18)$$

and

$$E[M^2(T)] = \frac{1}{T^2} \int_0^T \int_0^T [R(s-t) + X^2] dt ds, \quad (2-19)$$

if $s-t = \text{constant}$, so that $R(s-t) = \text{constant}$, we have a stationary time series. Therefore, we may simplify equation (2-19) through inspection of the area in the (s,t) plane over which the integration is performed. Choosing a coordinate system with one axis parallel to the lines $s-t = c$ simplifies evaluation of the integral because R will be constant on all lines parallel to the axis. Let

$$x = (s+t)/\sqrt{2}, \quad y = (s-t)/\sqrt{2}$$

Then,

$$E[M^2(T)] = \frac{1}{T^2} \int_0^{T/2} \int_{x=-2T+y}^{x=2T-y} [R(\sqrt{2}y) + \bar{X}^2] dx dy \quad (2-20)$$

Letting $U = \sqrt{2}y$,

$$E[M^2(T)] = \frac{2}{T} \int_0^T (1-U/T) [R(U) + \bar{X}^2] dU \quad (2-21)$$

$$\begin{aligned} E[(\hat{M}^2(T))] &= \lim_{L \rightarrow \infty} \frac{1}{L} \int_0^L \frac{1}{(2N)^2} \left[\sum_{i=1}^N \sum_{k=1}^N X(L+i\Delta t) X(L+k\Delta t) \right] dL \\ &+ \lim_{L \rightarrow \infty} \frac{1}{L} \int_0^L \frac{1}{(2N)^2} \left[\sum_{i=1}^N \sum_{l=1}^N X(L+i\Delta t) X(L+\Delta t_d + l\Delta t) \right] dL \\ &+ \lim_{L \rightarrow \infty} \frac{1}{L} \int_0^L \frac{1}{(2N)^2} \left[\sum_{j=1}^N \sum_{k=1}^N X(L+\Delta t_d + j\Delta t) X(L+k\Delta t) \right] dL \end{aligned}$$

$$+ \lim_{L \rightarrow \infty} \frac{1}{L} \int_0^L \frac{1}{(2N)^2} \left[\sum_{j=1}^N \sum_{l=1}^N X(L+\Delta t_d+j\Delta t)X(L+\Delta t_d+l\Delta t) \right] dL \quad (2-22)$$

Working out the integrals in (2-22) by almost the same procedure as above,

$$\begin{aligned} E[\hat{M}^2(T)] = \frac{1}{(2N)^2} & \left[2NxR(0) + 2NxR(\Delta t_d) + 2 \sum_{K=1}^{N-1} 2(N-K)R(K\Delta t) \right. \\ & + 2 \sum_{k=1}^{N-1} (N-K)R(K\Delta t + \Delta t_d) \\ & \left. + 2 \sum_{k=1}^{N-1} (N-K)R(K\Delta t - \Delta t_d) \right] \quad (2-23) \end{aligned}$$

$$\begin{aligned} E[\hat{M}(T)M(T)] &= \lim_{L \rightarrow \infty} \int_0^L \frac{1}{(2N)T} \left[\sum_{i=1}^N X(L+i\Delta t) \int_0^T X(L+t)dt \right] dL \\ &+ \lim_{L \rightarrow \infty} \int_0^L \frac{1}{(2N)T} \left[\sum_{j=1}^N X(L+\Delta t_d+j\Delta t) \int_0^T X(L+t)dt \right] dL \quad (2-24) \end{aligned}$$

Using the same procedure,

$$E[\hat{M}(T)M(T)] = \frac{1}{(2N)T} \int_0^T \left[\sum_{i=1}^N [R(t-i\Delta t) + X^2]dt + \sum_{j=1}^N \int_0^T [R(t-\Delta t_d-j\Delta t) + X^2]dt \right] \quad (2-25)$$

Finally, from (2-8), (2-21), (2-23) and (2-25),

$$\begin{aligned}
\sigma_e^2 = & \frac{2}{T} \int_0^T \left(1 - \frac{\tau}{T}\right) R(\tau) d\tau \\
& + \frac{1}{(2N)^2} \{ 2NR(0) + 2NR(\Delta t_d) \\
& + 2 \sum_{K=1}^{N-1} 2(N-K)R(K\Delta t) \\
& + 2 \sum_{K=1}^{N-1} (N-K)R(K\Delta t + \Delta t_d) \\
& + 2 \sum_{K=1}^{N-1} (N-K)R(K\Delta t - \Delta t_d) \} \\
& - \frac{2}{(2N)T} \left\{ \sum_{k=1}^N \int_0^T R(\tau - k\Delta t) d\tau + \sum_{k=1}^N \int_0^T R(\tau - k\Delta t - \Delta t_d) d\tau \right\}
\end{aligned} \tag{2-26}$$

2.2 Sun-synchronous Polar Orbit

For a sun-synchronous polar orbit, inserting $\Delta t_d = \Delta t/2 = 12$ hours in the general expression (2-26) suffices to describe the sampling error.

2.3 The Case of Two Simultaneous Sun-synchronous Satellite Observations

In observations by two simultaneous SSO satellites, it is assumed that precipitation is observed by the same microwave sensors and they are perfect so that no optimal weighting scheme is required due to different measurement errors for the different spacecrafts.

The two satellite observations can reduce the observation interval to shorter than 12 hours depending on their phase difference Δt_d . If Δt_d is six hours, four observations

are available in a day for a given area with 6 hour intervals. In this case, the estimated mean can be expressed by:

$$\hat{M}_{ss}(T) = \frac{1}{(2N)} \left[\sum_{i=1}^N X(t+it_0) + \sum_{j=1}^N (t+\Delta t_d+jt_0) \right], \quad (2-27)$$

where t_0 is 12 hours.

Following the same steps of calculations as in chapter 2.1, the MSE for 2 SSO satellite observations is the same as (2-26) except Δt is replaced by t_0 , and their difference is in the values of Δt , Δt_d , and t_0 .

I shall express the sampling error by standard error, that is in percent of monthly area-averaged mean rain rate ($100 \cdot \sigma_e / \bar{X}$).

3. SAMPLING CHARACTERISTICS OF A SATELLITE

3.1 Orbital Dynamics for Sampling Error Study

The sampling error defined in equation (2-26) depends on the sequence of satellite observing times and sampling intervals, since this sequence determines the accuracy of the estimated mean rain rate from satellite observations. In generating sequences of satellite overpasses, it is assumed that the orbits are circular.

According to Brooks (1977), the longitude-latitude history relative to an initial point on the equator is calculated as

$$\phi = \sin^{-1}[\sin(i) \sin((\Theta + \theta)t)] \quad (3-1)$$

$$\lambda = \tan^{-1}[\cos(i) \tan((\Theta + \theta)t)] - (\Omega - \omega)t \quad (3-2)$$

where

ϕ, λ latitude and longitude,

i inclination of satellite orbit,

Θ perturbed mean angular velocity of the satellite on its orbital plane,

θ angular velocity of precession on its orbital plane due to earth's oblateness,

ω angular velocity of precession on the equatorial plane due to earth's

oblateness,

Ω earth's angular velocity on the equatorial plane,

t time, and

h the satellite altitude.

Let $\Theta + \theta = \alpha$ and $\Omega - \omega = \beta$. Then from (3-1) and (3-2), we have

$$t = \frac{1}{\alpha} [2\pi n + \sin^{-1}\left(\frac{\sin\phi}{\sin i}\right)] = n\tau_n + 1/\alpha \sin^{-1}\left(\frac{\sin\phi}{\sin i}\right) \quad (3-3)$$

$$\lambda = -\frac{\beta}{\alpha} [2\pi n + \sin^{-1}(\frac{\sin \phi}{\sin i})] + \tan^{-1}[\cos i \tan(\sin^{-1}(\frac{\sin \phi}{\sin i}))]. \quad (3-4)$$

Where n (integer) is the number of rotations and τn is the nodal period of the satellite for the given orbit. Then (3-3) gives the time at which the satellite crosses latitude ϕ in rotation n , and (3-4) gives the longitude when the satellite passes latitude ϕ .
 $\tau_n = 2\pi/\alpha$.

For the ascending node,

$$t_a = \frac{1}{\alpha} [2\pi n + \sin^{-1}(\frac{\sin \phi}{\sin i})] \quad (3-5)$$

while for the descending node,

$$t_d = \frac{1}{\alpha} [2\pi n + \pi - \sin^{-1}(\frac{\sin \phi}{\sin i})]. \quad (3-6)$$

Similarly,

$$\lambda_a = -\frac{\beta}{\alpha} [2\pi n + \sin^{-1}(\frac{\sin \phi}{\sin i})] + \tan^{-1}[\cos i \tan(\sin^{-1}(\frac{\sin \phi}{\sin i}))], \text{ and} \quad (3-7)$$

$$\lambda_d = -\frac{\beta}{\alpha} [2\pi n + \pi - \sin^{-1}(\frac{\sin \phi}{\sin i})] + \pi - \tan^{-1}[\cos i \tan(\sin^{-1}(\frac{\sin \phi}{\sin i}))]. \quad (3-8)$$

From (3-5), (3-6), (3-7), and (3-8),

$$t_{a_{n+1}} - t_{a_n} = t_{d_{n+1}} - t_{d_n} = 2\pi/\alpha = \tau_n, \quad (3-9)$$

$$\lambda_{a_{n+1}} - \lambda_{a_n} = \lambda_{d_{n+1}} - \lambda_{d_n} = -2\pi \cdot \beta/\alpha = -\beta\tau_n, \quad (3-10)$$

and

$$t_d - t_a = 1/\alpha [\pi - \sin^{-1}(\frac{\sin \phi}{\sin i})] \quad (3-11)$$

$$\lambda_d - \lambda_a = \beta/\alpha [\pi - 2\sin^{-1}(\frac{\sin \phi}{\sin i})] + \pi - 2\tan^{-1}[\cos i \tan(\sin^{-1}(\frac{\sin \phi}{\sin i}))]. \quad (3-12)$$

Therefore, the ascending and descending nodes can be treated as separate sequences which differ in initial phase depending on ϕ . Define the repetition factor

$$Q = \Theta + \theta / \Omega - \omega = \alpha / \beta$$

Thus,

$$\Delta t = (t_{a_{n+1}} - t_{a_n}) \cdot Q = 2\pi / \beta = f(i, h) = \text{constant, for a given } i, h, \text{ and} \quad (3-13)$$

$$\Delta t_d = (t_{d_n} - t_{a_n}) \cdot Q = 1/\beta [\pi - 2\sin^{-1}(\sin\phi/\sin i)] = f(i, h, \phi) =$$

constant, for a given $i, h, \phi,$ (3-14)

Δt is the time from one observation by an ascending/descending node to the next observation by an ascending/descending node over a particular spot on the earth. Likewise, Δt_d is the time from one observation by an ascending/descending node. For the sun-synchronous orbit, Δt is equal to one day. If the orbital parameters do not satisfy the aforementioned condition, that is for a low inclination orbit, the orbital plane will precess either eastward ($\Delta t > 1$ day) or westward ($\Delta t < 1$ day) with respect to the earth. The deviations of Δt from one day for various orbits are summarized in figure 2. In this figure, the difference is in minutes between the visiting interval of the given low inclination orbit and that of a sun-synchronous. The visiting interval by an ascending/descending node will be limited to within 30 minutes of 24 hours.

3.2 Sampling Characteristics of the Satellites

I shall assume that the viewing characteristics of the satellites are similar to those of the Electrical Scanning Microwave Radiometer (ESMR) flown on the Nimbus-5 satellite. Even though this sensor is not aboard NOAA, I shall assume that it is. In fact, I consider the orbit of NOAA-10 with an imaginary ESMR (the one planned to fly

on TRMM satellites) flown on it. The ESMR measures the intensity of microwave radiation at 19.35 GHz in 78 fields of view (FOV's) during each scan of the instrument. The instrument scans perpendicularly to the direction of satellite motion, from about 50° to the left of nadir to about 50° to the right of nadir, requiring 4 seconds per scan. The beam widths of the FOV's ranged from $1.4^\circ \times 1.4^\circ$ near nadir to $1.4^\circ \times 2.2^\circ$ at the 50° extremes. This sensor is interesting in this study because its FOV's overlap substantially, and nearly complete coverage of the area within the view of the satellite is assured. This condition is necessary for the assumption of flush visits. Consequently, for a better and total coverage of the $5^\circ \times 4^\circ$ grid boxes, I extend the average effective size of the swath to about 54° on either side of nadir.

Knowing the scan angle (54°), the longitude and latitude of the grid box center, the altitudes of the satellites, and the size of the grid box (5° by 4°), the parameters of the orbits and the visiting times of the satellites are calculated using the computer model in Appendix. Table 1 summarizes those parameters for the TRMM orbit and the NOAA orbit satellites assumed to carry the ESMR. Figure 3 presents the variations of sampling interval Δt_d versus latitude for the TRMM orbit. This variation is caused by the orbit precession. For the sun-synchronous orbit, there is no orbital precession and Δt and Δt_d equal 12.00 and 6.00 hours respectively. Recall, for given inclination i , and altitude h , Δt is constant while Δt_d is function of latitude ϕ .

4. RAINFALL DISTRIBUTION IN TIME

4.1 Examples of Rainfall Distribution

Figure 4 gives the distribution of area-averaged rain rate over the grid boxes considered during the months of December, January and February for the GCM data. The monthly mean rain rates and their standard deviations are tabulated in Table 2 and presented in Figures 5 and 6. As can be seen, area-averaged rain rates are highly variable with respect to time and grid box location. Although the period considered corresponds to the rainy season of the region (south of the equator), the monthly averages of area-averaged rain rate are moderate. They vary from 0.08 mm/hr to 1.13 mm/hr during the three months. A close look at the rain rate distribution shows the existence of diurnal cycle, especially the rain rate distribution in the grid box centered at 150°E, 10°S. It should however be indicated that I did not study the temporal variability of rain rate.

4.2 The Autocovariance Functions

The autocovariance function is determined by investigating the GCM area-averaged rain rate time series and using the formula

$$R(\tau) = \lim_{L \rightarrow \infty} \frac{1}{L} \int_0^L [X(t) - \bar{X}][X(t+\tau) - \bar{X}] dt \quad (4-1)$$

The autocovariance functions calculated for different grid boxes for the three months of December, January and February are presented in Figures 7, 8, and 9. All the

derived curves almost appear to be examples of exponential decay. Each is least squared fitted to a function of the form

$$R(\tau) = B \exp(-|\frac{\tau}{\tau_0}|) \quad (4-2)$$

where B is the coefficient of variation and τ_0 is the autocorrelation time. This fit is simply a first-order Markov process. The best fit values of B and τ_0 are tabulated in Table 2 and Figure 8 presents the variation of the correlation time versus grid box center.

4.3 Final Note on the Sampling Error Derivation

The analytic form (4-2) of the autocovariance function allows for simpler evaluation of the sampling error using the following relationships:

$$\int_0^T R(\tau) d\tau = B\tau_0(1 - e^{-T/\tau_0}) \quad (4-3)$$

$$\int_0^T \tau R(\tau) d\tau = B(\tau_0^2 - \tau_0^2 e^{-T/\tau_0} - T\tau_0 e^{-T/\tau_0}) \quad (4-4)$$

$$\int_0^T R(\tau - k\Delta t) d\tau = 2B\tau_0 - B\tau_0^2 e^{-k\Delta t/\tau_0} - B\tau_0 e^{-T/\tau_0} e^{k\Delta t/\tau_0} \quad (4-5)$$

$$\int_0^T R(\tau - k\Delta t - \Delta t_d) d\tau = 2B\tau_0 - B\tau_0^2 e^{-T/\tau_0} e^{k\Delta t/\tau_0} e^{\Delta t_d/\tau_0} - e^{-k\Delta t/\tau_0} e^{\Delta t_d/\tau_0} \quad (4-6)$$

and the geometric series

$$\sum_{i=1}^N A^i = \frac{A(1-A^N)}{(1-A)} \quad (4-7)$$

Using (4-3), (4-4), (4-5), and (4-6) in (2-26) yields

$$\begin{aligned}
 \sigma_e^2 = & \frac{B}{(T/\tau_o)} \left[-2 + \frac{\Delta t}{2\tau_o} \left\{ \frac{(e^{\Delta t_d/\tau_o} + 1) + e^{\Delta t/\tau_o} (e^{-\Delta t_d/\tau_o} + 1)}{(e^{\Delta t/\tau_o} - 1)} \right. \right. \\
 & + \frac{(e^{-T/\tau_o} - 1)}{(T/\tau_o)} \left\{ 2 - \frac{\Delta t}{\tau_o} \left\{ \frac{(e^{\Delta t_d/\tau_o} + 1) + e^{\Delta t/\tau_o} (e^{-\Delta t_d/\tau_o} + 1)}{(e^{\Delta t/\tau_o} - 1)} \right. \right. \\
 & \left. \left. + \frac{1}{2} \left(\frac{\Delta t}{\tau_o} \right)^2 \frac{e^{\Delta t/\tau_o} (e^{-\Delta t_d/\tau_o} + 2 + e^{-\Delta t_d/\tau_o})}{(e^{\Delta t/\tau_o} - 1)^2} \right\} \right] \quad (4-8)
 \end{aligned}$$

For observations with one sun-synchronous polar orbiting satellite, $\Delta t_d = \Delta t/2 \approx 12$ hours. With simultaneous measurements from sun-synchronous polar-orbiting satellites, $\Delta t = t_o \approx 12$ hours and $\Delta t_d \approx 6$ hours.

5. SAMPLING RESULTS AND DISCUSSIONS

Table 2 summarizes the sampling errors of the monthly area averaged rain rate estimates for the three different orbits of TRMM, NOAA and the 2 simultaneous sun-synchronous orbit over the three months (December, January, and February) of the Northern Hemisphere winter. Figures 9 to 20 present the variation of sampling errors of the monthly area averaged rain rate versus grid box center, monthly mean area average rain rate, standard deviation of the rainfall and correlation time of the rainfall time series.

In December, on the average, the sampling error for the monthly mean rain rate estimate over a $5^{\circ} \times 4^{\circ}$ grid box is 9.33% for the proposed TRMM orbit satellite observations, 9.61% for the NOAA orbit satellite observations and 4.33% for simultaneous observations with two sun-synchronous polar orbiting satellites.

In January, it is 9.94% for the TRMM orbit satellite observations, 10.25% for the NOAA orbit satellite observations and 4.86% for simultaneous observations with two sun-synchronous polar orbiting satellites.

In February, it is 10.15% for the TRMM orbit satellite observations, 10.46% for the NOAA orbit satellite observations and 4.95% for simultaneous observations with two sun-synchronous polar orbiting satellites (see Figure 21).

As an observation, sampling errors for the three orbits increase somewhat from December to February. This is mainly due to the correlation of rainfall; the average correlation time decreases substantially from about 13.30 hours in December to about 10.00 hours in February. At the same time, the monthly mean, the standard deviation of

the area averaged rain rate and the coefficient of variation of the autocovariance function remain almost constant from December to January, and decrease from January to February (see Figure 22). The forms of the variations of sampling errors versus monthly rainfall mean or autocorrelation time or standard deviation of the rainfall distribution for the three orbits during the three months are similar. The differences, on the other hand, are in the magnitudes of the different parameters indicating that the overall area-averaged rain rate statistics are similar for given seasons and areas. As a consequence, one may use the same statistical model to study rainfall in an area during a season. Moreover, sampling errors have a tendency to decrease with increasing monthly mean area-averaged rain rate and to increase with increasing standard deviation because the less rainfall the satellite senses, the less accurate is the measurement. The more variable the rainfall distribution is in time, the less accurate is the measurement by the sensor. The non-linear decrease and pseudo wave-like variations depend on the contribution of the autocorrelation time τ_0 in the formulation of sampling error (see formula 4-8). The value of this parameter is not constant, therefore, its combination with exponentials affects greatly the sampling errors giving them sometimes pseudo-periodic variations. The visiting intervals Δt , is constant for a given orbit characteristic (inclination and altitude). The sampling intervals Δt_d on the other hand decreases linearly with increasing latitude. The wave-like variation of the sampling error against the autocorrelation time and latitude results from the same reason.

The sampling error of the TRMM orbit is almost equal to that of the SSO NOAA. The satellite orbit study shows that for grid boxes in the equatorial region, as it is in the case of the present study, the visiting time interval of a low inclination orbit satellite is almost equal to that of the sun-synchronous orbit. In Figure 3 we see that the sampling interval varies from 11.68 hours to 11.83 hours for the range of latitude

between 22°S and 14°N. This is not very different from the 12 hours of the sun-synchronous orbit. Typically, there are no more than two observations a day. As a result, the sampling errors are almost equal. Away from the equator, a low-inclination orbit satellite may revisit a given location more than twice a day. It follows then that the visiting interval reduces and so does the sampling error compared to that of the sun-synchronous orbit. Even though those two orbits provide almost the same sampling error, the FOV of the TRMM is smaller than that of the sun-synchronous orbit because of its low altitude (in the present study almost half of that of the sun-synchronous). Consequently, the error due to the beam-filling problem would be reduced. Furthermore, the expected additional errors due to the diurnal cycle of the rain field will be added to the sun-synchronous orbit because of its fixed visiting sequences, twice a day, while they tend to be cancelled by the TRMM orbit. Because of this, the overall error would be smaller with a TRMM orbit.

The sampling error reduces by a factor almost of two when considering simultaneous observations with two satellites sun-synchronous orbit. In the same vein, the diurnal cycle in the rain field would not be significant in this case because with four observations a day, the system can resolve all the harmonics of the diurnal cycle. Yet, the large field of view, due to the high altitude, could add large errors caused by the beam-filling problem.

When the monthly mean area-averaged rain rate is high, for instance, greater than 0.4 mm/hr, and when the autocorrelation time is less than or equal to 12 hours, the sampling error is roughly about 8% for the TRMM and sun-synchronous orbits and 3% for the two simultaneous sun-synchronous. This result agrees with the former studies done with the GATE data assuming flush visits and varying visiting time intervals (Shin and North, 1988).

6. SUMMARY AND RECOMMENDATIONS

A study of satellite orbits has been conducted to estimate sampling errors of area-time averaged rain rate caused by gaps in satellite observations. This study focused on the proposed low-inclination orbit of TRMM, the sun-synchronous polar orbit of NOAA-10 and simultaneous measurements from two sun-synchronous orbits. This estimate was done by performing a study of the autocovariance functions of the area-averaged rain rate time series. A model based on the exponential fit of the autocovariance function is also used for actual calculations. Varying visiting intervals and total coverage of the averaging area on each visit by the satellites were taken into account in the model.

Of the areas chosen (5° by 4° grid boxes located at 130°E , 150°E , 160°W with latitude varying from 22°S to 10°N), on average, the sampling error for the three months (December, January, and February) of the Northern Hemisphere winter, would be about 10% for a TRMM orbit. This error is within 1% of the sampling error produced by a polar-orbiting NOAA orbit. The systematic error is higher in sun-synchronous polar-orbiting satellites because of their large fields of view. On the other hand, satellites in low-inclination orbits have the potential of filtering expected diurnal cycles from the observation because of their relatively low orbit and inclination. Thus, the preceding findings indicates that tropical precipitation observations with low inclination orbits are more efficient. A simultaneous observation with a system of two sun-synchronous polar orbiting satellites would reduce the sampling error from 10% to about 5%. Such a system would be very effective in observing precipitation which is

very variable in space and time insofar as sampling error is concerned because its four or more observations a day can average out all the harmonics of the diurnal cycle. Still, the large field of view may introduce a large systematic error.

The results obtained in this work provide a quantitative and pedagogic basis for estimating sampling errors as far as the GCM data is concerned. The global results will apply only where the time scales (particularly the diurnal cycle) of the precipitation and the fractional visiting areas are simulated realistically by the model. Another question seldom touched on so far is the idea of merging data from different spacecrafts. Each will have its own measurement error structure as well as its own sampling characteristics. An optimal weighting scheme will have to be devised for the integrations. Microwave data from polar platform can be merged with the low inclination orbiter data by some optimal procedure. We also need to understand the contribution that can be made by integrating other satellites such as GOES. The data used in this work are simulated data. Also, the previous studies depended upon a single oceanic tropical rainfall data set. As a consequence, we must be concerned about their representativeness for conclusions. For rainfall statistics characteristic of the Inter Tropical Convergence Zone (ITCZ) conditions, the results are in line with those obtained with the GATE data for the same assumptions. However, one should be concerned about the uncertainties of some parameters in the statistical model such as the values of the autocorrelation times and coefficients of variation extrapolated from a least-square fit process.

Table 1. Orbits parameters for TRMM and NOAA-10.

ORBIT	TRMM	NOAA-10
ALTITUDE (kilometers)	350.0	833.0
INCLINATION (Degrees)	35.0	98.9
SCAN ANGLE (Degrees)	54.0	54.0
ALPHA (Radian/Second)	0.00114681	0.00102983
BETA (Radian/Second)	0.00007429	0.00007272
NODAL PERIOD (Minutes)	91.31	101.69
PRECESSION OF LONGITUDE (Degree/Orbit)	-23.32051	-25.04531
SWATH HALF-WIDTH (Kilometers)	510.37	1353.63
DELTAT ΔT (Hours)	23.49	24.00

Table 2. Rainfall statistics for December, January, and February.

DECEMBER

Longitude (degree)	Latitude (degree)	Mean Monthly Rain rate (mm/hr)	Standard Deviation (mm/hr)	Correlation Time (hours)	Coefficient of variation	Sampling Error for TRMM (percent)	Sampling Error for NOAA-10 (percent)	Sampling Error for 2 S.S.O. (percent)
130	-10	0.76	0.99	13.29	0.99	7.32	7.55	3.38
130	-6	0.51	0.87	13.18	0.78	9.72	10.02	4.50
130	-2	0.60	0.92	17.08	0.82	8.35	8.57	3.46
130	+2	0.86	1.06	11.35	1.18	7.26	7.50	3.50
130	+6	0.83	1.11	20.09	1.25	7.58	7.76	2.84
130	+10	0.73	1.02	14.89	1.06	7.74	7.97	3.43
150	-10	0.36	0.76	6.07	0.26	10.05	10.36	5.23
150	-6	0.71	0.86	13.31	0.75	6.74	6.95	3.11
-160	-22	0.08	0.24	7.49	0.06	20.46	21.11	10.47
-160	-18	0.24	0.58	14.99	0.35	13.58	13.97	5.99
-160	-14	0.47	0.65	10.72	0.41	7.99	8.25	3.90
-160	-10	0.72	0.78	13.22	0.60	5.98	6.16	2.76
-160	-6	0.39	0.63	15.59	0.37	8.54	8.79	3.71

Table 2, continued

JANUARY		Longitude (degree)	Latitude (degree)	Mean Monthly Rain rate (mm/hr)	Standard Deviation (mm/hr)	Correlation Time (hours)	Coefficient of variation	Sampling Error for TRMM (percent)		Sampling Error for NOAA-10 (percent)		Sampling Error for 2 S.S.O. (percent)	
130	-10			0.85	0.97	10.40	0.97	6.84	7.07	3.55			
130	-6			0.86	1.20	17.69	1.44	7.72	7.92	3.14			
130	-2			1.13	1.16	11.81	1.40	5.97	6.16	2.85			
130	+2			0.70	0.97	12.93	0.95	7.79	8.03	3.62			
130	+6			0.56	0.91	15.78	0.84	8.93	9.18	3.85			
130	+10			0.43	0.75	7.27	0.61	12.10	12.49	6.21			
150	-10			0.45	0.78	5.88	0.35	9.58	9.87	5.00			
150	-6			0.95	0.92	11.29	0.84	5.54	5.72	2.67			
-160	-22			0.14	0.38	7.08	0.15	17.99	18.56	9.25			
-160	-18			0.37	0.67	8.51	0.48	11.61	11.98	5.86			
-160	-14			0.35	0.64	6.38	0.47	13.55	13.97	7.03			
-160	-10			0.27	0.56	10.42	0.32	12.51	12.92	6.13			
-160	-6			0.43	0.73	12.76	0.48	9.03	9.31	4.22			

Table 2, continued

FEBRUARY

Longitude (degree)	Latitude (degree)	Mean Monthly Rain rate (mm/hr)	Standard Deviation (mm/hr)	Correlation Time (hours)	Coefficient of variation	Sampling Error for TRMM (percent)	Sampling Error for NOAA-10 (percent)	Sampling Error for 2 S.S.O. (percent)
130	-10.0	0.67	0.85	18.44	0.68	6.83	7.01	2.71
130	-6.0	0.79	0.98	13.49	0.96	6.87	7.08	3.15
130	-2.0	0.83	1.01	11.50	1.01	6.97	7.19	3.35
130	+2.0	0.60	0.91	5.34	0.98	12.40	12.78	6.52
130	+6.0	0.22	0.56	9.42	0.32	15.84	16.36	7.89
130	+10.0	0.21	0.42	3.93	0.20	18.42	18.95	9.92
150	-10.0	0.38	0.74	6.60	0.31	10.01	10.32	5.18
150	-6.0	0.59	0.71	9.09	0.53	7.54	7.79	3.78
-160	-22.0	0.12	0.35	4.00	0.13	24.74	25.45	13.31
-160	-18.0	0.48	0.59	5.61	0.41	9.85	10.15	5.16
-160	-14.0	0.48	0.57	8.78	0.33	7.45	7.69	3.75
-160	-10.0	0.36	0.51	7.59	0.27	9.38	9.69	4.80
-160	-6.0	0.43	0.71	15.01	0.51	9.22	9.49	4.07

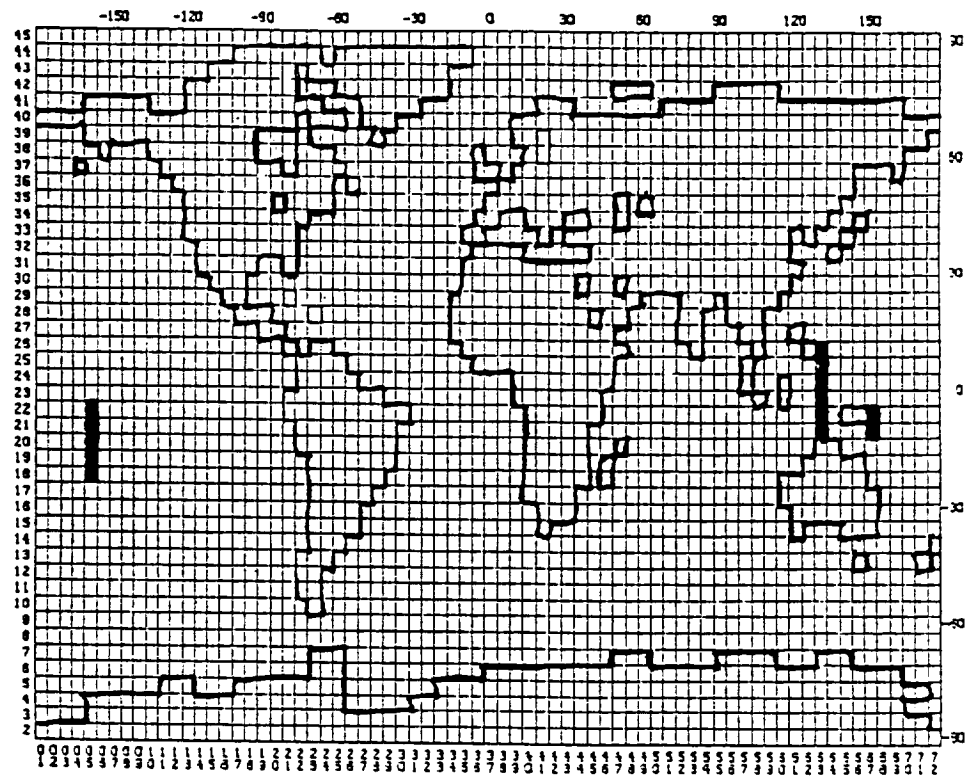


Figure 1. Grid box map.

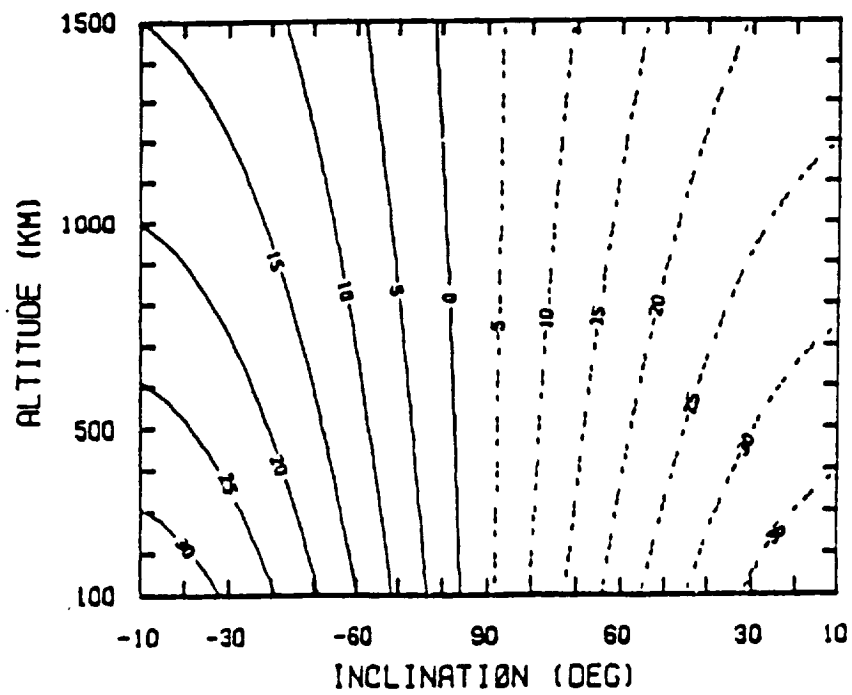


Figure 2. The visiting time differences from that of a sun-synchronous orbit in minutes.

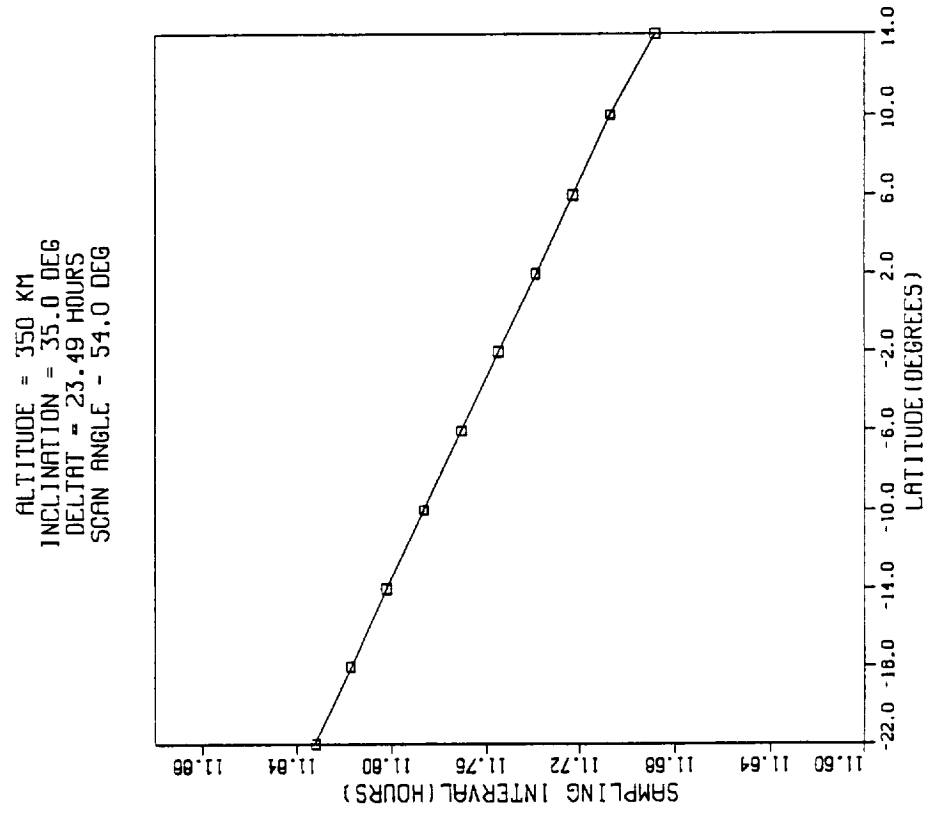


Figure 3. Variation of the sampling intervals versus grid box latitude for the TRMM orbit.

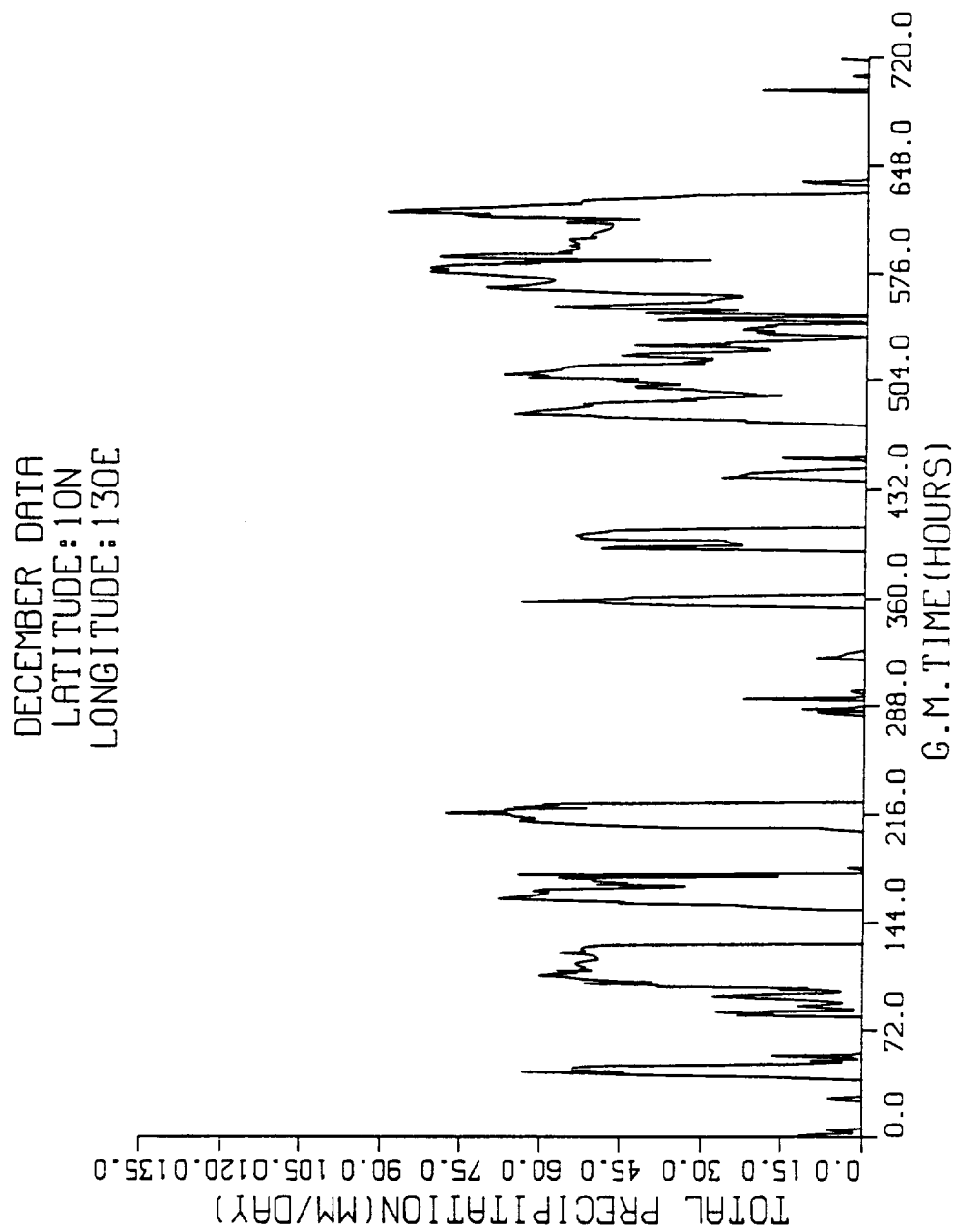


Figure 4. Distribution of the monthly area averaged rain rates versus time for different grid box locations in December, January and February.

DECEMBER DATA
LATITUDE:06N
LONGITUDE:130E

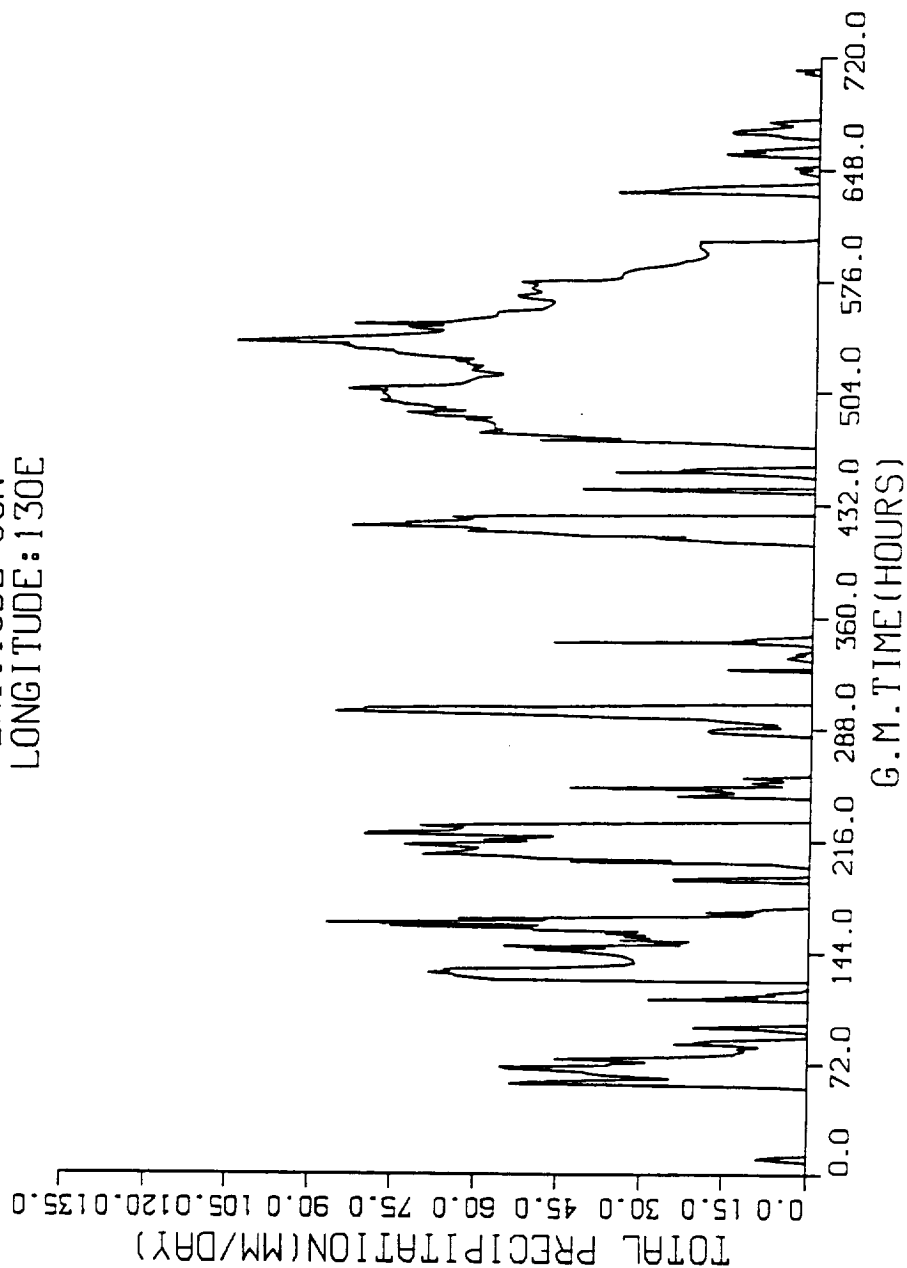


Figure 4, continued

DECEMBER DATA
LATITUDE:02N
LONGITUDE:130E

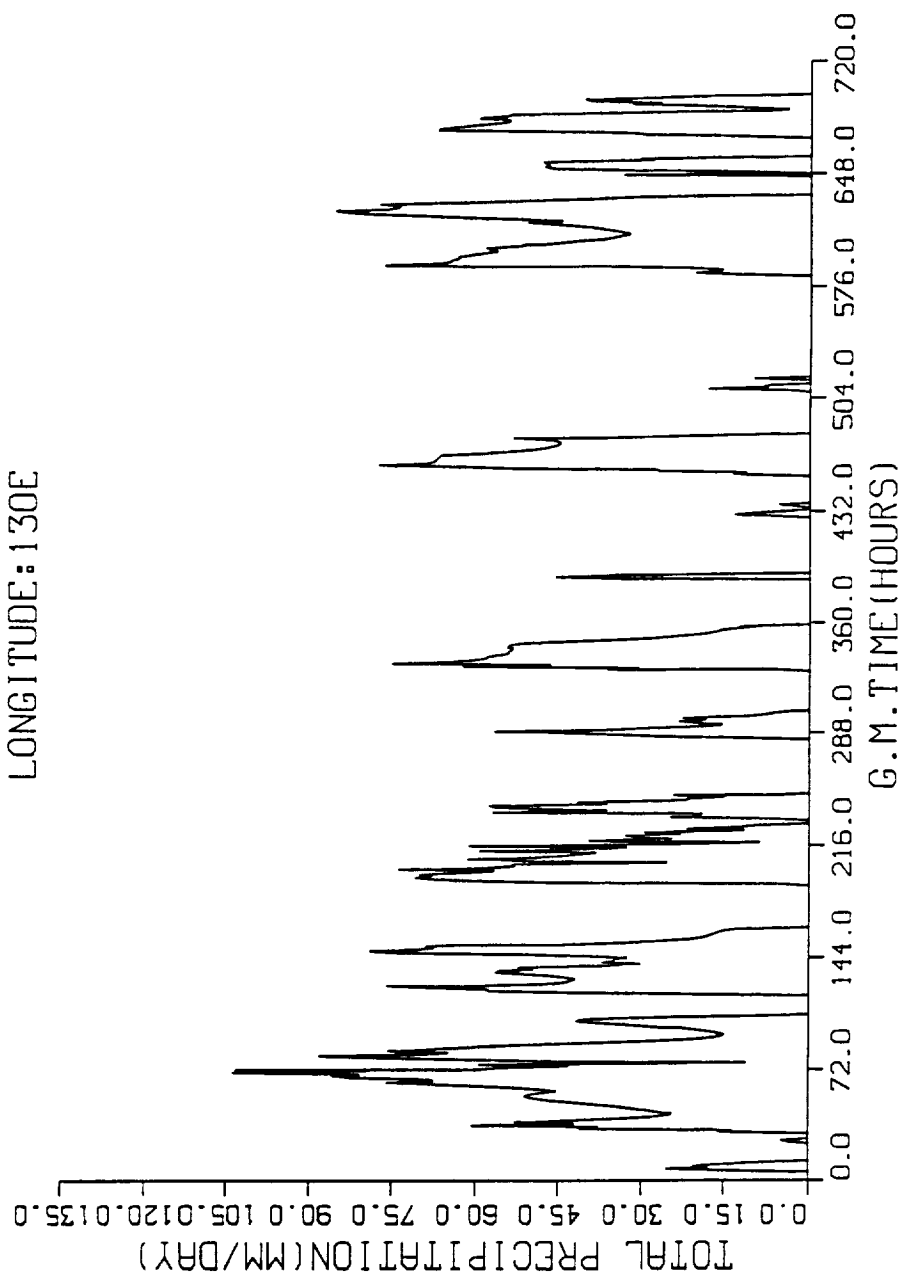


Figure 4, continued

DECEMBER DATA
LATITUDE:02S
LONGITUDE:130E

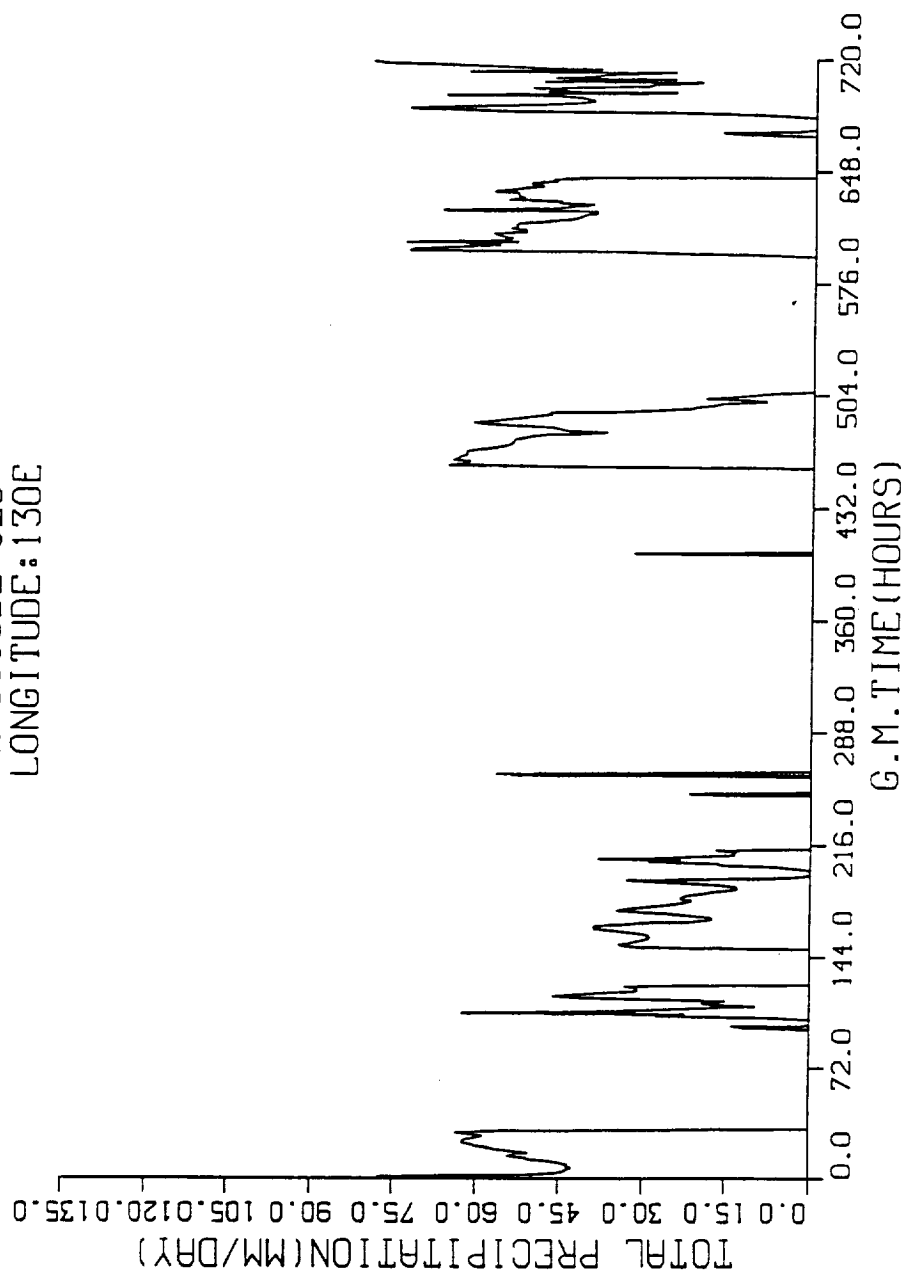


Figure 4, continued

DECEMBER DATA
LATITUDE:06S
LONGITUDE:130E

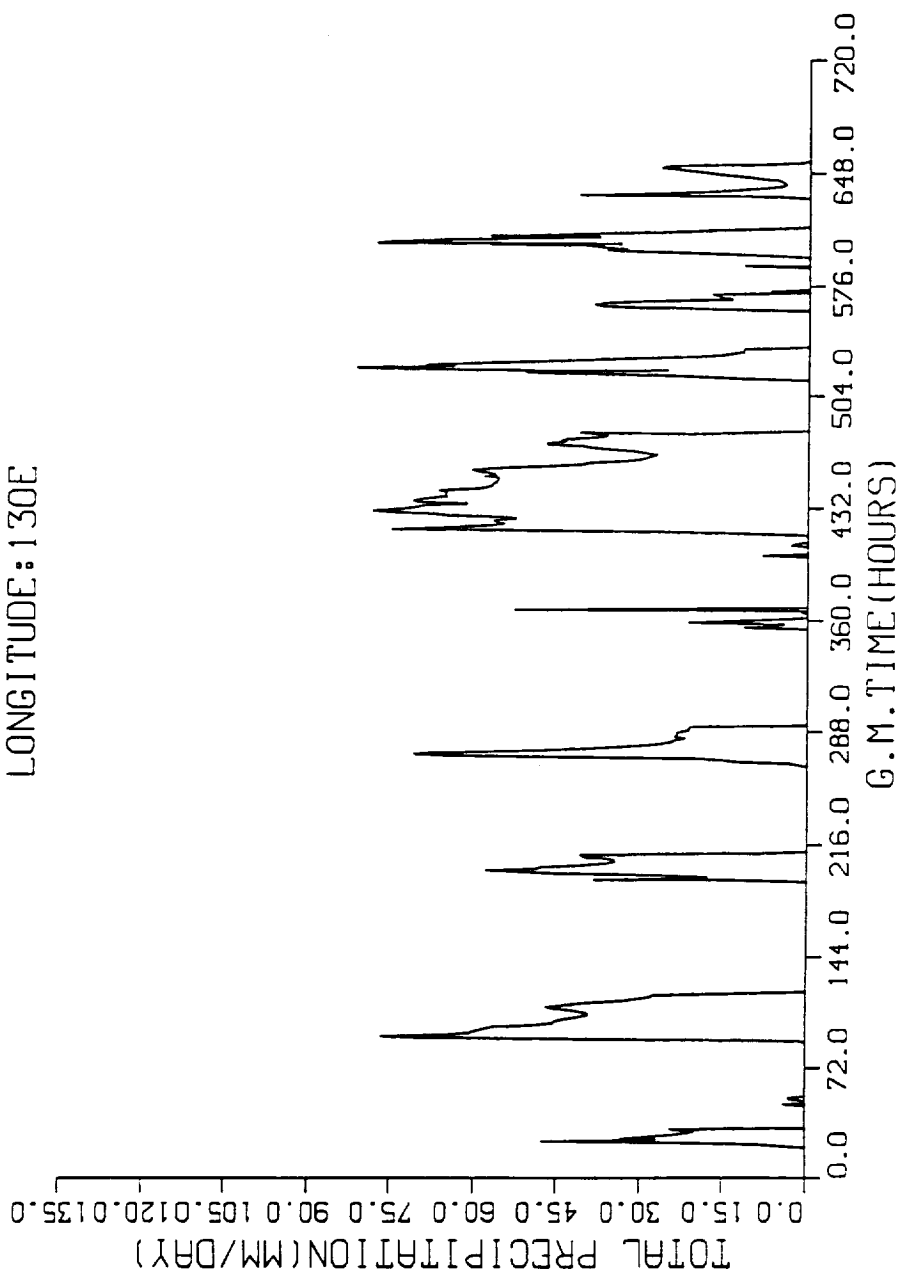


Figure 4, continued

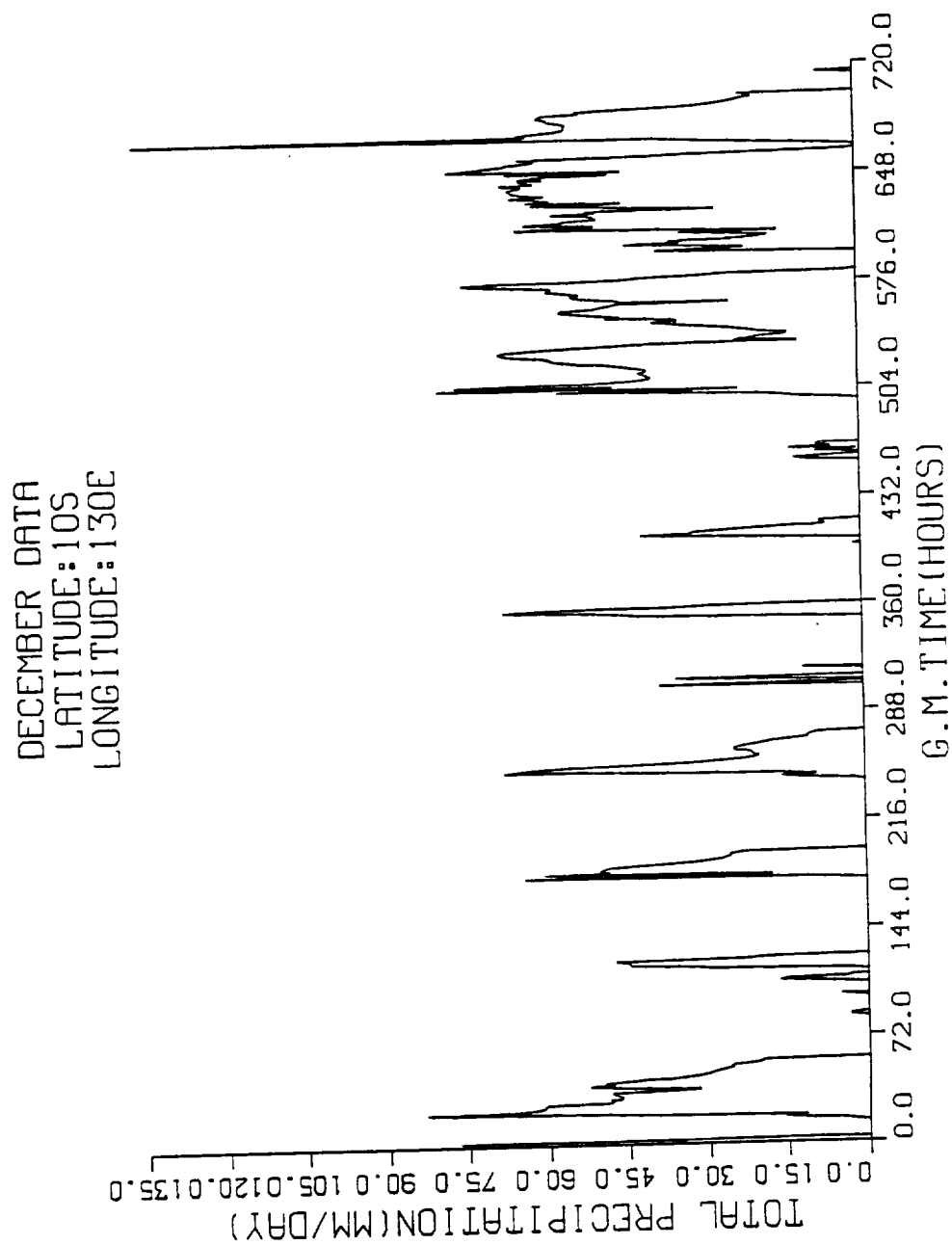


Figure 4, continued

DECEMBER DATA
LATITUDE:10S
LONGITUDE:150E

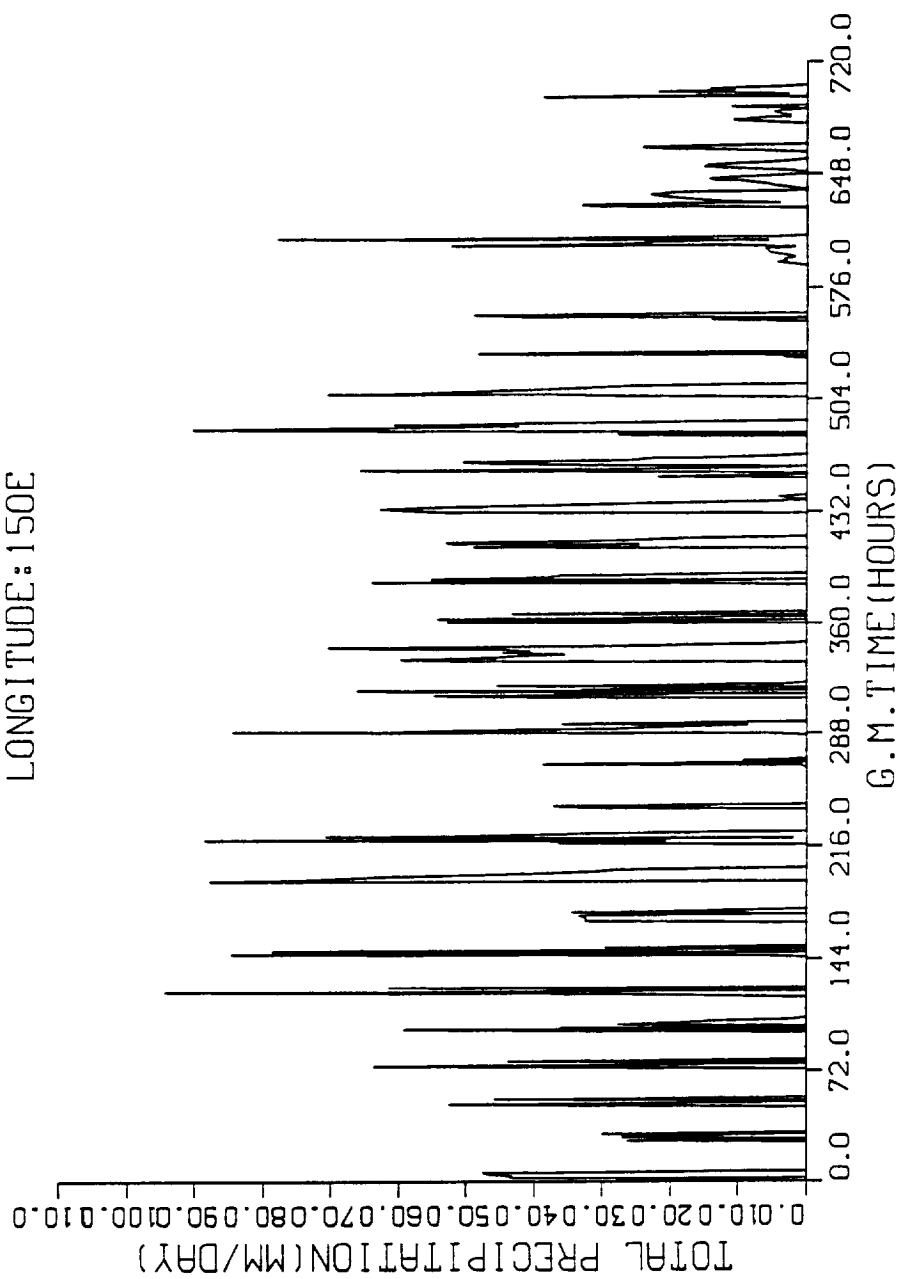


Figure 4, continued

DECEMBER DATA
LATITUDE:06S
LONGITUDE:150E

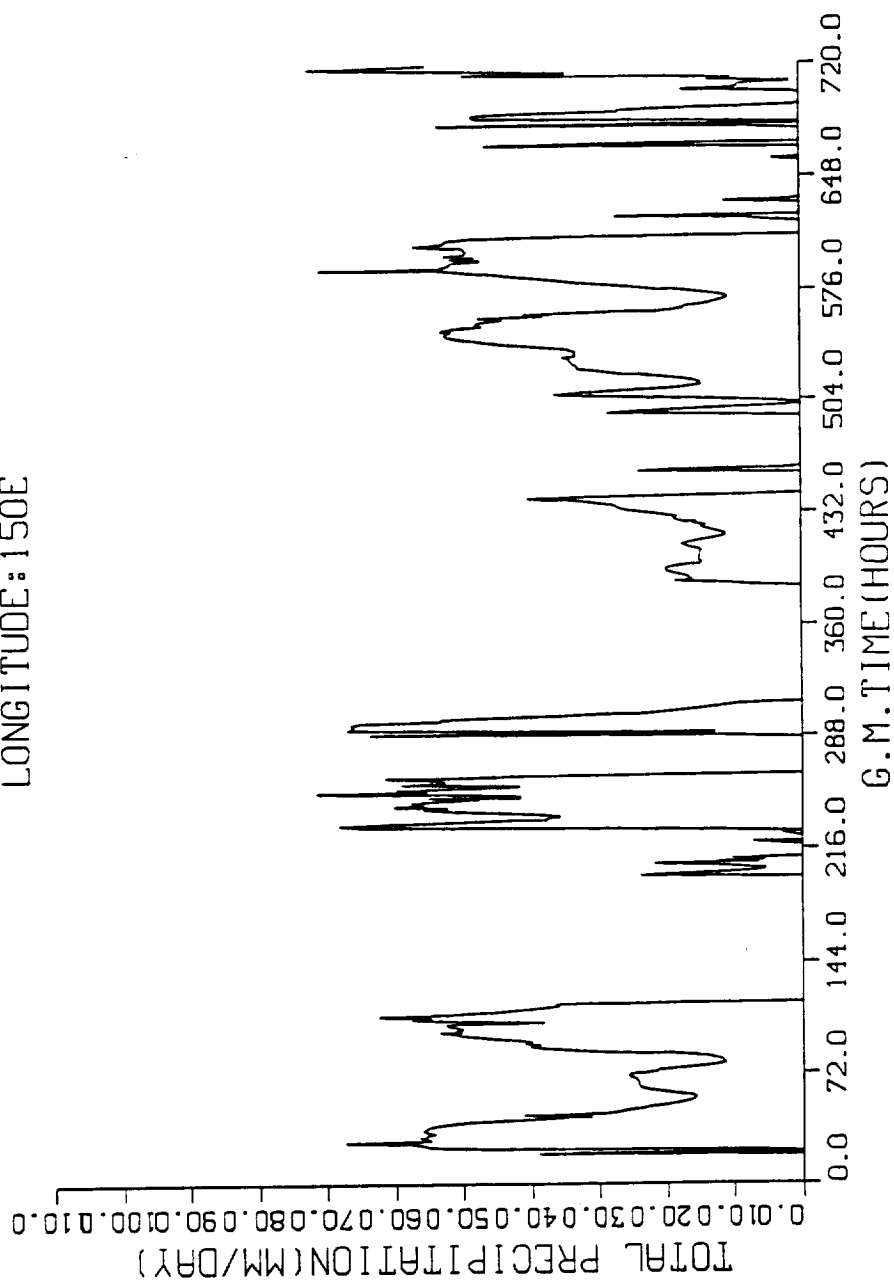


Figure 4, continued

DECEMBER DATA
LATITUDE:06S
LONGITUDE:160W

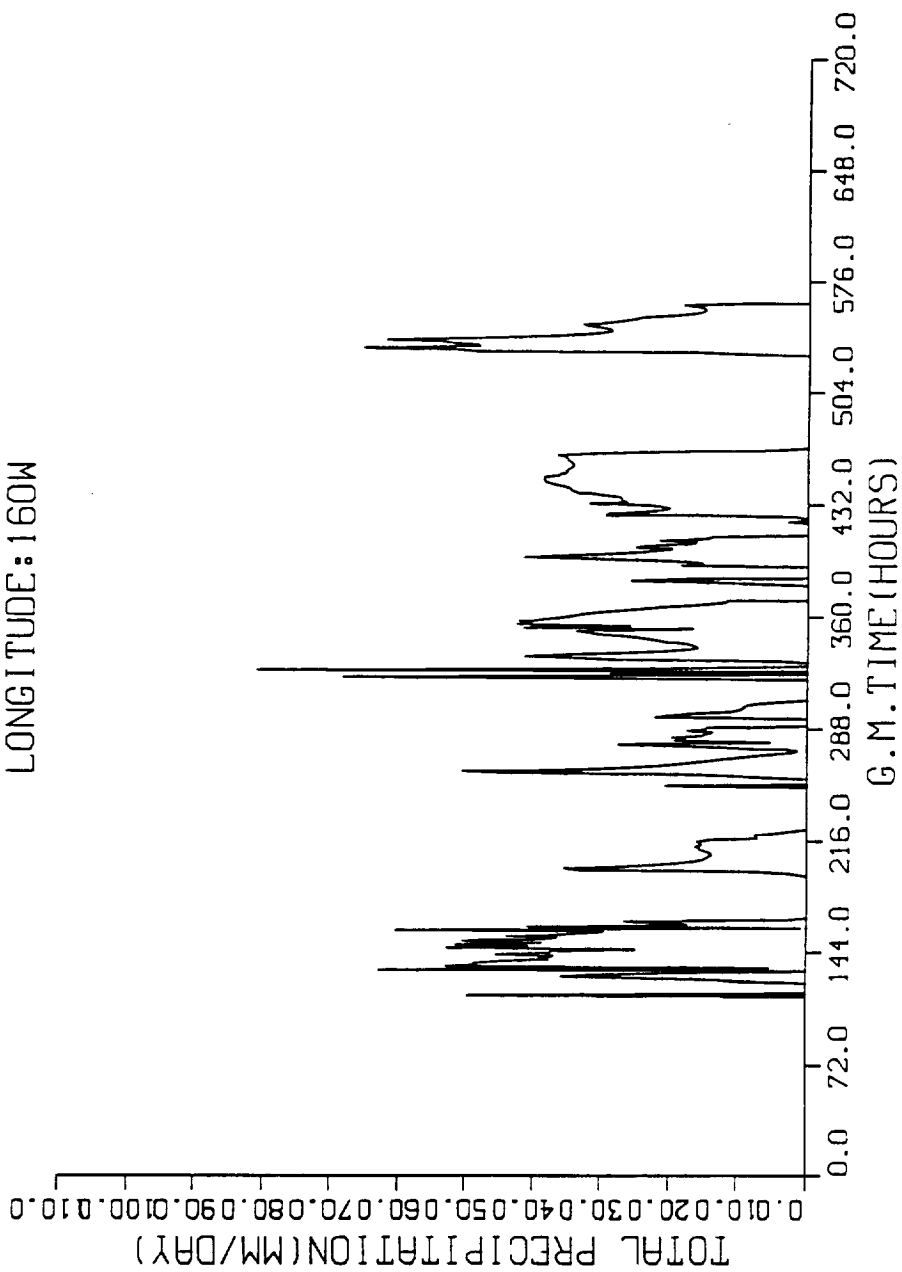


Figure 4, continued

DECEMBER DATA
LATITUDE:10S
LONGITUDE:160W

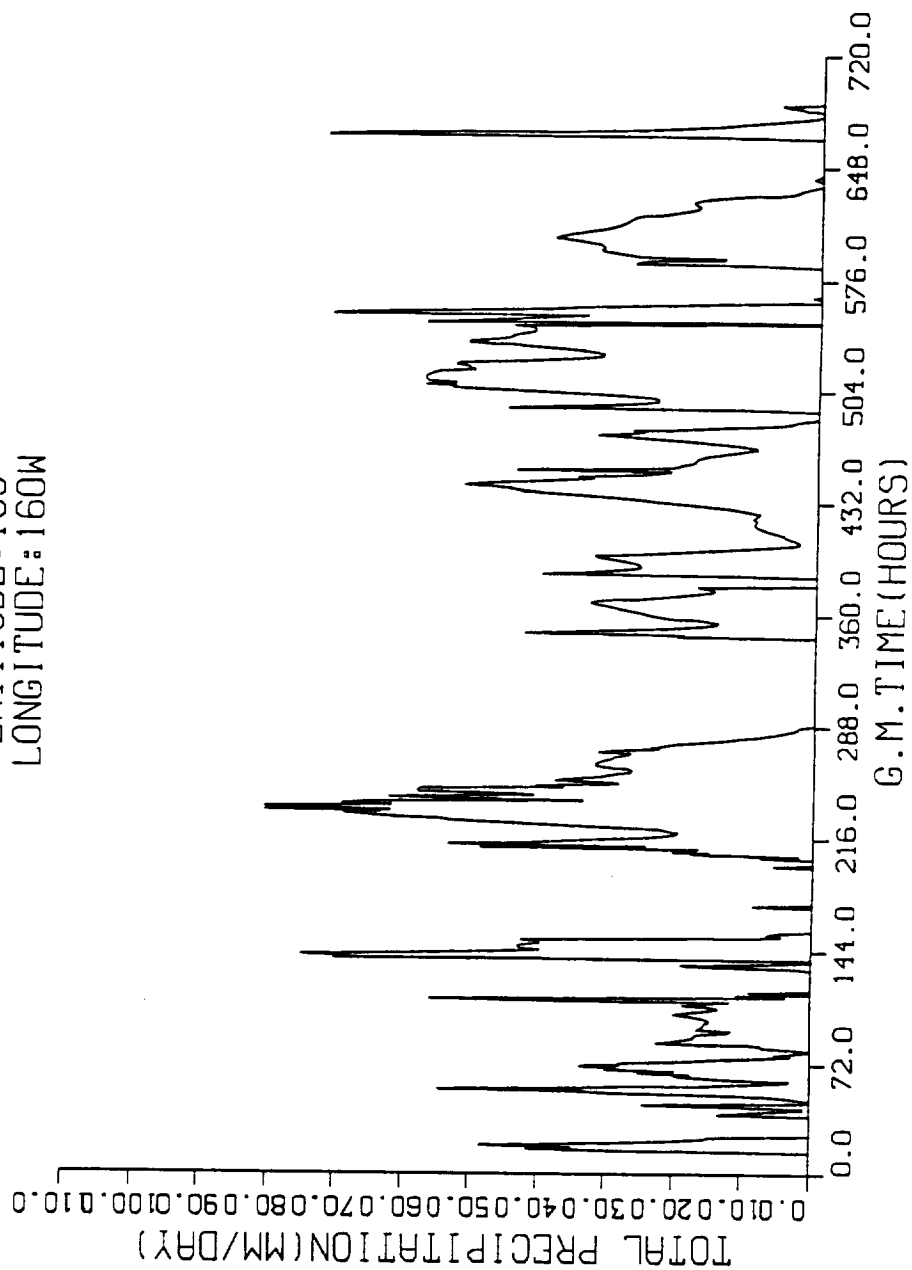


Figure 4, continued

DECEMBER DATA
LATITUDE:14S
LONGITUDE:160W

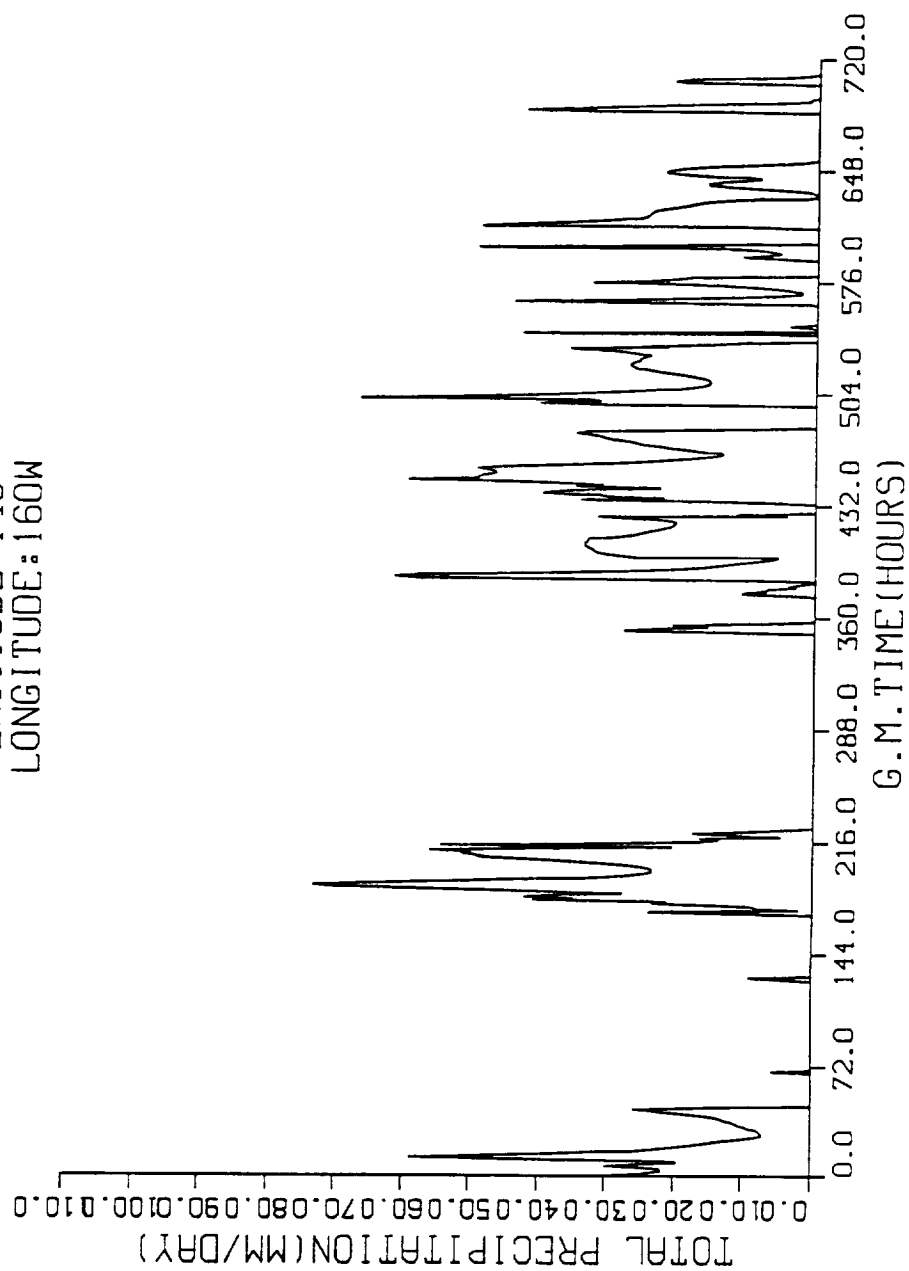


Figure 4, continued

DECEMBER DATA
LATITUDE:18S
LONGITUDE:160W

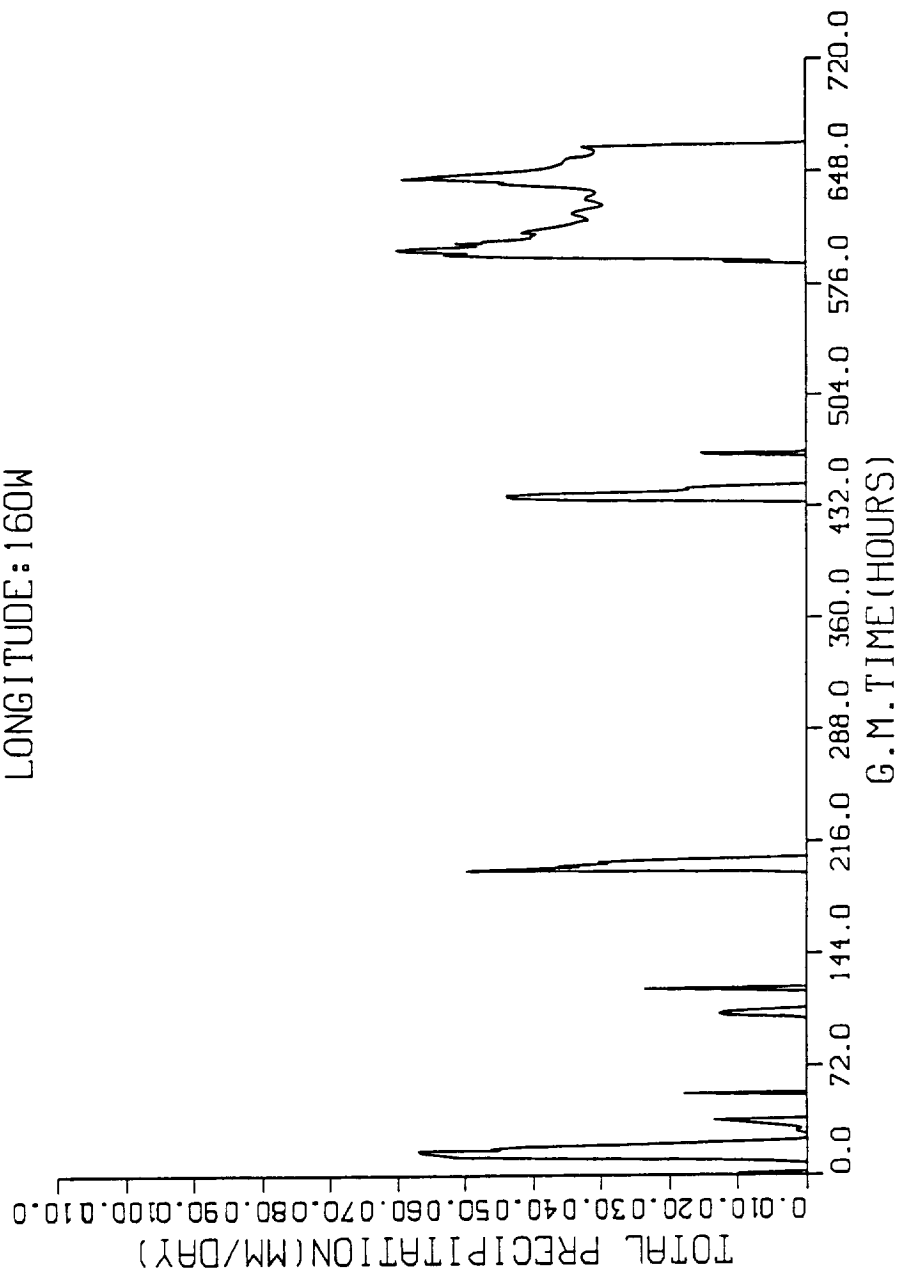


Figure 4, continued

JANUARY DATA
LATITUDE:06N
LONGITUDE:130E

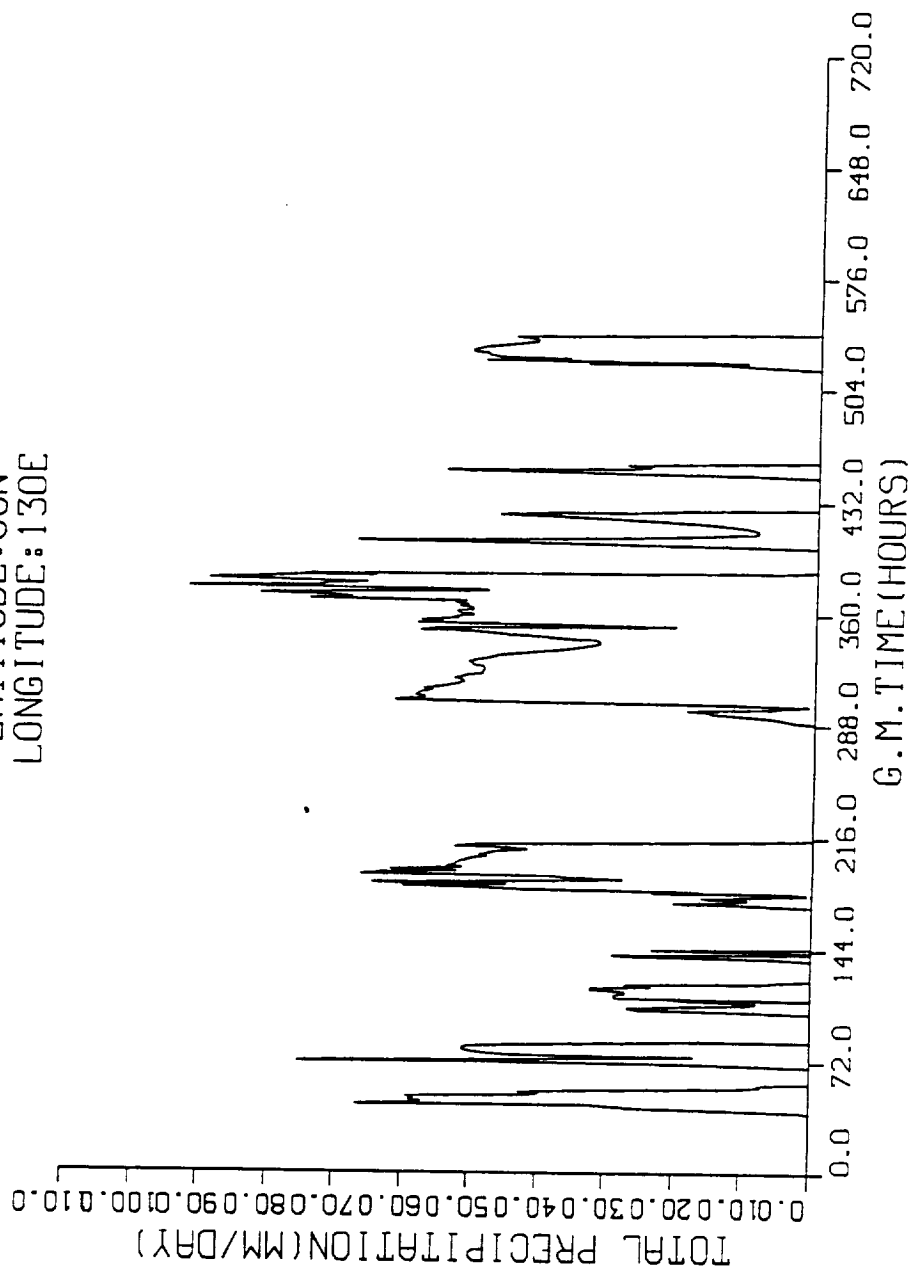


Figure 4, continued

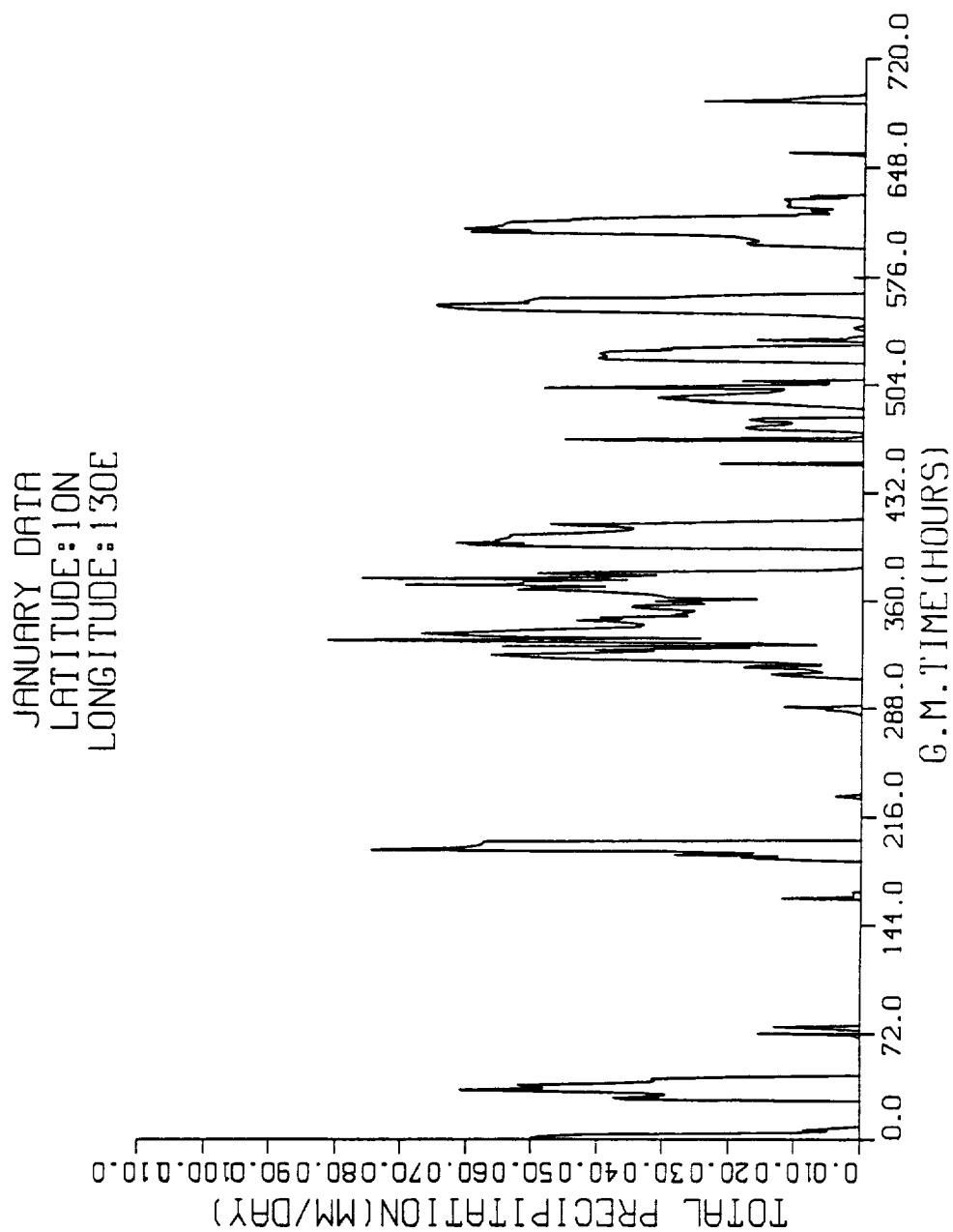


Figure 4, continued

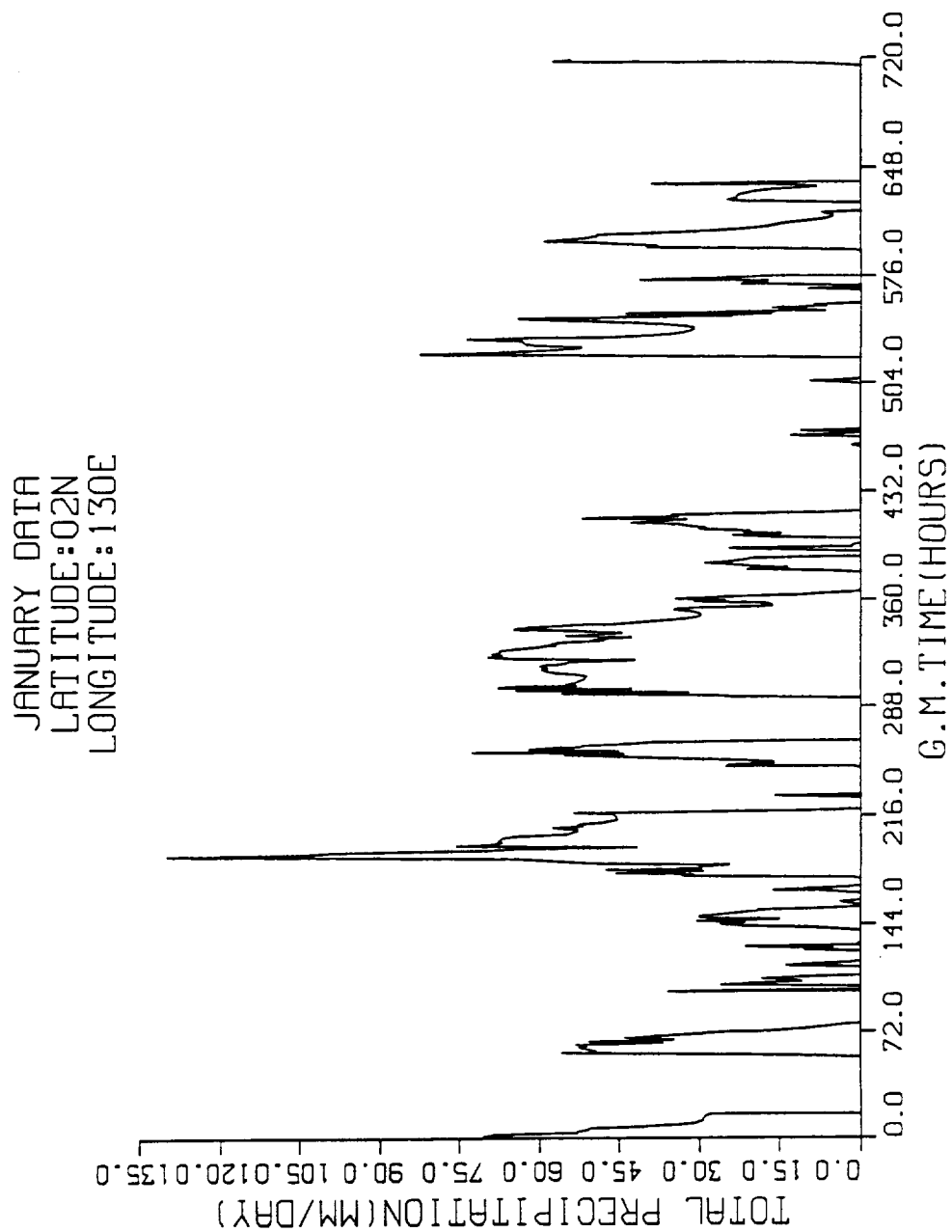


Figure 4, continued

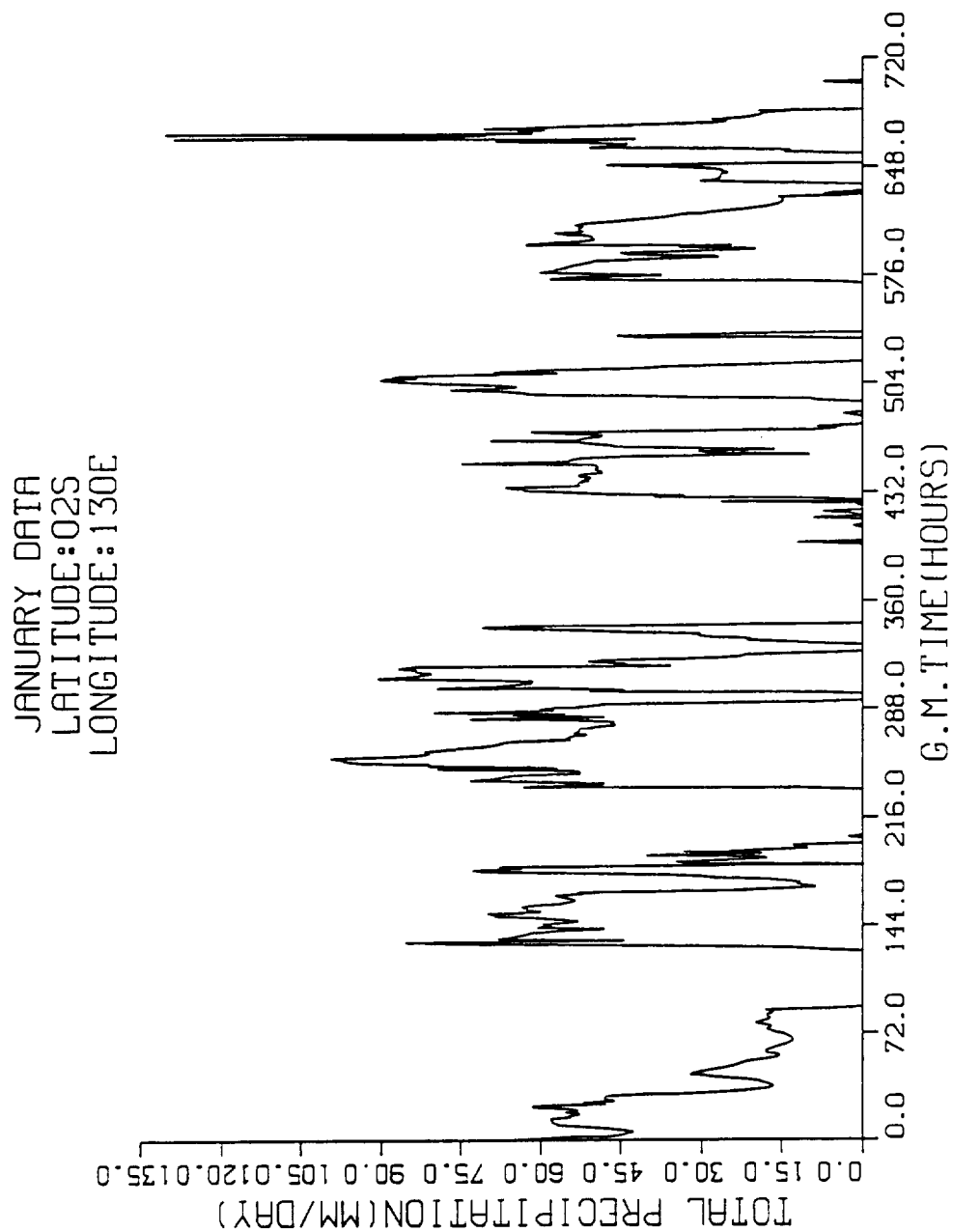


Figure 4, continued

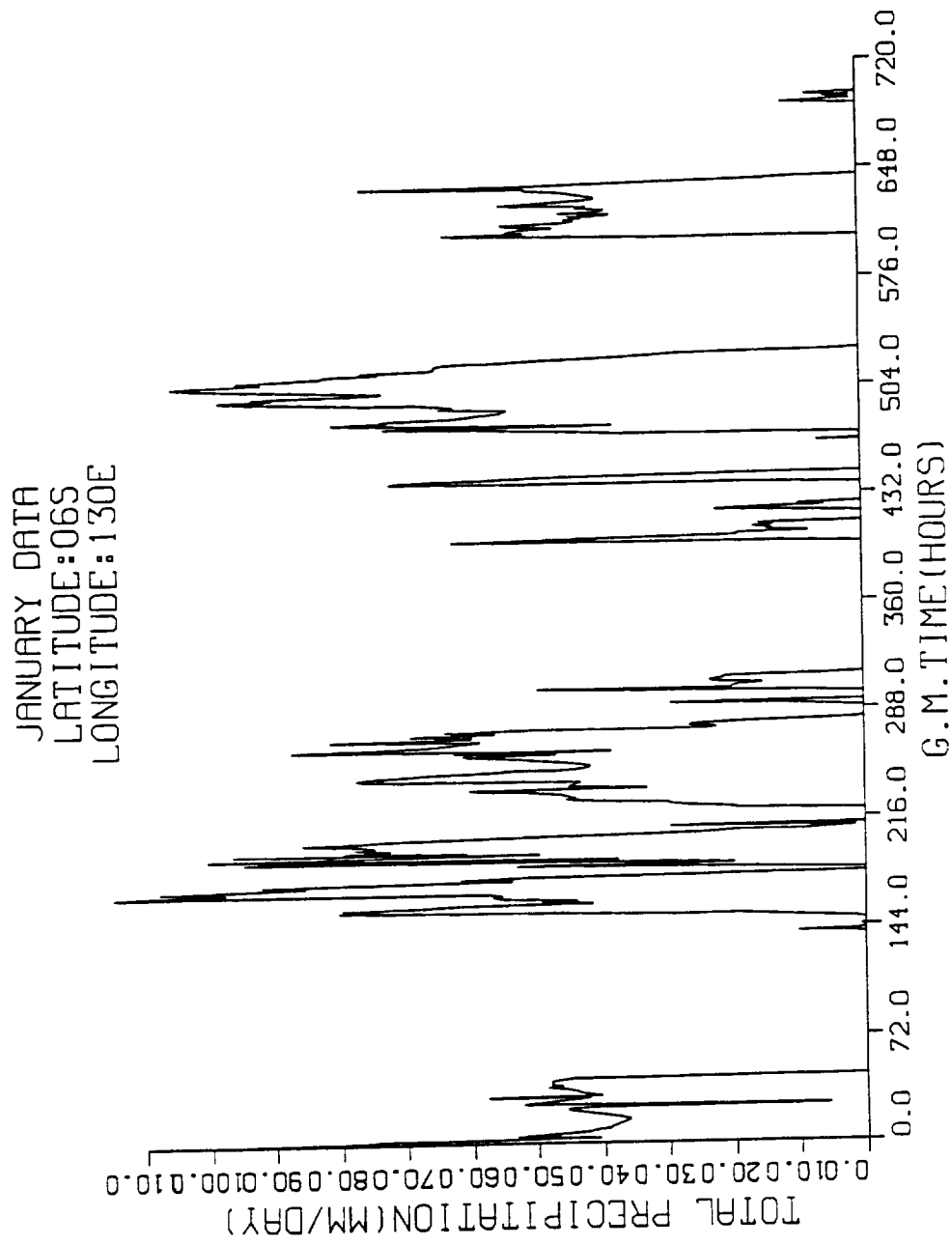


Figure 4, continued

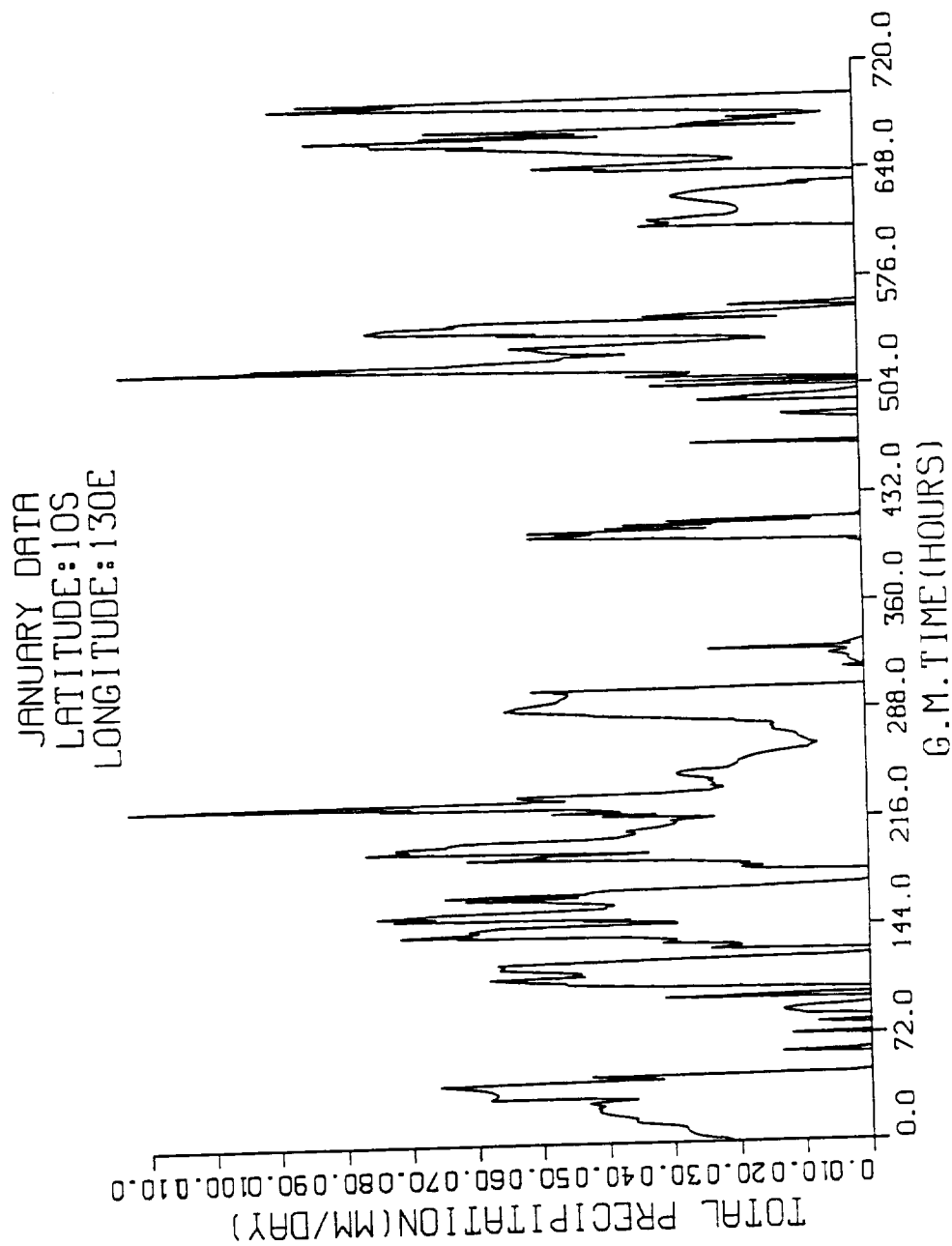


Figure 4, continued

JANUARY DATA
LATITUDE:06S
LONGITUDE:150E

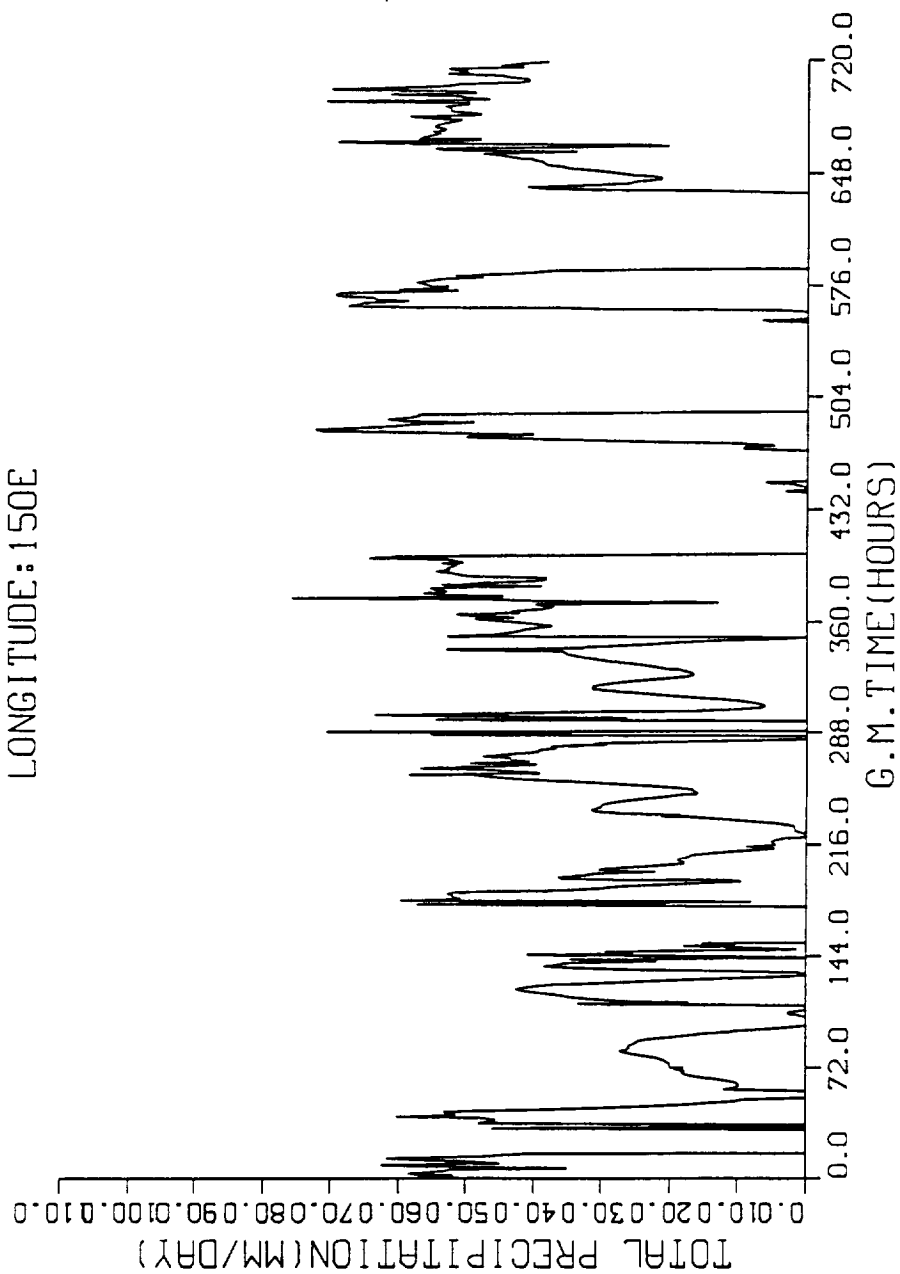


Figure 4, continued

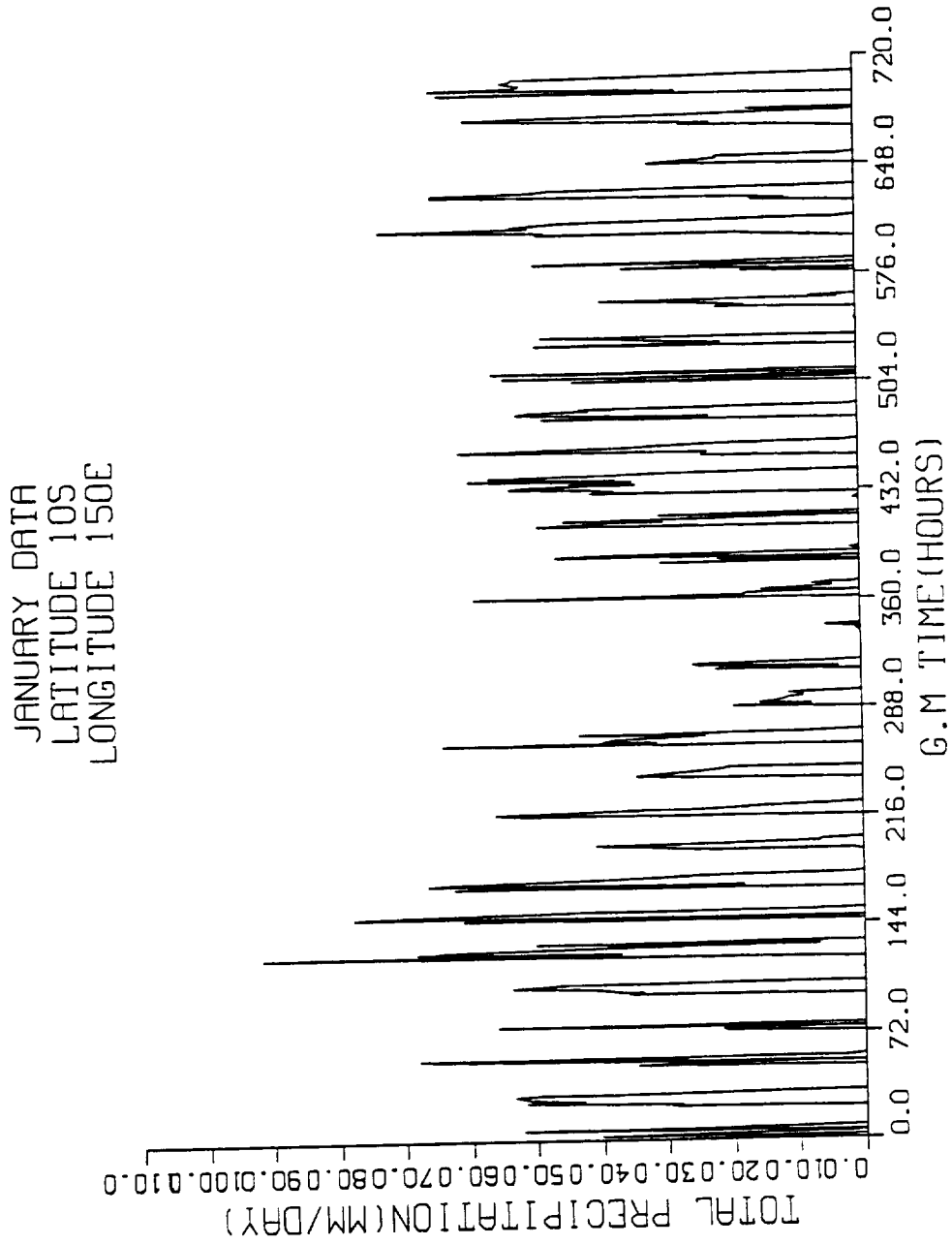


Figure 4, continued

JANUARY DATA
LATITUDE:06S
LONGITUDE:160W

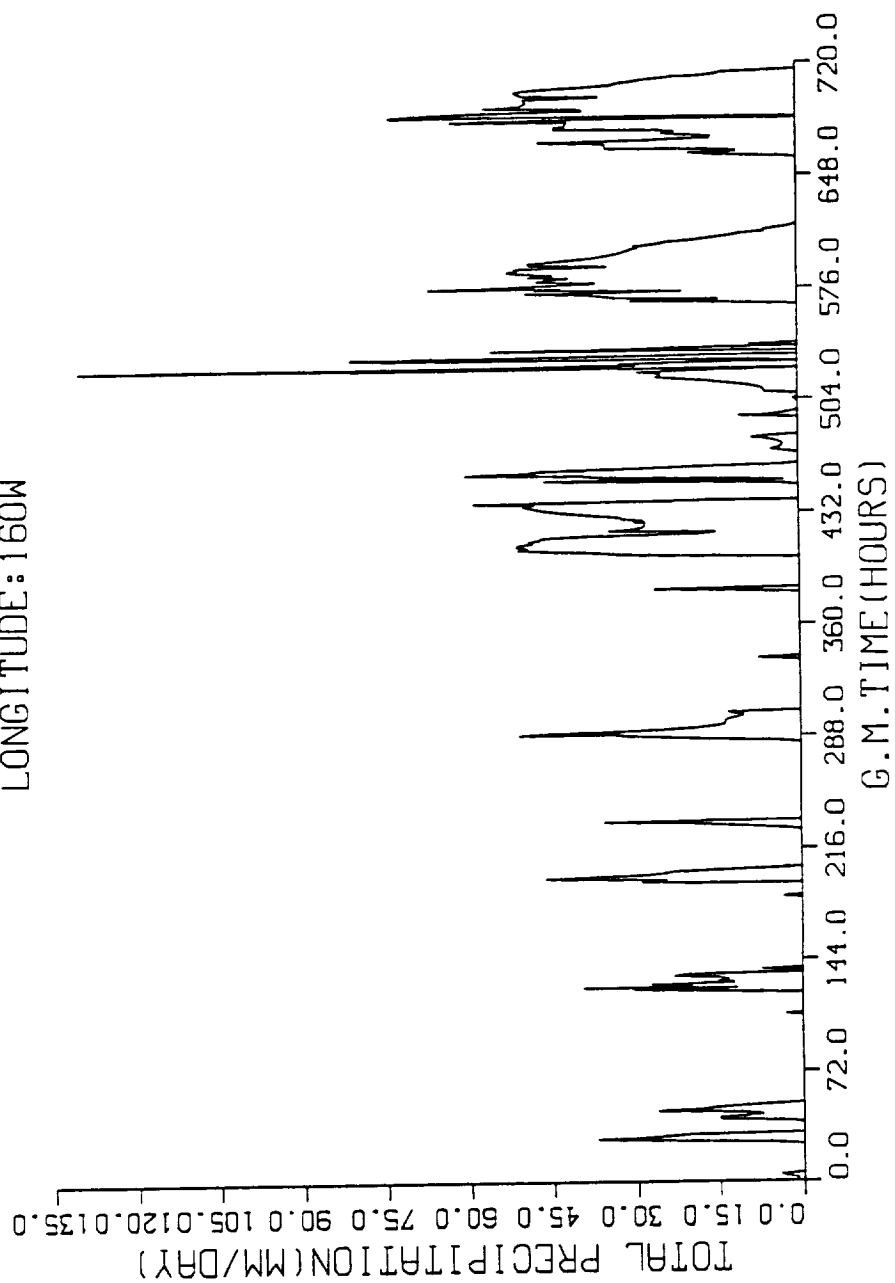


Figure 4, continued

JANUARY DATA
LATITUDE:10S
LONGITUDE:160W

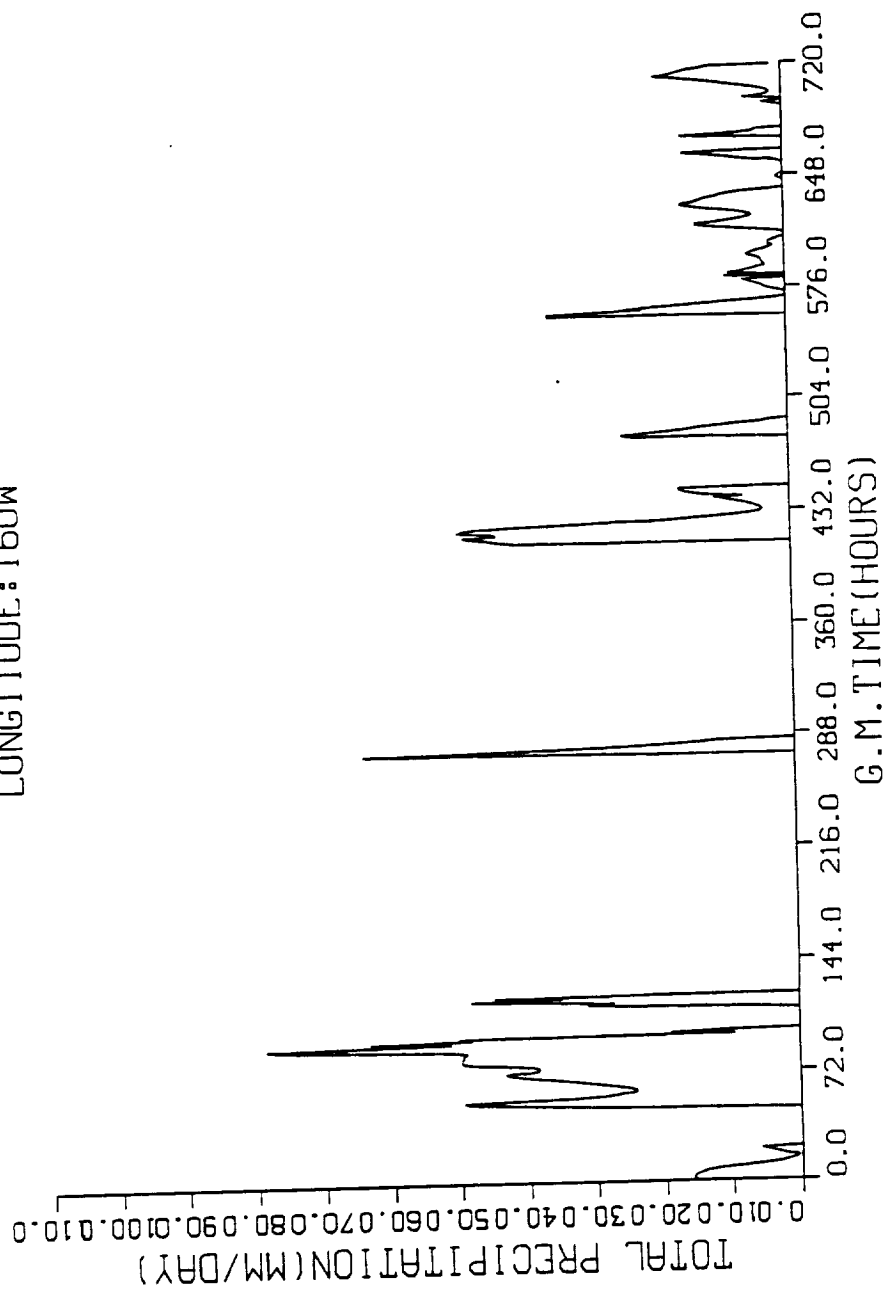


Figure 4, continued

JANUARY DATA
LATITUDE:14S
LONGITUDE:160W

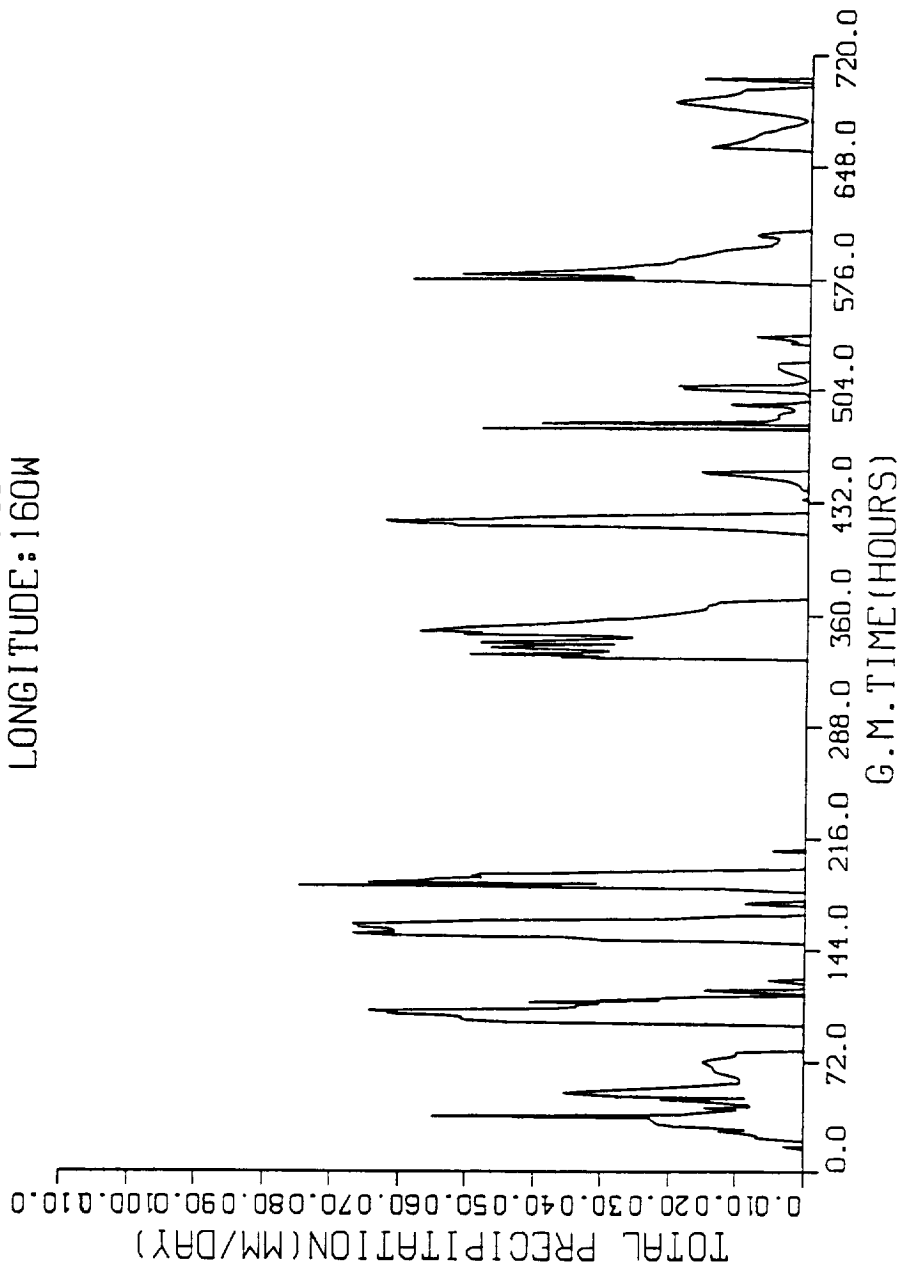


Figure 4, continued

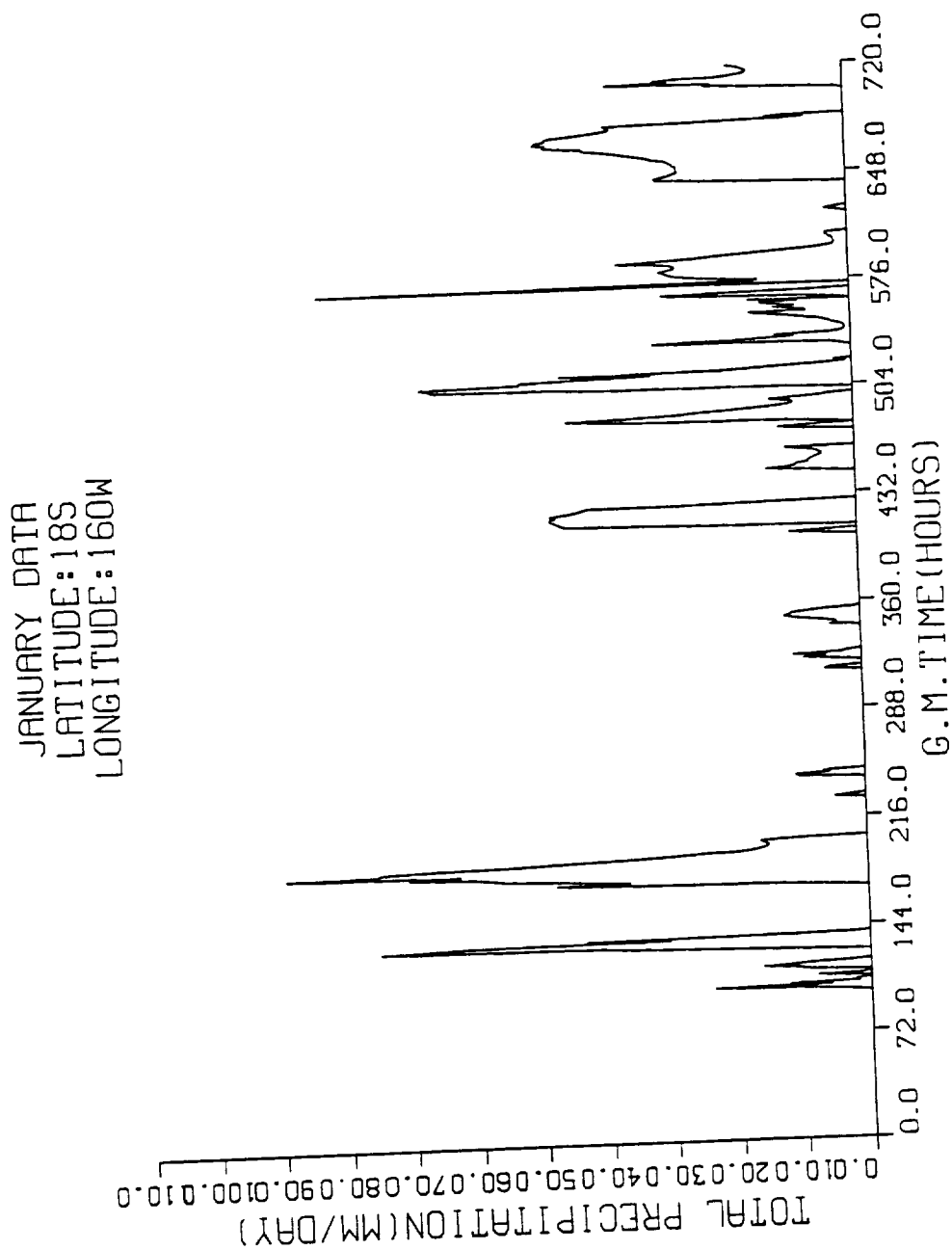


Figure 4, continued

FEBRUARY DATA
LATITUDE:10N
LONGITUDE:130E

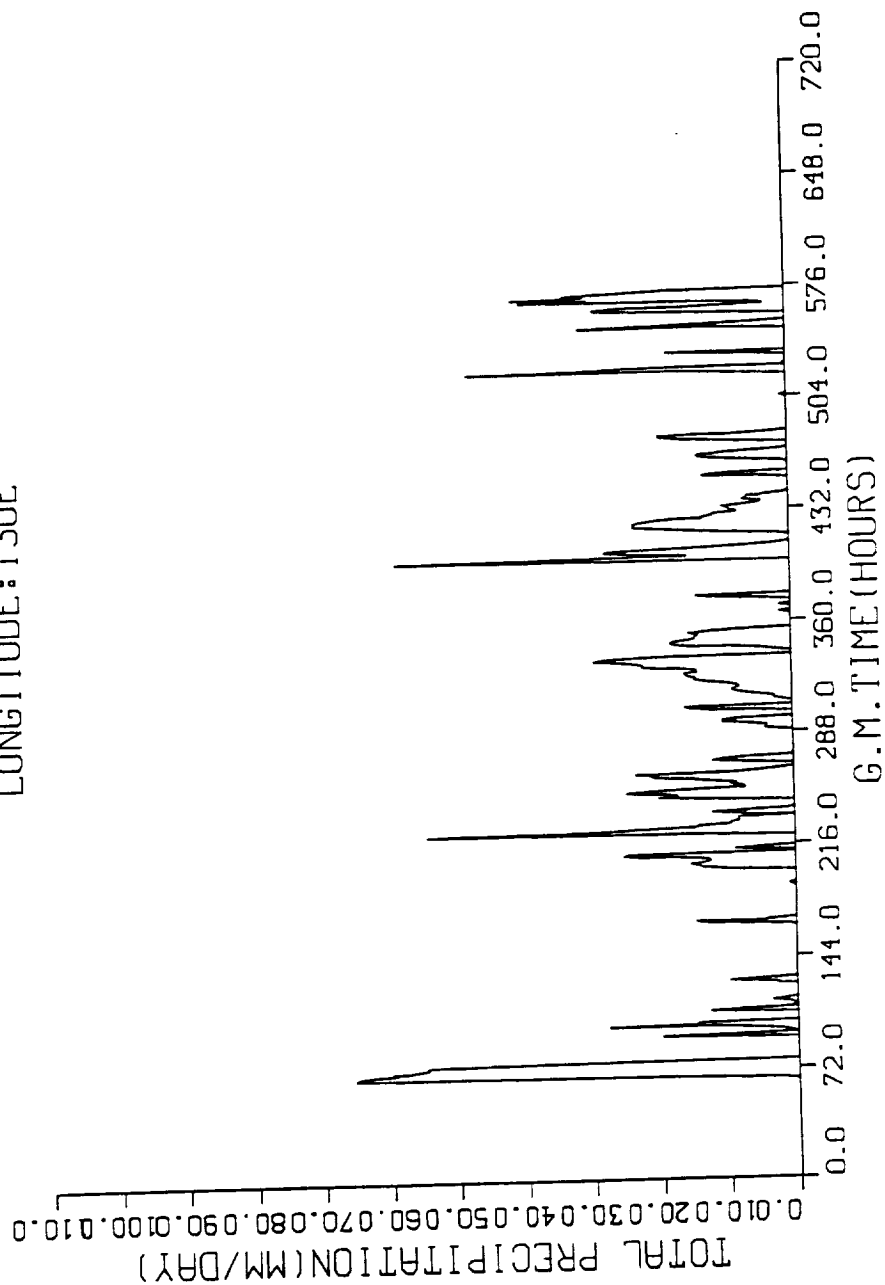


Figure 4, continued

FEBRUARY DATA
LATITUDE:06N
LONGITUDE:130E

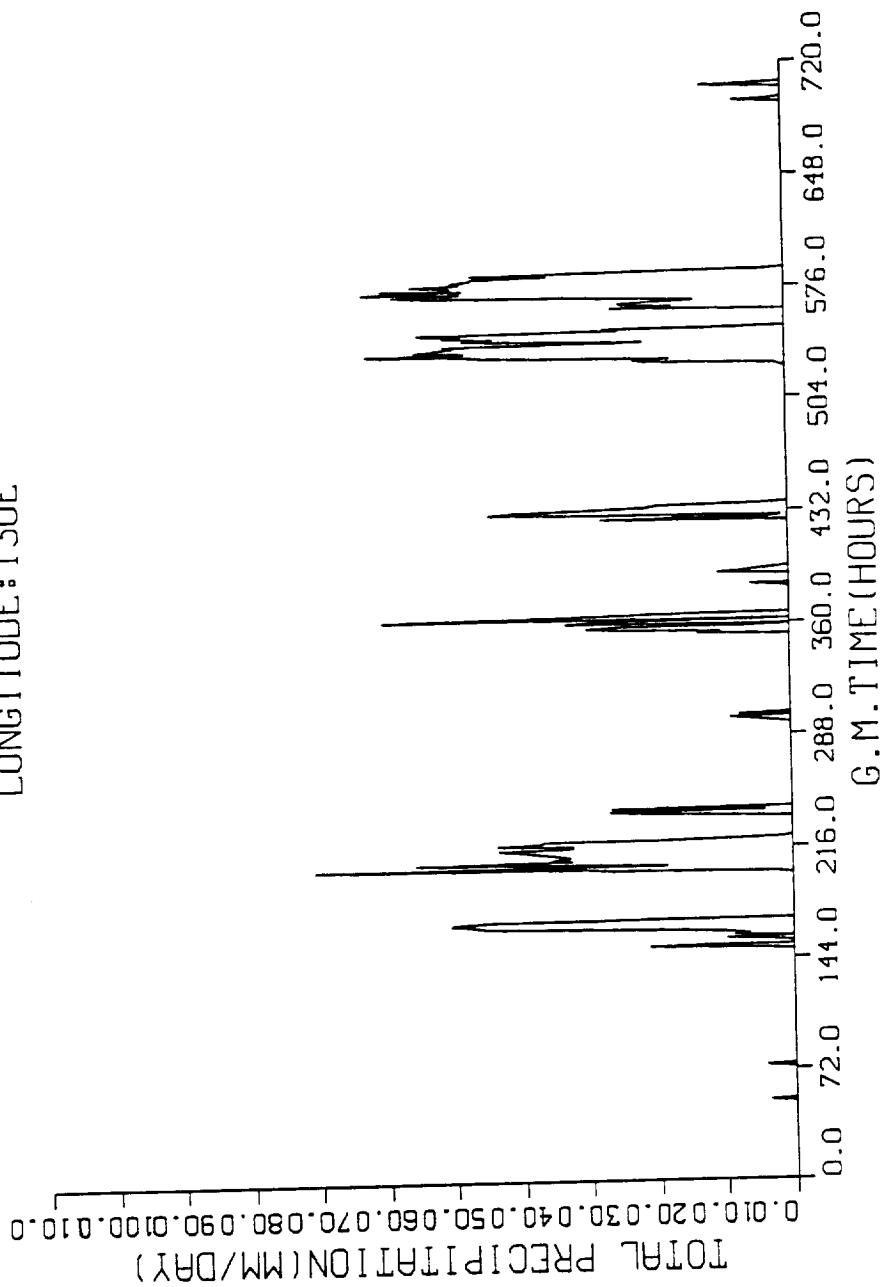


Figure 4, continued

FEBRUARY DATA
LATITUDE:02N
LONGITUDE:130E

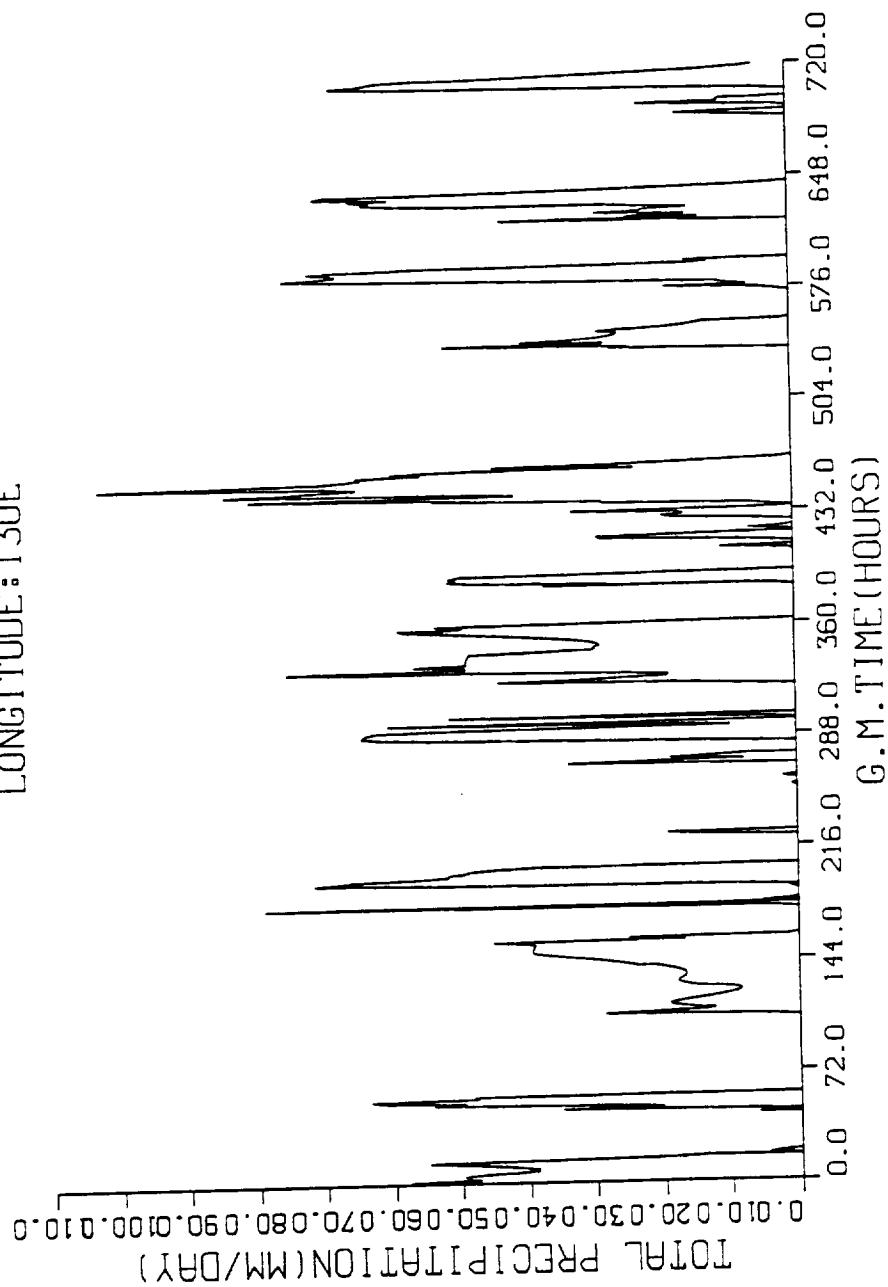


Figure 4, continued

FEBRUARY DATA
LATITUDE:02S
LONGITUDE:130E

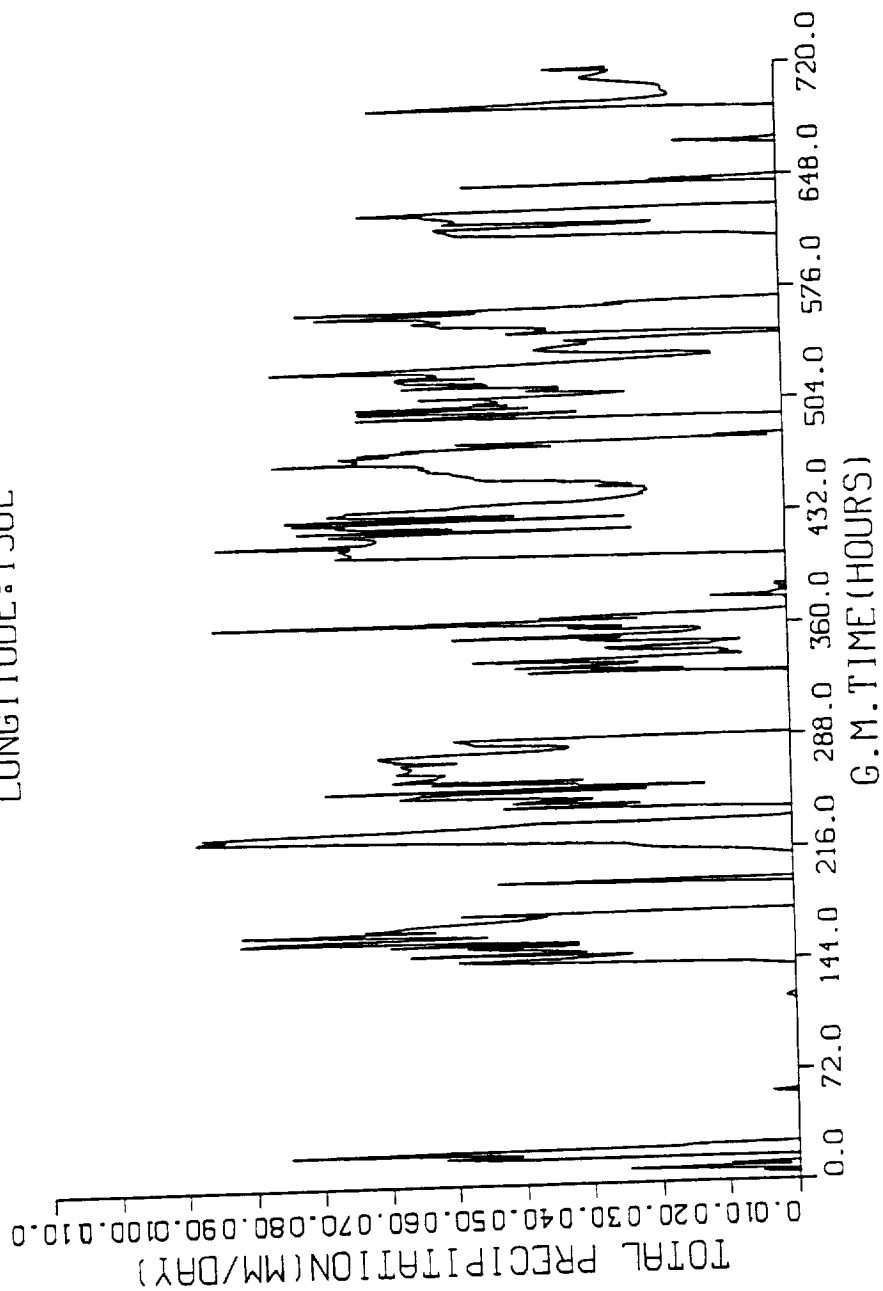


Figure 4, continued

FEBRUARY DATA
LATITUDE:06S
LONGITUDE:130E

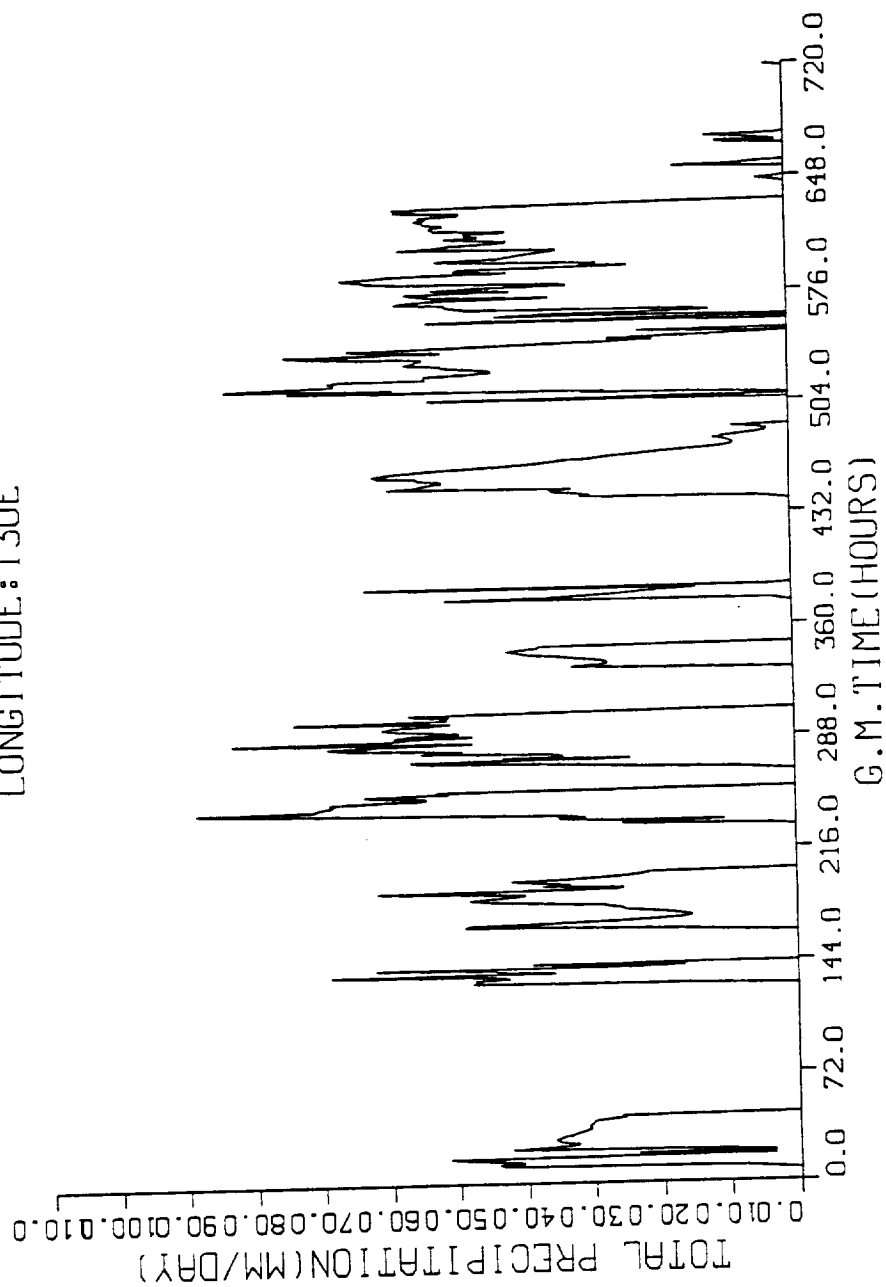


Figure 4, continued

FEBRUARY DATA
LATITUDE:10S
LONGITUDE:130E

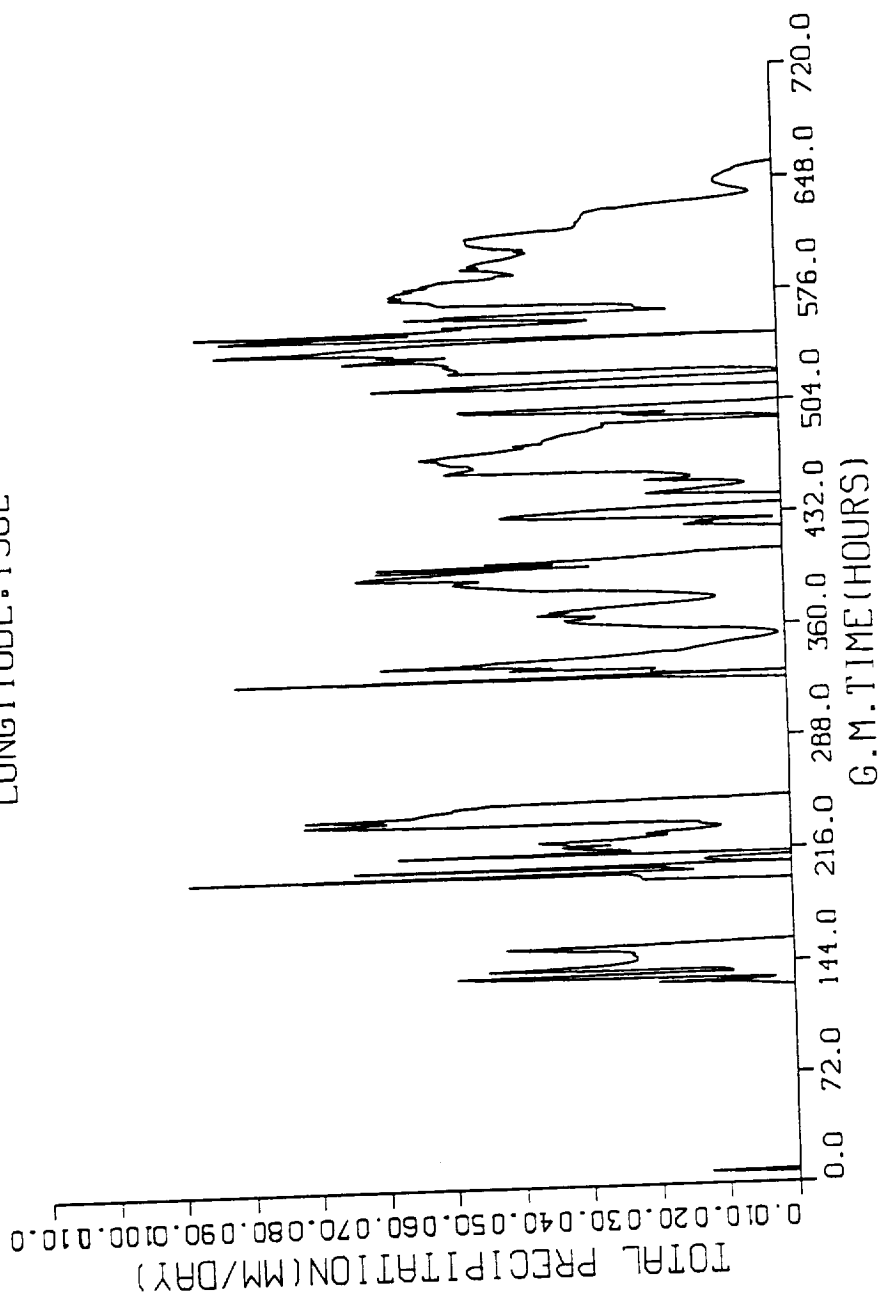


Figure 4, continued

FEBRUARY DATA
LATITUDE:06S
LONGITUDE:150E

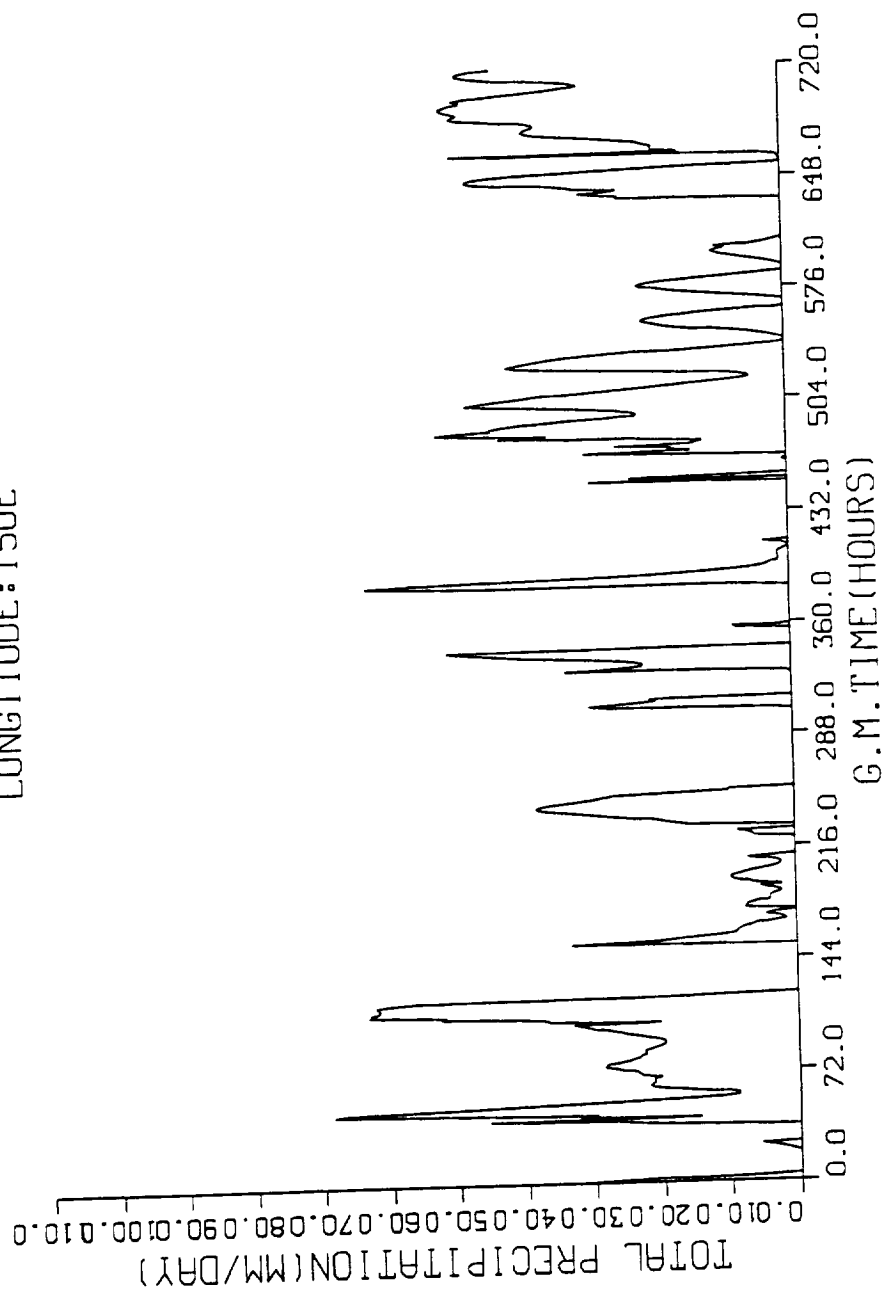


Figure 4, continued

FEBRUARY DATA
LATITUDE:10S
LONGITUDE:150E

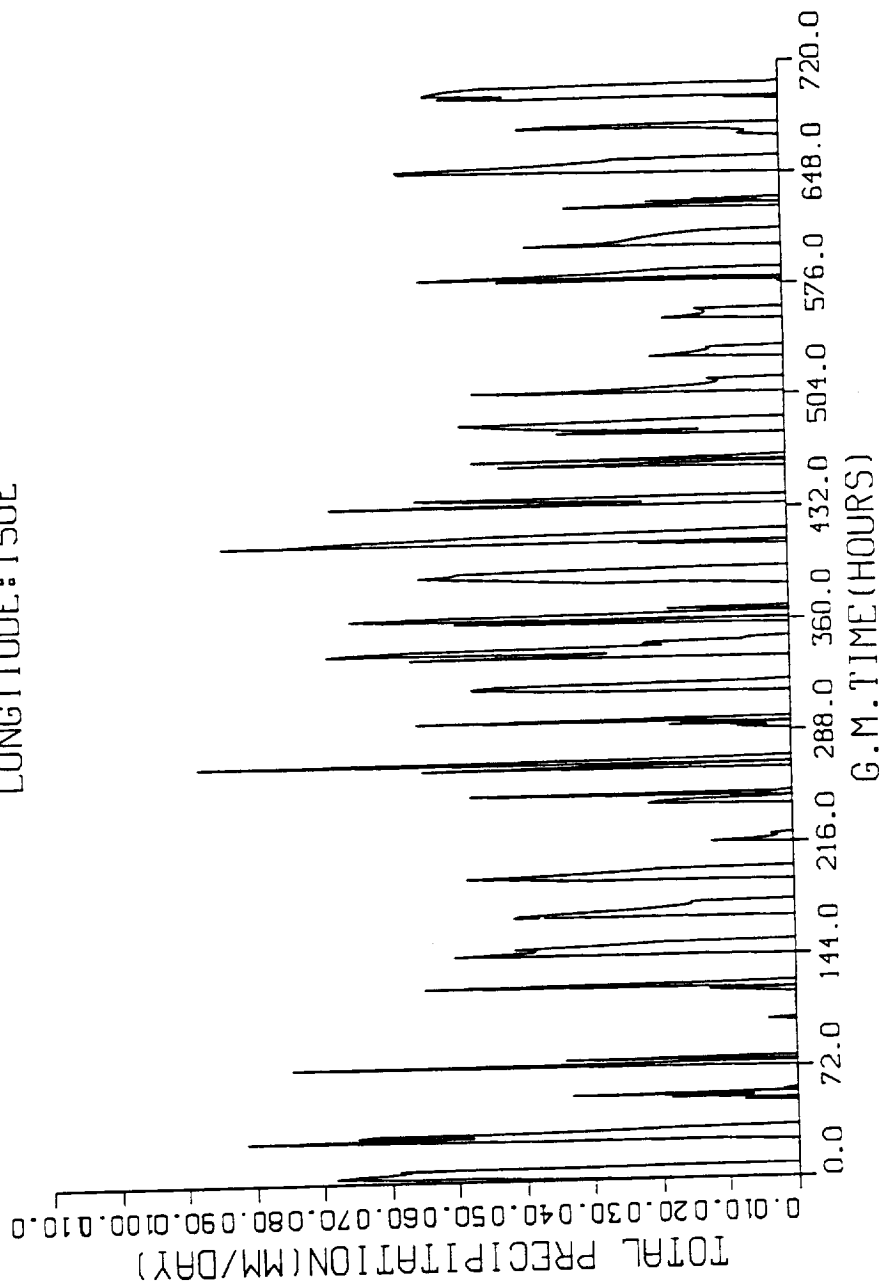


Figure 4, continued

FEBRUARY DATA
LATITUDE:06S
LONGITUDE:160W

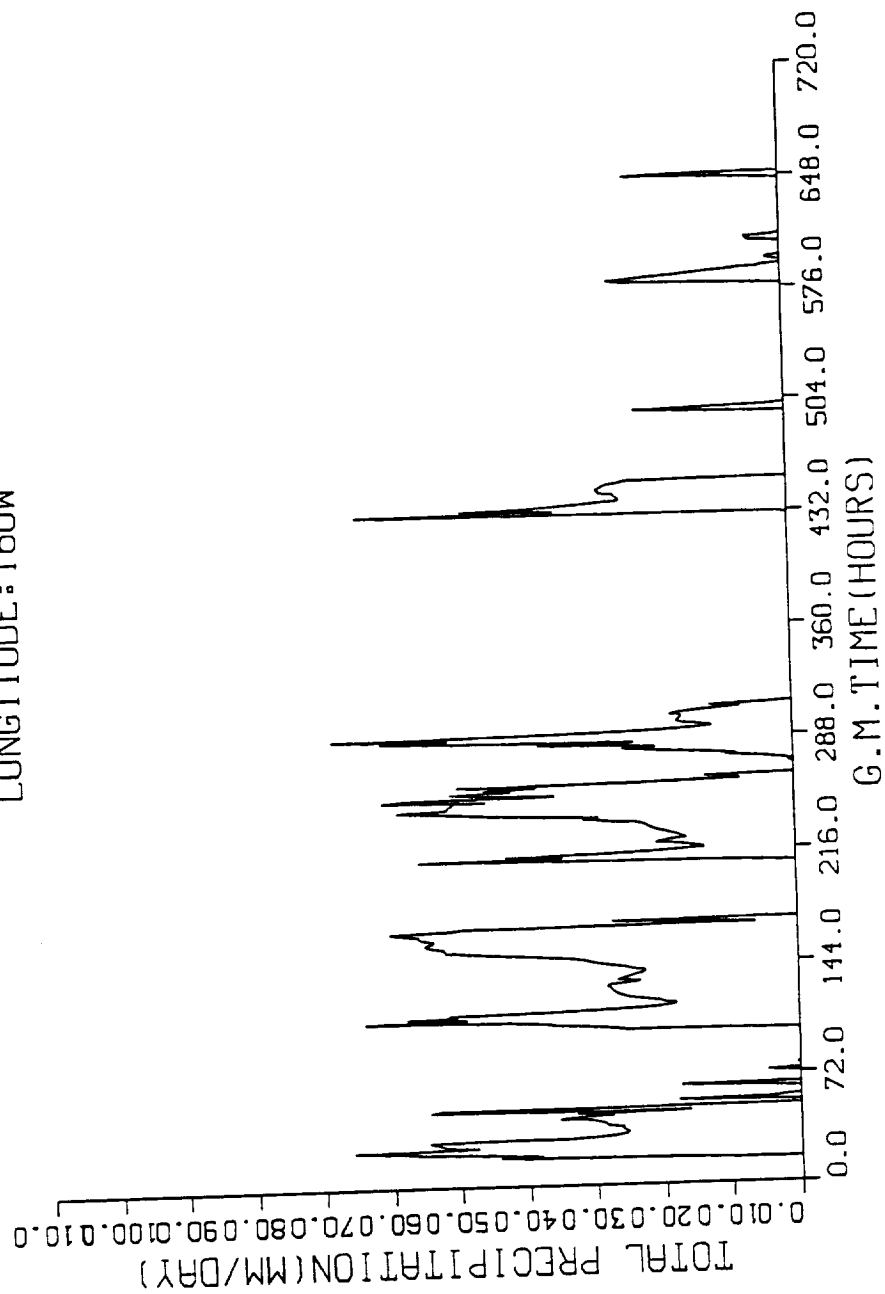


Figure 4, continued

FEBRUARY DATA
LATITUDE:10S
LONGITUDE:160W

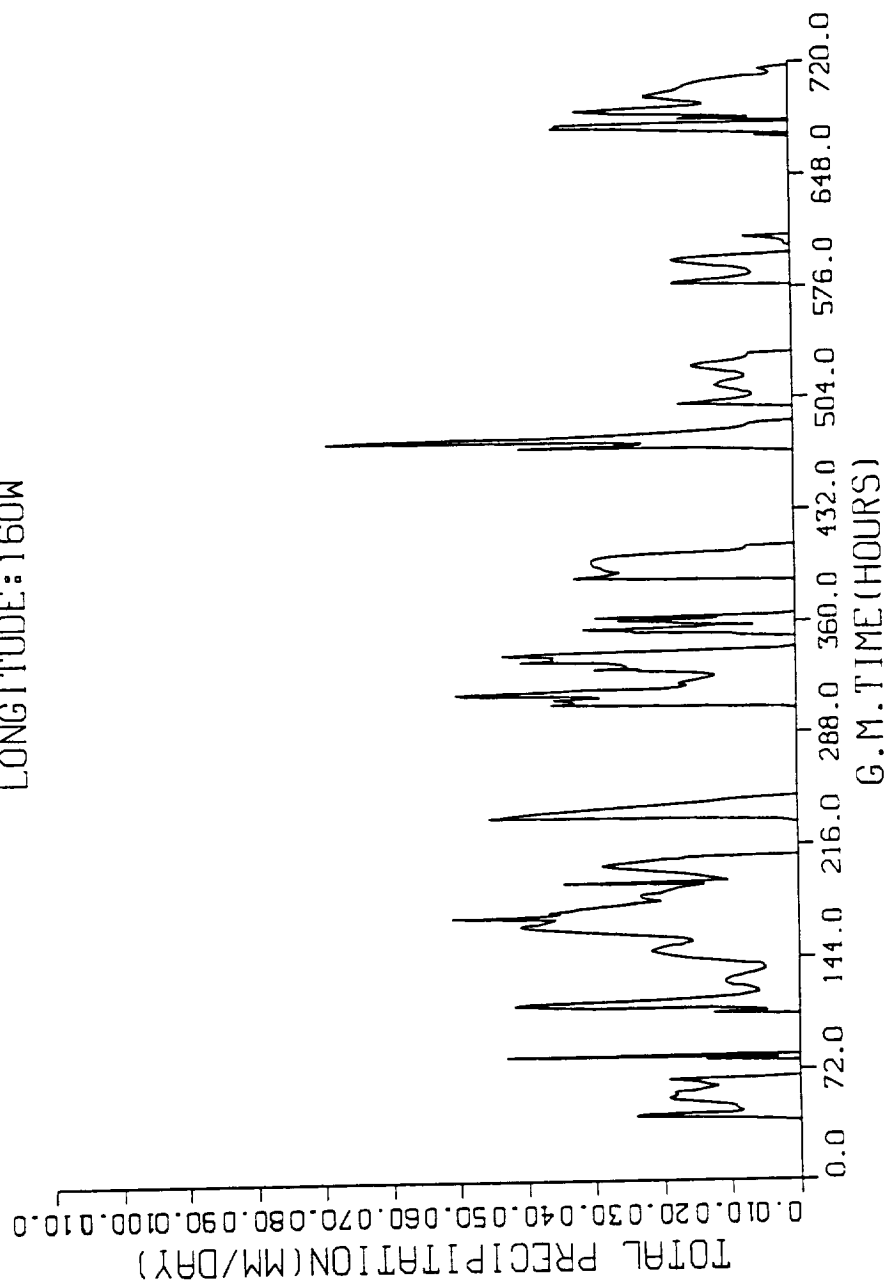


Figure 4, continued

FEBRUARY DATA
LATITUDE:14S
LONGITUDE:160W

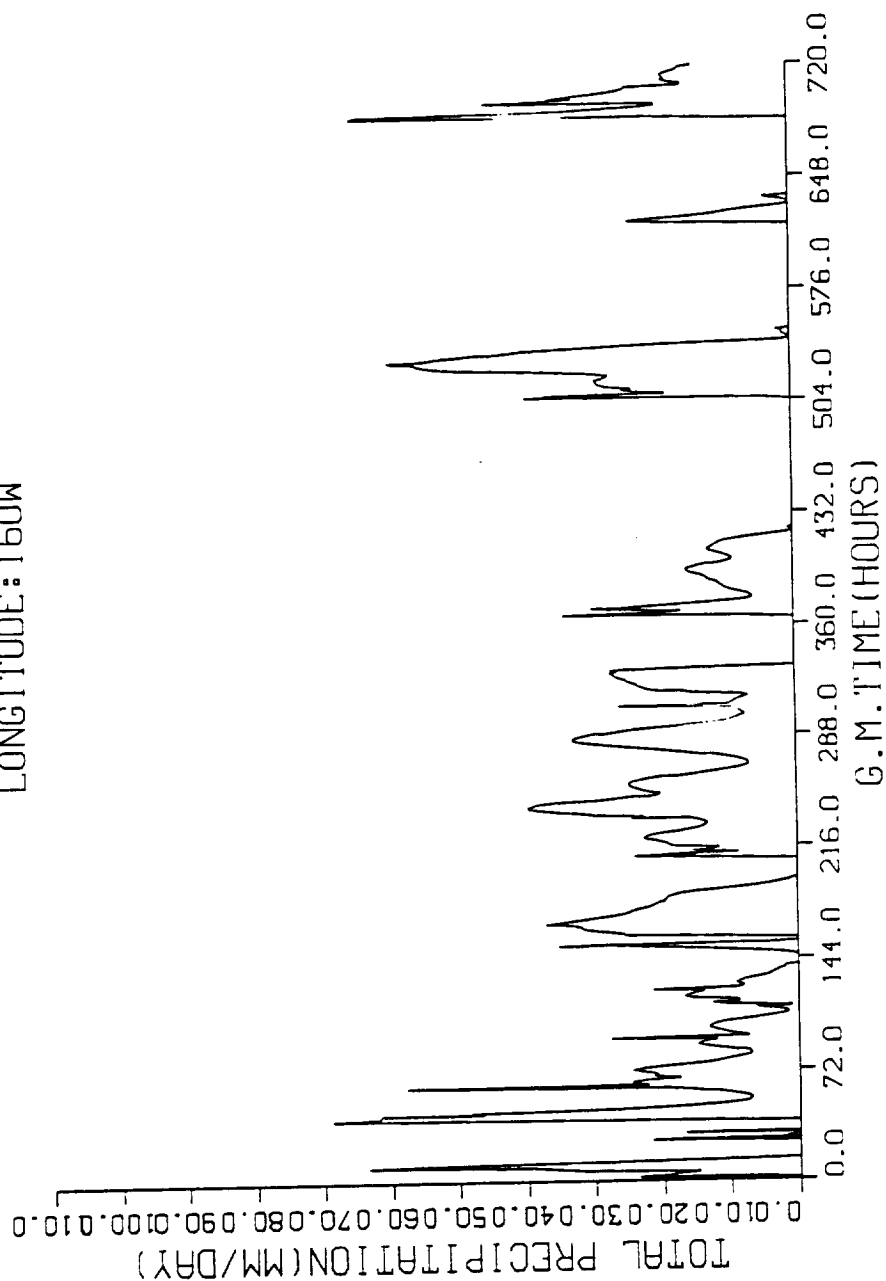


Figure 4, continued

FEBRUARY DATA
LATITUDE:18S
LONGITUDE:160W

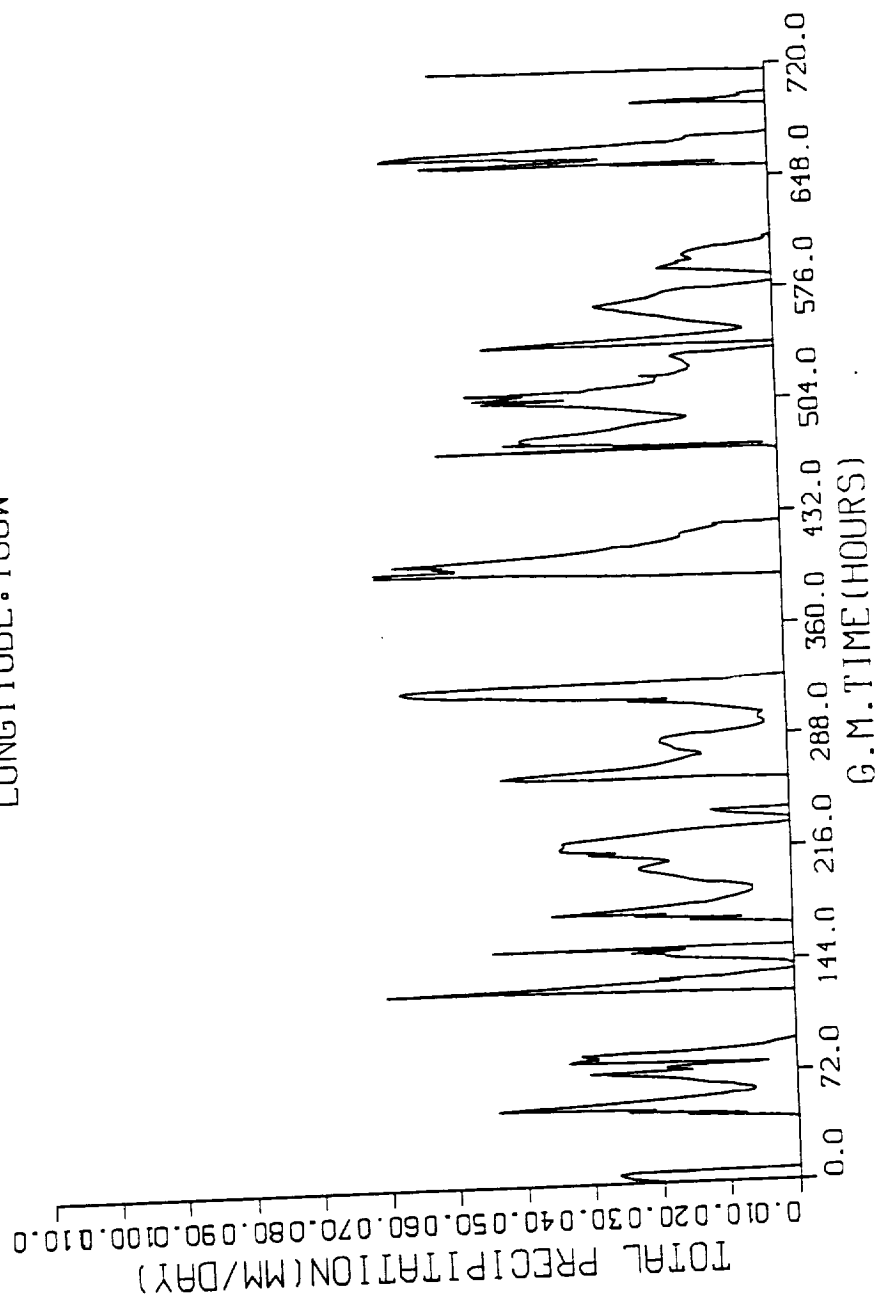


Figure 4, continued

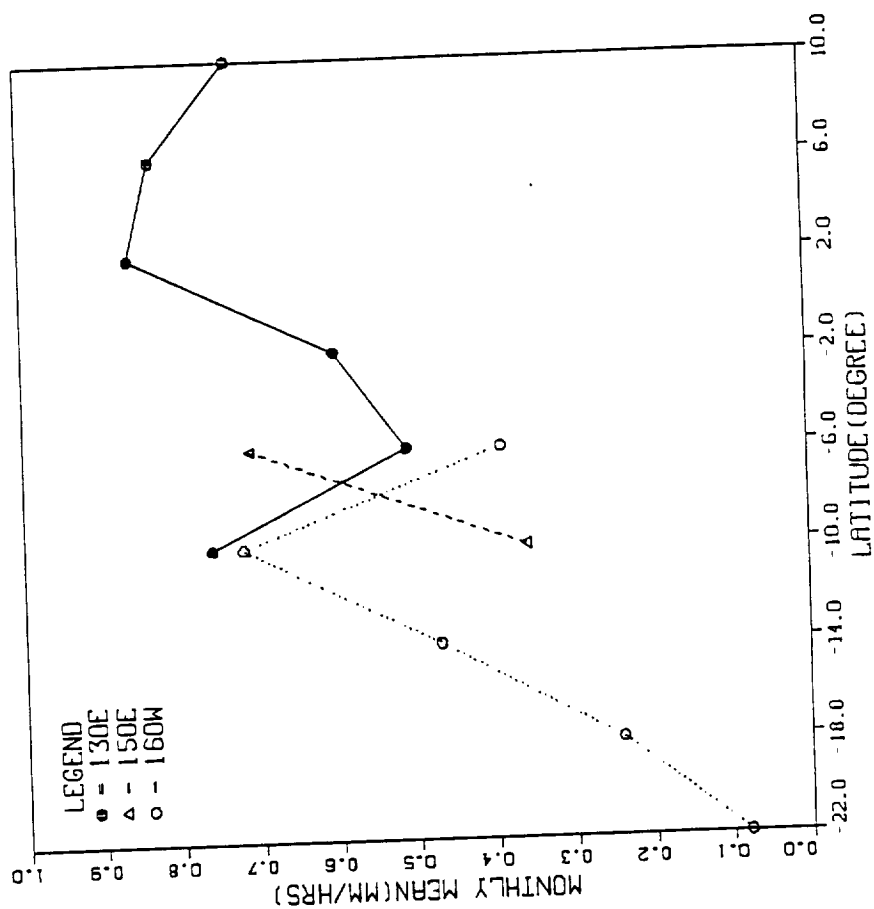


Figure 5. Variation of the monthly mean rain rates versus grid box location in December, January, and February.

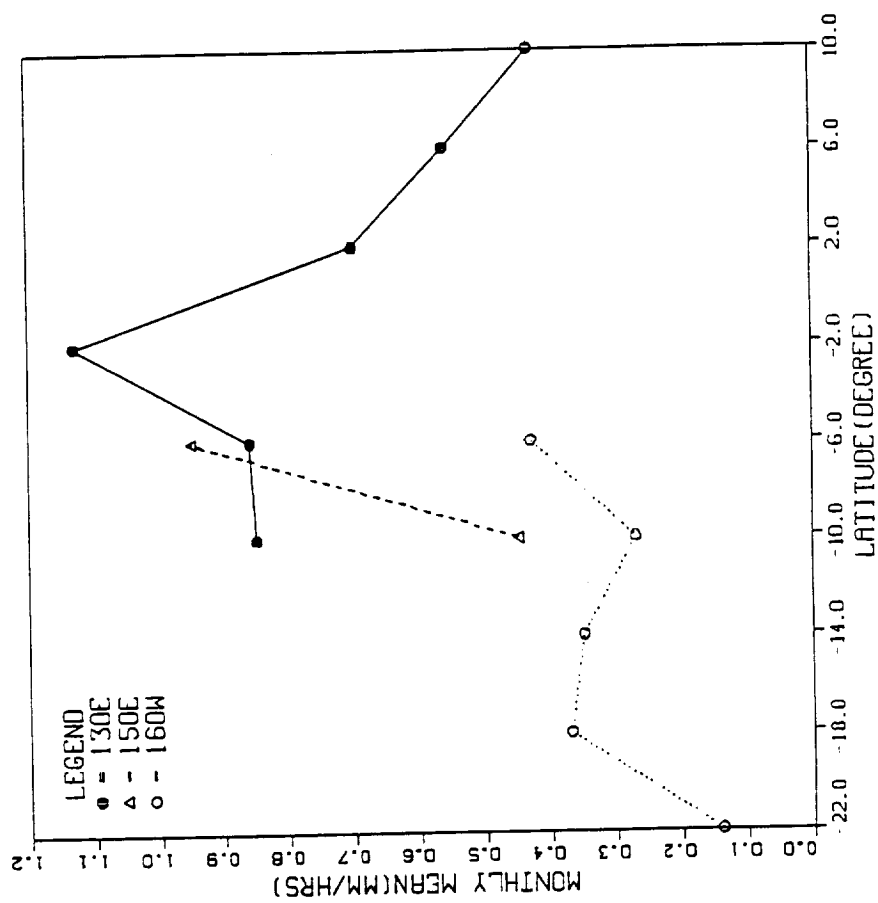


Figure 5, continued

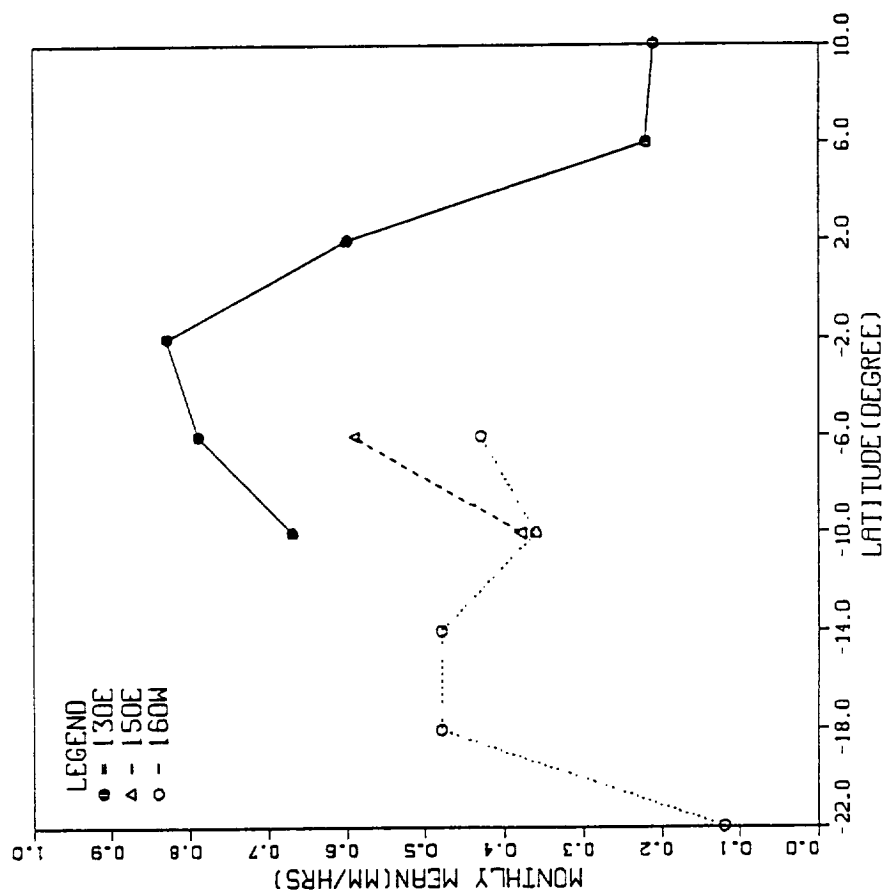


Figure 5, continued

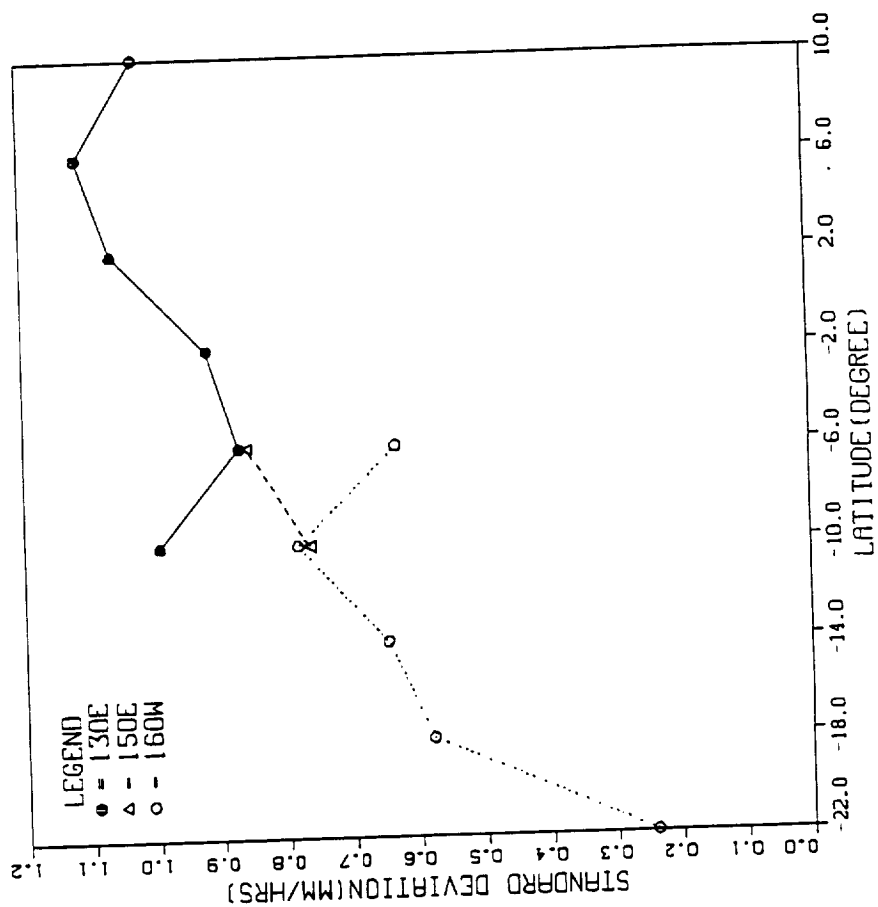


Figure 6. Variation of the monthly rain rate standard deviations versus grid box locations in December, January, and Feb

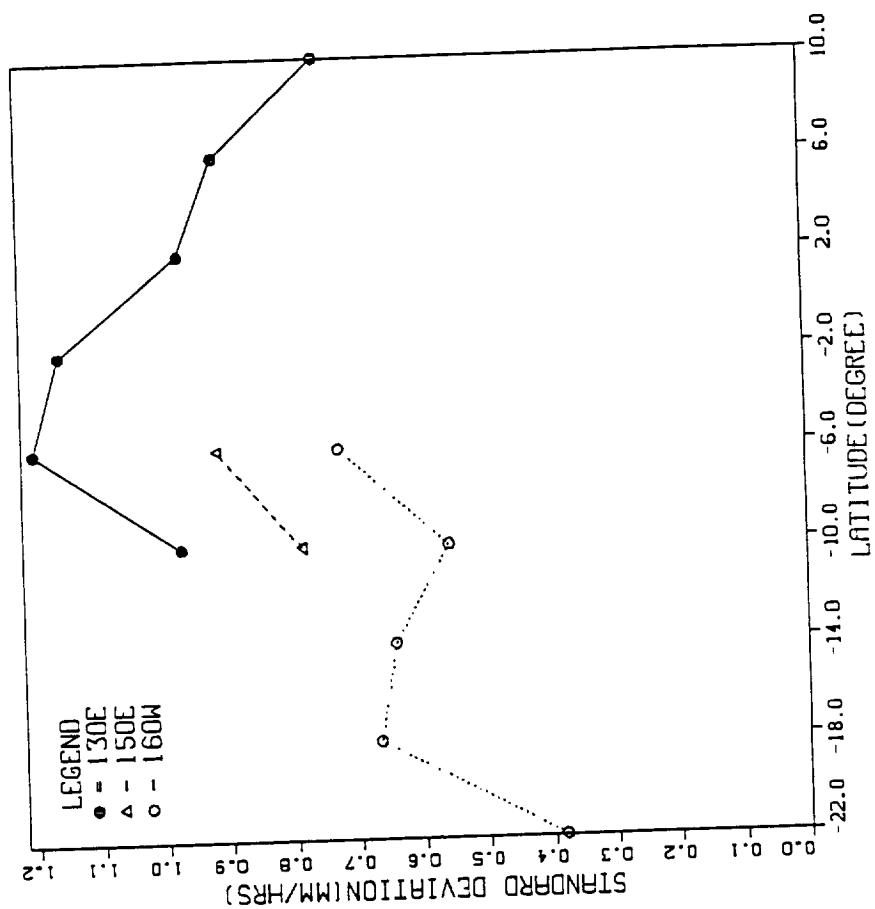


Figure 6, continued

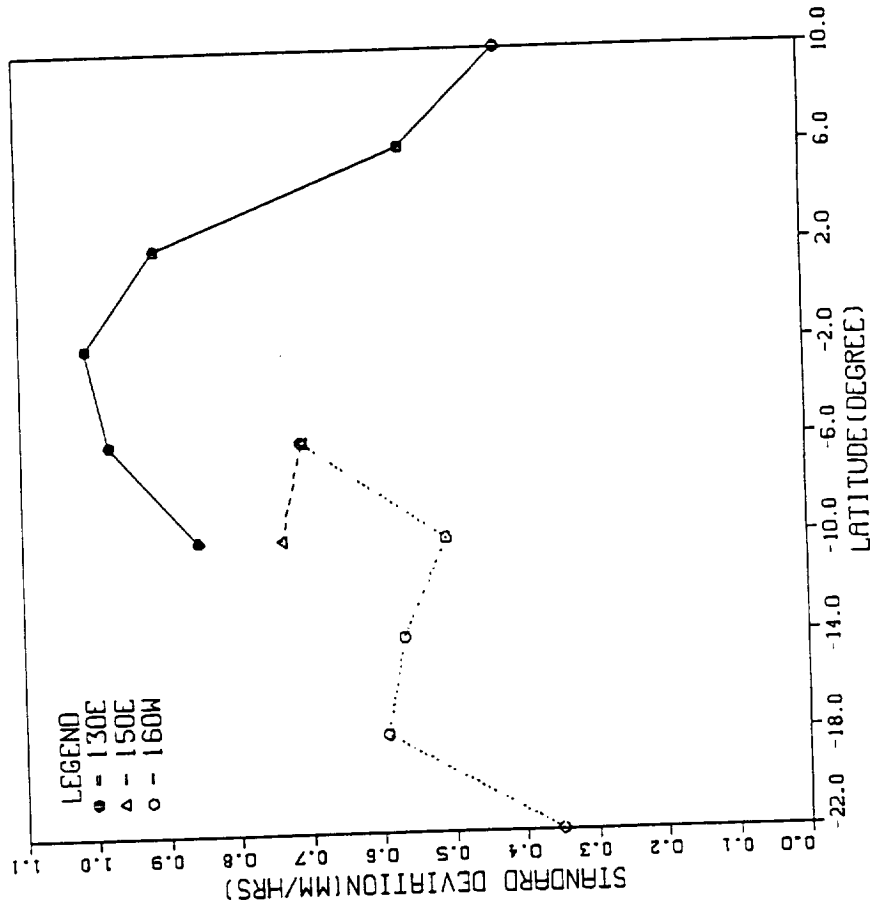


Figure 6, continued

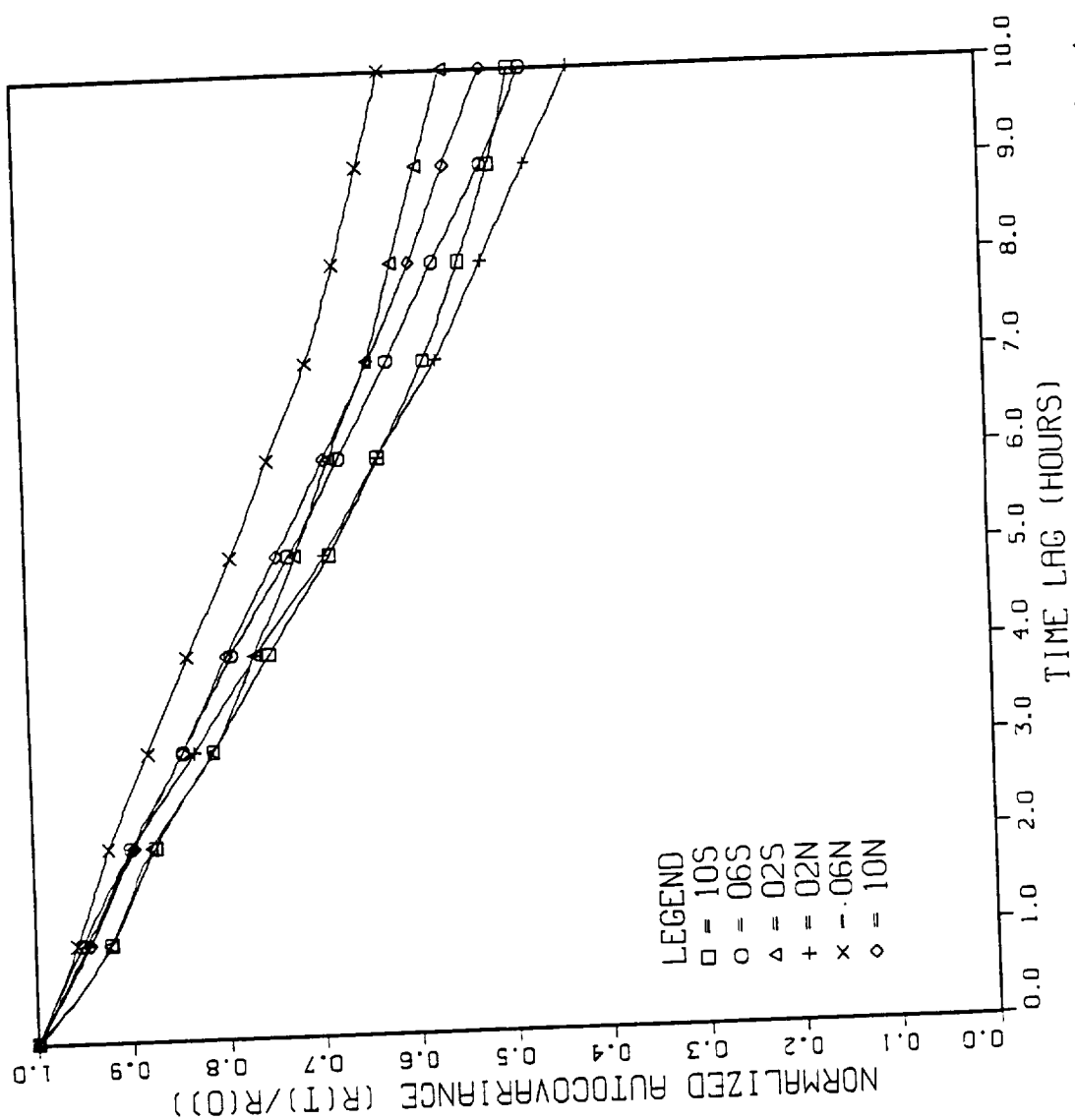


Figure 7. Variation of the autocovariance functions versus time lag for different grid box locations

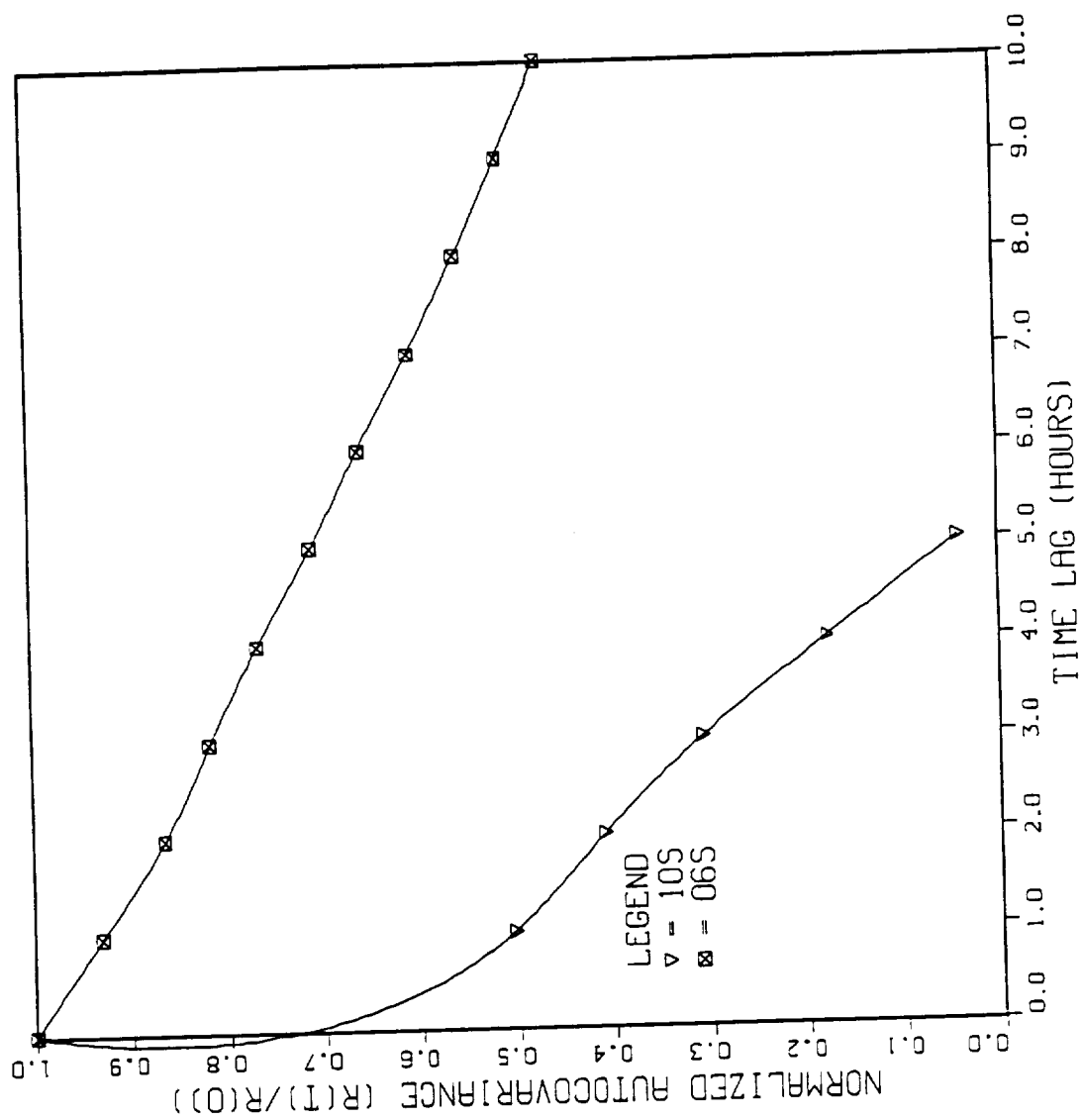
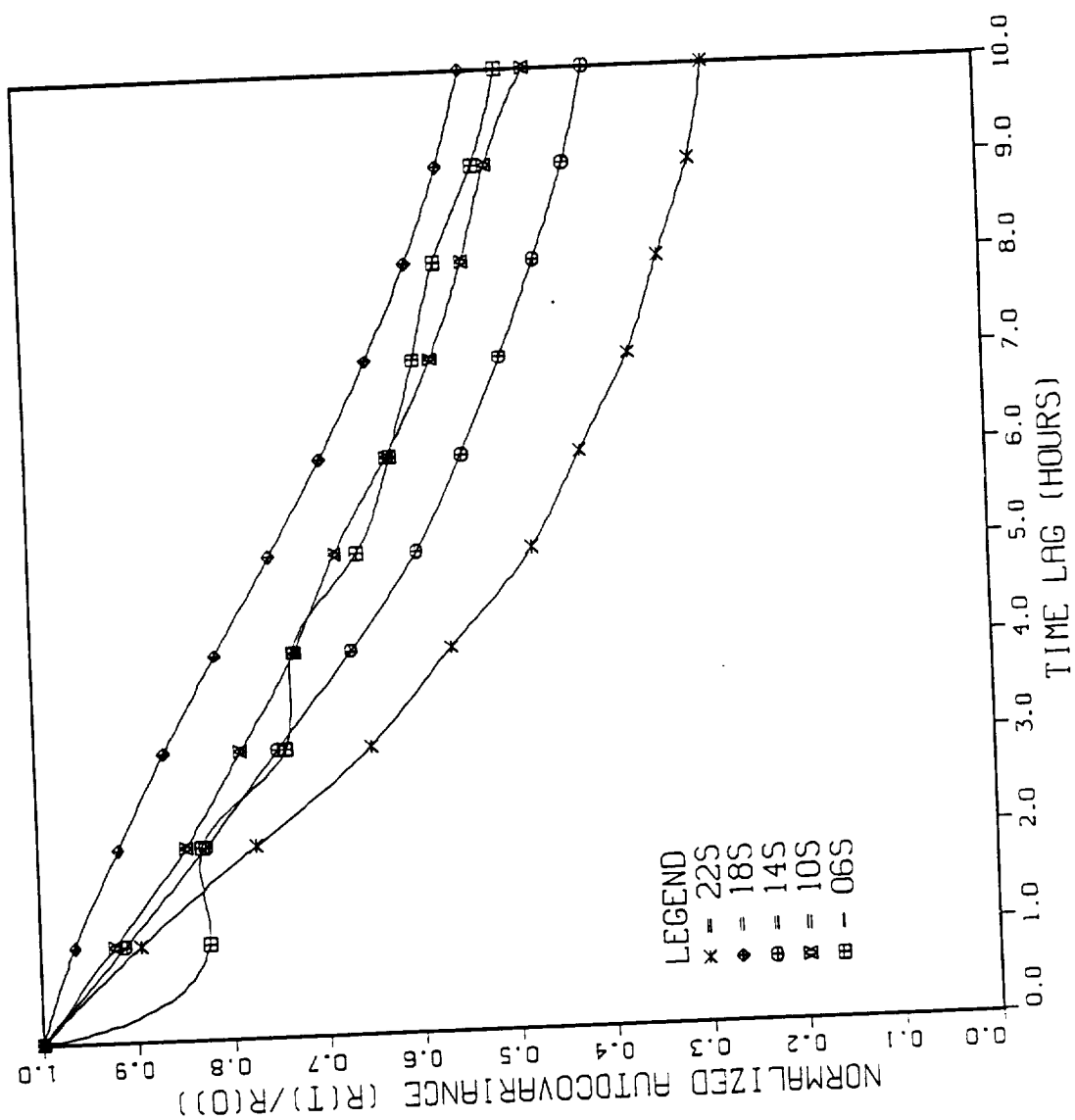


Figure 7, continued



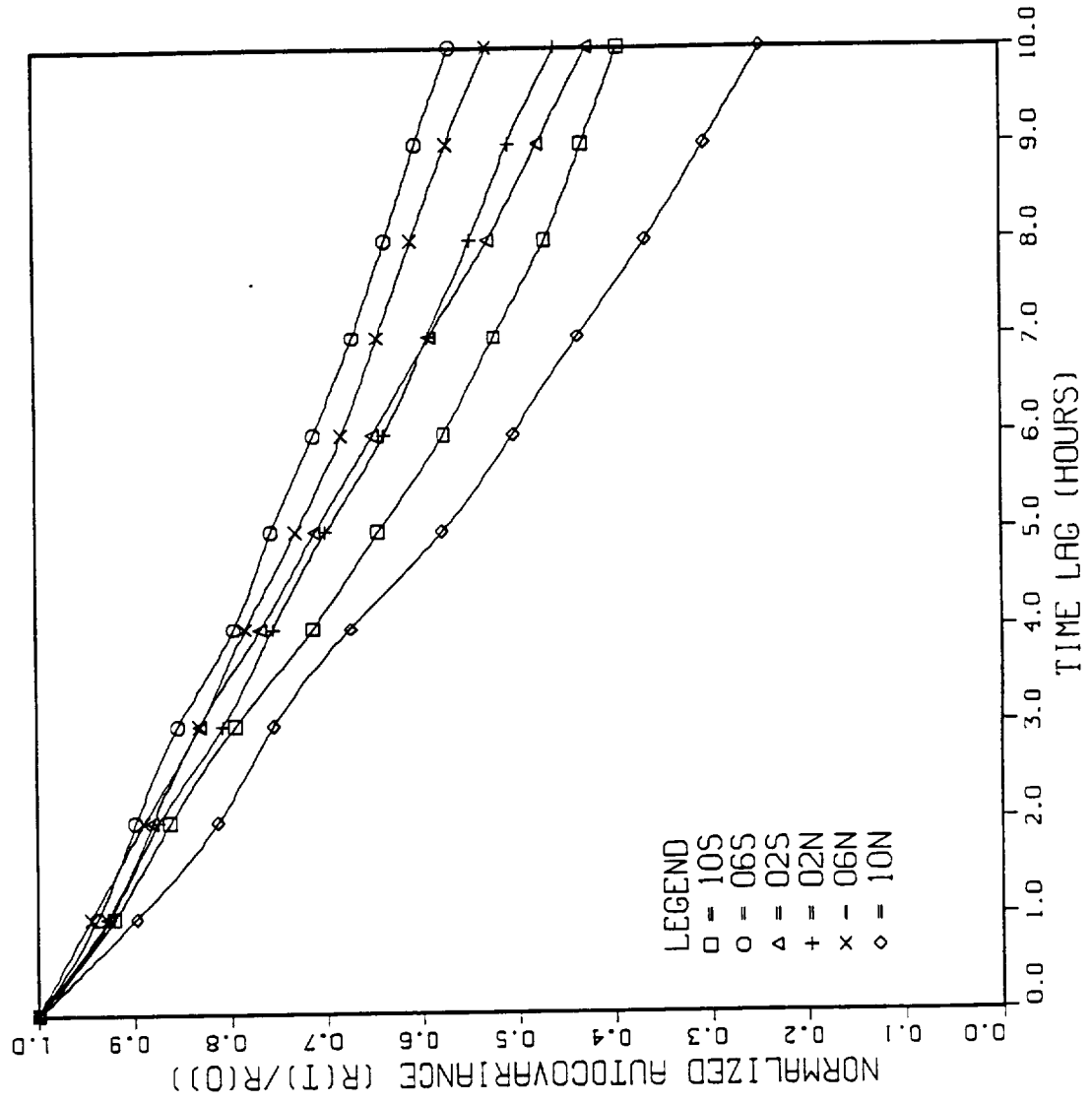


Figure 7, continued

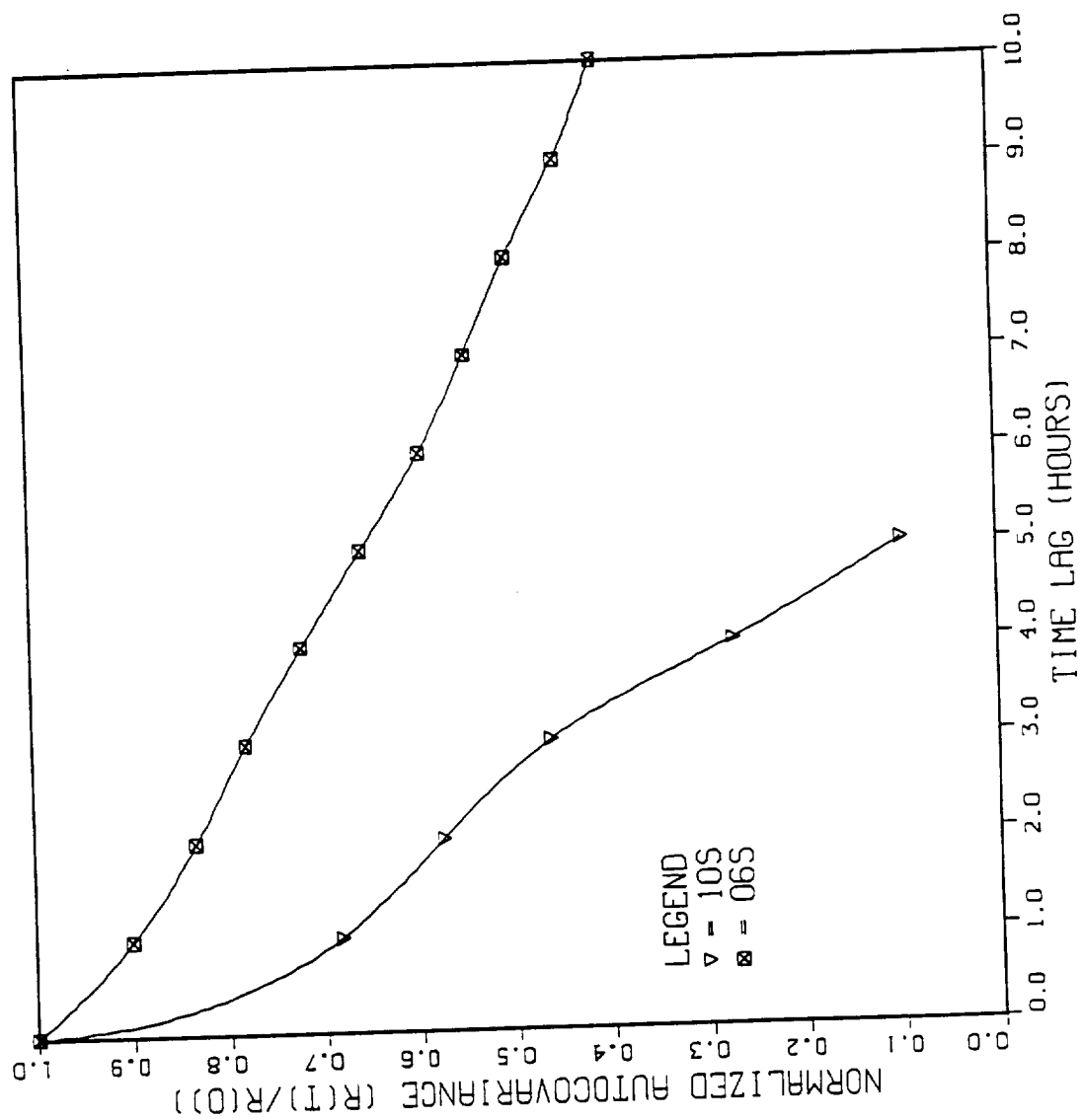


Figure 7, continued

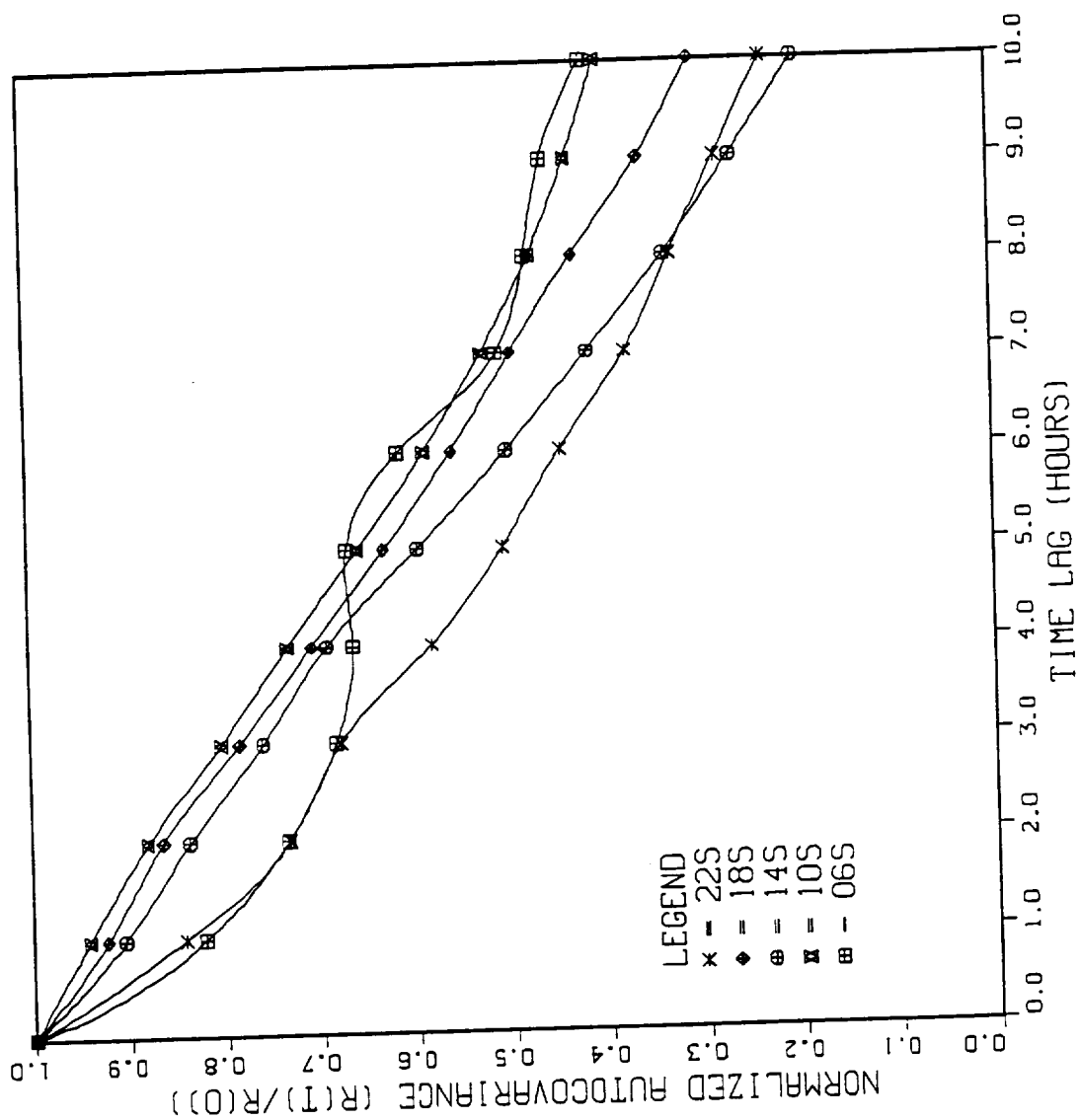


Figure 7, continued

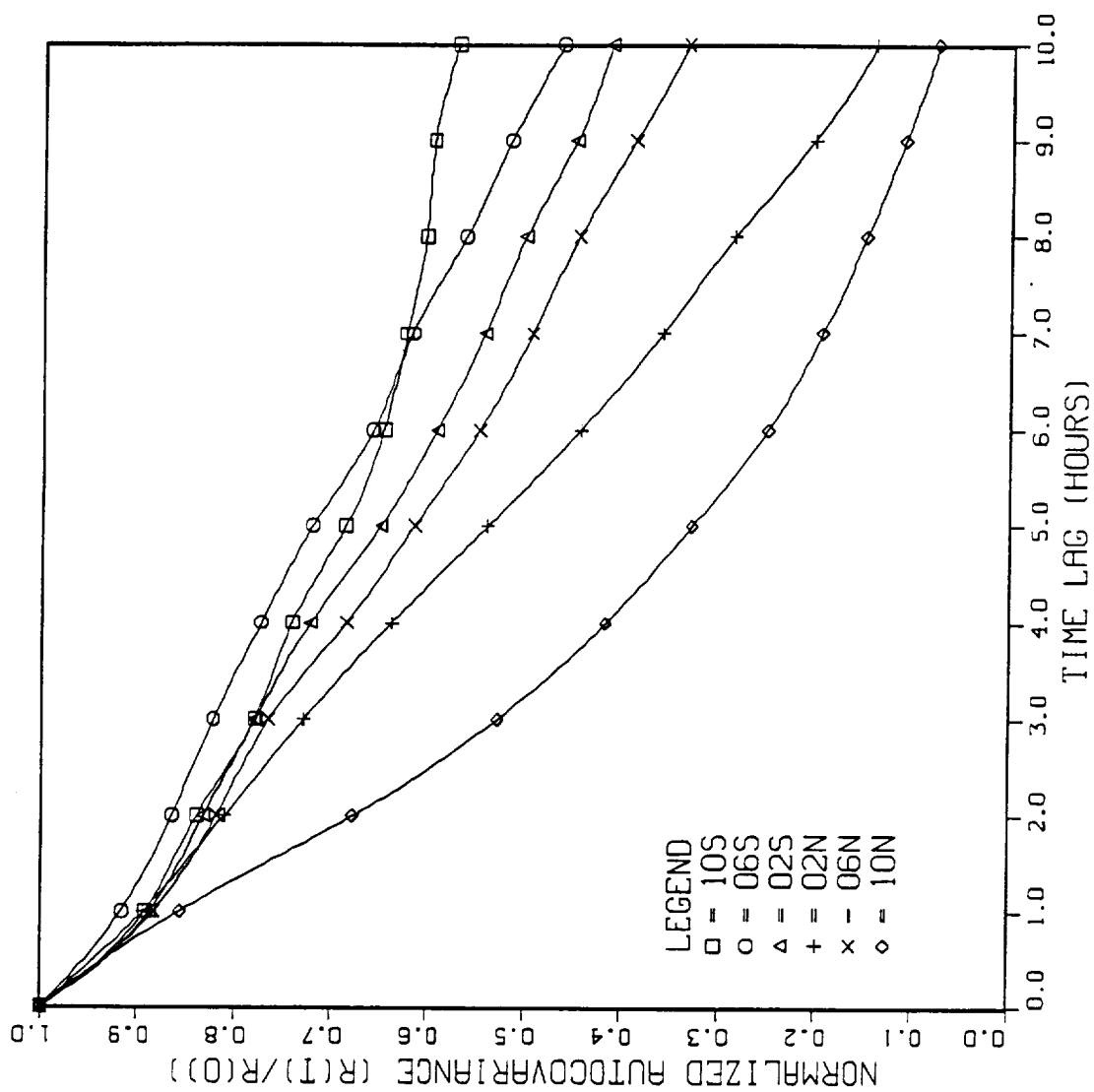


Figure 7, continued

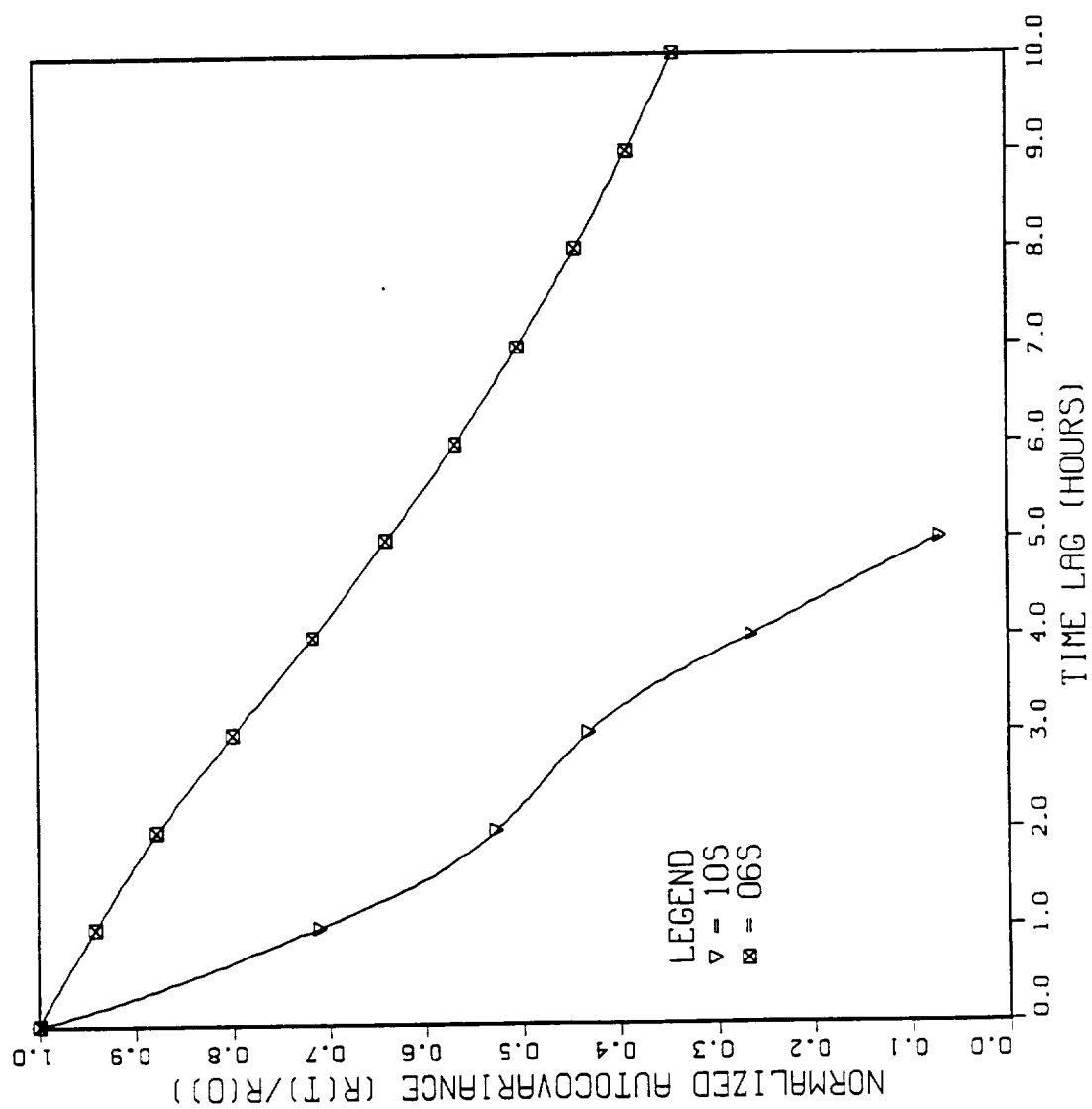


Figure 7, continued

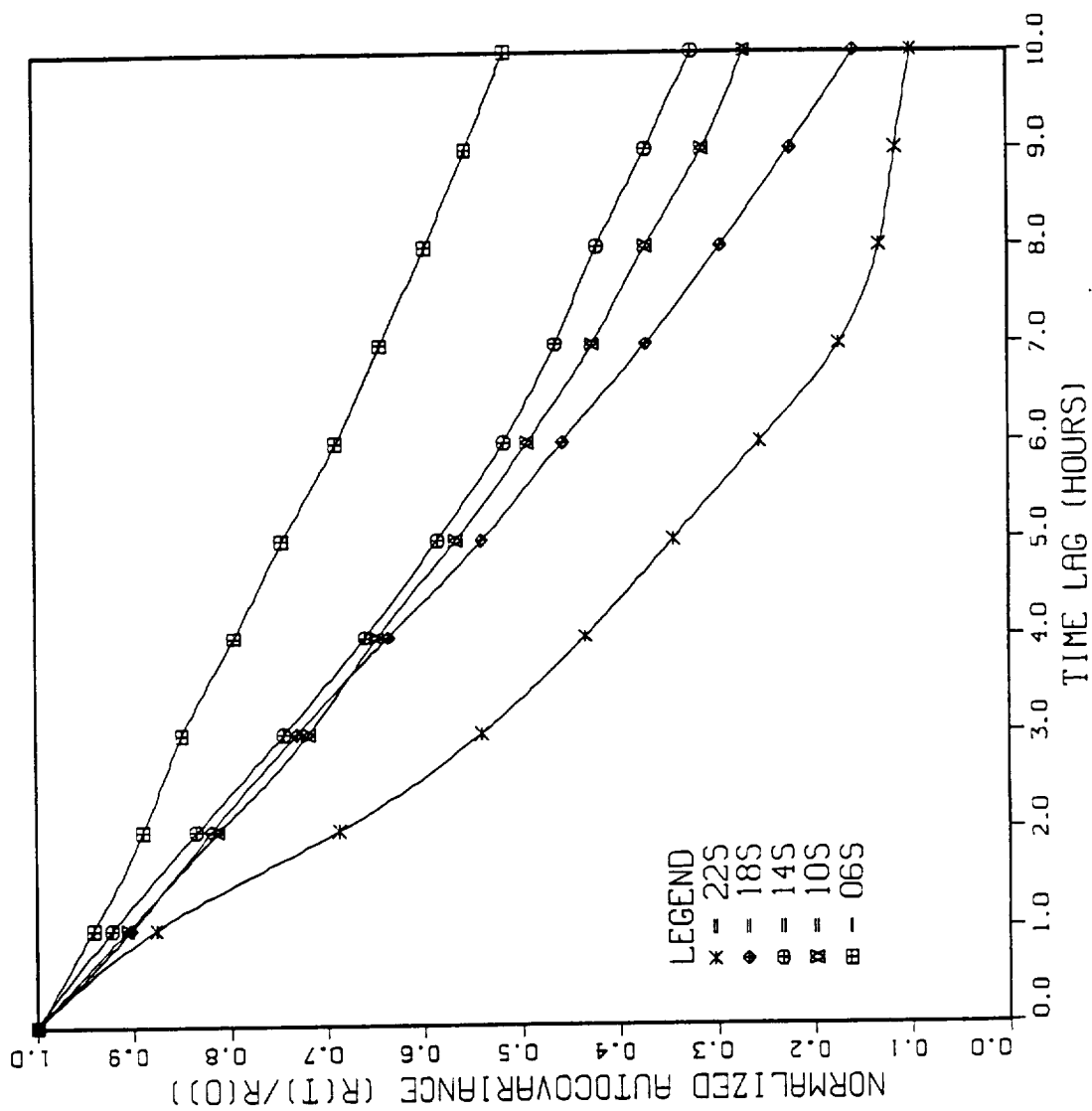


Figure 7, continued

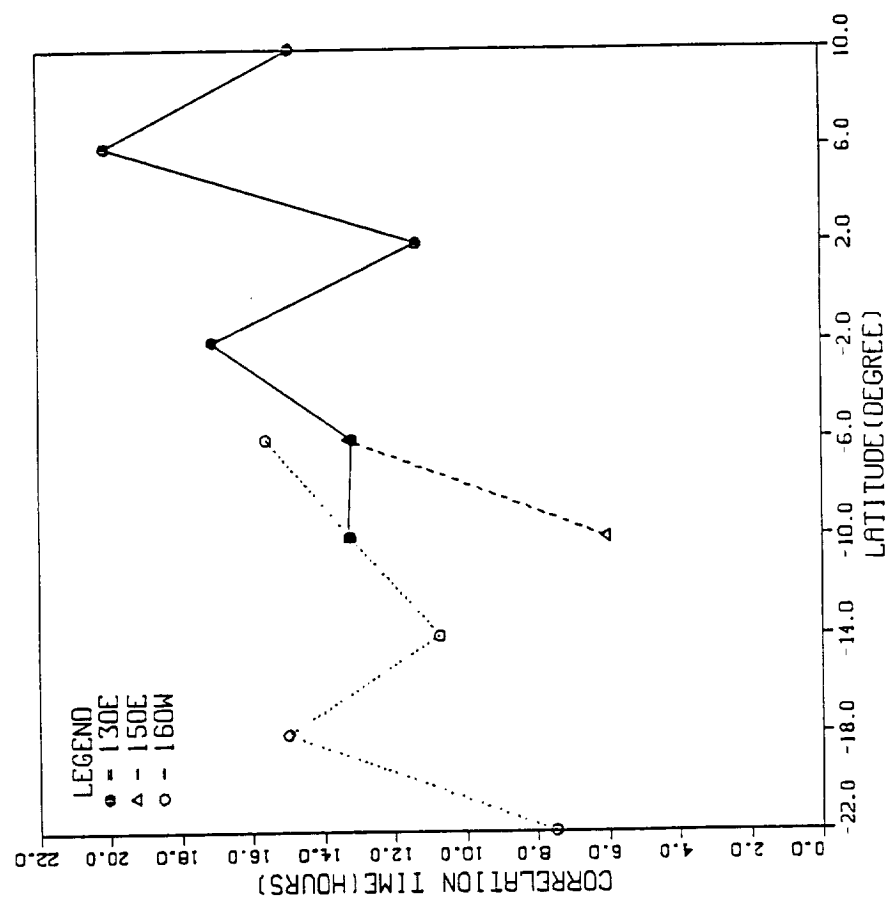


Figure 8. Variation of the correlation times versus grid box locations in December, January, and February.

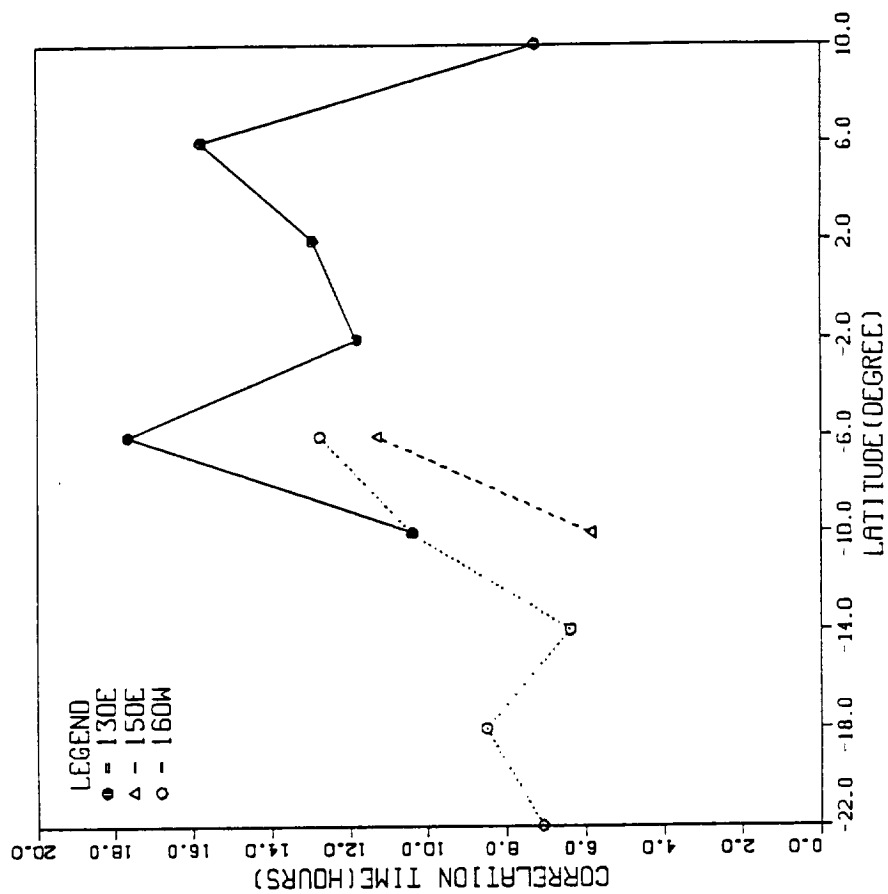


Figure 8, continued

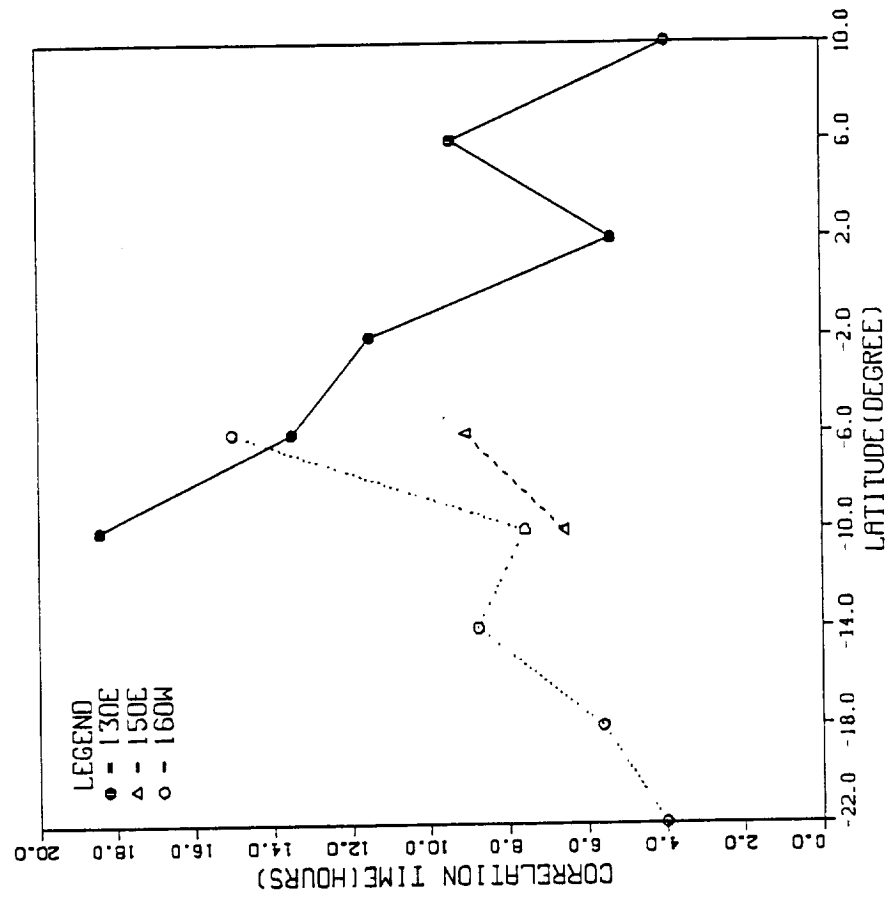


Figure 8, continued

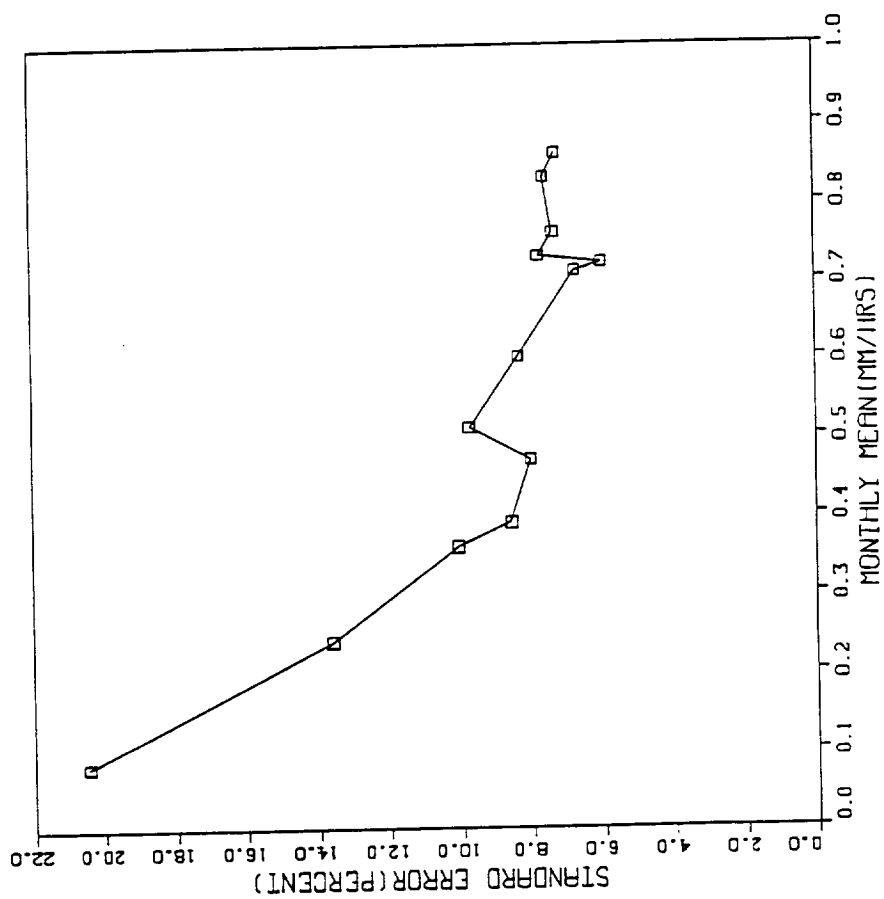


Figure 9, Variation of the standard sampling errors versus monthly mean rain rates in December for the TRMM, NOAA-10, and two sun-synchronous orbits.

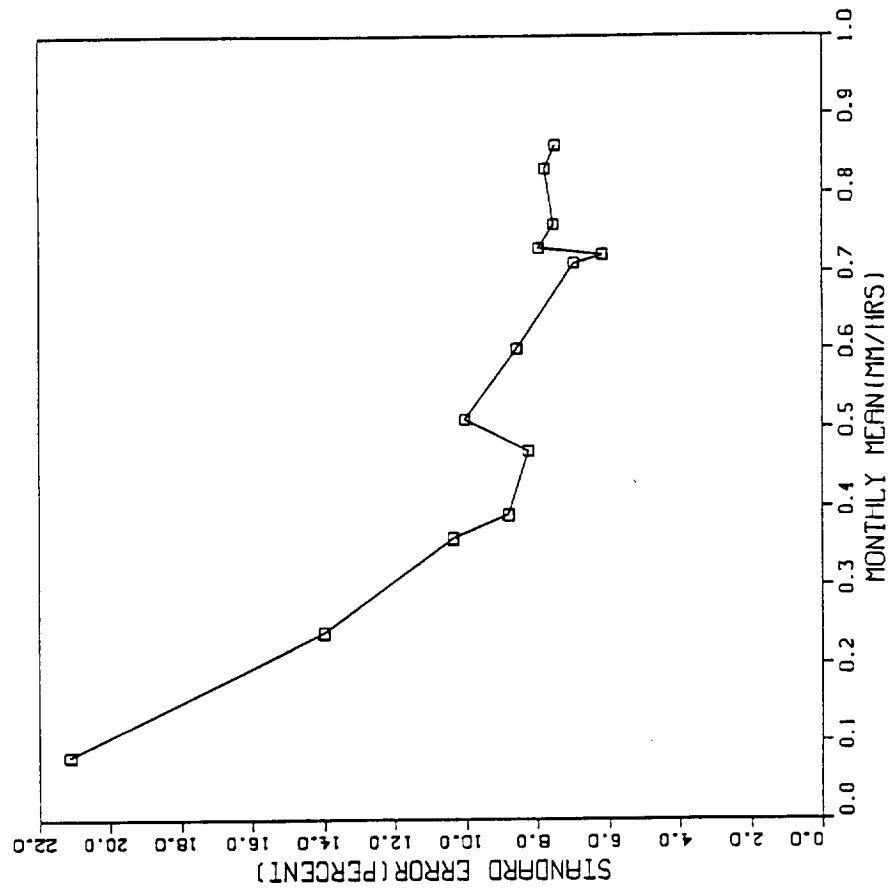


Figure 9, continued

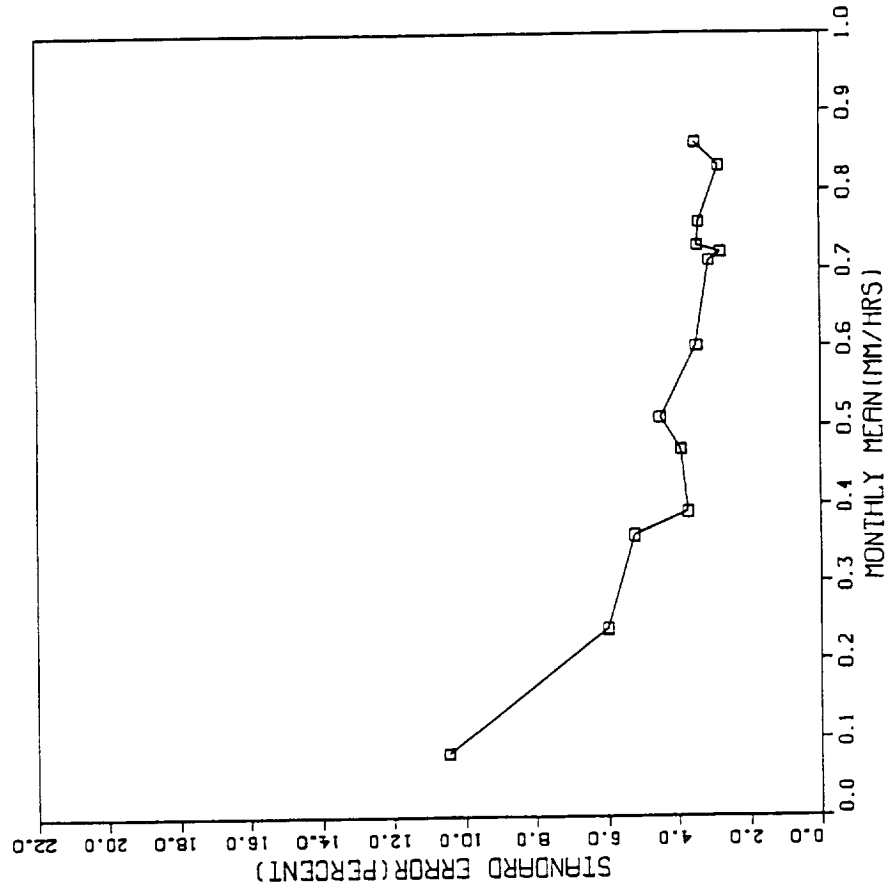


Figure 9, continued

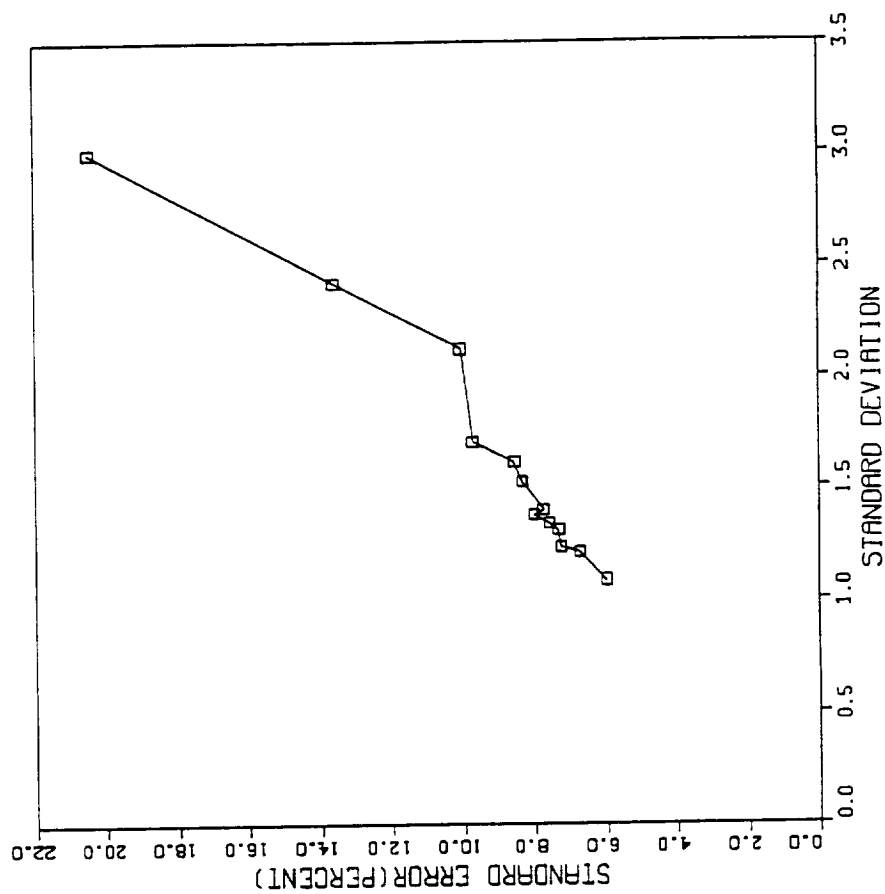


Figure 10. Variation of the standard sampling errors versus monthly rain rates standard deviation in December for the TRMM, NOAA-10, and two sun-synchronous orbits.

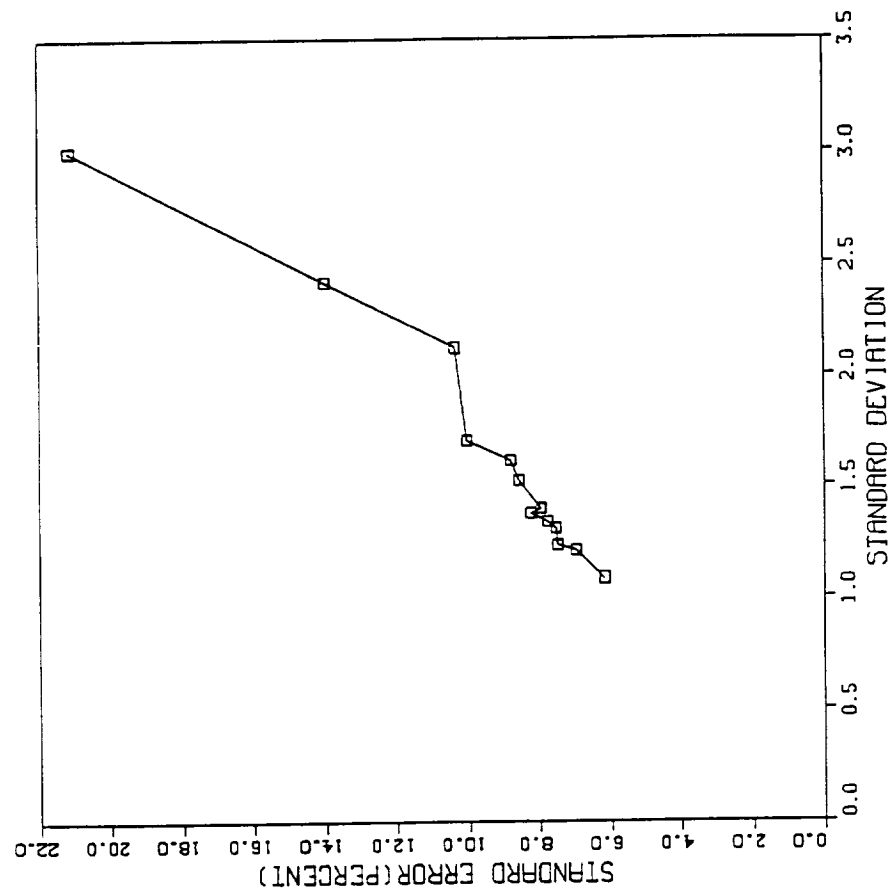


Figure 10, continued

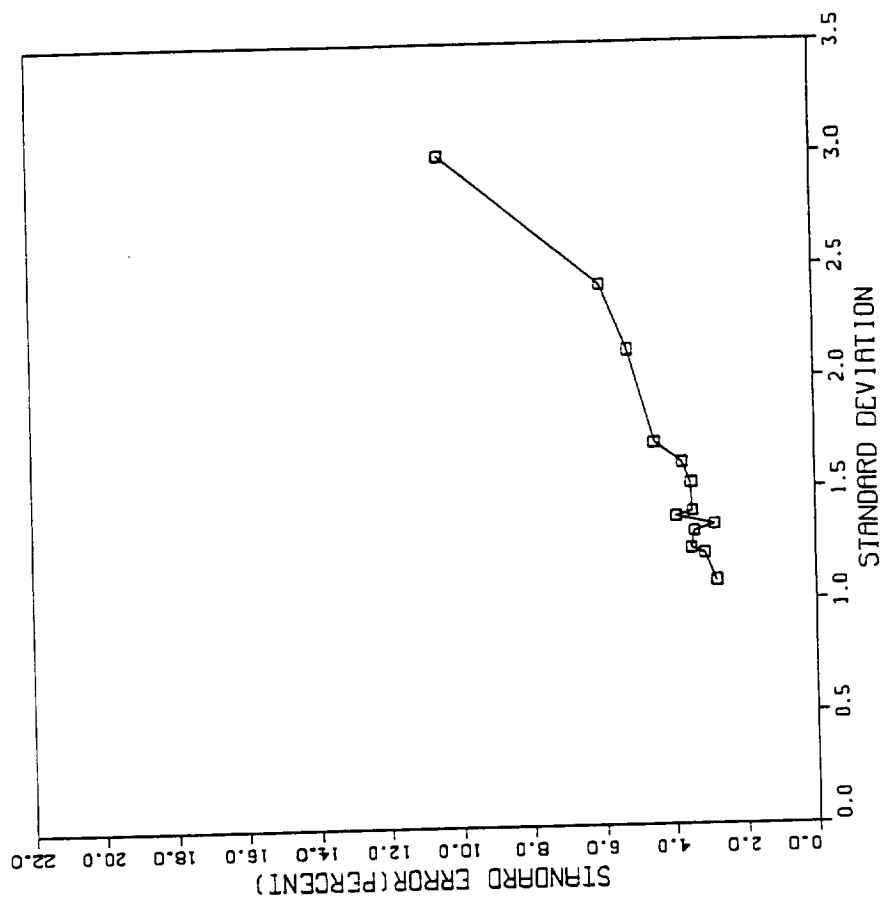


Figure 10, continued

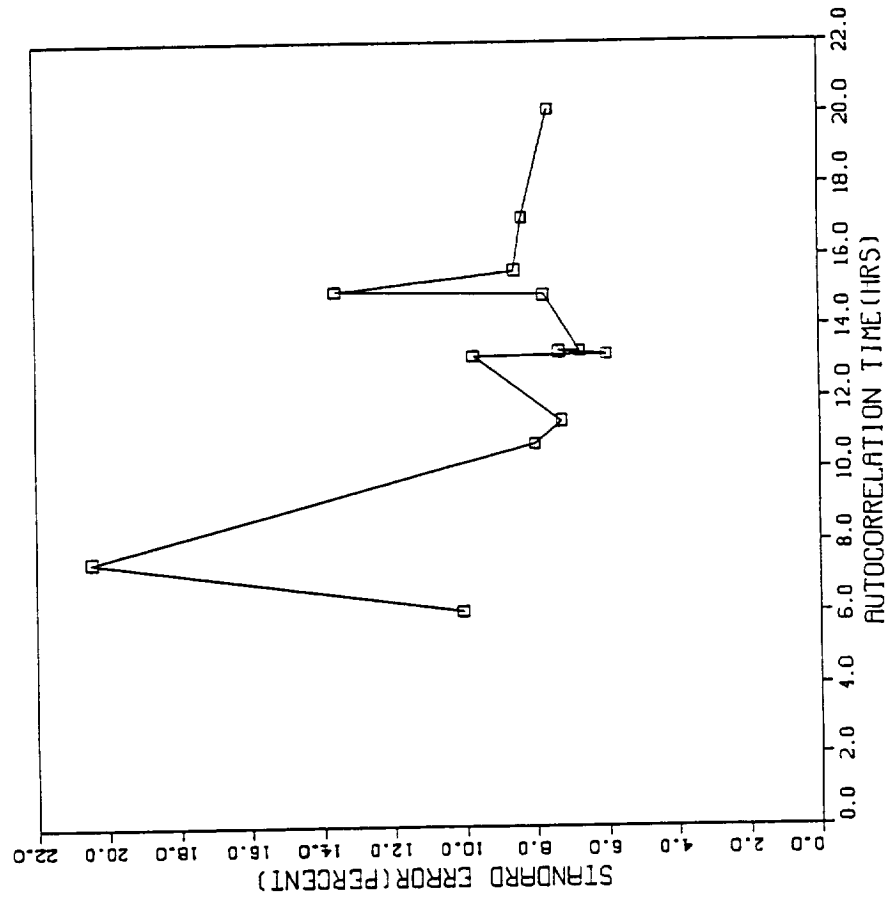


Figure 11. Variation of the standard sampling errors versus correlation times in December for the TRMM, NOAA-10, and sun-synchronous orbits.

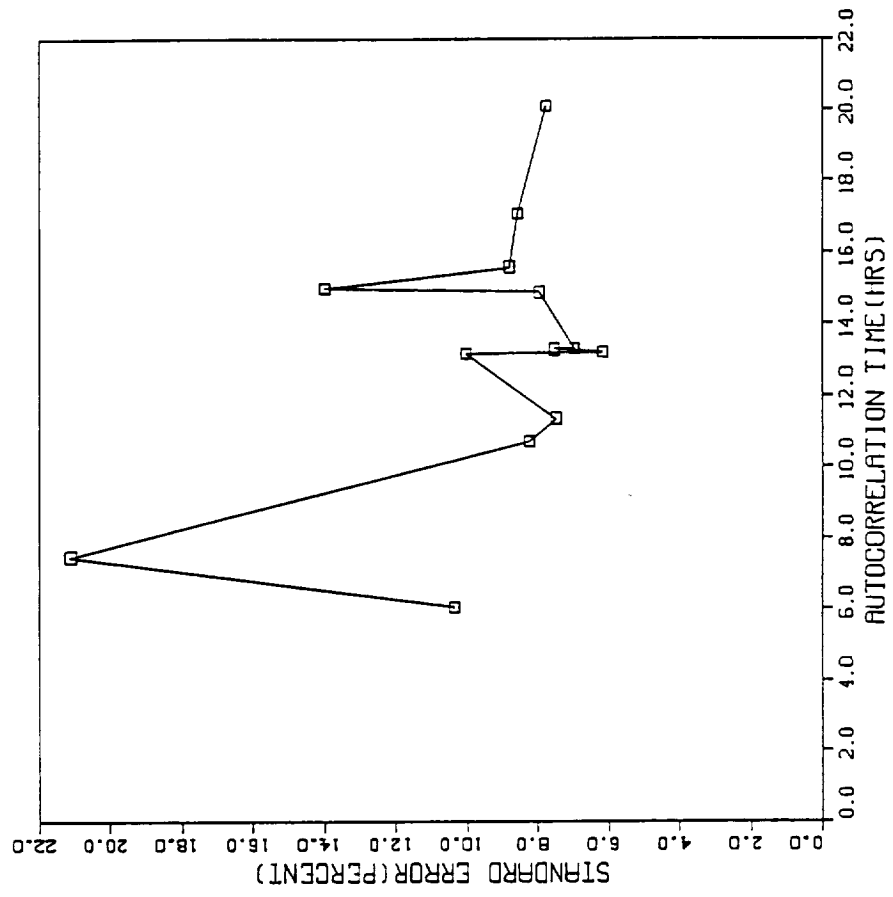


Figure 11, continued

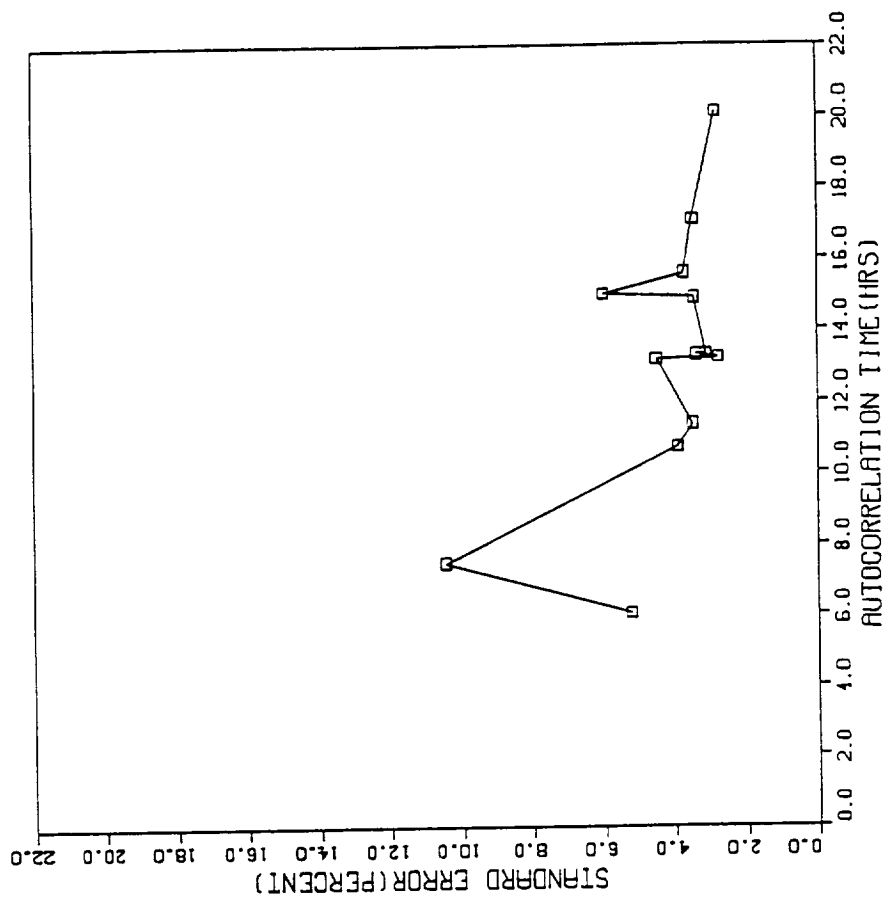


Figure 11, continued

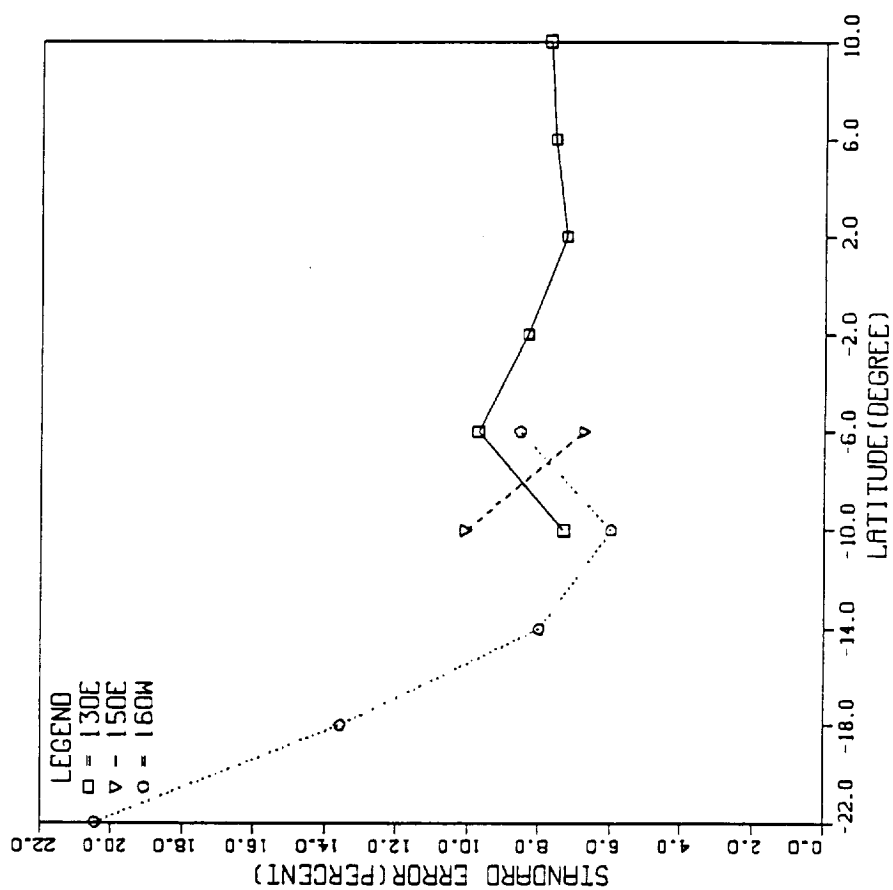


Figure 12. Variation of the standard sampling errors versus grid box location in December for the TRMM, NOAA-10, and sun-synchronous orbits.

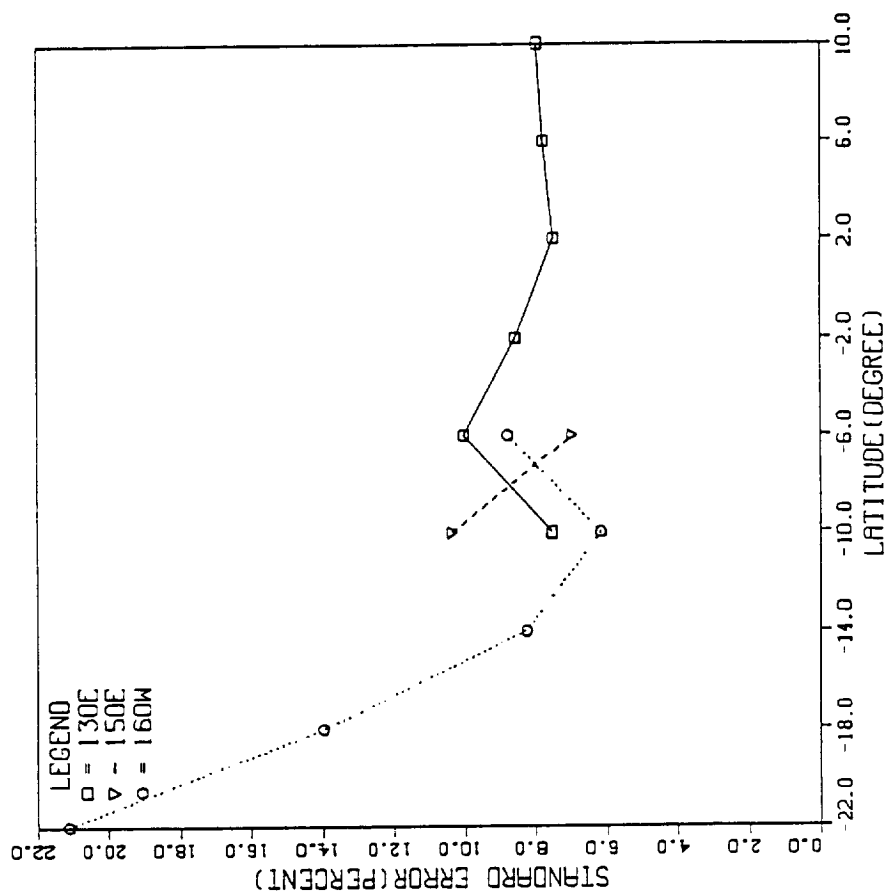


Figure 12, continued

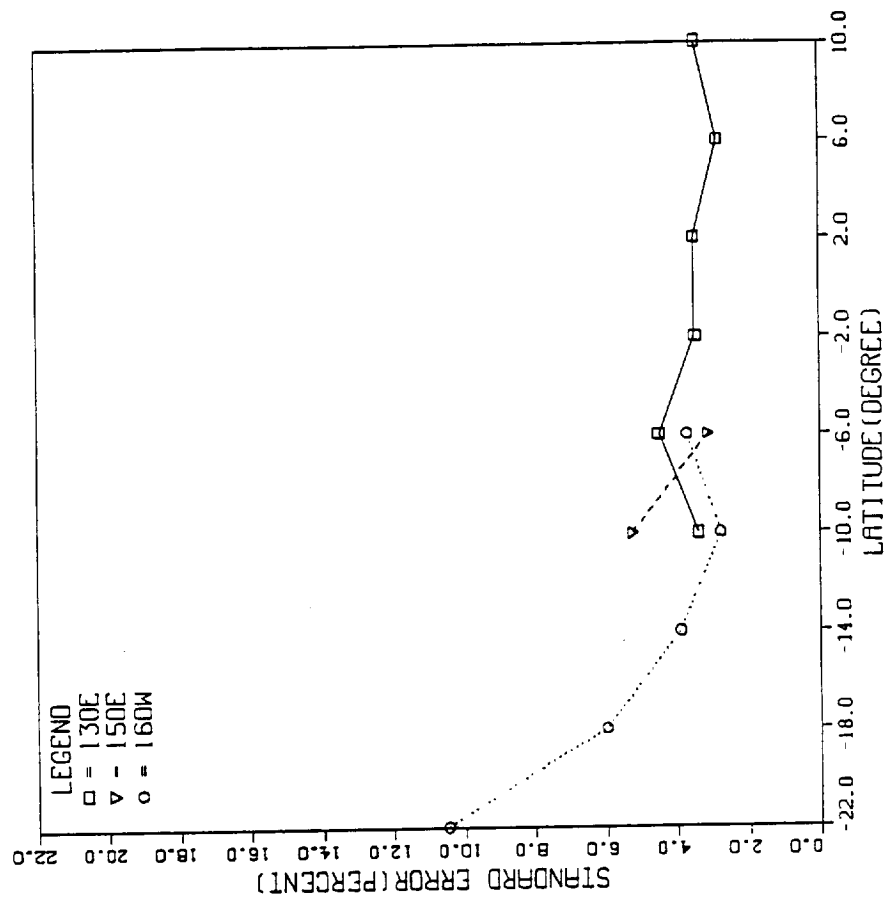


Figure 12, continued

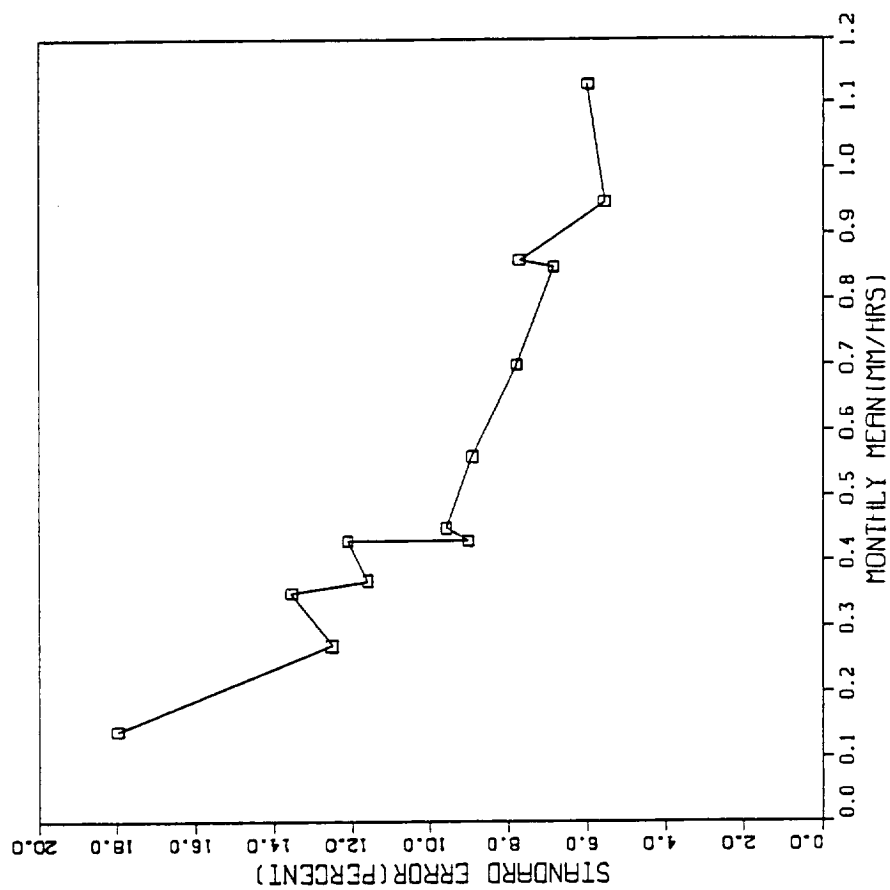


Figure 13. Same as Figure 9 but in January.

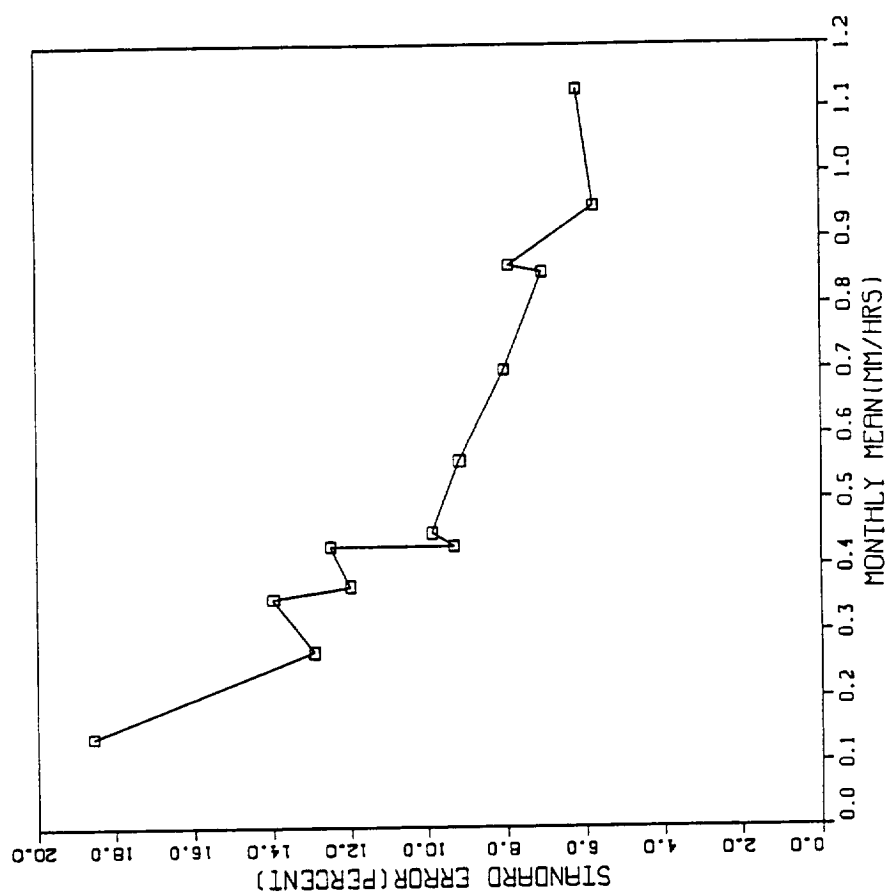


Figure 13, continued

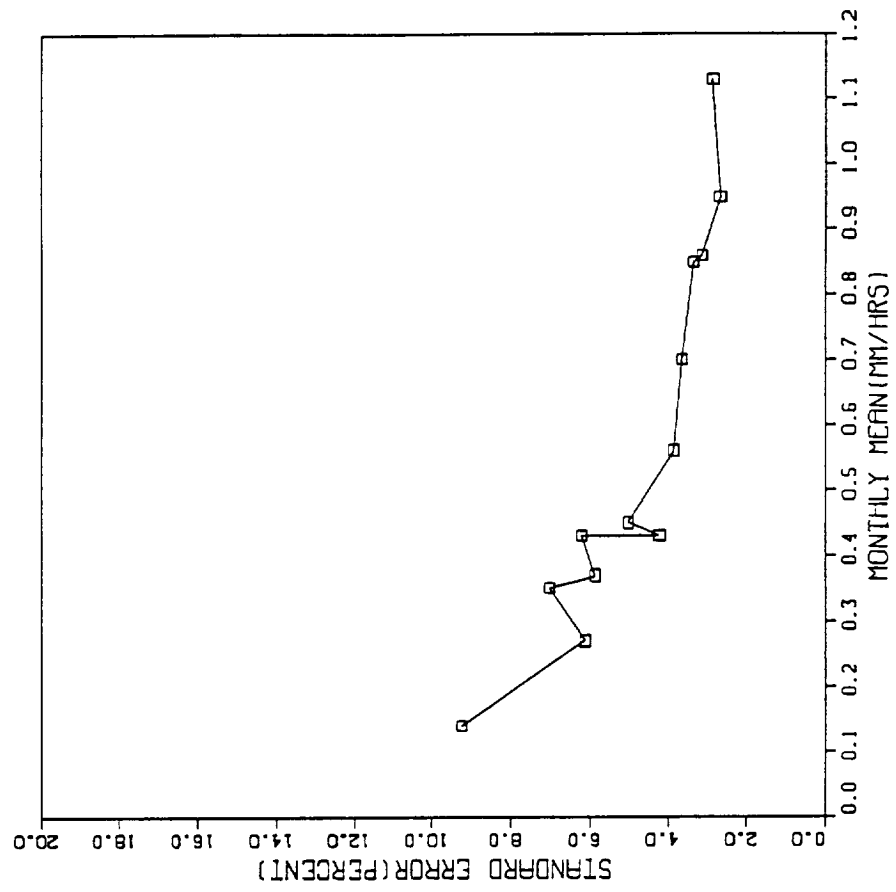


Figure 13, continued

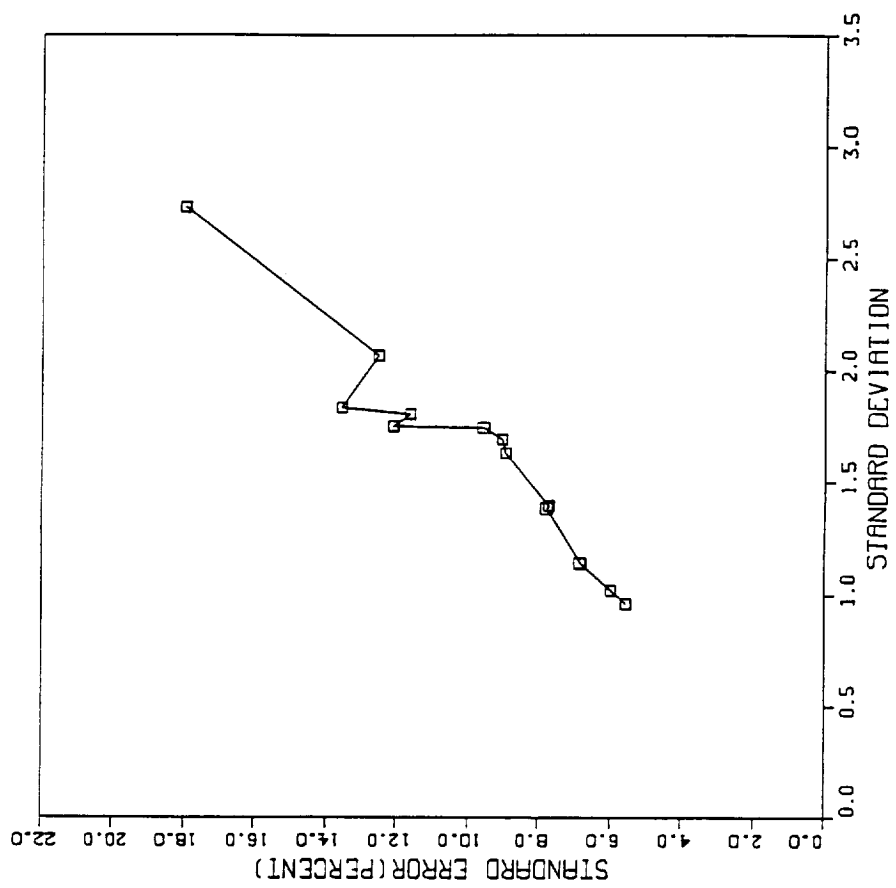


Figure 14. Same as Figure 10 but in January.

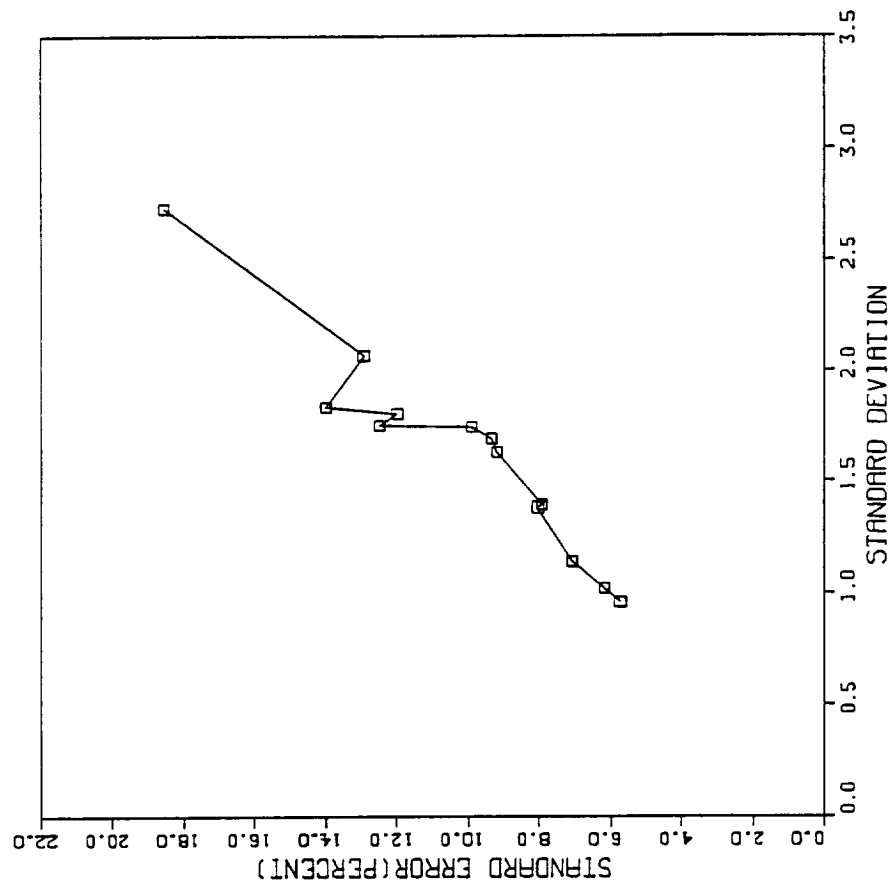


Figure 14, continued

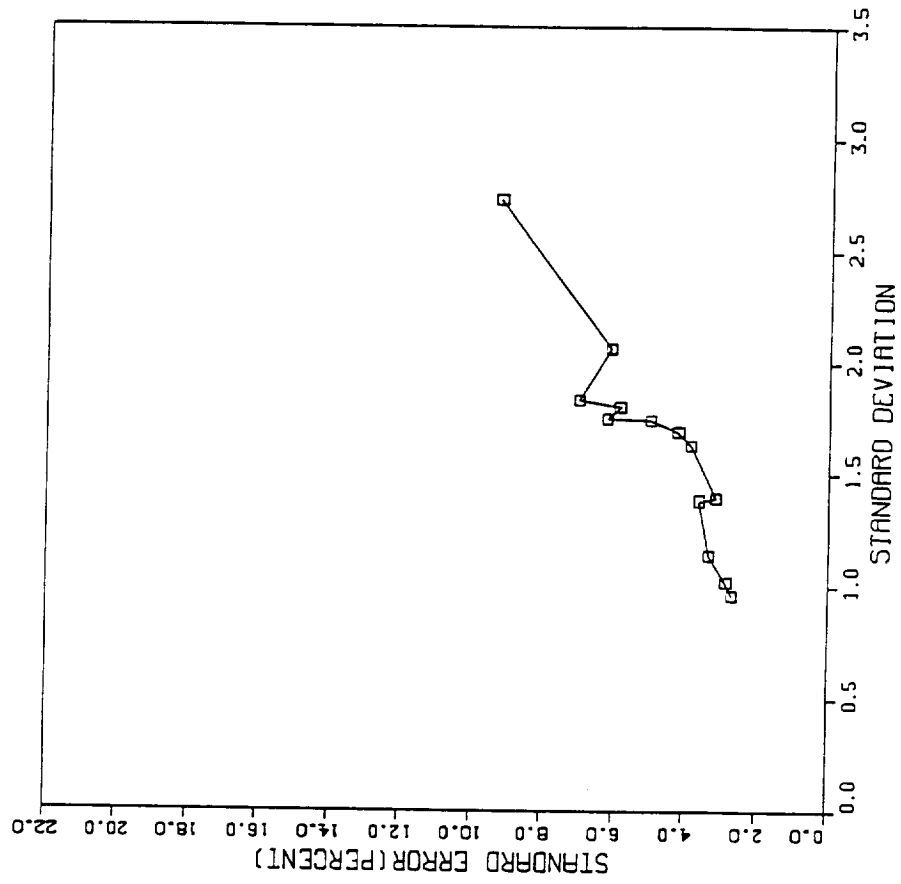


Figure 14, continued

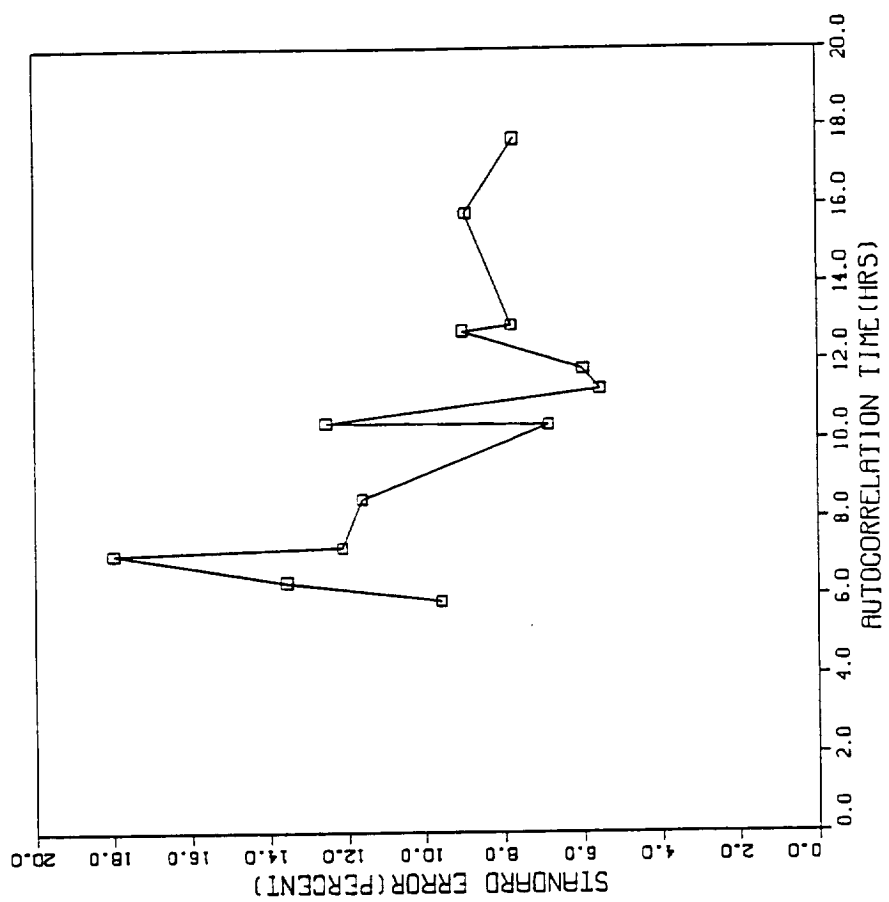


Figure 15. Same as Figure 11 but in January.

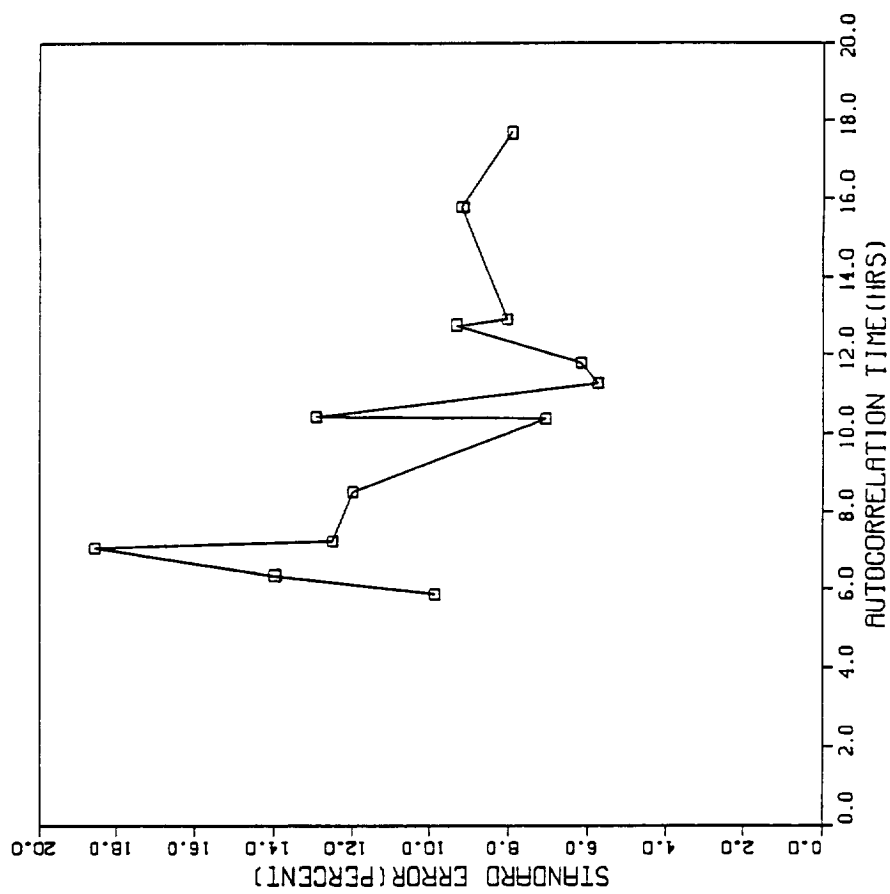


Figure 15, continued

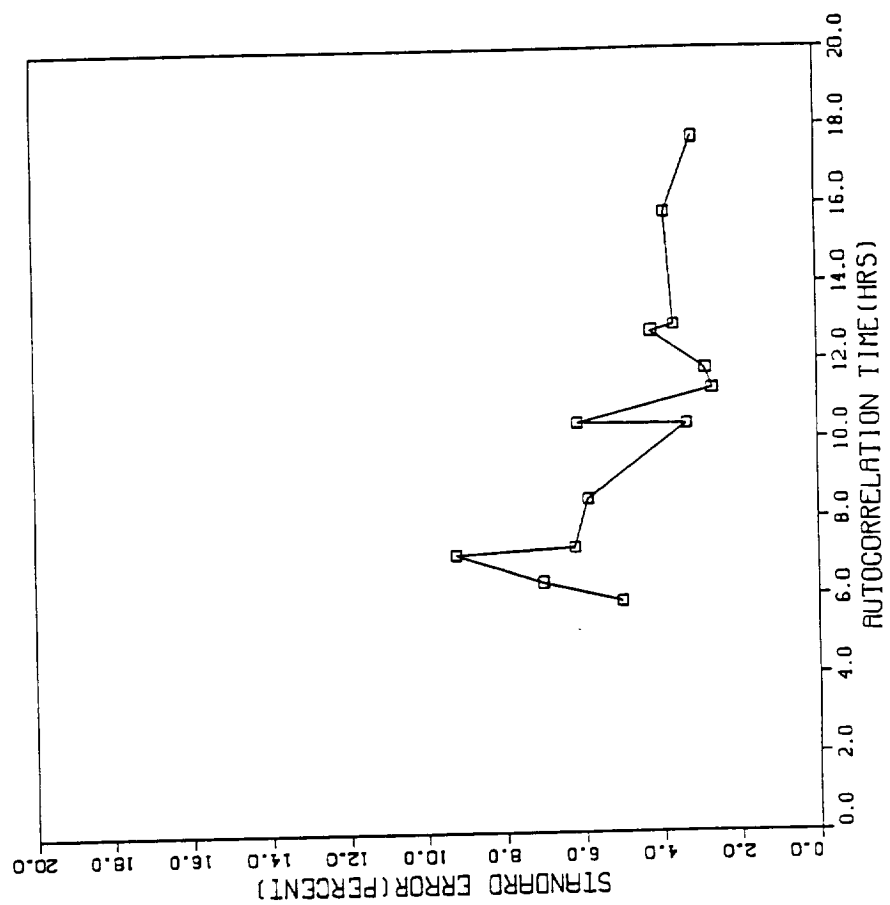


Figure 15, continued

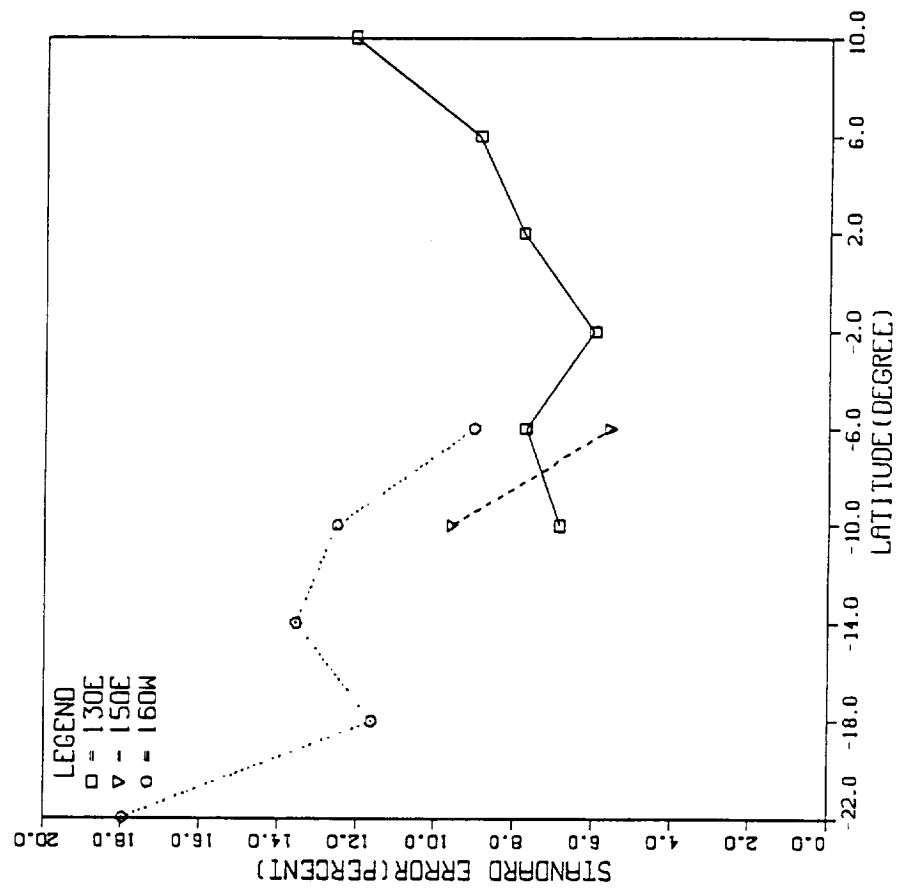


Figure 16. Same as Figure 12 but in January.

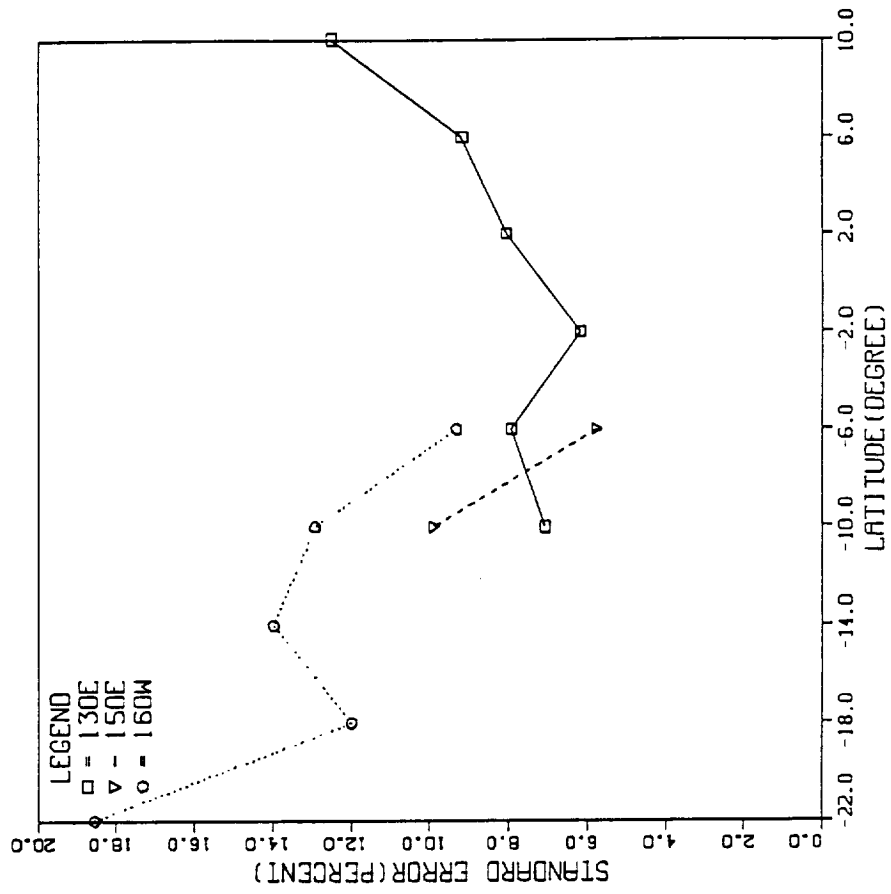


Figure 16, continued

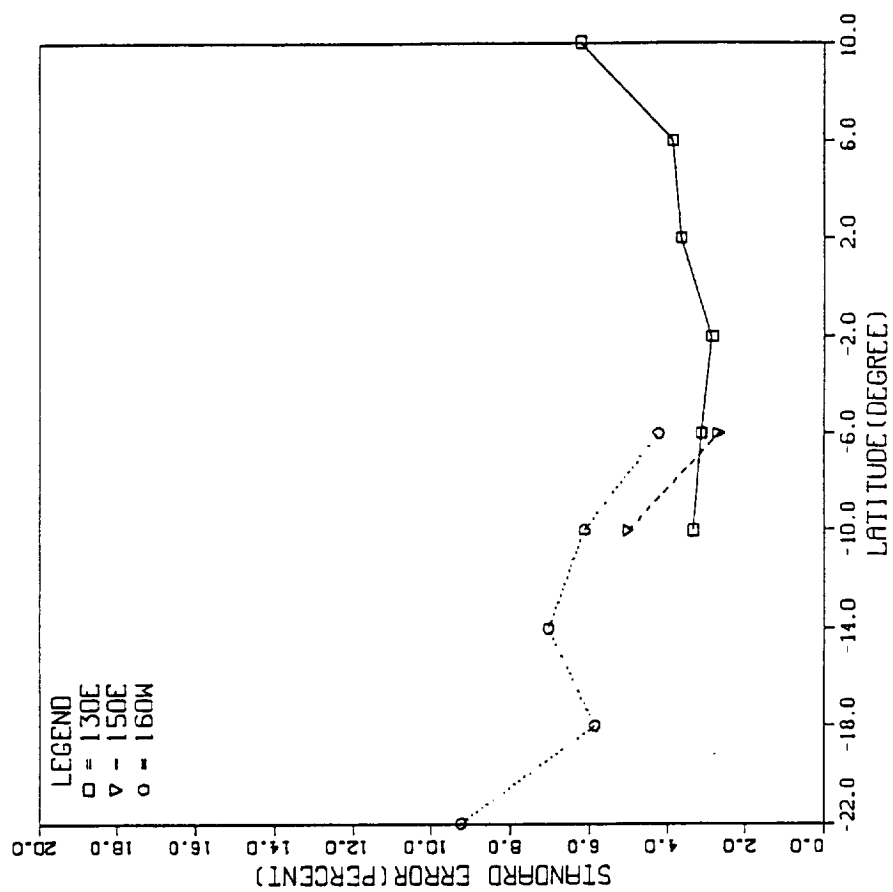


Figure 16, continued

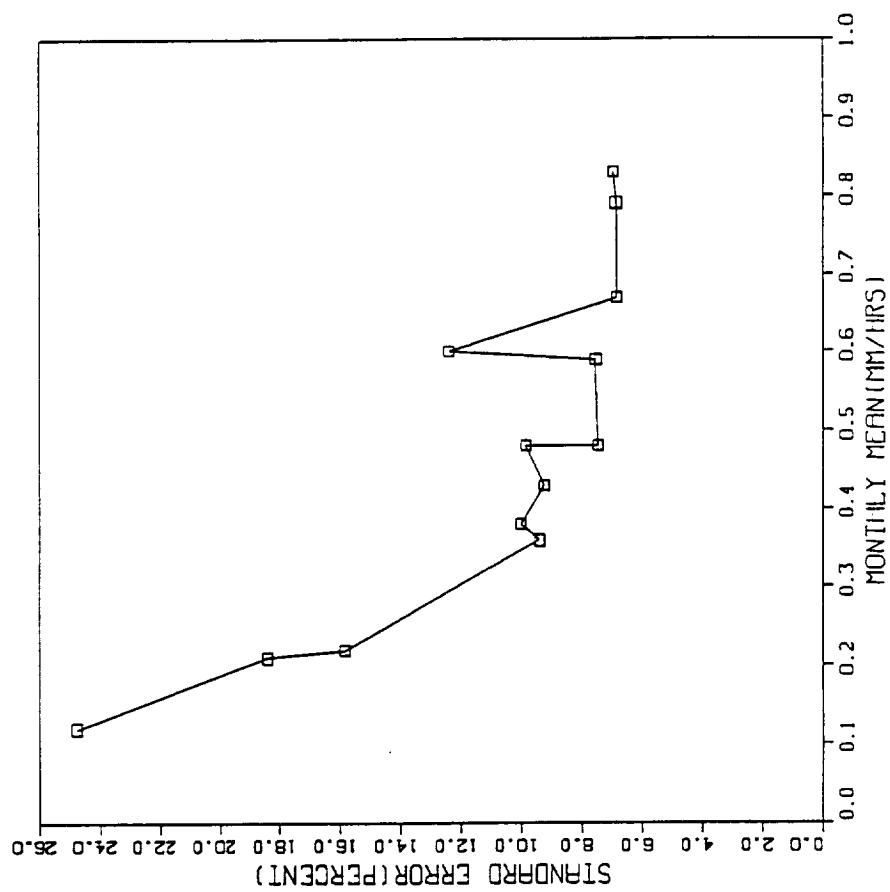


Figure 17. Same as Figure 9 but in February.

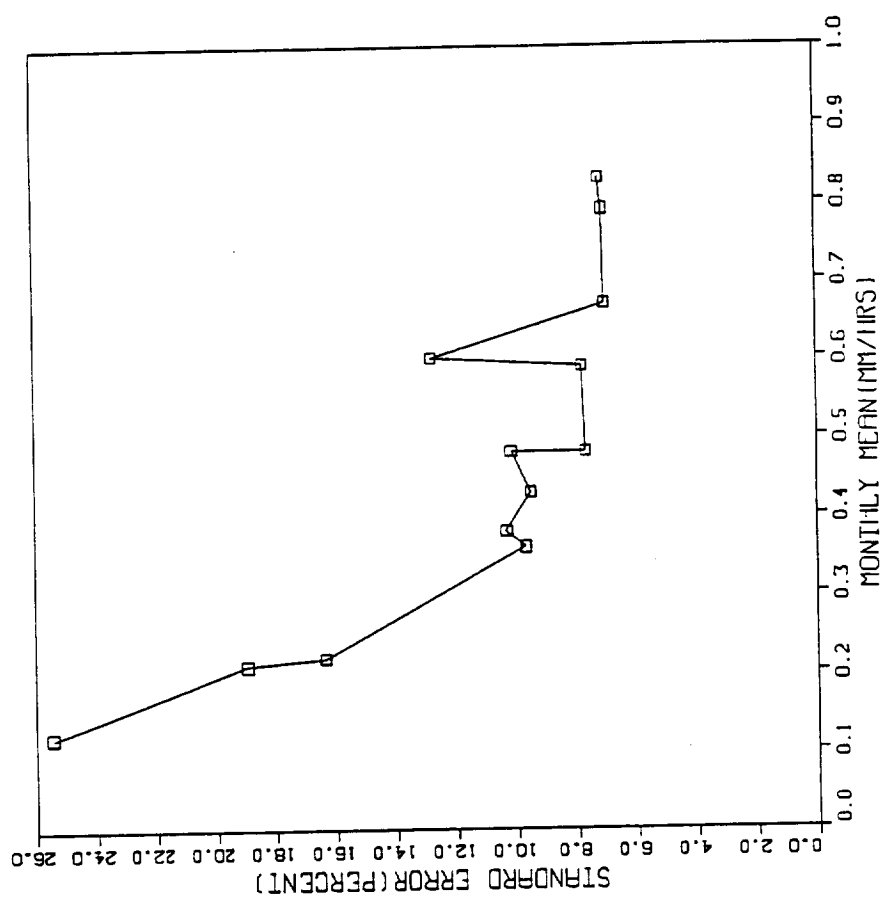


Figure 17, continued

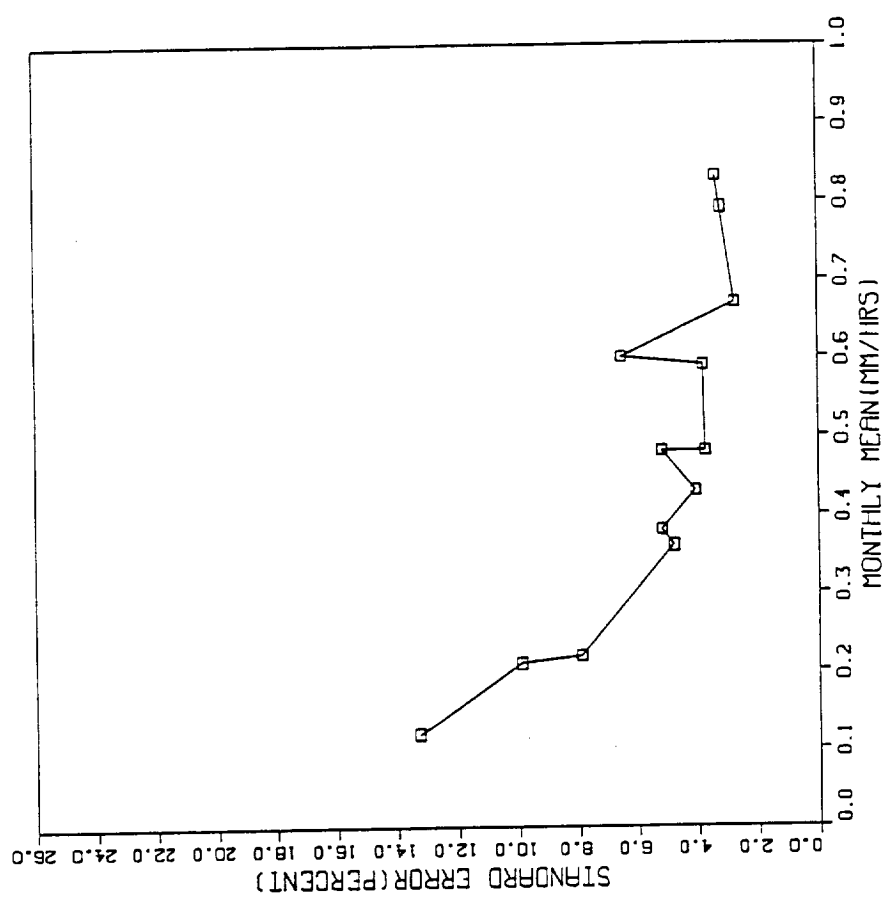


Figure 17, continued

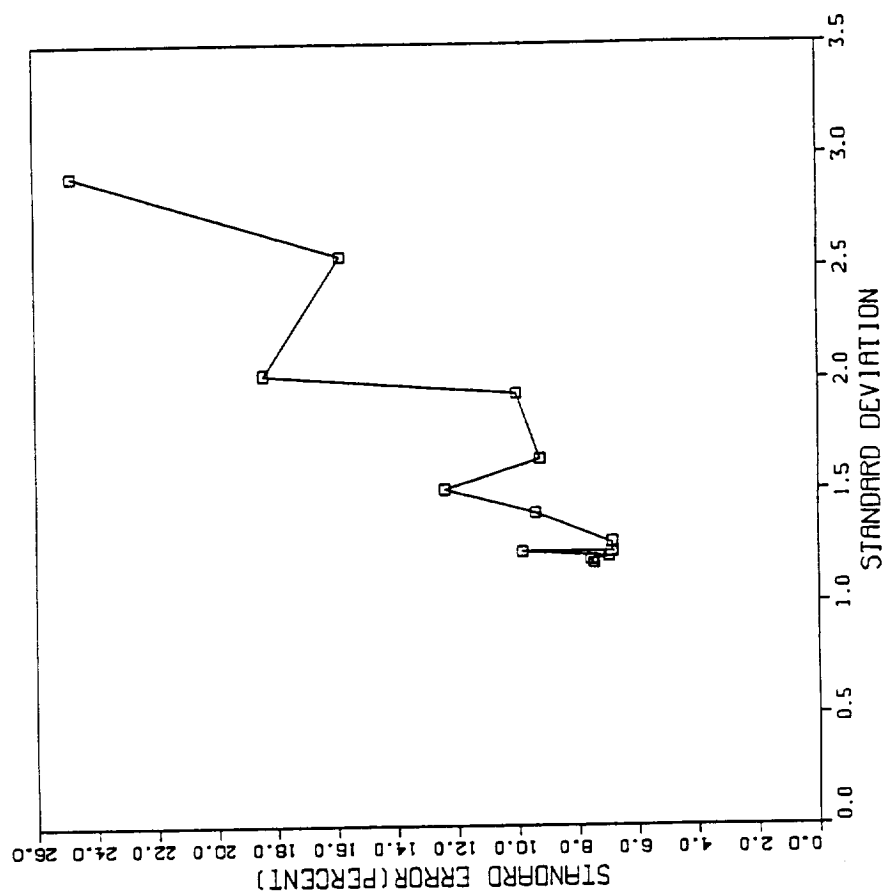


Figure 18. Same as Figure 10 but in February.

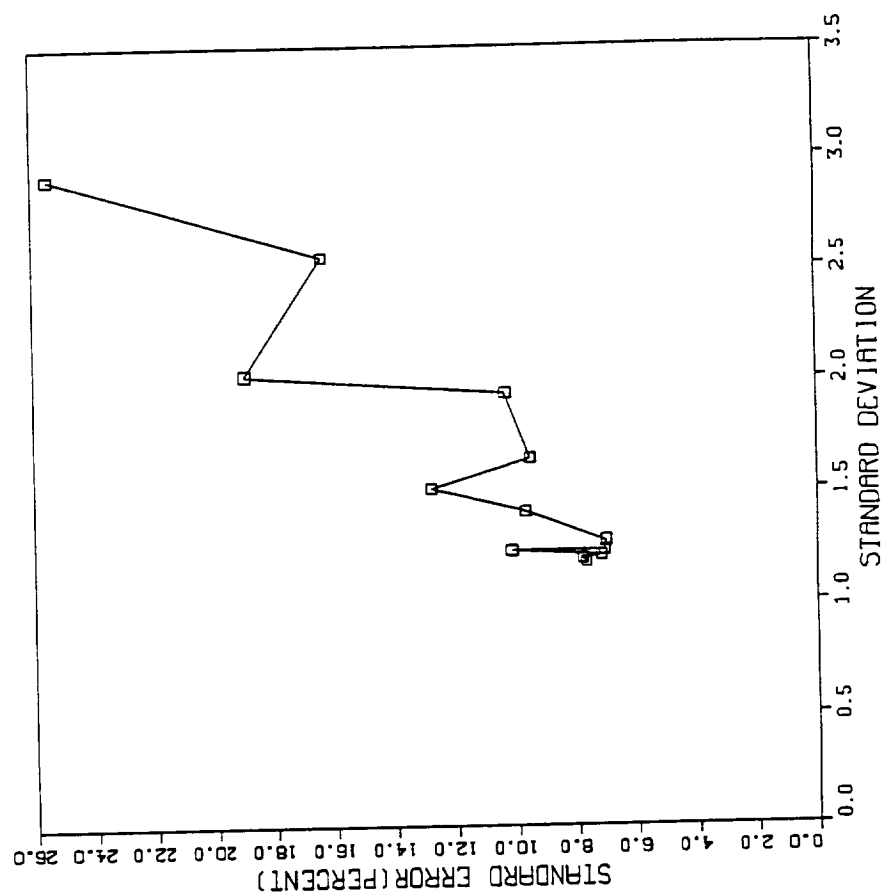


Figure 18, continued

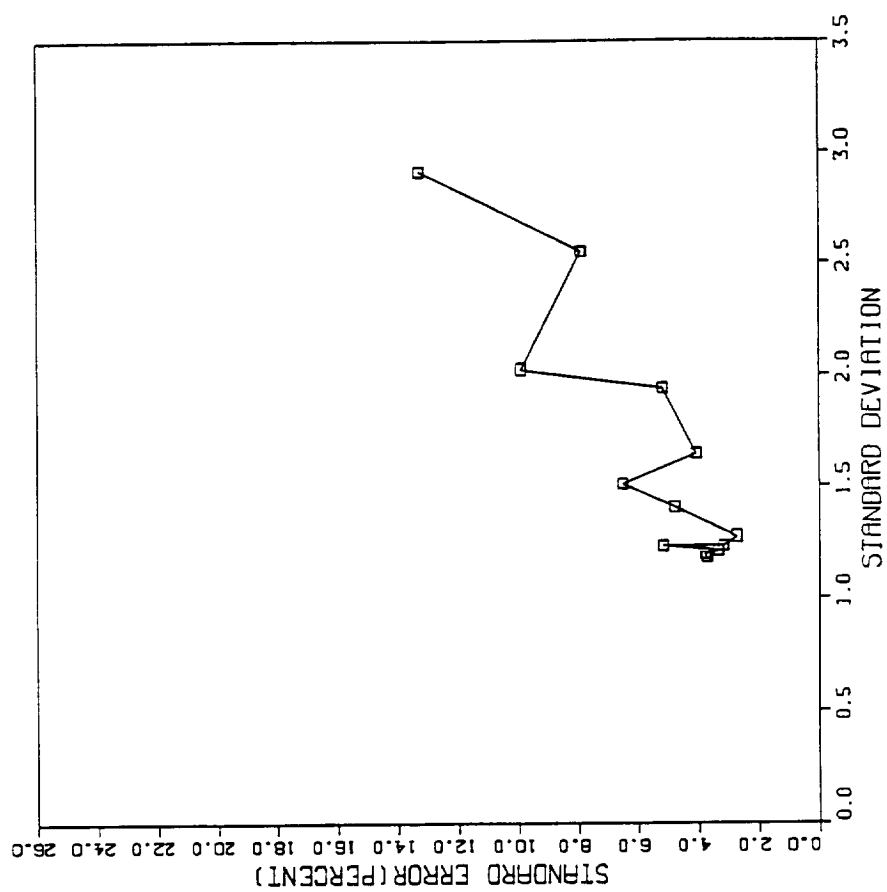


Figure 18, continued

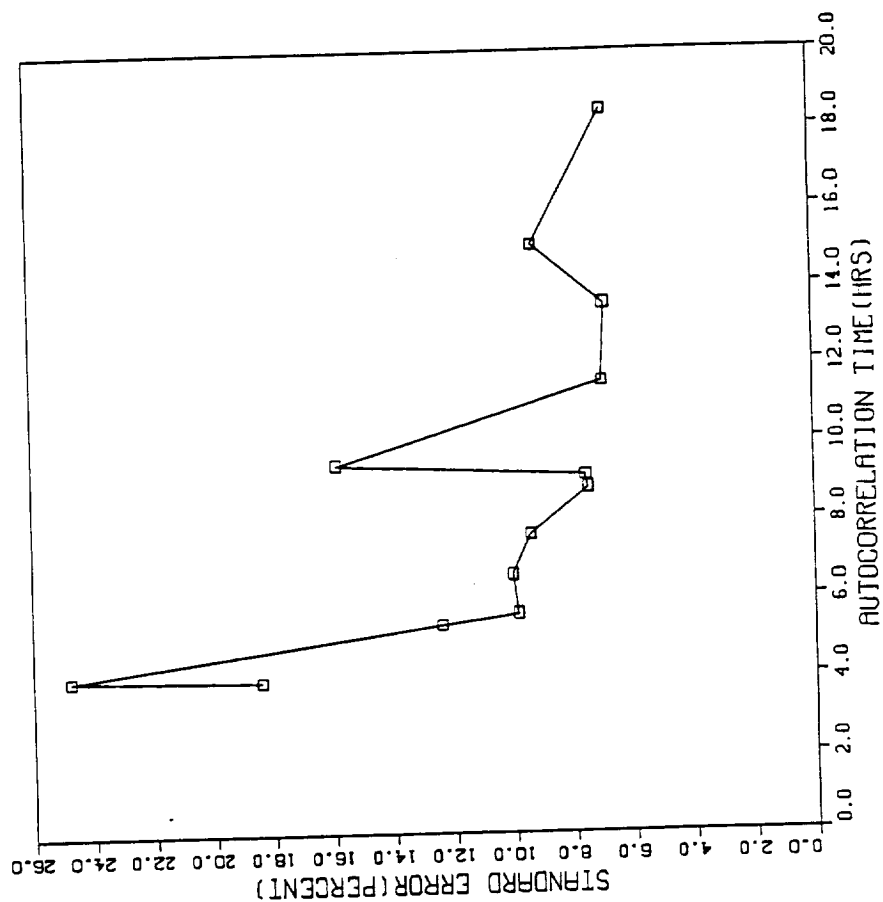


Figure 19. Same as Figure 11 but in February.

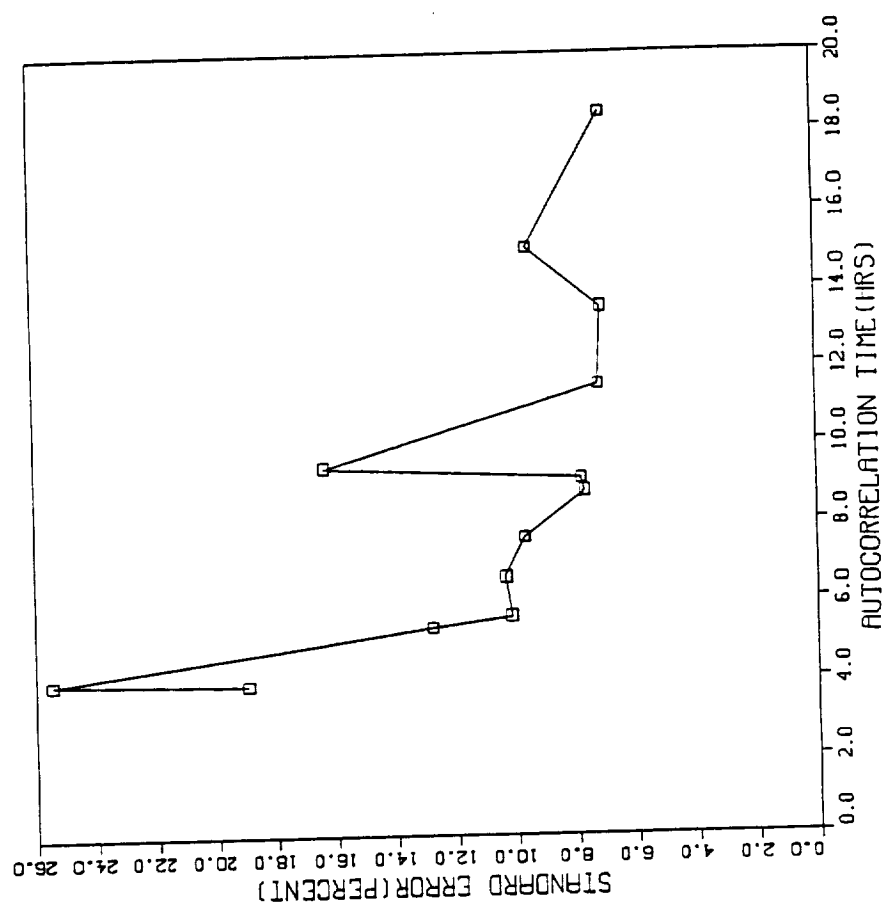


Figure 19, continued

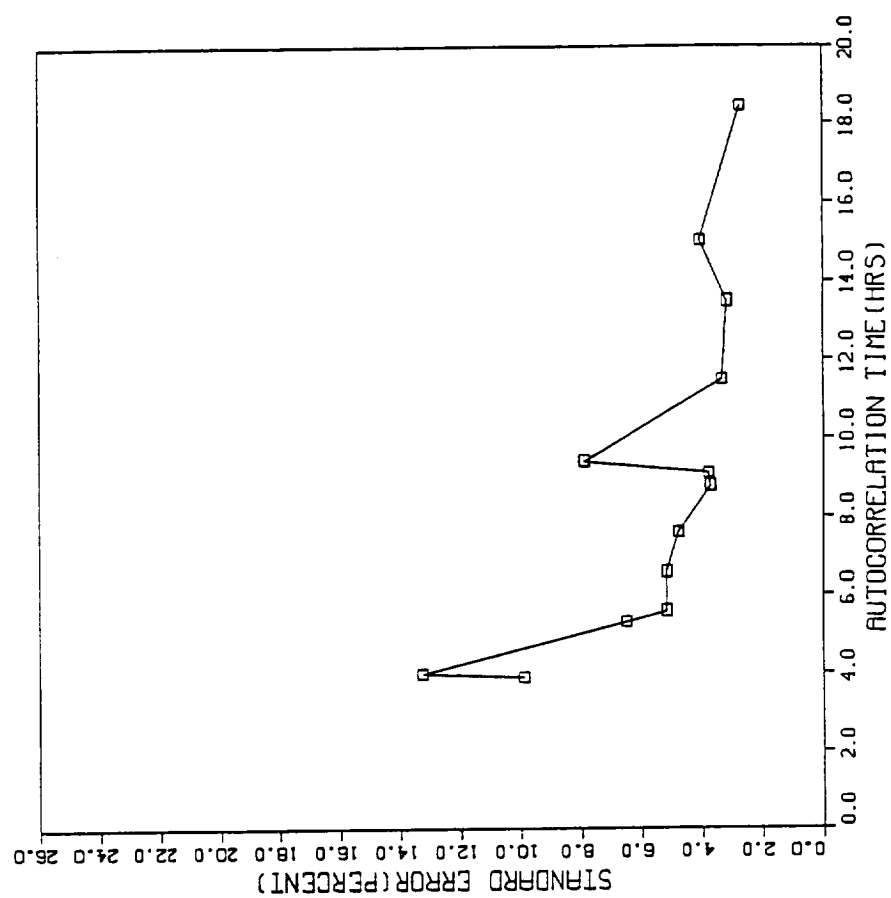


Figure 19, continued

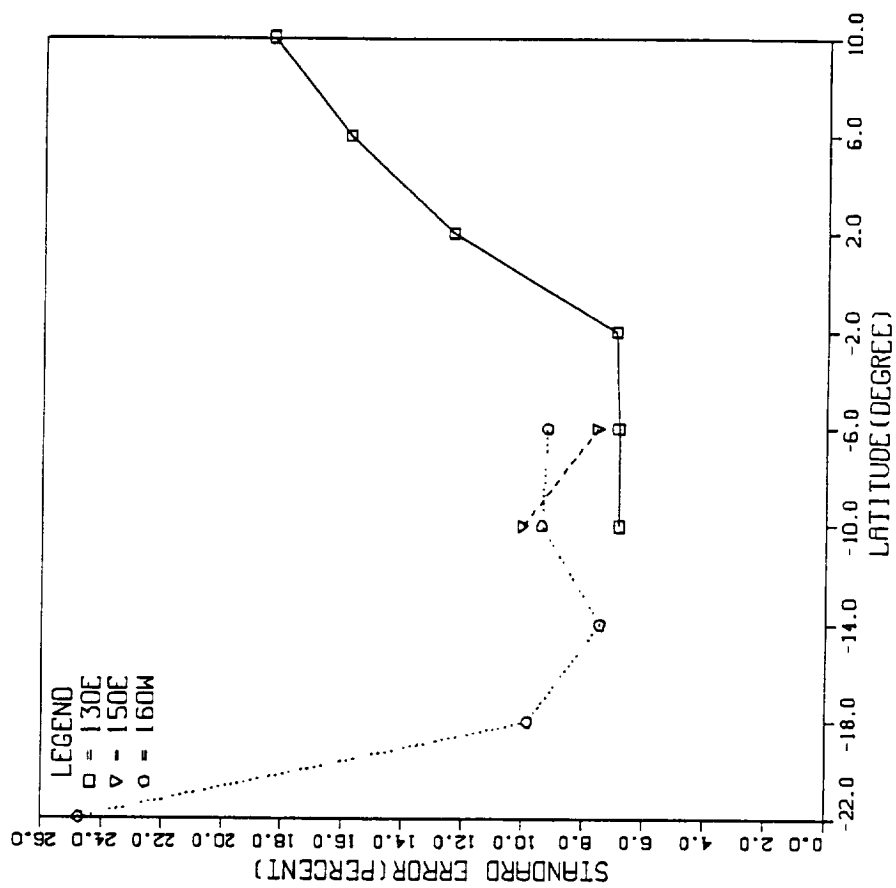


Figure 20. Same as Figure 12 but in February.

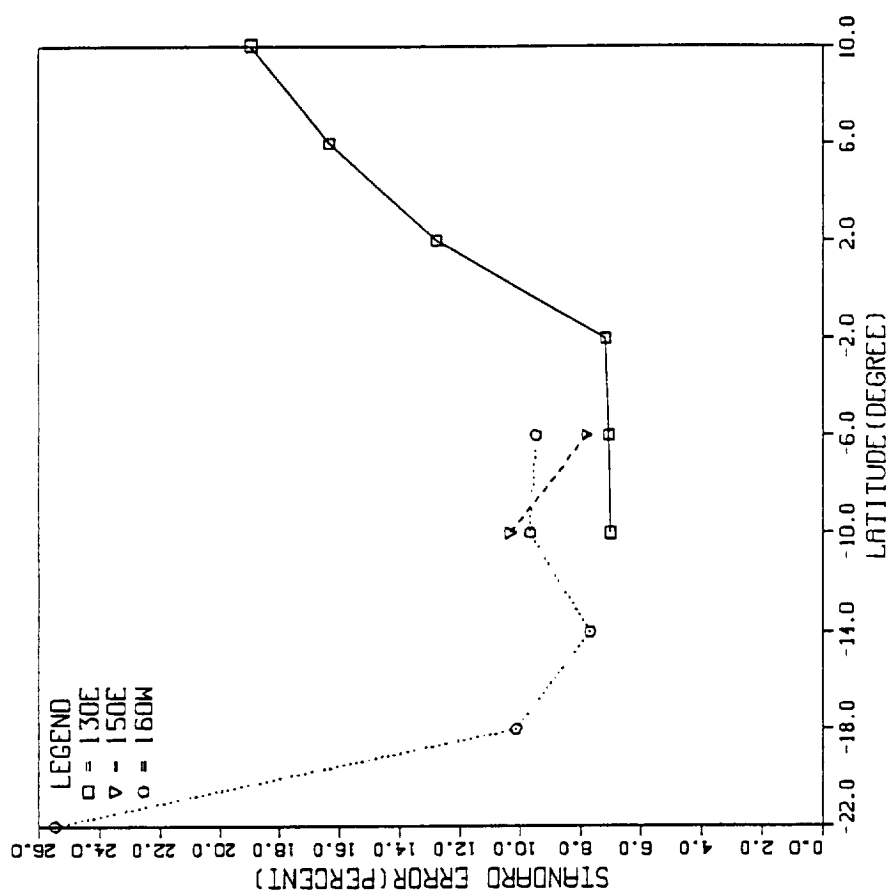


Figure 20, continued

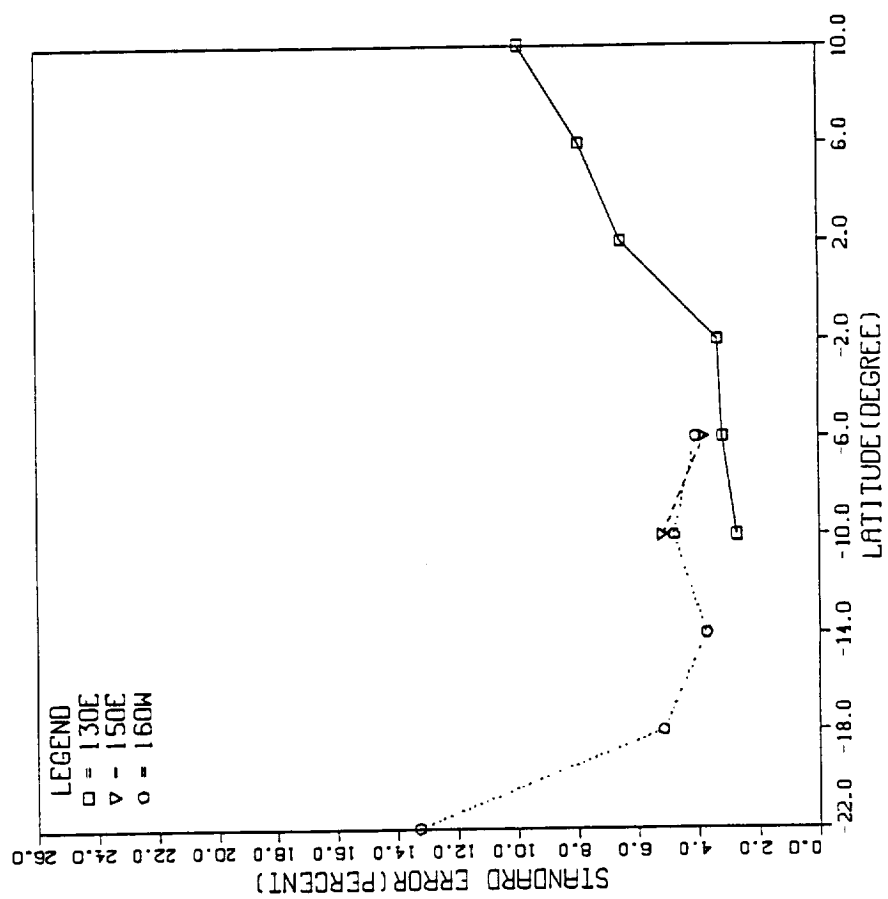


Figure 20, continued

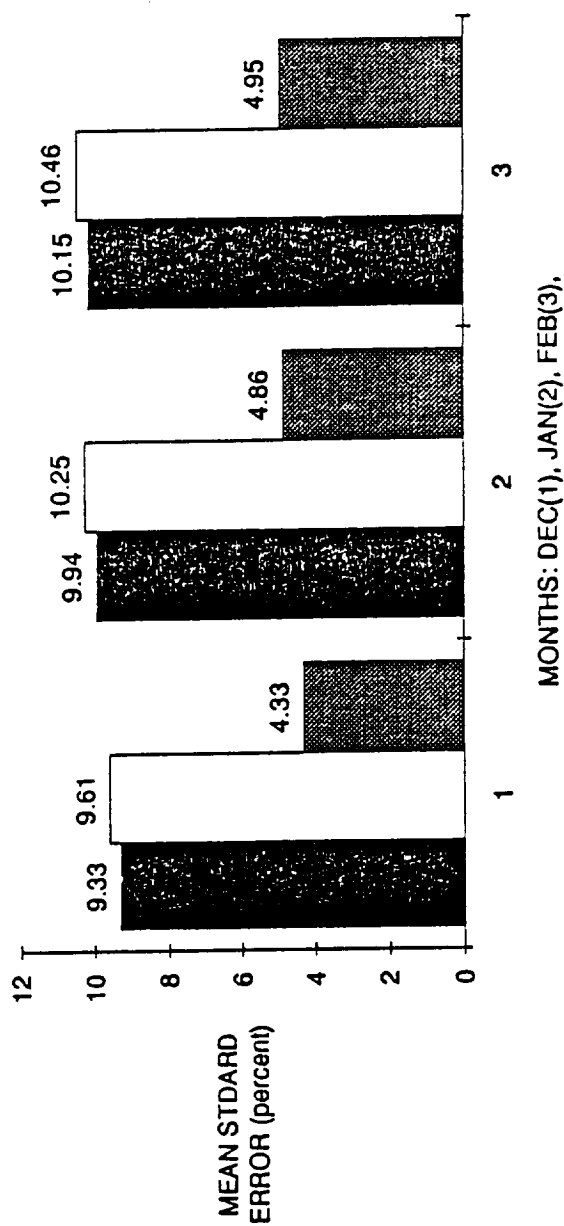


Figure 21. Average standard sampling error for the TRMM, NOAA-10, and the two sun-synchronous orbits in December, January, and February.

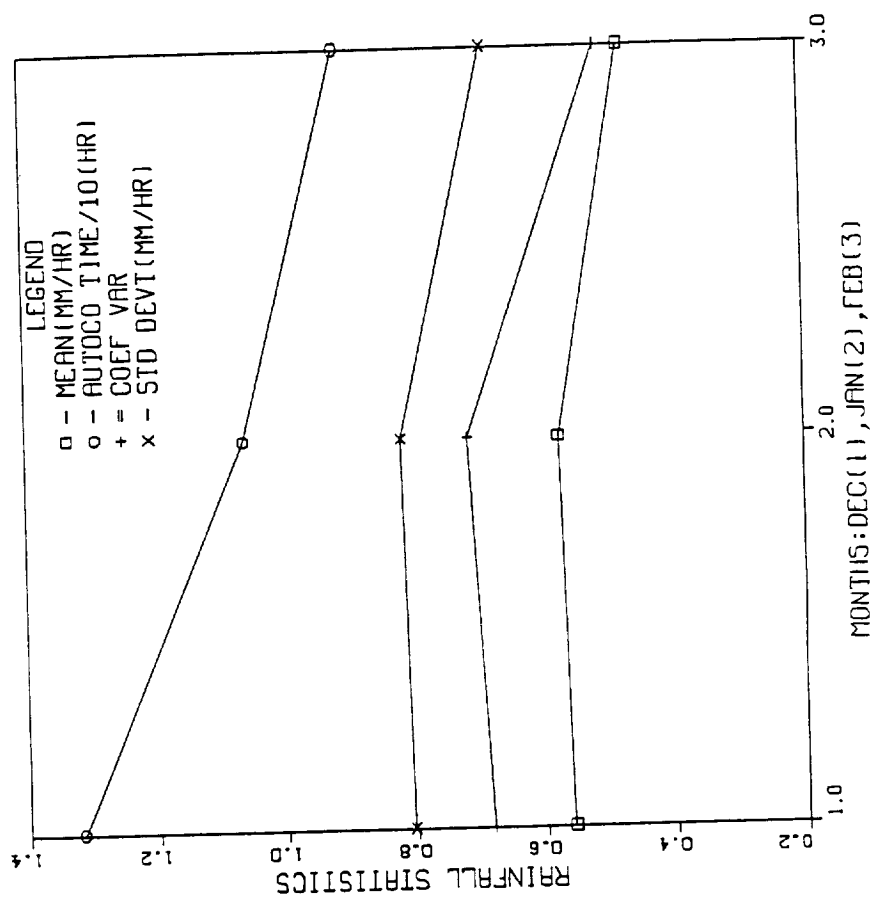


Figure 22. Variation of averaged rain rate statistics from December to February.

LIST OF REFERENCES

LIST OF REFERENCES

- Bell, T.L., 1987: A space-time stochastic model of rainfall for satellite remote-sensing studies. *J. Geophys. Res.* **92**, 9631-9643.
- _____, A. Abdullah, R.L. Martin, and G.R. North, 1989: Sampling errors for satellite-derived tropical rainfall: Monte Carlo study using a space-time stochastic model. Submitted to *J. Geophys. Res.*
- _____ and N. Reid, 1989: Statistical problems in rainfall measurements. Submitted to *J. Amer. Stat. Ass.*
- Brooks, D.R., 1977: An introduction to orbit dynamics and its application to satellite based earth monitoring missions. NASA Ref. Publication 1009 Washington, DC, 80 pp. [NTIS No. 7812113].
- Laughlin, C.R., 1981: On the effect of temporal sampling on the observation of mean rainfall. *Precipitation Measurement from Space*, Atlas D. & O. Thiele (editors), NASA/GSFC.
- McConnell, A. and G. North, 1987: Sampling errors in satellite estimates of tropical rainfall. *J. Geophys. Res.*, **92**, 9567-9570.
- Randall, D.A., H. Harshvardhan, D.A. Dazlich, and T.G. Corsetti, 1989: Interactions among radiations, convection, and large-scale dynamics in a general circulation model. *J. Atmos. Sci.*, **46**, 1943-1970.
- Simpson, J.R., R. Adler, and G. North, 1988: A proposed tropical rainfall measuring mission (TRMM) satellite. *Bull. Amer. Meteor. Soc.*, **67**, 1226-1232.

APPENDIX

```

#include<stdio.h>
#include<math.h>
#include"out_hdr.h"
#include"orb_func.h"
#include"orb_func.c"
#include"orb_plot.c"

void main()
{
    /******
    /

    int whichOne;    /* Set whichOne = NUMOBS, WHERE SAT, or
BOXOBS */

    /******
    /

    if( setupOutput() ) goto error;

    whichOne = BOXOBS;

    switch ( whichOne ) {
        case NUMOBS:
        {
            if ( NumObserv() ) {
                printf("\nProblem in NumObserv!");
                goto error;
            }
            break;
        }
        case WHERE SAT:
        {
            WhereSat();
            break;
        }
        case BOXOBS:
        {
            if ( BoxObserved() ) {
                printf("\nProblem in BoxObserved!");
                goto error;
            }
            break;
        }
    }
    error;;
}

```

```

/*      *      *      *      *      *      *      *      *      *      *
*      *      *      *      *      *      *      *      *      *
GLOBAL VARIABLES */

int direction, printLevel=1, boxMatters, retrograde, symmetryUsed;
double
Pi, TwoPi, Pi2, DtoR, RtoD, incR, sinInc, cosInc, alpha, beta, betaOalpha;
double maxLatTr, delta, sinDelta, cosDelta, retroPi, tauN;
double
t, longSat, travelTime, crossLong, crossTime, dt, tStart, tLim, longBoxR;
double phiN, phiS, longW, longE, t1;
double longLeft, windowLong, dTdL[2], tLeft[2];

/* 'printLevel' indicates how much printing is allowed.
   'boxMatters' indicates how much box size needs to be specified.
   'retrograde' is set to 1 if a retrograde orbit, i.e., inc >=
90!.
   'symmetryUsed' is set to 1 if box center is south of Equator.
*/

/*      *      *      *      *      *      *      *      *      *      *
*      *      *      *      *      *      *      *      */

int setConstants ( )

/* Sets up constants needed for orbital calculations
   and prints out some interesting
orbital parameters */

{
    int i, direct0, swathWidthInKms, boxSizeInDegs;
    double alt, inc, scan, phiBox, longBox, delx, dely, swathWidth;
    double rEarth, ThrHfJo2, mu;
    double
rSat, reOrsat, tau0, M0, Mdot, omegaDot, omegaEarth, omegaCapDot;
    double longShift, temp, phiSat0, longSat0;
    double phiBoxR, phiTrack, longTrack, side, delLat, delLong;
    /*-----
    *
                                Initial conditions
    *-----
    */

    /* Define parameters of orbit and scan angle */
    alt = 870.0; /* altitude of satellite in kms */
    inc = 98.89; /* inclination of orbit plane in degrees
*/
    swathWidthInKms = NO; /* Next line ignored if NO */
    swathWidth = 1200.; /* Side-to-side swath width in kms
*/
    scan = 54.0; /* Scan angle in degrees. Ignored if
swathWidth-
                                InKms = YES. */

    /* Define location of box observed */
    phiBox = 14.0; /* Latitude of box center in degrees */
    longBox = 130.0; /* Longitude of box center */
    /* Define size of box. */
    boxSizeInDegs = YES;
    delx = 512.; /* width of box, kms */

```

```

        dely = 512.;          /* height of box, kms */
        /* The next two specifications are used if
boxSizeInDegs = YES. */
        dellong = 5.;        /* width of box in degs. */
        dellat = 4.;        /* height of box in degs. */

        /* Define initial conditions for satellite */
        phiSat0 = 0.;        /* initial latitude
*/
        longSat0 = 0.;        /*      "      longitude      */
        t = 0.;              /*      "      direction;
        direct0 = 1;          direction = 0 for
descending orbit,            direction = 1 for
ascending orbit */
        tLim = (30.) * 86400.; /* Time (secs) allowed satellite to
orbit */

        dt = 1. * 60.;        /* WhereSat() shows sat.
posit. every dt (secs) */
        tStart = 0.;          /* Time when WhereSat() starts
printing satellite           position. */

        if( printLevel > 0) {
            SHOW "Satellite altitude = %6.1f kms.\n",alt);
            SHOW "      inclination = %6.1f
degrees.\n",inc);
            if ( ! swathWidthInKms )
                SHOW "Scan angle = %6.1f
degrees.\n\n",scan);
            if ( boxMatters ) {
                if ( boxMatters == BOXOBS ) {
                    SHOW "Latitude of box center = %6.1f
degrees.\n",phiBox);
                    SHOW "Longitude of box center =
%6.1f degrees.\n",longBox);
                }
                if ( boxSizeInDegs ) {
                    if ( boxMatters == BOXOBS )
                        SHOW "Box width = %6.1f
degs.\n",delLong);
                    SHOW "Box height = %6.1f
degs.\n\n",delLat);
                }
                else {
                    if ( boxMatters == BOXOBS )
                        SHOW "Box width = %6.1f
kms.\n",delx);
                    SHOW "Box height = %6.1f
kms.\n\n",dely);
                }
            }
            if ( boxMatters != NUMOBS ) {
                SHOW "Initial conditions for
satellite:\n";
                SHOW "\tLatitude = %6.1f
degrees.\n",phiSat0);
                SHOW "\tLongitude = %6.1f
degrees.\n",longSat0);
            }
        }

```



```

                                SHOW "\tTime = %6.1f secs.\n",t);
                                SHOW "\tdirection = %d.\n\n",direct0);
                                SHOW "\tTime Limit = %6.2f
days.\n\n",tLim/86400.);
                                }
                                }

                                /*Now do a lot of calculations and introduce physical
constants
                                necessary for calculations */
                                Pi = PI;
                                TwoPi = Pi + Pi;
                                Pi2 = PI2;
                                DtoR = Pi/180.;
                                /* Pi / 2 */
                                /* for converting degrees to radians
*/
                                RtoD = 180./Pi;
                                /* " " radians to degrees
*/
                                rEarth = 6378.145;
                                ThrHfJo2 = 0.0016238235;
                                /* radius of earth, kms */
                                /* Three halves J/2, e's quad
moment */
                                mu = 398601.2;
                                /* gravitational const of earth */

                                rSat = alt + rEarth; /* radius of sat. orbit */
                                incR = inc * DtoR;
                                sinInc = sin(incR);
                                cosInc = cos(incR);

                                retrograde = (cosInc <= 0. ) ? YES : NO;
                                maxLatTr = incR;
                                if ( retrograde ) maxLatTr = Pi - incR; /* Maximum orbit
latit. */
                                retroPi = ( retrograde ? -Pi : Pi );
                                /* Used in getting
longitude */
                                if ( cosInc == 0. ) retroPi = 0.;
                                /* from alphasat. */

                                reOrsat = rEarth / rSat;
                                if ( swathWidthInKms )
                                    delta = .5 * swathWidth / rEarth;
                                else
                                {
                                    temp = (rSat/rEarth)*sin(scan*DtoR);
                                    if(temp > 1.) temp = 1.;
                                    /* check if view extends
beyond earth*/
                                    delta = asin(temp) - scan*DtoR;
                                }
                                /* swath width in radians */

                                sinDelta = sin(delta);
                                cosDelta = cos(delta);

                                tau0 = TwoPi * rSat * sqrt(rSat / mu);
                                /* unperturbed
period, secs */
                                M0 = TwoPi / tau0;
                                /* unperturbed mean motion,
rads/sec */
                                Mdot = M0 * (1.+ThrHfJo2 * reOrsat*reOrsat* (1.-1.5*sinInc *
sinInc));
                                /* perturbed mean
motion, rads/sec */
                                /* Shin's capital
theta */
                                omegaDot = ThrHfJo2 * reOrsat*reOrsat * Mdot * (2.-
2.5*sinInc*sinInc);

```

```

/* perigee
velocity, rads/sec */
    tauN = TwoPi / (Mdot + omegaDot); /* nodal period, secs */
    omegaEarth = (360.9856473 / 86400.)*Dtor; /* earth rotation
rate,
    rads/sec */
    omegaCapDot = -ThrHfJo2 * reOrsat*reOrsat* cosInc * Mdot;
/* prec. rate of
orbital plane, rad/s*/
    alpha = Mdot + omegaDot;
    beta = omegaEarth - omegaCapDot;
    betaOalpha = beta / alpha;
    longShift = - beta * tauN; /*change in satellite long.
after 1 orbit*/
    crossLong = longShift;
    crossTime = tauN;

    if( printLevel > 0) {
        SHOW "Swath half-width = %5.2f degrees\n",delta*RtoD);
        SHOW "Swath half-width = %5.2f kms\n\n",delta*rEarth);
        SHOW "Nodal period = %9.4f mins.\n",tauN/60.);
        SHOW "alpha = %10.8f radians/sec.\n",alpha);
        SHOW "beta = %10.8f radians/sec.\n",beta);
        SHOW "beta/alpha = %10.5f.\n",betaOalpha);
        SHOW "precession of longitude = %10.5f
degrees/orbit.\n\n",longShift * RtoD);
    }
    if ( ! boxMatters )
        goto endorbit; /* Following is needed for running
BoxObserved
and NumObserv */

/* B O X M A T T E R S */

/* Determine boundaries of box observed */

if ( boxMatters == NUMOBS) { /* If NumObserv is being run
*/
    phiBox = 0.;
    longBox = 0.;
    dellLong = delx = 0.;
}
phiBoxR = phiBox * Dtor;
longBoxR = longBox * Dtor;
if ( boxSizeInDegs )
{
    temp = 0.5 * dellLat * Dtor;
    phiN = phiBoxR + temp;
    phiS = phiBoxR - temp;
    temp = 0.5 * dellLong * Dtor;
}
else /* box size specified in kms */
{
    temp = 0.5 * dely / rEarth;
    phiN = phiBoxR + temp;
    phiS = phiBoxR - temp;
    temp = 0.5 * delx / (rEarth * cos(phiBoxR));
}
if ( boxMatters == BOXOBS && temp > Pi ) {

```

```

        printf("\n The box is too wide.");
        return(1);
    }
    longE = temp;
    longW = -temp;

    symmetryUsed = NO;
    if ( phiN < fabs(phiS) )      /* Check whether box position
requires */                      /* reflection
    {
        symmetry to be used. */
        temp = -phiN;
        phiN = -phiS;
        phiS = temp;
        direct0 = -direct0; /* In this case all latitudes must be */
        phiSat0 = -phiSat0; /* In this case all latitudes must be */
        symmetryUsed = YES; /* output in BoxObserv
with opposite signs. */
    }

    switch ( i = boxCheck() ) {
        case 1: {
            printf("\n Box height too large.");
            return(i);
        }
        case 2: {
            printf("\n Box outside latitudes viewed by
satellite.");
            return(i);
        }
        case 3: /* Box seen every orbit! */
        {
            printf("\n Box is at least partially viewed
every orbit.");
            printf("\n Unable to compute portion seen each
time.");
            return(i);
        }
    }
    /* Since the box long. has been moved to 0, the
satellite has to
    have its longitude also shifted. Note that in outputting
any
    longitude, longBox should be added. */

    longSat0 -= longBox; /* Note that this does not affect
WhereSat */

    if ( boxMatters == NUMOBS )
        return(0); /* Satellite position doesn't matter to
NumObserv */

    /* END OF BOX MATTERS */

    endorbit: /* follow satel. to Eq. and get its longitude
there... */
    direction = direct0;
    getLong0 ( phiSat0*DtoR,longSat0*DtoR,1-
direction,0.,&longSat );

```

```

        /* Note that if satellite was descending, it has now
been moved          to longitude at equator where it is ascending.
*/
    longSat = Normalong ( longSat );
    t += travelTime; /* Set time to time of equator crossing */
    direction = 1;   /* Satellite is at equator, ascending,
ready for          orbiting. */

    return(0);
}

/*      *      *      *      *      *      *      *      *      *      *
*      *      *      *      *      *      *      */

int boxCheck()
{
    /* Checks how box is observed by satellite and reports
result */

    if(phiN>Pi2 || phiS<-Pi2 )
        return(1);

    /* Now check whether box is never observed, or always.
*/
    if ( phiS > maxLatTr + delta )      /* Box never seen. */
        return(2);

    if ( (maxLatTr + delta < Pi && phiS <= - maxLatTr + delta )
||
        (maxLatTr + delta > Pi && phiN >= Pi - maxLatTr -
delta) )
        return(3);      /* Box seen every
orbit */

    return(0);
}

/*      *      *      *      *      *      *      *      *      *      *
*      *      *      *      *      *      *      */

void orbitSat( drawPtr0, frcPtr0, longlist, nCross, nWindows, draw )

DRAWTEMPLATE *drawPtr0;
FRACCOEFS *frcPtr0;
double longlist[];
int nCross, nWindows, draw;

/* Called by boxObserved. Gives observation times of box until t =
tLim.
Assumes entry with satellite at equator, t at current time,
longSat current longitude, and necessary parameters
calculated
in getConstants. */
{
    int ilam, index;
    double longRel, tObs, frac, dlam;
    FRACCOEFS *frcPtr;
    DRAWDATA saw;

    SHOW "\n\nDay      Hour      Fraction");

```

```

while ( t < tLim )
{
    longRel = my_fmod ( longSat - longLeft, TwoPi);
    /* Check sat. position relative to
window */
    if( longRel < windowLong &&
        ( ilam =
whichIntrvl(longRel,longlist,nCross,nWindows)) >= 0 ) )
        /* Box seen! */
        {
            dlam = longRel - longlist[ilam];
            index = (nWindows == 1) ? 0 : ilam/8;
            tObs = t + tLeft[index] + dTdL[index] * (longRel
- longlist[8*index]);
            frcPtr = frcPtr0 + ilam;
            frac = frcPtr->bf + dlam * (frcPtr->mf + dlam *
frcPtr->qf);
            tellTF ( &tObs,&frac );
            /*if ( draw )
            {
                getDrawData ( &dlam,drawPtr0+ilam,&saw);
                showPartSeen ( &saw );
            } */
            /* Go to next crossing of equator */
            longSat = Normalong(longSat + crossLong);
            t += crossTime;
        }
    return;
}

/*      *      *      *      *      *      *      *      *      *      *
*      *      *      *      *      *      *      */

void tellTF ( ptSec,pfrac )

/* Break tSec up into day, hour and send to output file. Later,
more
processing may be done. */
double *ptSec, *pfrac;
{
    int day;
    double hour,intptr,fraction;

    day = *ptSec / 86400. - (*ptSec < 0.);
    /* hour = (*ptSec - (double) day * 86400.) / 3600. ;*/
    hour = (*ptSec) / 3600. ;
    fraction = modf(hour,&intptr);
    if(fraction > .5)
        hour = ceil(hour);
    else
        hour = floor(hour);
    /*if(hour == 24.)
        hour = 0.; */
    SHOW "\n%2d    %6.2f    %6.3f",day,hour,*pfrac);
    /*SHOW "\t%6.3f",*pfrac);*/
    return;
}

/*      *      *      *      *      *      *      *      *      *      *
*      *      *      *      *      *      *      */

int NumObserv()

```

```

/* Runs through specified box center latitudes and prints out the
average number of times in 24 hours points in the box are seen
by
satellite. */
{
    extern int printLevel;
    extern double getFrac();

    int i;
    double boxCtr,dellLat,numObs,obsPerDay,latStep,latStep2;

    /* Print out some header information */
    boxCtr = 0.; /* In degrees of latitude */
    boxMatters = NUMOBS; /* Let setConstants we are running
NumObserv */
    printLevel = 1;
    printf("Working on latitude %7.2f\n",boxCtr);

    if ( setConstants() )
        return(1);

    dellLat = phiN; /* Assumes box center is set at Equator in
setConstants */
    obsPerDay = 24. * 3600./ tauN;
    SHOW "**\n"); /* To help Cricket Graph ingestion */
    SHOW "Latitude\tNumber\n");
    numObs = obsPerDay * getFrac();
    SHOW "%7.2f\t%7.3f\n",boxCtr,numObs);

    printLevel = 0;
    latStep = 2.5 * 0.99999999;
    latStep2 = 1.0 * latStep;
    for( boxCtr = 2.5; boxCtr <= 40.; boxCtr += latStep)
    {
        if(boxCtr > 23.) latStep = latStep2;
        printf("Working on latitude %7.2f\n",boxCtr);

        phiN = boxCtr*DtoR + dellLat;
        phiS = boxCtr*DtoR - dellLat;
        if ( i = boxCheck() )
        {
            if ( i != 2 )
                printf ("\nUnable to proceed because of
box size.");
            break;
        }
        numObs = obsPerDay * getFrac();
        SHOW "%7.2f\t%7.3f\n",boxCtr,numObs);
    }
    return(0);
}

/*
*
*
*
*
*
*
*
*
*
*
*
*/

WhereSat()

/* Prints out latitudes and longitudes of satellite nadir, right
and left
swath edge, and time, starting satellite at equator and time t,
longitude

```

```

    longSat, correcting for shift in longitude to put boxCtr at 0!
long. */
{
    extern int direction;
    extern double
t, dt, tStart, RtoD, alpha, beta, sinInc, cosInc, longSat, longBoxR;
    double phiEdge, longEdge, side, longSatShift;
    double
tShift, tSat, pSat, lSat, fabs(), sin(), cos(), atan2(), Normalong();
    double s, c, temp, tLimit;

    boxMatters = WHERE SAT; /* Tell setConstants that WhereSat is
being run. */
    setConstants ();

    longSatShift = longSat;
    tShift = t;
    tSat = -travelTime;          /* Gets the satellite back
from equator to */
    lSat = 0.;                  /* its starting position.
"travelTime" is*/
    pSat = 0.;                  /* left over from call to
getlLong0 in setC. */
    tSat += tStart - t;          /* Move to starting time. */

    SHOW
"\nMins.\tlatNadir\tlongNadir\tlatR\tlongR\tlatL\tlongL\n");
    tLimit = tSat + tLim; /* Set tLimit so that satellite
orbits that long*/
    while ( tSat <= tLimit )
    {
        s = sin( (temp = tSat * alpha) );
        c = cos( temp );
        pSat = asin( sinInc * s );
        lSat = atan2( cosInc*s, c );
        if( fabs(lSat) > Pi2 )
            direction = 0;
        else
            direction = 1;
        lSat = Normalong( lSat - beta*tSat + longSatShift );
        SHOW
"%10.1f\t%7.2f\t%7.2f\t", (tSat+tShift)/60., pSat*RtoD, lSat*RtoD);
        side = 1.;
        SwathEdge( pSat, lSat, side, &phiEdge, &longEdge );
        longEdge = Normalong(longEdge);
        SHOW "%7.2f\t%7.2f\t", phiEdge*RtoD, longEdge*RtoD);
        side = -1.;
        SwathEdge( pSat, lSat, side, &phiEdge, &longEdge );
        longEdge = Normalong(longEdge);
        SHOW "%7.2f\t%7.2f\n", phiEdge*RtoD, longEdge*RtoD);
        tSat += dt;
    }
    return;
}
/*      *      *      *      *      *      *      *      *      *      *
*      *      *      *      *      *      *      */

int BoxObserved()

/* Runs OrbitSat when called from main. Assumes all parameter
values
are specified in setConstants. */

```

```

{
    int nCross,nWindows,index,gap,vNum,sLab,dirx,bs,draw;
    double boxCtr,longlist[16],temp,l,phiSw,longSw,pos;
    CROSSINGS *tableCross(),*pCross,*pCross0;
    DRAWTEMPLATE *drawTempPtr0,*drwPtr;
    FRACCOEFS *frcCoefPtr0,*frcPtr;

    boxMatters = BOXOBS;      /* Inform setConstants that
BoxObserved will be run */
    printLevel = 1;
    draw = NO ;
    if ( setConstants() > 0 )
        goto error;

    if ( (pCross0 = tableCross (&nCross,&nWindows)) == NULL )
        goto error;
    SHOW "\nTable of Equatorial Crossings. nCross=%2d",nCross);
    SHOW "\n\nindex  longit.  vertex  side  dirx");
    for ( index=0,pCross = pCross0; index < nCross ;
pCross++,index++ )
    {
        l = pCross->longEq * RtoD;
        vNum = pCross->vertex;
        sLab = pCross->SwEd;
        dirx = pCross->dir;
        SHOW "\n%3d  %9.3f  %4d  %4d  %4d",index,l,vNum,sLab,dirx);
    }

    /* Allocate memory for tables */
    drawTempPtr0 = (DRAWTEMPLATE *) malloc ( (unsigned)
((nCross-1) *
                                                                    sizeof
( DRAWTEMPLATE )) );

    if ( drawTempPtr0 == NULL ) {
        printf("\nTrouble getting memory allocation for
drawTemplate!");
        goto error;
    }
    frcCoefPtr0 = (FRACCOEFS *) malloc ( (unsigned) ((nCross-1)
*
                                                                    sizeof
( FRACCOEFS )) );
    if ( frcCoefPtr0 == NULL ) {
        printf("\nTrouble getting memory allocation for
fracCoefs!");
        goto error;
    }
    /* Construct tables of coefficients for running
orbitSat */

    if ( getCoefs (
nCross,nWindows,pCross0,drawTempPtr0,frcCoefPtr0,draw ))
        goto error;

    /* Set up list of relative longitudes */
    pCross = pCross0;
    temp = pCross->longEq;
    for ( index=0 ; index<nCross ; index++,pCross++ )
        longlist[index] = my_fmod ( pCross->longEq - temp ,
TwoPi );

```



```

        /* Get window size. Satellite w/ longitudes beyond
this sees nothing. */
        windowLong = longlist[ nCross-1 ];

        /* Get time interpolation */
        gap = (nWindows==2) ? 7 : nCross-1;
        pCross = pCross0;
        for ( index=0 ; index<nWindows ; index++,pCross++ )
        {
            getLong0 ( 0.,pCross->longEq,1-pCross->dir,pCross-
>latTrk,&temp );
            tLeft[index] = travelTime;
            pCross += gap;
            getLong0 ( 0.,pCross->longEq,1-pCross->dir,pCross-
>latTrk,&temp );
            dTdL[index] = (travelTime - tLeft[index]) /
longlist[gap];
        }
        longLeft = pCross0->longEq;

        if ( free ( (void *) pCross0 ) ) /* Release memory used by
pCross */
            goto error;

        orbitSat (
drawTempPtr0,frCoefPtr0,longlist,nCross,nWindows,draw );

        return(0);

    error:
        return(1);
}

```

Technical Report

Section 2

The feasibility of obtaining the longwave radiation budget at
the surface from satellite data.

Relationship between the Longwave Cloud Radiative Forcing at the Surface and the Top of the Atmosphere

HARSHVARDHAN

Department of Earth and Atmospheric Sciences, Purdue University, West Lafayette, Indiana

DAVID A. RANDALL AND DONALD A. DAZLICH

Department of Atmospheric Science, Colorado State University, Fort Collins, Colorado

(Manuscript received 2 April 1990, in final form 20 June 1990)

ABSTRACT

Attempts to map the global longwave surface radiation budget from space have been thwarted by the presence of clouds. Unlike the shortwave, there is no physical relationship between the outgoing longwave and the surface longwave under cloudy skies. Therefore, there is no correlation between spatial and temporal averages of the outgoing longwave radiation and net longwave radiation at the surface. However, in regions where a particular cloud regime exists preferentially, a relationship between the mean longwave cloud radiative forcing (CRF) at the top of the atmosphere and at the surface can be shown to exist. Results from a general circulation model suggest that this relationship for monthly means is coherent over fairly large geographical areas. For example, in tropical convective areas, the longwave CRF at the top is very large, but at the surface it is quite small because of the high opacity of the lowest layers of the atmosphere. On the other hand, in areas of stratus over cool ocean surfaces, the longwave CRF at the top is very small but at the surface, it is quite substantial.

To the extent that the cloudiness simulated in the model mimics the real atmosphere, it may be possible to estimate the monthly mean longwave CRF at the surface from the Earth Radiation Budget Experiment cloud forcing at the top. The net longwave radiation at the surface can then be mapped if monthly means of the clear-sky fluxes are obtained by some independent technique.

1. Introduction

Currently, there is a need in the atmospheric and oceanographic communities for reliable estimates of the components of the surface radiation budget (WCP-92 1984). This is particularly crucial in the study of the coupled atmosphere-ocean system in the tropics (NAS 1983). Since there are very few surface stations measuring the radiation budget routinely and reliably, it has been realized that space-based observations are the only means to obtain global coverage. Several investigators have had considerable success in obtaining the solar flux components at the surface using radiances measured at the top of the atmosphere by operational satellites (e.g., Gautier et al. 1980; Raschke and Preuss 1979; Tarpley 1979; Pinker and Ewing 1985; Justus et al. 1986). This success can be explained on theoretical grounds. The atmosphere is a conservatively scattering medium over a major portion of the solar spectrum, and the total atmospheric absorption in the presence of clouds is not very different from the clear-sky value (Ramanathan 1986). This is because clouds absorb at

roughly the same near infrared wavelengths as water vapor, and this absorption is therefore at the expense of vapor absorption below the cloud deck.

In the case of longwave radiation, it is not at all evident that the surface radiation budget components can be obtained from top of the atmosphere (TOA) radiance measurements. Even for clear-sky conditions, it may be shown that the bulk of the downward longwave radiation emanates from the lowest hundreds of meters of the atmosphere (Schmetz et al. 1986; Gupta 1989). Fairly accurate estimates of the near surface air temperature and humidity, and the sea-surface or ground temperature are prerequisites for the computation of the longwave fluxes at the surface. This problem is further compounded by the presence of clouds. The downward emission from the cloud base is a major component of the downward longwave flux unless the cloud base is very high and the boundary layer is very moist. Since there is as yet no proven technique for locating cloud bases from space, investigators have been forced to rely on other means to estimate the downward emission.

There is now considerable literature available on estimates of the surface longwave fluxes, both regionally and globally. All of them rely on estimates of near surface conditions or the vertical profile of temperature

Corresponding author address: Prof. Harshvardhan, Department of Earth and Atmospheric Sciences, Purdue University, West Lafayette, IN 47907.

and humidity to compute clear sky fluxes using bulk formulae or a radiative transfer model and modifications for observed or climatological cloudiness. Fung et al. (1984) reviewed several bulk formulae used for this purpose and compared them with a radiative transfer model. They concluded that uncertainties in the longwave fluxes due to lack of knowledge about cloud properties is larger than that due to expected uncertainties in temperature or humidity. Frouin et al. (1988) compared several methods arranged in order of decreasing sophistication to compute the downward longwave surface fluxes for comparison with observation taken during the Mixed Layer Dynamics Experiment (MILDEX). A technique that can be used only during daytime involving an estimate of the liquid water column amount in the cloud had the best correlation with observed fluxes. A relationship between cloud properties in the solar and cloud thickness was also used by Schmetz et al. (1986). Chou (1985) used cloud thicknesses based on London's (1957) climatology whereas Darnell et al. (1986) and Gupta (1988) used a fixed cloud thickness of 50 mb.

Apart from the problem of locating the cloud base, there is also the question of the fractional coverage of clouds that should be used in weighting the clear and cloudy sky contributions. Recently, Wu and Cheng (1989) have used HIRS2/MSU sounding data to extract all the relevant cloud parameters needed for their algorithm to compute the downward longwave flux globally for January and July 1979. There is no satisfactory verification for any of these methods.

In this paper we present a theoretical framework that avoids the explicit computation of cloud fraction and the location of cloud base. Our hope is that global maps of the monthly mean net longwave flux at the surface may eventually be obtained in this manner.

2. Surface radiation budget

In general, the surface radiation budget has four components: the upward and downward directed longwave radiation, the incoming solar radiation at the surface, and the reflected solar radiation. The latter two components are, of course, present only during daylight hours. For some applications it is sufficient to know the net radiation, which is the algebraic sum of the upward and downward components.

The net solar radiation at the surface is the surface absorption and varies from 0 to 1200 W m^{-2} , while the net longwave at the surface is a radiative loss by the surface that can range from -200 W m^{-2} for a warm desert surface under clear-sky conditions to near zero in the presence of low thick clouds. The theory underlying techniques for estimating these quantities from space based observation systems is the relationship between the upwelling radiation at the top of the atmosphere and the components of radiation at the surface.

The theoretical basis for such a relationship in the case of solar radiation has been discussed by several authors, e.g., Gautier et al. (1980). All techniques for inferring the solar radiation at the surface rely on essentially the same principle. The chief uncertainty is in assigning absorption by water vapor in the clear atmosphere and by clouds and vapor for the cloudy case. As pointed out by Ramanathan (1986), compensating effects result in this absorption being fairly insensitive to location and in fact, cloudiness conditions. Modeling studies quoted by Ramanathan (1986) and Weare (1989) confirm that there should be a strong correlation, at least for monthly means, between the net solar radiation at the top of the atmosphere, which is the absorption by the surface and atmosphere, and the net at the surface which is simply the surface absorption. However, the same modeling studies show that there is no correlation whatsoever between the net longwave radiation at the top of the atmosphere and the net longwave at the surface.

Although Weare (1989) confirmed Pinker et al.'s (1985) finding that there is a strong correlation between the net total radiation at the top of the atmosphere and that at the surface, this is explained by the fact that the variation in the net total radiation at the surface is dominated by solar radiation.

An illustrative way to show the correlation or lack thereof is with a scatter diagram of the radiation field at the top of the atmosphere plotted against the surface quantity. This can be done for contemporaneous measurements made at a surface site and satellite measurements of the same general area. This is, in fact, the usual manner in which regression equations for the surface radiative fluxes are calibrated. The regressions could also be for temporal means, or if several surface sites are available, an area average may be considered. Model simulations of the radiation fields can also be shown on a scatter plot.

Following Ramanathan (1986), we show in Figs. 1a,b, the monthly mean net longwave radiation at the top and the surface as simulated by the UCLA/CSU General Circulation Model (GCM). Details of the radiation and cloud parameterization in the model and simulated fields of cloudiness and radiative fluxes may be found in Harshvardhan et al. (1989). A brief description of the GCM may be found in the Appendix of Randall et al. (1989). Each point represents the mean for one grid point of the model for January and July, respectively. The horizontal resolution of the model is 4° in latitude by 5° in longitude. It is evident that the longwave radiation at the top is uncorrelated with that at the surface, and Ramanathan (1986) has shown that this holds true even if selected regions are considered in isolation. Although total fluxes are not correlated, the hope that window radiances provide information on near-surface conditions has led to the development of hybrid techniques in which satellite measurements are used to reconstruct the temperature

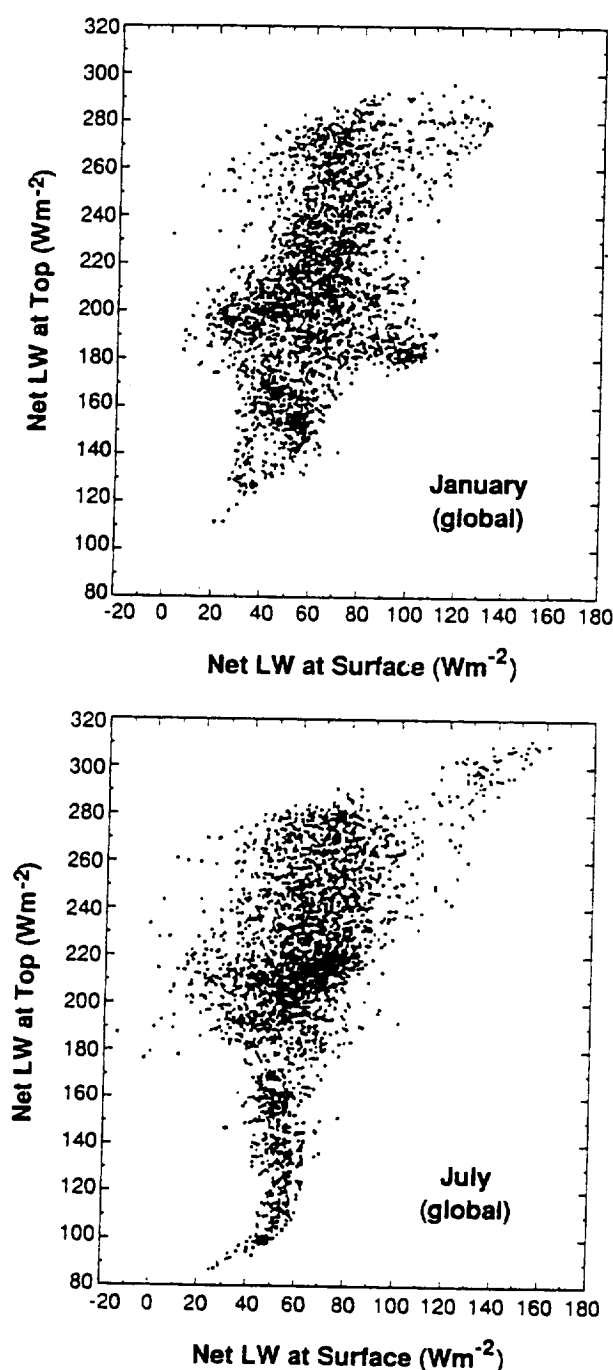


FIG. 1. Scatter plots of the monthly mean net longwave radiation at the top of the atmosphere vs the net longwave radiation at the surface for (a) January, and (b) July. Results are from a simulation of the UCLA/CSU GCM and each data point on the plot represents a 4° Latitude \times 5° Longitude grid point.

and humidity profile and a radiative transfer code is used to compute the downward longwave flux (e.g., Frouin et al. 1988; Gupta 1989; Wu and Cheng 1989). As stated earlier, all techniques suffer from uncertain-

ties or even total lack of knowledge concerning cloud cover and cloud base location.

3. Cloud Radiative Forcing

The role of clouds in modifying the radiation field can be studied through the analysis of the cloud radiative forcing (CRF). Although originally introduced in connection with the exiting shortwave and longwave fluxes at the top of the atmosphere (Charlock and Ramanathan 1985; Ramanathan 1987), the cloud radiative forcing at the surface may be defined as

$$\text{surface CRF} = \text{surface flux} - \text{clear-sky surface flux.} \quad (1)$$

In the above, the flux at the surface may be shortwave, longwave, or total, and could refer to the downward or net flux at the surface. The clear sky flux in a model may be obtained in one of two ways. The radiation fluxes may be computed at every grid point for the diagnosed cloud cover and also for zero cloud cover at the same time. The clear sky values may then be subtracted from the actual values to yield the CRF. This has been called "Method II" by Cess and Potter (1987) and is the method used in this study. An alternate approach is to sample the clear-sky fluxes only when clouds do not occur and build up a clear-sky climatology for a particular grid point over an integrating time interval, such as a month. This is "Method I" and is used in the Earth Radiation Budget Experiment (ERBE; Ramanathan 1987) and is, of course, the only option in any measurement program.

The importance of cloud radiative forcing at the surface may be illustrated by examining the energy budget at the atmosphere-ocean interface and implications regarding the required meridional energy transport in the ocean for global balance over the annual cycle. Esbensen and Kushnir (1981) have computed the individual components of the heat budget over the oceans using standard bulk formulae (Sellers 1965; Budyko 1974). Over a complete annual cycle, assuming that there is no heat storage in the oceans, an implied poleward energy transport across latitude belts may be computed based on the excess or deficit of energy at each latitude. The results of Esbensen and Kushnir are shown in Fig. 2 by the solid line labeled EK. An independent estimate of the meridional oceanic transport has been made by Carissimo et al. (1985) who have updated the earlier work of Oort and Vonder Haar (1976). This is shown by the solid line in Fig. 2 labeled COV. They computed the poleward transport of energy by the oceans and atmosphere using measurements of net radiation at the top of the atmosphere. The procedure for estimating the atmospheric component is described in Oort and Peixoto (1983). The oceanic transport is then obtained as a residual.

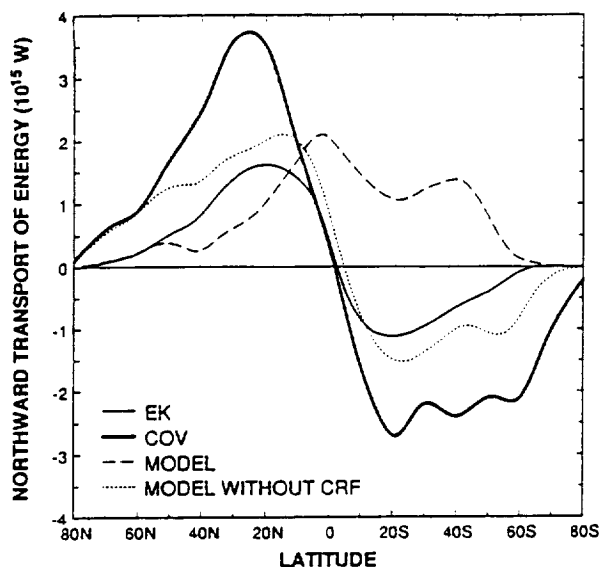


FIG. 2. Estimates of the annual meridional energy transport in the oceans. Solid line is from Carissimo et al. (COV) and Esbensen and Kushnir (EK). Dashed line is from an atmospheric general circulation model. Dotted line is from the same model but without cloud radiative forcing (CRF). Northward transport is positive.

Figure 2 also shows by dashed lines the implied meridional transport in the oceans from a five-year annual cycle run of an atmospheric general circulation model with prescribed seasonally varying sea surface temperatures. The procedure used to obtain the transport is the same as for the EK curve, except that the simulated components of the energy budget have been used. Although the magnitude of the transport in the Northern Hemisphere is within the range of the other estimates, it is the implied transport in the Southern Hemisphere that is truly striking. Over the annual cycle, the net oceanic transport is northward at all latitudes! The situation is improved markedly by the removal of the radiative contribution of clouds, as shown by the dotted line. An examination of the radiation budget in the Southern Hemisphere midlatitudes indicates that there is a gross underestimation of cloud cover in that region. Since the sea surface temperature is prescribed in the model, these errors are of no consequence as far as the atmospheric simulation is concerned. However, errors such as this could prove to be disastrous in a coupled interactive atmosphere-ocean climate model.

Figure 3 is a scatter plot of the monthly mean shortwave CRF at the top of the atmosphere versus the shortwave CRF at the surface as simulated by the UCLA/CSU GCM. Each point represents the monthly mean (July in this case) value for each grid point. The CRF has been computed using Method II, in that clear-sky values were calculated and stored for every computation of the radiative fluxes. A linear correlation is evident and simply indicates that a loss of solar insolation at the surface due to cloud cover appears as an

increase in the solar radiation reflected to space. The net shortwave at the top and surface vary in lock step with changing cloud cover. It is this feature that is primarily responsible for the success of surface shortwave insolation techniques based on satellite measurements of reflected radiances.

It is instructive to investigate the simulated relationships between the longwave CRF at the top and surface, to see if any correlations are predicted by the model. The shortwave correlations could have been anticipated by inspection of Fig. 10 in Harshvardhan et al. (1989) in which the zonal means of the cloud radiative forcing from the same model are displayed. The zonal mean shortwave cloud radiative forcing at the top of the atmosphere is virtually identical to the forcing at the surface with the atmospheric component alone being essentially zero. As explained in section 1 this is because the cloud layer absorbs solar radiation at the expense of water-vapor absorption below the cloud deck and the vertically integrated column absorption is therefore virtually unchanged in the presence of clouds (although the heating profile is certainly quite different).

Figure 4 shows a scatter plot of the monthly means of the longwave CRF at the top of the atmosphere versus the surface CRF for every grid point in the GCM. Note the radically different distribution from Fig. 1, which is a plot of the net longwave radiation. Although the scatter is incoherent as the shortwave CRF shown in Fig. 3, there are unmistakable correlations among groups of points. It appears, in fact, that certain clusters of points are linearly organized, albeit with different slopes. These groups of points represent grid points at which, for the month considered, a preferred type of

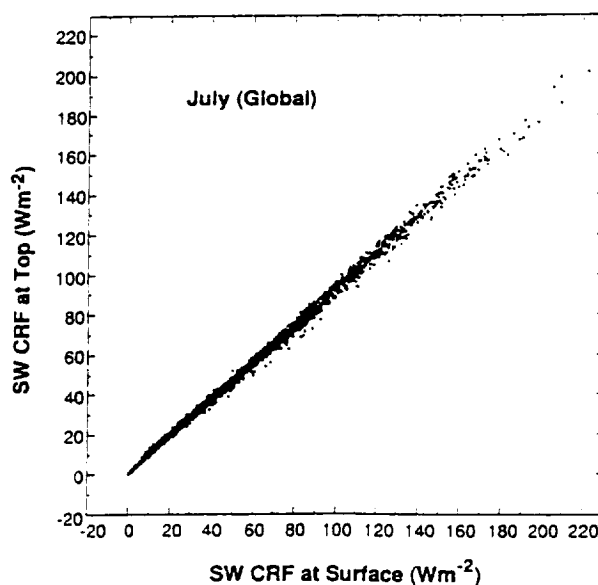


FIG. 3. Scatter plot of the July mean shortwave cloud radiative forcing (SWCRF) at the top of the atmosphere vs the SWCRF at the surface as simulated by the UCLA/CSU GCM for all grid points.

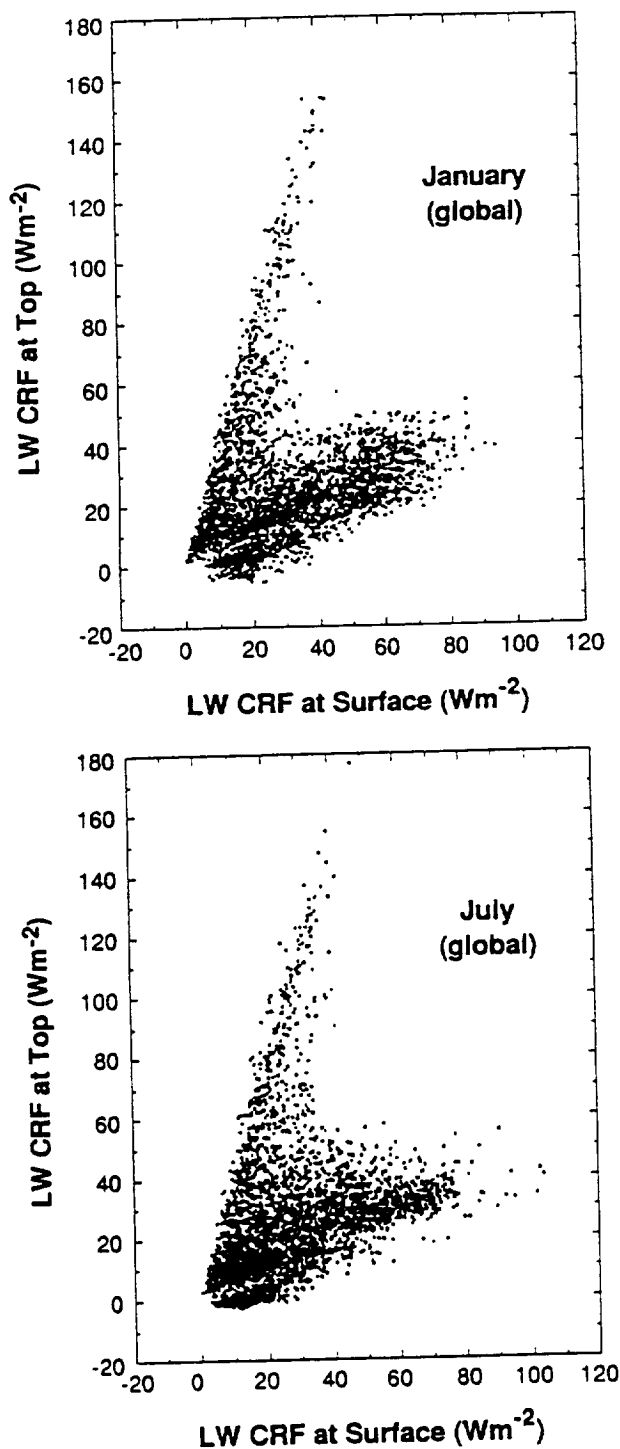


FIG. 4. As in Fig. 3 but for the longwave cloud radiative forcing (LWCRF) for (a) January and (b) July.

cloud cover exists such as low or convective. This becomes clear when subsets of the global grid are considered where one would expect this sort of preference to hold.

Figure 5a shows the scatter plot for two zonal strips in the tropics in July. The points are all the GCM grids centered at 10° and 14°N (144 in all). Figure 5b is the same plot for two bands centered at 58° and 62°S . The former includes areas of high convective clouds whereas the latter is a region of low stratus. The longwave CRF at the top of the atmosphere in the tropics can be very large since the cold cloud tops diminish the outgoing longwave radiation considerably. However, at the surface, in the tropics, clouds have a minimal effect on longwave radiation because the lowest layers of the atmosphere have a very high water-vapor content, essentially saturating most of the longwave

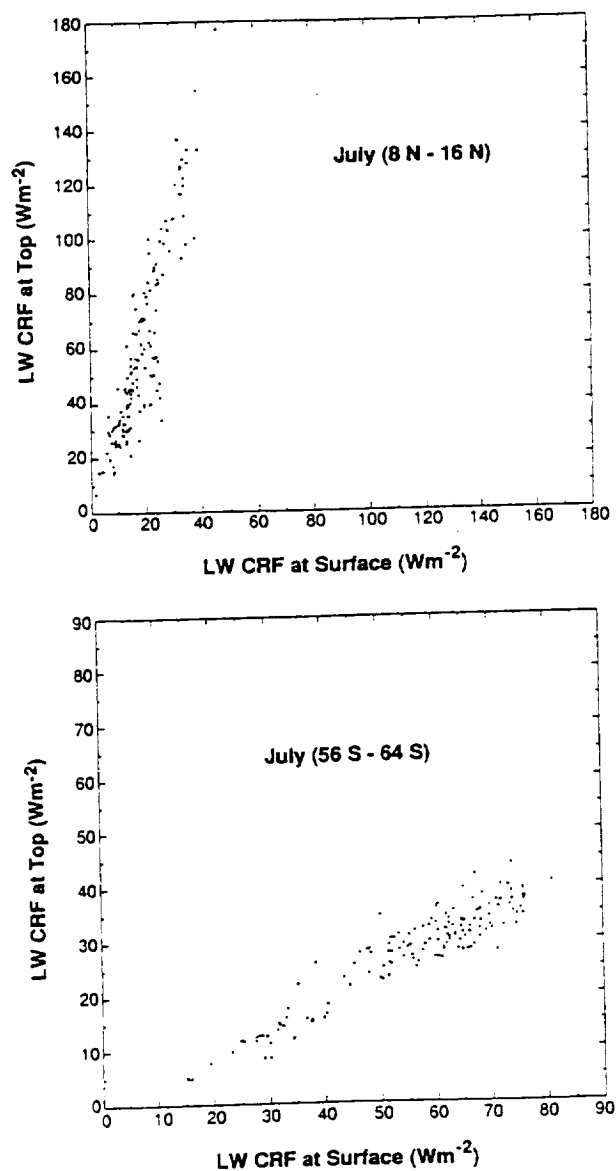


FIG. 5. As in Fig. 4 for July but only for grid points in zonal belts centered at (a) 10° and 14°N and (b) 58° and 62°S .

spectrum for downwelling radiation. The presence of an emitting cloud base does not result in much enhanced downward longwave radiation. Moreover, in the model, low-level convective clouds are ignored in that the cloud fraction is set to zero, so the cloud base is quite high unless stratiform clouds occur simultaneously. The situation at high latitudes in drier conditions is just the opposite. Stratus clouds do not modify the outgoing longwave radiation much, but radically alter the downward longwave flux towards the surface. Figure 5b also indicates that middle and high clouds occurred infrequently, if at all, during this time period at the grid points considered.

The points in both Fig. 5a,b are not clustered at the upper right-hand corner of the distribution, but are spread out fairly even along the line of correlation. The position of a point is an indication of the monthly mean cloud cover for the grid point in question. From Eq. (1) we note that the first term on the rhs includes the cloud cover implicitly, such that if there is zero cloud cover at a grid point, the CRF at both the top of the atmosphere and surface will be zero.

The character of the correlations shown in Fig. 4a,b can be best appreciated by considering the simulated longwave CRF at the top of the atmosphere and surface for standard atmospheric profiles in which clouds are inserted at different levels in isolation. We have chosen to show standard profiles from McClatchey et al. (1972) and cloud layers corresponding to the 9-layer UCLA/CSU GCM. Optical properties of the clouds are as in the GCM (Harshvardhan et al. 1989); essen-

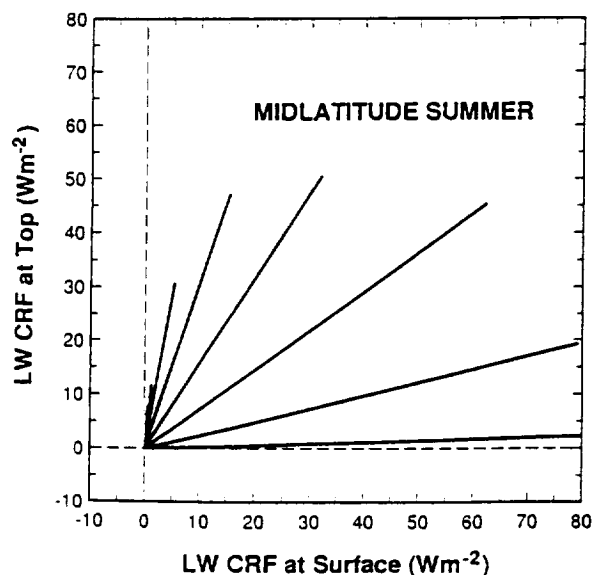


FIG. 6. The locus of points representing the variation of LWCRF at the top of the atmosphere vs the LWCRF at the surface when cloud cover varies from 0% to 100% in each layer of a model in isolation. A midlatitude summer atmospheric profile is used and the cloud properties and layer positions are as in the UCLA/CSU GCM.

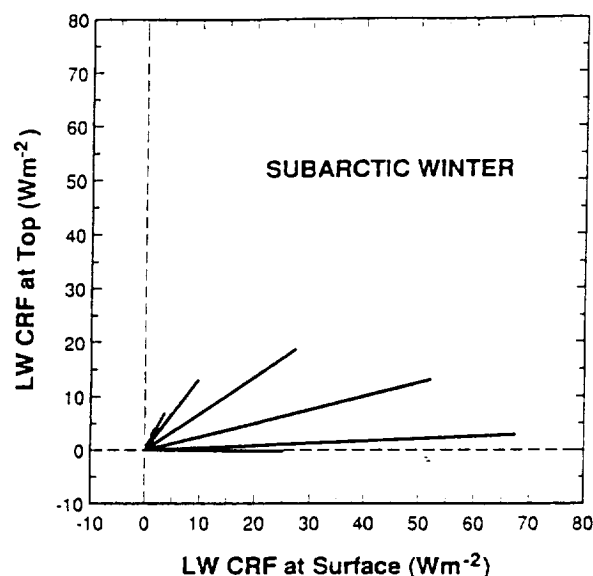


FIG. 7. As in Fig. 6 but for a subarctic winter atmospheric profile.

tially, the longwave emittance is a function of temperature and cloud thickness, but, for all practical purposes, this dependence exists only for temperatures well below freezing. For water clouds and ice clouds that form as convective anvils, the emittance is unity.

Figure 6 is a plot of the longwave CRF at the top of the atmosphere versus the surface CRF. It shows the locus of all points representing cloud cover in one layer of the model for a midlatitude summer atmospheric profile. There are eight different lines, one for each layer in which clouds are permitted to occur in the GCM. The origin represents the case of no cloud cover while the terminus of each line represents 100% cloud cover. The line with the lowest values of longwave CRF at the top and highest values of longwave CRF at the surface corresponds to a cloud in the lowest layer of the model. Clouds in higher layers proceed in a counterclockwise sense up to the topmost cloud layer in the model.

The CRF of a cloud in the highest layer, with a top at 100 mb, is barely perceptible because the emittance is close to zero and even complete cloud cover hardly affects the outgoing longwave radiation. It should be stressed that points on a scatter plot would follow these lines only if cloud existence occurred in that particular layer alone, not if clouds existed simultaneously in more than one layer.

Figure 7 is similar to Fig. 6, but for a subarctic winter atmospheric profile. Figure 8 is for the particular case of tropical convective anvils, which in the model extend from about 400 mb to the top of the detrainment layer in the convective parameterization (Randall et al. 1989). These anvils then have the same base level, but have varying tops up to 100 mb. Low-level convective

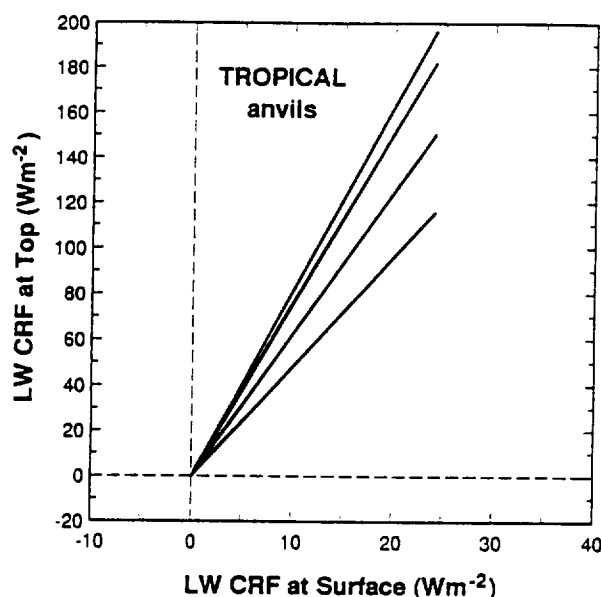


FIG. 8. As in Fig. 6 but for convective anvils and a tropical atmospheric profile.

clouds are completely ignored, at present, in the radiation computations.

The simulations shown in Figs. 6–8 explain the nature of the scatter plots shown in Figs. 4, 5. The model tends to generate a preferred type of cloud at a particular grid point during a particular season. Although simultaneous occurrence of multilayer clouds is simulated, there are several regions in which a particular cloud type predominates. For example, Fig. 5a clearly shows the effects of tropical anvils. Some grid points along these zonal bands exhibit a slightly different cloud pattern, but there is a large area of coherence. The same is true of Fig. 5b, which is dominated by low-level clouds, and may be compared with the lowest line in Fig. 6.

Regions with a preferred type of cloudiness were identified by Hartmann and Short (1980) using the day-to-day variability of the outgoing longwave radiation and shortwave albedo. They found that the characteristic slope of the line of regression of changes in outgoing longwave radiation and shortwave albedo was a very sensitive indicator of low cloud regimes.

We have shown that the characteristic slope of the line of regression of the longwave CRF at the top of the atmosphere and the surface CRF also identifies cloud regimes. Following Hartmann and Short (1980) maps of the ratio of the longwave CRF at the top of the atmosphere to the longwave CRF at the surface for January and July are shown in Figs. 9a,b, respectively. The map was produced from the data in the scatter plots shown in Figs. 4a,b. Regions for which this ratio is small can be identified with areas of predominantly low-level clouds or clouds in high latitudes in the win-

ter. Large values of the ratio indicate convective anvils. The maps in Figs. 9a,b are thus an indication of the regional cloud climatology of the model. This identification can perhaps be utilized to estimate the monthly mean net longwave radiation at the surface.

4. Conclusions

All methods for extracting the surface longwave radiation suffer from uncertainties regarding cloud cover and cloud base temperature. The analysis presented in this study suggests a technique that may be able to avoid this problem. The longwave cloud radiative forcing (LWCRF) at the top of the atmosphere is currently being compiled by the Earth Radiation Budget Experiment (ERBE). The mean downward longwave radiation can be computed for clear sky conditions if a mean profile of temperature and water-vapor mixing ratio is available. The upward longwave radiation at the surface may be computed from a retrieved ground temperature. The LWCRF at the top contains information on the mean cloud cover and cloud type for the time period considered. If monthly means are used, the LWCRF at the surface may be obtained from a global map of the LWCRF at the top if maps of the ratio, such as shown in Fig. 9, were available. This would not require explicit knowledge of the mean cloud fraction. Of course, acceptance of the results of a general circulation model is not a viable option. To some extent the standard deviation of daily mean values of the ratio of cloud forcing from the model could be used to judge the appropriateness of this technique for a particular grid point. This will involve reliance on the model that is probably not warranted at this stage. Some information can also be obtained, however, from the results of recent or planned field experiments.

Certain elements required for this procedure to be tested are already in place. The data products released by the International Satellite Cloud Climatology Project (ISCCP, Schiffer and Rossow 1983) can be directly used in this scheme. ISCCP provides a daily profile of temperature and precipitable water as well as surface temperature at a $2.5^\circ \times 2.5^\circ$ horizontal resolution that may be used to generate clear sky downward longwave fluxes and upward fluxes, at least over the oceans where the once-a-day sampling is acceptable. As part of ISCCP, there have been field experiments to study cirrus and marine stratus cloud regions (Starr 1987; Albrecht et al. 1988). At least for these cases, an estimate of the mean LWCRF at the surface for an integrating time period comparable to ERBE can be obtained. On a global scale, of course, model simulations are the only choice.

Since current needs for surface radiation budget estimates are being determined primarily for application in the tropical oceans (WCP-92 1984), a start could perhaps be made to generate monthly mean surface longwave radiation maps for the tropical Pacific using

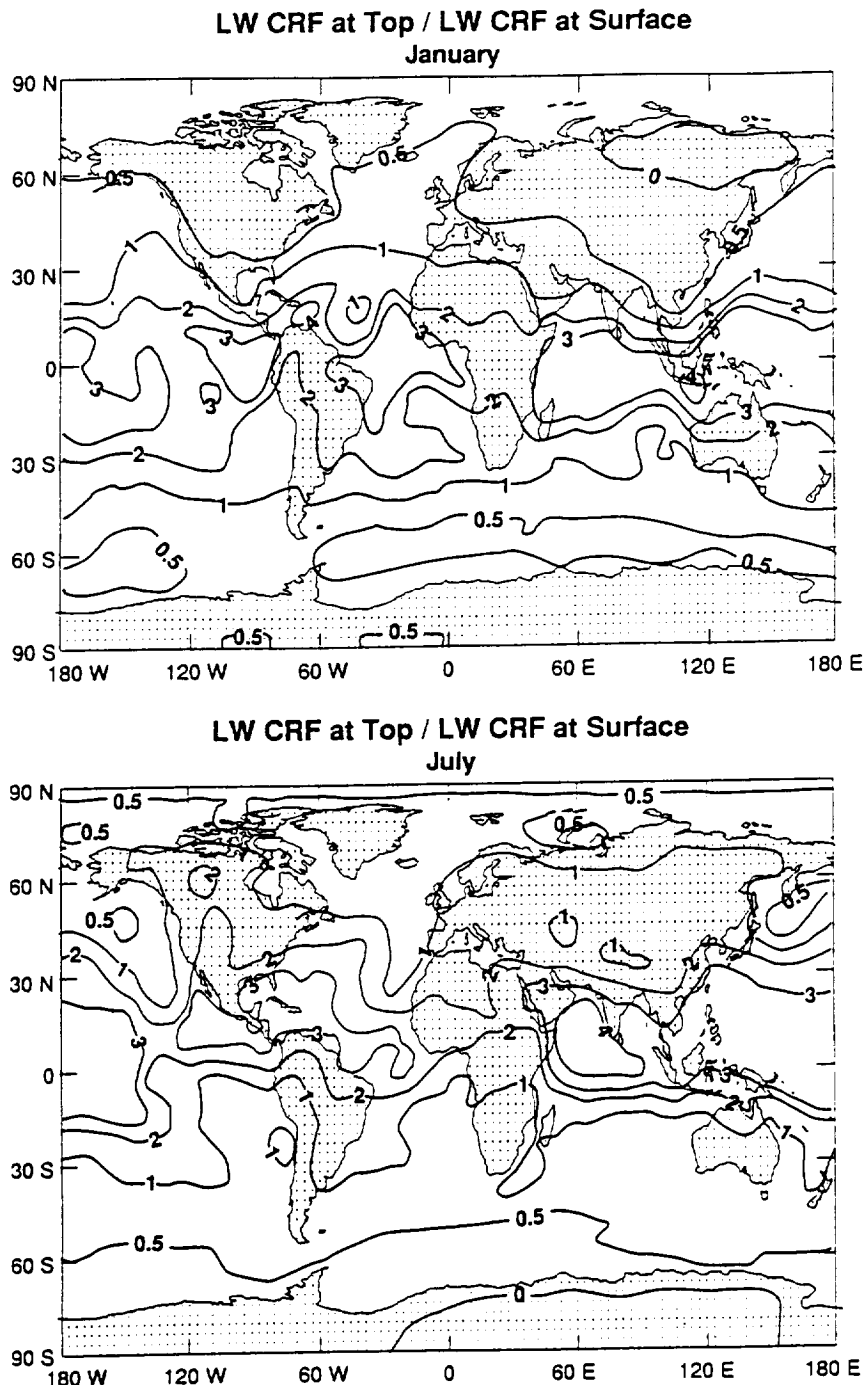


FIG. 9. Global maps of the ratio of the LWCRF at the top and at the surface for (a) January, and (b) July constructed from a simulation of the UCLA/CSU GCM. The ratio was obtained from points plotted in Fig. 4.

the procedure outlined in this study. The method should have a greater chance of success in that region based on the correlation shown in Fig. 5a. A test could be made as soon as ERBE and ISCCP data are available for the same time period.

To summarize, although it appears at first glance that longwave fluxes measured at the top of the atmosphere provide very little information on surface fluxes, it is possible to extract information from an analysis of the mean cloud radiative forcing that can

be used to generate regional, if not global, maps of the net surface longwave radiation. We have not attempted to estimate quantitatively, the accuracy of the final product, but have merely suggested a methodology that utilizes cloud and radiation datasets that are currently being compiled under the auspices of ISCCP and ERBE.

Acknowledgments. This study was made possible by the support of the National Aeronautics and Space Administration through grants NAG5-1125 to Purdue University and NAG5-1058 to Colorado State University. Computing resources were provided by the Numerical Aerodynamic Simulation Facility at NASA/Ames. Mr. Hui Zhi of Purdue University provided programming assistance. Useful discussions with Wayne Darnell and Shashi Gupta of NASA/Langley are gratefully acknowledged.

REFERENCES

- Albrecht, B. A., D. A. Randall and S. Nicholls, 1988: Observation of marine stratocumulus clouds during FIRE. *Bull. Amer. Meteor. Soc.*, **69**, 618-626.
- Budyko, M. I., 1974: Climate and life. *Int. Geophys. Ser.*, **18**, Academic Press, 508 pp.
- Carissimo, B. C., A. H. Oort and T. H. Vonder Haar, 1985: Estimating the meridional energy transports in the atmosphere and ocean. *J. Phys. Oceanogr.*, **15**, 82-91.
- Cess, R. D., and G. L. Potter, 1987: Exploratory studies of cloud radiative forcing with a general circulation model. *Tellus*, **39A**, 460-473.
- Charlock, T. P., and V. Ramanathan, 1985: The albedo field and cloud radiative forcing produced by a general circulation model with internally generated cloud optics. *J. Atmos. Sci.*, **42**, 1408-1429.
- Chou, M. D., 1985: Surface radiation in the tropical Pacific. *J. Climate Appl. Meteor.*, **24**, 83-92.
- Darnell, W. L., S. K. Gupta and W. F. Staylor, 1986: Downward longwave surface radiation from sun-synchronous satellite data: validation of methodology. *J. Climate Appl. Meteor.*, **25**, 1012-1021.
- Esbensen, S. K., and Y. Kushnir, 1981: The heat budget of the global ocean: An atlas based on estimates from marine observations. Climate Research Institute Rep. No. 29, Oregon State University, Corvallis, OR.
- Frouin, R., C. Gautier and J.-J. Morcrette, 1988: Downward longwave irradiance at the ocean surface from satellite data: methodology and in situ validation. *J. Geophys. Res.*, **93**, 597-619.
- Fung, I. Y., D. E. Harrison and A. A. Lacis, 1984: On the variability of the net longwave radiation at the ocean surface. *Rev. Geophys. Space Phys.*, **22**, 177-193.
- Gautier, C., G. Diak and S. Masse, 1980: A simple physical model to estimate incident solar radiation at the surface from GOES satellite data. *J. Appl. Meteor.*, **19**, 1005-1012.
- Gupta, S. K., 1989: A parameterization for longwave surface radiation from sun-synchronous satellite data. *J. Climate*, **2**, 305-320.
- Harshvardhan, D. A. Randall, T. G. Corsetti and D. A. Dazlich, 1989: Earth radiation budget and cloudiness simulations with a general circulation model. *J. Atmos. Sci.*, **46**, 1922-1942.
- Hartmann, D. L., and D. A. Short, 1980: On the use of earth radiation budget statistics for studies of clouds and climate. *J. Atmos. Sci.*, **37**, 1223-1250.
- Justus, C. G., M. V. Paris and J. D. Tarpley, 1986: Satellite-measured insolation in the United States, Mexico, and South America. *Remote Sens. Environ.*, **20**, 57-83.
- London, J., 1957: A study of the atmospheric heat balance. College of Engineering, Dept. of Meteor. and Oceanogr., New York University, 99 pp. [NTIS PB 115626].
- McClatchey, R. A., R. W. Fenn, J. E. A. Selby, F. E. Voiz and J. S. Garing, 1972: Optical properties of the atmosphere. 3rd ed., AFCRL-72-0497, 108 pp. [NTIS N7318412], [Available from Air Force Cambridge Res. Lab., Bedford, Ma.]
- National Academy of Sciences, 1983: *El Nino and the Southern Oscillation: A scientific plan*. National Academy Press, 72 pp.
- Oort, A. H., and T. H. Vonder Haar, 1976: On the observed annual cycle in the ocean-atmosphere heat balance over the Northern Hemisphere. *J. Phys. Oceanogr.*, **6**, 781-800.
- , and J. P. Peixoto, 1983: Global angular momentum and energy balance requirements from observations. *Adv. Geophys.*, **25**, Academic Press, 355-489.
- Pinker, R. T., and J. A. Ewing, 1985: Modeling surface solar radiation: model formulation and validation. *J. Climate Appl. Meteor.*, **24**, 389-401.
- Pinker, R. T., J. A. Ewing and J. D. Tarpley, 1985: The relationship between the planetary and surface net radiation. *J. Climate Appl. Meteor.*, **24**, 1262-1268.
- Ramanathan, V., 1986: Scientific use of surface radiation budget data for climate studies. *Surface Radiation Budget for Climate Studies*. J. T. Suttles and G. Ohring, Eds., NASA reference publication 1169, 132 pp.
- , 1987: The role of Earth radiation budget studies in climate and general circulation research. *J. Geophys. Res.*, **92**, 4075-4095.
- Randall, D. A., Harshvardhan, D. A. Dazlich and T. G. Corsetti, 1989: Interactions among radiation, convection, and large-scale dynamics in a general circulation model. *J. Atmos. Sci.*, **46**, 1943-1970.
- Raschke, E., and H. J. Preuss, 1979: The determination of solar radiation budget at the Earth's surface from satellite measurements. *Meteor. Rundsch.*, **32**, 18-28.
- Schiffer, R. A., and W. B. Rossow, 1983: The International Satellite Cloud Climatology Project (ISCCP): the first project of the world climate research program. *Bull. Amer. Meteor. Soc.*, **64**, 779-784.
- Schmetz, P., J. Schmetz and E. Raschke, 1986: Estimation of daytime downward longwave radiation at the surface from satellite and gridpoint data. *Theor. Appl. Climatol.*, **37**, 136-149.
- Sellers, W. D., 1965: *Physical Climatology*. University of Chicago, 272 pp.
- Starr, D. O'C., 1987: A cirrus-cloud experiment: intensive field observations planned for FIRE. *Bull. Amer. Meteor. Soc.*, **68**, 119-124.
- Tarpley, J. D., 1979: Estimating incident solar radiation at the surface from geostationary satellite data. *J. Appl. Meteor.*, **18**, 1172-1181.
- WCP-92, 1984: *World Climate Research Programme*. WMO, 41 pp.
- Weare, B. C., 1989: Relationships between net radiation at the surface and the top of the atmosphere derived from a general circulation model. *J. Climate*, **2**, 193-197.
- Wu, M.-L. C., and C.-P. Cheng, 1989: Surface downward flux computed by using geophysical parameters derived from HIRS 2/MSU soundings. *Theor. Appl. Climatol.*, **40**, 37-51.

**A HYBRID TECHNIQUE FOR COMPUTING THE MONTHLY
MEAN NET LONGWAVE SURFACE RADIATION OVER
OCEANIC AREAS**

Hui Zhi and Harshvardhan

*Department of Earth and Atmospheric Sciences
Purdue University
West Lafayette, Indiana
U.S.A.*

Theoretical and Applied Climatology, 1993

Summary

Global maps of the monthly mean net upward longwave radiation flux at the ocean surface have been obtained for April, July, October 1985 and January 1986. These maps were produced by blending information obtained from a combination of general circulation model cloud radiative forcing fields, the top-of-the-atmosphere cloud radiative forcing from ERBE and TOVS profiles and sea surface temperature on ISCCP C1 tapes. The fields are compatible with known meteorological regimes of atmospheric water vapor content and cloudiness. There is a vast area of high net upward longwave radiation flux ($> 80 \text{ W m}^{-2}$) in the eastern Pacific Ocean throughout most of the year. Areas of low net upward longwave radiation flux ($< 40 \text{ W m}^{-2}$) are the tropical convective regions and extra tropical regions that tend to have persistent low cloud cover. The technique used in this study relies on GCM simulations and so is subject to some of the uncertainties associated with the model. However, all input information regarding temperature, moisture and cloud cover is from satellite data having near global coverage. This feature of the procedure alone warrants its consideration for further use in compiling global maps of the net longwave radiation at the surface over the oceans.

1. Introduction

The surface radiation budget, i.e., the net solar radiation absorbed minus the net longwave radiation emitted, and its spatial and temporal variations are key parameters in climate and weather studies. This budget plays a major role in determining radiative heating, as well as sensible and latent heat fluxes over ocean and land surfaces. As a result, the net radiative flux constitutes an important boundary forcing for the general ocean circulation and a crucial parameter for determining meridional oceanic heat transport, ocean-atmosphere interaction and land-atmosphere interaction. Moreover, it is a useful parameter when addressing issues related to climate change due to CO₂ and other trace gases, and in the validation of radiation schemes used in climate models. Therefore, it is understandable for the atmospheric and oceanic communities to need reliable estimates of the surface radiation budget (WCP-92, 1984).

Direct high-quality radiation measurements at the surface are difficult to make, particularly over the oceans which cover more than 60% of the Earth's surface. Actually there are very few surface stations measuring the radiation budget routinely and reliably because of the requirement of careful instrument calibration and temperature correction for the radiation, especially longwave, measurement. In addition, because of operating costs, it is not feasible to maintain a network of surface stations over the oceans. Although an attempt has been made to use ships to observe some meteorological parameters such as sea surface temperature, air temperature, specific humidity near the surface and even fractional cloud coverage, there has not been much progress in the measurement of surface radiation. Few ships measure radiation quantities because of special needs that require a dedicated facility for this purpose. Moreover, regular ship observations are limited along commercial shipping lanes, and vast geographic gaps still exist, especially in the southern hemisphere. Consequently, the empirical formulas used to derive budgets have been validated only over limited regions, and when applied globally, large errors are inevitable. Therefore, direct measurement of shortwave and longwave radiation fluxes at the surface globally has not been possible.

Since there are difficulties in obtaining radiative data from surface stations routinely and reliably, it has been realized that space based observations are the only means to have global coverage. However, because of the intervening atmosphere, the surface radiation budget is difficult to measure from satellites, whereas the top-of-the-atmosphere (TOA) radiation balance can be measured directly. Over the past decades, considerable effort has been expended in the global measurement of the TOA radiation budget. Attempts at inferring the surface radiation budget from space based measurements have only begun recently.

There has been some success in obtaining the solar radiation budget at the surface (e.g. Raschke and Preuss, 1979; Tarpley, 1979; Gautier et al., 1980; Pinker and Ewing, 1985; Justus et

al., 1986). The progress in surface longwave radiation budget measurements from space, however, has been much slower. Currently, some techniques are available to estimate the downward longwave component of the surface flux (Darnell et al., 1983, 1986; Chou, 1985; Schmetz et al., 1986; Frouin et al., 1988; Ardanuy et al., 1989; Wu and Cheng, 1989; Breon et al., 1991). The net longwave component at the surface can be estimated by the difference between the upwelling and downwelling fluxes. The upward component is determined directly from sea surface temperature since the oceanic surface emits essentially as a blackbody. The downward flux, however, is more difficult to obtain since it depends on many meteorological parameters such as atmospheric moisture, temperature and cloud cover. Because of the uncertainty of the measurement of these meteorological parameters, at present there is a need for improvement in the estimation of net longwave radiation fluxes at the surface.

Two types of methods have been used to estimate the downward longwave flux at the surface: statistical and physical. As the name implies, statistical methods rely on correlations between fluxes and observed meteorological parameters. The physical techniques are based on modeling radiative processes occurring in the atmosphere (clear and cloudy atmosphere). The downward flux is computed from radiative transfer models which utilize parameters obtained from satellite radiance data. These parameters include temperature and water vapor mixing ratio profiles, fraction of cloud coverage and cloud emittance. However, all physical methods currently under consideration have to make certain assumptions regarding both the presence of clouds and their vertical extent. Recent examples of these attempts are Chou (1985), Schmetz et al. (1986), Darnell et al. (1986), Gupta (1989), and Wu and Cheng (1989). The treatment of longwave radiation transmittance in the presence of clouds becomes more complex since knowledge of cloud top and base heights and emittances are required. For this reason, it is important to determine the vertical profile of cloudiness as well as the horizontal distribution of clouds and associated emittances. Unfortunately, determination of the vertical profile of cloudiness from space based measurements is difficult since overlap of cloudy layers is common in the real atmosphere. Therefore, because of the uncertainties in assumed cloudiness, all these methods often give unreliable results.

The method used here to obtain monthly mean quantities avoids the explicit computation of cloud fraction and the location of cloud base in estimating the downward longwave radiation globally (Harshvardhan et al., 1990). An advantage of this technique is that no independent knowledge or assumptions regarding cloud cover for a particular month are required. The only information required is a relationship between the cloud radiative forcing (CRF) at the top of the atmosphere and that at the surface, which is obtained from a general circulation model (GCM) simulation.

As in all methods that rely on models, the uncertainties and errors present in the model are transferred to the flux computations. In the method discussed here, this carryover is minimized since actual cloud fraction or the details of the vertical distribution of clouds simulated by the GCM is not used. Instead, a monthly mean estimate of the cloud forcing at the surface and the top of the atmosphere is used. These depend on the climatology of the location and appear to be quite reasonable (Harshvardhan et al. 1990). Since the model resolution is only 4° in latitude and 5° in longitude, higher resolution features such as coastal stratus cannot be simulated. Also for reasons explained later, the method is applied only over oceanic areas.

2. Method

The cloud radiative forcing (CRF) has been defined as the difference between the radiative flux as measured or computed and the clear sky flux (Charlock and Ramanathan, 1985; Ramanathan, 1987). For example, the longwave cloud radiative forcing at the surface is:

$$\text{Surface LWCRF} = \text{Surface LW Flux} - \text{Clear Sky Surface LW Flux.} \quad (1)$$

Previous studies have shown that there is no correlation between the spectrally integrated outgoing longwave radiation and the net longwave at the surface (Ramanathan, 1986; Weare, 1989). But Harshvardhan et al. (1990) have recently come to the conclusion that there is a relationship between the longwave CRF at the top of the atmosphere and the surface in model simulations. This relationship has been explained on the grounds that clouds of a certain type tend to form preferentially over certain geographic areas. The technique proposed by Harshvardhan et al. (1990) to estimate surface longwave fluxes starts with the GCM simulated climatological ratio of the CRF at the top and at the surface along with the longwave CRF at the top of the atmosphere obtained from the Earth Radiation Budget Experiment (ERBE; Ramanathan, 1987) to compute the surface longwave CRF for the particular month. In this way, no independent knowledge or assumptions about cloud cover are involved, thus avoiding the most uncertain step in other methods of estimating the longwave radiation budget at the surface. The next step in the procedure is to obtain an estimate of the clear sky downward longwave flux and upward emission at the surface.

As mentioned before, the downwelling longwave radiation at the surface can not be measured directly from space, but profiles of temperature and water vapor mixing ratio in clear columns are routinely obtained from inversions of measured radiances. Most attempts to compute the downwelling longwave fluxes have relied on these retrieved profiles to furnish the flux using a radiative transfer model.

Here we show results using the once daily profile contained in the data released by the International Satellite Cloud Climatology Project (ISCCP; Rossow and Schiffer, 1991). ISCCP

CI data provides a daily profile of temperature and precipitable water as well as surface temperature at a $2.5^\circ \times 2.5^\circ$ horizontal resolution. This information from TOVS (TIROS Operational Vertical Sounder) is used to generate clear sky downward longwave fluxes globally and upward fluxes only over the ocean where the once-a-day sampling is acceptable. The diurnal cycle of surface temperature precludes using this technique over land. The radiation code used to compute the clear sky downward flux is the one used in the UCLA/GLA (now CSU) GCM (Harshvardhan et al., 1989; Randall et al., 1989, 1991).

A flow diagram of the technique used to obtain surface longwave fluxes is shown in Fig. 1. Calculations start from the relationship between the longwave CRF at the top of the atmosphere and at the surface (Harshvardhan et al., 1990). Results for the months of January, April, July and October are used in this study and represent the simulated monthly characteristics of this relation over the annual cycle. The longwave CRF at the top of the atmosphere as obtained from ERBE is combined with the relationship to obtain the longwave CRF at the surface for each of the four months. Then, by means of the radiative transfer model, with input meteorological parameters such as temperature profile and water vapor mixing ratio profile and sea surface temperature from ISCCP data as well as standard ozone vertical distributions, the clear-sky downward longwave radiative flux and the clear-sky net longwave upward radiation flux at the surface are obtained. Because ozone is primarily confined to the stratosphere, its contribution to downward longwave flux is much less than that of other parameters such as water vapor in the lower atmosphere. Therefore, use of a standard ozone profile is justified. Trace gases such as methane and freons are not included in the code. This omission leads to an overestimate of the outgoing longwave clear sky flux by 5 to 10 W m^{-2} (Briegleb, 1992). However, the downward clear sky flux is dominated by water vapor emission and the effect of trace gases is neglected here.

In this study, the clear sky fluxes are computed for the atmospheric structure under cloudy conditions, but assuming a cloud-free sky. This is referred to as "Method II" by Cess and Potter (1987). The ERBE clear sky climatology is constructed by averaging fields that are classified as being clear. The method of determining the samples to be included in this category introduces errors. Hartmann and Doelling (1991) have shown that fluctuations in temperature and water vapor can result in misclassification. As a result of this, the clear sky OLR over the oceans could be an overestimate by $\sim 3 \text{ W m}^{-2}$ (Harrison et al., 1990). This bias will also appear in the surface CRF computed using the procedure outlined in Fig. 1. Once the CRF at the surface and the clear-sky radiative fluxes at the surface are available, based on the definition of the CRF shown in eq. (1), the actual radiative fluxes can be calculated simply as the clear-sky flux plus the corresponding CRF.

3. Results

3.1 Longwave CRF at the Surface (global)

The mean monthly distributions of the longwave cloud radiative forcing (CRF) at the surface are presented in Fig. 2 for the months of April, July and October 1985 and January 1986. They are derived by combining the longwave CRF at the top of the atmosphere from ERBE (Harrison et al., 1990) and the ratios of the CRF at the top to that at the surface. Based on the definition in eq. (1), the longwave CRF is the difference between the mean longwave flux and clear sky longwave flux for the same period. Here the longwave CRFs at the top of the atmosphere are retrieved from ERBE satellite data according to this definition. In the original ERBE data, there are a few regions in the tropics where clear sky longwave radiative fluxes at the top of the atmosphere are unavailable because of the lack of clear sky pixels during the experiment period. Therefore, an interpolation is performed to make up the missing data using neighboring points.

There are several noteworthy features of these distributions. First, regions with small surface longwave CRF are concentrated in the tropical and the subtropical oceanic areas (Fig. 2). Surface CRF is small in the tropics because the boundary layer there is moist and radiatively opaque even for clear skies. In the central Pacific Ocean, the areas with surface longwave CRF below 20 W m^{-2} dominate throughout the year. This is also the case for the northern and central Indian Ocean in both April 1985 and January 1986. Areas with large surface longwave CRF occur over oceanic areas southwest of Indonesia, with a maximum of more than 60 W m^{-2} in October and more than 80 W m^{-2} in July 1985. Both of these maxima correspond to areas of tropical convective activity. In the central Atlantic Ocean, the surface longwave CRF is below 30 W m^{-2} .

Larger values of surface CRFs are found over the midlatitude continents than over oceans during October, January and April. This may seem surprising since cloud cover over the oceans is greater than that over land (Rossow and Schiffer, 1991) and the longwave CRF at the top of the atmosphere is larger over the oceans (Harrison et al., 1990). The results could be an artifact of the method but are not inconsistent with meteorological conditions for the following reason.

The surface LWCRF defined in eq. (1) can be rephrased as:

$$\text{Surface LWCRF} = C(F_{\text{sfovc}} - F_{\text{sfcldr}}) \quad (2)$$

where C is the cloud fraction, F_{sfovc} is the surface longwave flux for overcast conditions and F_{sfcldr} is the corresponding value for clear skies. The surface LWCRF is thus the product of two terms. The land-ocean difference in the quantity is therefore:

$$\Delta \text{LWCRF} = C_o(F_{\text{sfovc}} - F_{\text{sfclr}})_o - C_l(F_{\text{sfovc}} - F_{\text{sfclr}})_l, \quad (3)$$

where the suffix o refers to ocean and l to land.

There is no doubt that $C_o > C_l$ but the difference in the downward surface longwave flux between clear and overcast conditions is larger over dry, cold continents than over moist, warm oceans (Chou, 1989). In fact, the maximum LWCRF at the surface occurs over the Himalayas (Wu and Cheng, 1989). Whether the larger flux difference fully compensates for the difference in cloud cover cannot be known without observational verification. Comparison with other modeled values is not sufficient grounds for rejecting this possibility.

An example of the possibility mentioned above is a comparison of the net flux difference between overcast and clear skies for two disparate areas in the month of January 1986. We have considered an oceanic area in the western Pacific, which is the site of the TOGA-COARE experiment (WCP-92, 1984) and a continental area in eastern North America. Net upward longwave fluxes at the surface have been calculated using ECMWF (European Centre for Medium Range Forecasts) analyses and the radiation code used in this study for clear sky conditions and two separate overcast cases, one with the cloud base at 850 mb and the other with the base at 931 mb.

The clear sky net upward flux at the surface in the TOGA-COARE area is about 60 W m^{-2} , while in the continental region in North America it is about 100 W m^{-2} . The mean difference between overcast and clear in the oceanic area is 41 W m^{-2} for the 850 mb cloud base and 48 W m^{-2} when the base is at 931 mb. The corresponding mean differences in the continental area are 96 W m^{-2} and 95 W m^{-2} respectively. It should be noted that there is a pronounced temperature inversion in the analyzed fields for this region. These values are the terms in parenthesis in eq. (3), such that even if C_o is substantially greater than C_l , the cloud forcing over land could exceed that over the oceans.

There are two continents, Africa and Australia, which always have small surface CRFs throughout the year because of their large desert and semi-arid areas. Here the cloud fraction is low and the first term in eq. (2) determines the forcing. Fig. 2 shows the surface CRFs there to be often below 30 W m^{-2} , especially in northern Africa, where the values are always below 20 W m^{-2} . It is worthwhile noting that a persistent large surface CRF region exists in the tropical region of South America. Obviously, this results from the persistent cloud cover in this region. Over high latitude regions, some areas with the largest surface longwave CRFs are found over the region poleward of 65°S , with a maximum of 150 W m^{-2} in July and some areas over the Arctic, with a maximum of more than 140 W m^{-2} in October and January. Two explanations are possible for this phenomenon. Physically, it is reasonable that persistent low clouds over these

regions lead to high surface longwave CRF. On the other hand, an underestimate of high cloud over the polar regions in the GCM simulation can also result in the surface longwave CRFs being somewhat unreasonably high. Also, ERBE cloud forcing for these high latitudes may not be reliable. Finally, areas with the average range of $30 - 50 \text{ W m}^{-2}$ dominate most mid-latitude oceanic regions of both hemispheres. This is attributable to the increase in oceanic stratus in these regions.

3.2 *Downward Longwave Radiation Flux at the Surface (global)*

Downward longwave radiative fluxes at the surface for cloud-free skies, as calculated by the radiation code in the UCLA/GLA GCM in conjunction with the input meteorological parameters from the ISCCP satellite data and U. S. standard atmosphere (COESA, 1976), are presented in Fig. 3 for April, July and October 1985 and January 1986 respectively.

Over the oceanic areas, clear sky surface downward longwave fluxes have pronounced zonal distributions, especially in mid-latitudes and near polar regions. In the tropical and subtropical areas, the regions with large downward fluxes (larger than 400 W m^{-2}) are centered over Southeast Asia in April and October 1985 and shift a little northward in July 1985 and, as expected, a little southward in January 1986. This is not surprising since the surface downward longwave fluxes for clear skies are related closely with seasonal changes in temperature and moisture. In the northern spring (April) and fall (October), for the quite symmetrical solar irradiance distribution at that time, surface downward longwave fluxes also have a symmetrical distribution with respect to the equator. In the northern summer (July) and winter (January), the maps of clear sky surface downward fluxes show a shift northward and southward respectively with the changing seasons. This result is consistent with the fact that clear sky downward fluxes are determined by the near surface temperature which is closely related to the incident solar energy. Evidently, the high values (larger than 400 W m^{-2}) in Southeast Asia correspond to areas where, due to the high surface temperature of islands, the atmosphere is warmer than elsewhere along the same latitudinal belt. In particular, there is an area with values larger than 420 W m^{-2} centered east of Papua New Guinea in January 1986, corresponding to very warm and moist near surface conditions. In contrast, the low values (less than 200 W m^{-2}) near the polar regions correspond to areas where the atmosphere is cold and dry throughout the year.

Over the continents, symmetrical distributions of clear sky downward fluxes disappear and more complicated features of distributions emerge, corresponding to the land surface. There is a pronounced center of low values of downward fluxes over the Tibetan Plateau in Asia throughout the year because the mean elevation of the Tibetan Plateau is more than 4000 m above sea level so that surface air temperature is quite low except in summer. However even though high temperatures often occur there in summer, its high elevation makes the air still very

dry. Since the major contribution to longwave downward flux at the surface comes from the water vapor in the lower atmosphere, the dry air over that region results in an area of low values of downward fluxes. Over southern Africa, relatively higher values along the same latitude result from the higher air temperature and more moist air. In northern Africa, although the surface temperature is very high, the dry air, due primarily to its desert areas, results in downward fluxes that are lower along the same latitude. In addition, a pronounced trough line along the Rocky Mountains in Fig. 3 represents higher altitudes and a drier atmosphere in that region compared to surrounding areas.

Surface downward longwave fluxes, as derived from the formula described in eq. (1) with given clear sky fluxes and the longwave CRF at the surface, are presented in Fig. 4 for April, July and October 1985 and January 1986 respectively. Over the oceanic areas, the zonal distribution for the clear sky case is no longer apparent. The presence of clouds increases the downward fluxes at the surface globally throughout the year. Fluxes with values larger than 400 W m^{-2} are found over areas associated with the intense convective cloud systems, such as the ITCZ, as well as the summer and winter monsoon areas. It is reasonable because, in these regions, clouds occur frequently and the air temperatures are high. An area with values larger than 440 W m^{-2} is found over northeast Australia in January 1986, corresponding to the high temperatures in the austral summer. Also, an area with high values is centered over southwest Indonesia in July 1985.

Compared with clear sky maps, larger changes occur over land than over the oceans throughout the year. In addition, the regions of high values are still distinguishable in these months except in April 1985. Low downward fluxes (less than 280 W m^{-2}) are found over high latitudes and polar regions, where the precipitable water is low and air temperature is cold. As seen in Fig. 4, contour lines of downward fluxes are spaced very densely in high latitudes during the whole year. As we mentioned before, these sharp changes perhaps result from uncertainties in modeling the meteorological parameters in these regions, an unavoidable consequence of the inability to distinguish cloud cover from background snow and ice and hence compute the cloud forcing. In addition, seasonal variations of surface downward fluxes are still notable in Fig. 4, even though they are not as remarkable as in the clear sky case.

3.3 *Net Upward Longwave Radiation Flux at the Surface (ocean only)*

The clear sky net upward longwave flux at the surface is the difference of the upward flux minus the downward surface flux assuming no clouds. The upward flux here is computed from the sea surface temperature, which is a reported parameter in ISCCP C1 satellite data. There are three surface temperatures (TS) from imaging radiometers provided by ISCCP: mean TS from a clear sky composite, mean TS for IR-clear pixels, and mean TS for VIS/IR-clear

pixels for only day time. Also listed is a TOVS surface temperature. In order to compute the surface emission, it is not necessary to use any of these fields but instead rely on an independent source such as the sea surface temperature provided by NOAA's Climate Analysis Center (CAC). This is a blend of in situ data, Advanced Very High Resolution Radiometer (AVHRR) satellite data, and ice data (Reynolds, 1988). Fig. 5 shows the zonally averaged sea surface temperatures for January 1986 for the three ISCCP fields and the CAC field. In high latitude regions, the CAC sea surface temperature is much higher than the ISCCP values because ice surface temperature is set to be the freezing point of sea water (-1.8°C). Fig. 5 indicates that the clear sky composite TS is warmest among the three ISCCP sea surface temperatures, while the IR clear sky TS is the coldest. This is to be expected since IR clear pixels are contaminated by low level clouds. We chose the VIS/IR clear sky as the most representative quantity for this study.

The difference between the surface emission computed from daytime mean TS for VIS/IR clear pixels and the CAC sea surface temperature is presented in Fig. 6 for January 1986. This difference is a measure of the uncertainty one may expect in the upward longwave radiation flux computed using different sources for the sea surface temperatures. The dominant feature of this map is a set of biases of less than 10 W m^{-2} present over the tropical and subtropical regions except around southeast Asia, where the surface emission from mean TS for VIS/IR clear pixels exceeds that from CAC temperature by as much as 30 W m^{-2} . This could be a result of differences in the particular algorithms used by ISCCP and CAC to account for water vapor absorption in the atmospheric window and cloud screening procedures. Also any ship observations used are not necessarily representative of the skin temperature of the ocean surface but this effect should be small. The areas with differences larger than 10 W m^{-2} are found over high latitudes in the Pacific and Atlantic Ocean. Positive differences (less than 10 W m^{-2}) are located over the central Pacific ocean and eastern Indian ocean, whereas areas with negative difference are found in other locations. The maximum absolute difference is around 5%. However, it is disturbing that the uncertainty in the upward component of the surface longwave flux is of the order of the accuracy in the net radiation requested by the scientific community (WCP-92, 1984).

Fig. 7 shows the clear sky net upward longwave fluxes at the surface for April, July and October 1985 and January 1986 respectively. Physically the maps of clear sky net upward longwave fluxes primarily reflect the distribution of water vapor content in the boundary layer. The area with lowest values is found over Southeastern Asia throughout the year. In this region, even in the absence of clouds, the clear sky net upward longwave fluxes are quite small because of the high water vapor mixing ratio near the surface. Areas with values larger than 100 W m^{-2} are found over the mid-latitude subsidence zones between 15° and 45° latitude in both

hemispheres in April, October 1985 and January 1986, and in the southern hemisphere in July 1985. These are regions in which a dry atmosphere overlies a moderately warm ocean surface. Also, in July 1985, there is a minimum of less than 40 W m^{-2} off the coast of central America and, in the other three months, a minimum of less than 40 W m^{-2} just along the west coast of Colombia, Ecuador and Peru; all these minima correspond to the presence of a relatively moist atmosphere.

Net upward longwave flux, a difference field of the clear sky net upward flux minus the surface longwave CRF (Fig. 2) as described in eq. (1), is presented in Fig. 8 for April, July and October 1985 and January 1986. In this case, the areas with smaller values are still found over Southeast Asia. Here, the near saturation of the boundary layer results in low values of the net upward longwave flux for both clear and cloudy conditions resulting in low values in the monthly mean. Also, small net upward fluxes with values less than 40 W m^{-2} are found in high latitudes and polar regions where there is persistent cloud cover and temperatures are low throughout the year. Values larger than 80 W m^{-2} are found over some areas in the tropical and mid-latitude zone. It is worth noting that the negative values near the Antarctic in July 1985 result from the large longwave CRF at the surface derived previously. Since negative values are possible but unlikely, one may conclude that the unreasonable high surface CRF is a result of the modeling and computation errors but not physical processes. Generally, the influence of clouds in the stratus regime causes the net longwave flux to be reduced by $50 - 60 \text{ W m}^{-2}$ throughout the year.

4. Discussion

Monthly mean longwave radiation fluxes at the surface for four months have been determined from currently available satellite data. Because of the diurnal variation of surface temperature over the continents, surface net longwave fluxes, which involve the surface temperatures, are presented only over the oceanic areas. The method discussed here avoids the use of an independent estimate of the frequency of occurrence of clouds or even cloud top heights in determining the surface longwave fluxes. Current methods of modeling the longwave radiation processes in the atmosphere require certain assumptions regarding the presence of clouds and their horizontal and vertical extent. Because of the complicated nature of cloud radiation and uncertainties in the observation of clouds, large errors are inevitable in this procedure. The procedure used in this study provides an alternative means of obtaining longwave radiative fluxes at the surface without the knowledge of cloud distribution. All meteorological parameters required in this method can be obtained from currently available satellite data sets. The ISCCP data and U.S. Standard Atmosphere (COESA, 1976) provide the profiles of temperature, water vapor mixing ratio and ozone as well as sea surface temperatures. The distributions of the longwave CRF at the top of the atmosphere are retrieved from ERBE

data which is currently being completed for several years of measurements.

The weakest link in this procedure is the use of simulated CRF ratios that relate the CRF at the top and surface. Errors in the cloud generation scheme of the model used will affect the ratio and hence, the final product. It is also not feasible to verify these ratios observationally on a global scale, although it would be useful to verify the model result in some specific regions where simultaneous observations at the top of the atmosphere and the surface are available over an extended period of time.

The final product can be compared with field data for a few regions and periods during which extended time observations were made from ships. Note that the fields generated are area averaged monthly means and comparisons with point measurements over short periods of time do not provide any corroboration. Observations reported by Reed and Halpern (1975) off the Oregon coast covered an eight week period in July - August 1973 and included measurements taken from two sites, one 13 km from the shore and the other 120 km away. Lind and Katsaros (1987) have reported measurements taken off the California coast during the first two weeks of November 1984. Radiation budget data from GATE (Cox and Griffith, 1979) was an amalgam of direct radiation measurements and modeled fields based on soundings. The authors point out the futility of computing area and time mean quantities directly from measurements even for a dedicated field campaign over a (relatively) small portion of the oceanic area of the globe.

The daily mean net longwave radiative flux at the surface reported by Reed and Halpern (1975) varied from 71 W m^{-2} for days when the daily mean cloud cover was 10% - 20% to between $11 - 15 \text{ W m}^{-2}$ for 70% - 100% cloud cover. An unweighted mean of the ten daily mean values taken at two stations over the period July 5 - August 26 is 33 W m^{-2} . The corresponding estimate for July 1985 from Fig. 8 is around 40 W m^{-2} . This suggests that the procedure used here is able to provide a good measure of the mean cloud fraction which is the strongest determinant of the net longwave radiation for this region. This bears out our thesis that a reliable measure of the effect of clouds is a necessary condition for obtaining global fields of the net longwave radiation at the surface.

Lind and Katsaros (1987) have reported ship based observations of the upward and downward longwave radiation taken off the California coast from October 30 - November 14 1984. The daily mean net longwave radiation from R/P FLIP ranged from 11 W m^{-2} to 69 W m^{-2} . Although there is no reported cloud cover, inspection of the daily mean insolation shows that the extremes correspond to days of complete cloud cover and essentially clear skies, respectively. The mean for the 15 day period at the single station was 45 W m^{-2} . The mean for October 1985 and January 1986 from Fig. 8 is 75 W m^{-2} . This compares favorably with the satellite and model based results of Wu and Cheng (1989) for January 1979. The discrepancy

with the point measurement is significant but it is difficult to draw any conclusions based on the information available. From Fig. 3, the clear sky downward longwave flux for this region is about 315 W m^{-2} in October 1985 and 275 W m^{-2} in January 1986. The data from Lind and Katsaros (1987) indicate that the minimum daily mean value over the period was 340 W m^{-2} , presumably on the clearest day. Inspection of the temporal data shows that the absolute minimum value reached was 300 W m^{-2} on the night of November 7 - 8. This indicates that the clear sky element of the procedure is acceptable. The discrepancy is in the cloud estimate and there is no reasonable means of comparing the point measurement with an area average (for a different year). This highlights the difficulties inherent in validating global fields for a quantity that is measured only occasionally. Wu and Cheng (1989) have published maps of the downward and net upward longwave fluxes for January and July 1979 obtained by their physically based satellite retrieval. Their maps for July 1979 are reproduced in Fig 9. Comparison with the July 1985 panels in Fig. 4 and Fig. 8 show similarities and differences but the main features are common and can be considered to be the July climatology of the longwave fluxes at the surface. Wu and Chang (1991) have compared retrieved moisture, temperature and cloud cover from five sources and conclude that differences in the downward flux at the surface of $15 - 30 \text{ W m}^{-2}$ should be expected when computations are made based on data from these different sources.

Some further generalizations can be made about the uncertainty in the global fields. Fung et al. (1984) state that a 1 g kg^{-1} uncertainty in the water vapor mixing ratio at low levels and a 100 mb error in the cloud base each translate to a 10 W m^{-2} uncertainty in the net longwave flux over oceans. The presence of low level haze which is only now being mapped from space based measurements (Rao et al., 1989) and is not considered in the GCM is equivalent to underestimating low cloud cover, hence surface forcing. In certain regions this error could range from $5 - 10 \text{ W m}^{-2}$. Moreover, if one makes the gross assumption that low clouds cover the oceans 50% of the time everywhere, it may be shown that the net longwave at the surface will range from $40 - 60 \text{ W m}^{-2}$ for any reasonable temperature and mixing ratio profile. The departure from this range of values shown in Fig. 8 is the true information contained in the maps and reflects the satellite based cloud information that has been used.

5. Conclusions

An attempt has been made to produce monthly mean global fields of the net longwave radiation flux at the surface over the oceans without resorting to direct measurements. The key ingredients in the technique are the satellite derived temperature and moisture profiles (which are available operationally), the top of the atmosphere cloud radiative forcing from ERBE (which is an experimental data product but could be available in the future) and the cloud distributions from a general circulation model. It should be stressed that the actual cloud cover generated by

the model (which is subject to a great deal of uncertainty) is not used directly, but only information on cloud type is used through a ratio of the cloud radiative forcing at the top and surface. This parameter has the advantage that it involves simulated radiation fluxes and not the cloud fraction. The latter quantity may vary considerably from model to model and also be quite different from satellite derived estimates. However, the radiation parameterization is usually such that the fluxes at the top of the atmosphere simulated by these models compare quite favorably with observations. Examples of this apparent contradiction are in Harshvardhan et al. (1989), and Kiehl and Ramanathan (1990).

Although it is preferable to map global fields of the longwave radiation at the surface using space and ground based measurements alone, it is evident that the introduction of large scale numerical models into this effort is unavoidable. The surface is inaccessible to space based instruments at these wavelengths under cloudy conditions. Moreover, since the fluxes are extremely sensitive to water vapor mixing ratios near the surface, even clear sky estimates are subject to a great deal of uncertainty. Any global surface measurement program over the oceans is impractical. Hybrid techniques such as the one reported here that use several sources of data, both real and simulated, are the only options.

Acknowledgements

This study has been supported by NASA Grant NAG5-1125. We wish to thank Ms. Lola Olsen and her group at NSSDC, Goddard Space Flight Center, for their promptness in supplying us with all the satellite data used in this study, Dave Randall and Donald Dazlich of CSU for providing us with the GCM results, Man Li Wu for the HIRS2/MSU derived fluxes in Fig. 9, Perry Ramsey for the ECMWF calculations, Diane Milgate for help with the graphics, and Wanda Curtis for typing the manuscript.

REFERENCES

- Ardanuy, P.E., Stowe, L.L., Gruber, A., Weiss, M., Craig, S.L., 1989: Longwave cloud radiative forcing as determined from Nimbus—7 observations. *J. Climate*, **2**, 766-799.
- Breon, F.-M., Frouin, R., C. Gautier, 1991: Downward longwave irradiance at the ocean surface: an assessment of in situ measurements and parameterizations. *J. Appl. Meteor.*, **30**, 17-31.
- Briegleb, B.P., 1992: Longwave band model for thermal radiation in climate studies. *J. Geophys. Res.*, **97**, 11,475-11,485.
- Cess, R.D., Potter, G.L., 1987: Exploratory studies of cloud radiative forcing with a general circulation model. *Tellus*, **39A**, 460-473.
- Charlock, T.P., Ramanathan, V., 1985: The albedo field and cloud radiative forcing produced by a general circulation model with internally generated cloud optics. *J. Atmos. Sci.*, **42**, 1408-1429.
- Chou, M.D., 1985: Surface radiation in the tropical pacific. *J. Climate Appl. Meteor.*, **24**, 83-92.
- Chou, M.D., 1989: On the estimation of surface radiation using satellite data. *Theor. Appl. Climatol.*, **40**, 25-36.
- COESA, U.S. Standard Atmosphere, 1976: U.S. Government Printing Office, Washington D. C.
- Cox, S.K., Griffith, K.T., 1979: Estimates of radiative divergence during phase III of GATE, I, Methodology. *J. Atmos. Sci.* **36**, 576-585.
- Darnell, W.L., Gupta, S.K., Staylor, W.F., 1983: Downward longwave radiation at the surface from satellite measurement. *J. Climate Appl. Meteor.* **22**, 1956-1960.
- Darnell, W.L., Gupta, S.K., Staylor, W.F., 1986: Downward longwave surface radiation from sun-synchronous satellite data: Validation of methodology. *J. Climate Appl. Meteor.* **25**, 1012-1021.
- Frouin, R., Gautier, C., Morcrette, J., 1988: Downward longwave irradiance at the ocean surface from satellite data: Methodology and in situ validation. *J. Geophys. Res.*, **93**, 597-619.
- Fung, I.Y., Harrison, D.E., Lacis, A.A., 1984: On the variability of the net longwave radiation at the ocean surface. *Rev. of Geophys. and Space Phys.*, **22**, 177-193.

- Gautier, C., Diak, G., Masse, S., 1980: A simple physical model to estimate incident solar radiation at the surface from GOES satellite data. *J. Appl. Meteor.*, **19**, 1005-1012.
- Gupta, S.K., 1989: A parameterization for longwave surface radiation from sun-synchronous satellite data. *J. Climate*, **2**, 305-320.
- Harrison, E.F., Minnis, P., Barkstrom, B.R., Ramanathan, V., Cess, R.D., Gibson, G.G., 1990: Seasonal variation of cloud radiative forcing derived from the Earth radiation budget experiment. *J. Geophys. Res.*, **95**, 18,687-18,703.
- Harshvardhan, Randall, D.A., Corsetti, T.G., Dazlich, D.A., 1989: Earth radiation budget and cloudiness simulations with a general circulation model. *J. Atmos. Sci.*, **46**, 1922-1942.
- Harshvardhan, Randall, D.A., Dazlich, D.A., 1990: Relationship between the longwave cloud radiative forcing at the surface and the top of the atmosphere. *J. Climate*, **3**, 1435-1443.
- Hartmann, D.L., Doelling, D., 1991: On the net radiative effectiveness of clouds. *J. Geophys. Res.*, **96**, 869-891.
- Justus, C.G., Paris, M.V., Tarpley, J.D., 1986: Satellite-measured insolation in the United States, Mexico, and South America. *Remote Sens. Envir.*, **20**, 57-83.
- Kiehl, J.T., Ramanathan, V., 1990: Comparison of cloud forcing derived from the Earth Radiation Budget Experiment with that simulated by the NCAR community climate model. *J. Geophys. Res.*, **95**, 11,679-11,698.
- Lind, R.J., Katsaros, K.B., 1987: Radiation measurements from R/P FLIP and R/V Acania during the Mixed Layer Dynamics Experiment (MILDEX). Technical Report, Dept. of Atmospheric Sciences, University of Washington, Seattle, WA., 44 pp. (available from the authors).
- Pinker, R.T., Ewing, J.A., 1985: Modeling surface solar radiation: Model formulation and validation. *J. Climate Appl. Meteor.*, **24**, 389-401.
- Ramanathan, V., 1986: Scientific use of surface radiation budget data for climate studies. *Surface Radiation Budget for Climate Studies*. J.T. Suttles, G. Ohring, Eds., NASA reference publication 1169, 132pp.

- Ramanathan, V., 1987: The role of Earth radiation budget studies in climate and general circulation research. *J. Geophys. Res.*, **92**, 4075-4095.
- Randall, D.A., Harshvardhan, Dazlich, D.A., Corsetti, T.G., 1989: Interactions among radiation, convection, and large-scale dynamics in a general circulation model. *J. Atmos. Sci.*, **46**, 1943-1970.
- Randall, D.A., Harshvardhan, Dazlich, D.A., 1991: Diurnal variability of the hydrologic cycle in a general circulation model. *J. Atmos. Sci.*, **48**, 40-62.
- Rao, C.R.N., Stowe, L.L., McClain, E.P., 1989: Remote sensing of aerosols over the oceans using AVHRR data. Theory, practice and applications. *Int. J. Remote Sens.*, **10**, 743-749.
- Raschke, E., Preuss, H.J., 1979: The determination of solar radiation budget at the Earth's surface from satellite measurements. *Meteor. Rundsch.*, **32**, 18-28.
- Reed, R.K., Halpern, D., 1975: Insolation and net longwave radiation off the Oregon coast. *J. Geophys. Res.*, **80**, 839-844.
- Reynolds, R. W., 1988: A real-time global sea surface temperature analysis. *J. Climate*, **1**, 75-86.
- Rossow, W.B., Schiffer, R.A., 1991: ISCCP Cloud data products. *Bull. Amer. Meteor. Soc.*, **72**, 2-20.
- Schmetz, P., Schmetz, J., Raschke, E., 1986: Estimation of daytime downward longwave radiation at the surface from satellite and grid point data. *Theor. Appl. Climatol.*, **37**, 136-149.
- Tarpley, J.D., 1979: Estimating incident solar radiation at the surface from geostationary satellite data. *J. Appl. Meteor.*, **18**, 1172-1181.
- WCP-92, 1984: Report of TOGA workshop on sea surface temperature and net surface radiation. World Climate Research Programme, WMO, GENEVA, Switzerland.
- Weare, B.C., 1989: Relationships between net radiation at the surface and the top of the atmosphere derived from a general circulation model. *J. Climate*, **2**, 193-197.

- Wu, M.-L.C., Cheng, C.-P., 1989: Surface downward flux computed by using geophysical parameters derived from HIRS 2/MSU soundings. *Theor. Appl. Climatol.*, **40**, 37-51.
- Wu, M.-L.C., Chang, L.A., 1991: Differences in global data sets of atmospheric and surface parameters and their impact on outgoing longwave radiation and surface downward flux calculations. *J. Geophys. Res.*, **96**, 9227-9262.

Authors' address: Harshvardhan, Department of Earth and Atmospheric Sciences, 1397 CIVL,
Purdue University, West Lafayette, IN 47907-1397, U.S.A.

Figure Captions

- Figure 1. Flow diagram of the procedure to obtain maps of the monthly mean net upward longwave radiation flux at the surface using information provided by a general circulation model (GCM), data from the Earth Radiation Budget Experiment (ERBE) and the International Satellite Cloud Climatology Project (ISCCP).
- Figure 2. Monthly mean longwave cloud radiative forcing at the surface for April, July, October 1985 and January 1986 obtained from ERBE top-of-the-atmosphere cloud forcing and GCM simulations of cloudiness.
- Figure 3. Monthly mean clear sky downward longwave radiation flux at the surface for April, July, October 1985 and January 1986 obtained from TOVS profiles on the ISCCP C1 tapes and a broad band radiation code.
- Figure 4. Monthly mean atmospheric downward longwave radiation flux at the surface for April, July, October 1985 and January 1986 obtained from the clear sky values shown in Figure 3 and the cloud forcing shown in Figure 2.
- Figure 5. Zonal mean sea surface temperatures (SST) for January 1986 from three different parameters on the ISCCP C1 tapes and the blended SST from the Climate Analysis Center (CAC).
- Figure 6. Difference between the monthly mean surface emission in W m^{-2} for January 1986 computed using the CAC SST and the VIS/IR clear TS on the ISCCP C1 tapes. A positive difference indicates that the surface emission implied by the CAC SST is higher.
- Figure 7. Monthly mean clear sky net upward longwave radiation flux at the ocean surface for April, July, October 1985 and January 1986.
- Figure 8. Monthly mean atmospheric net upward longwave radiation flux at the ocean surface for April, July, October 1985 and January 1986.
- Figure 9. Monthly mean atmospheric downward longwave radiation flux at the surface (a) and the net upward longwave radiation flux at the surface (b) for July 1979 from Wu and Cheng (1989).

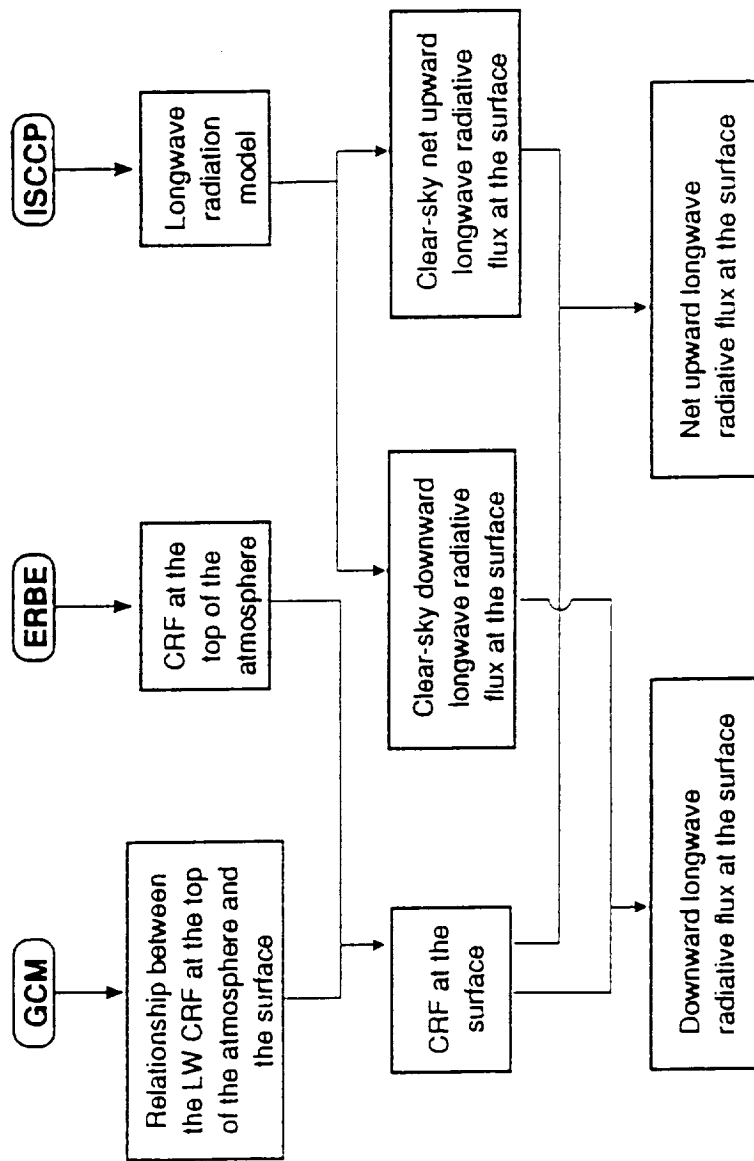


Figure 1

Longwave Cloud Radiative Forcing at the Surface

(W m⁻²)

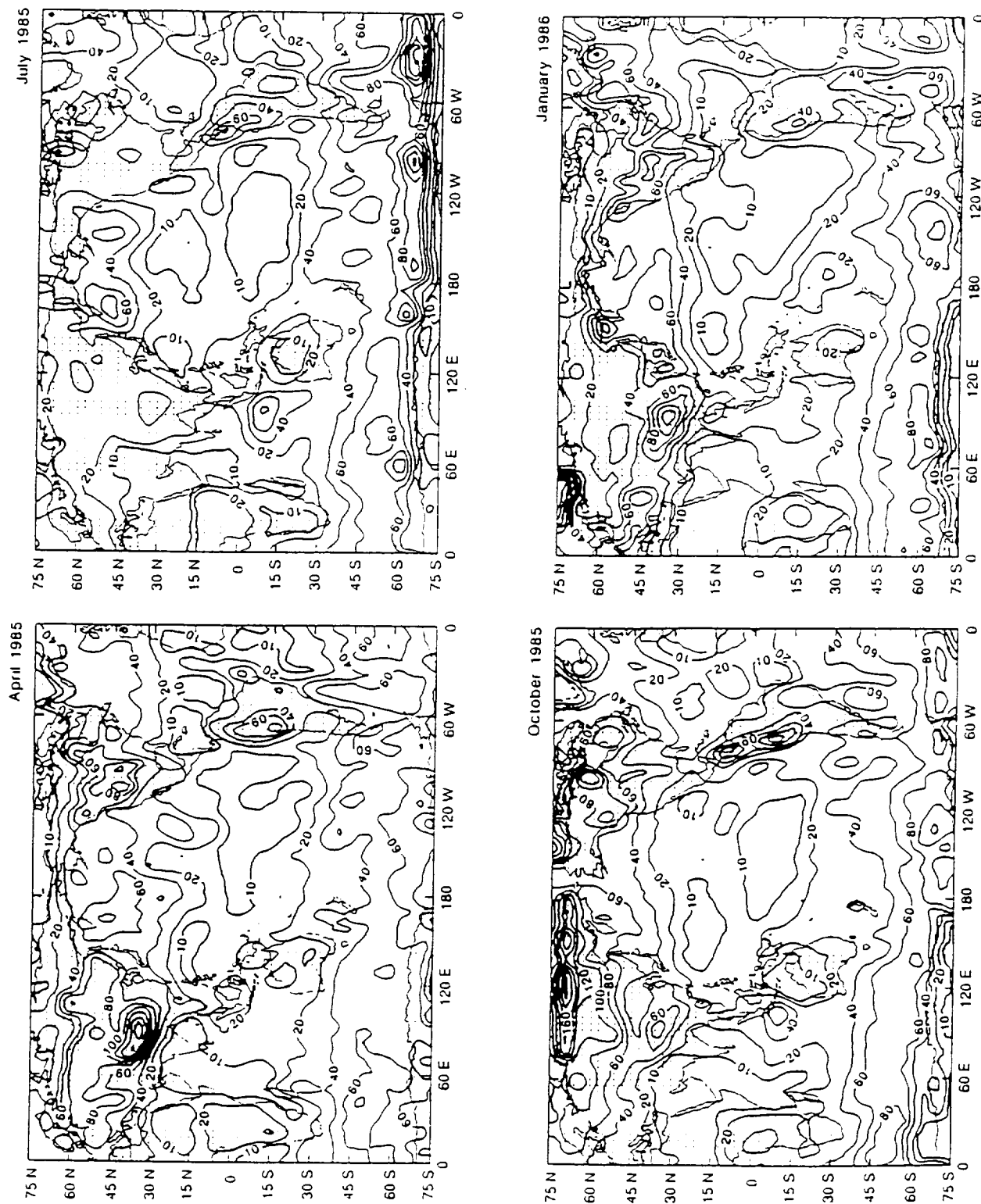


Figure 2

Clear Sky Downward Longwave Flux at the Surface

(W m^{-2})

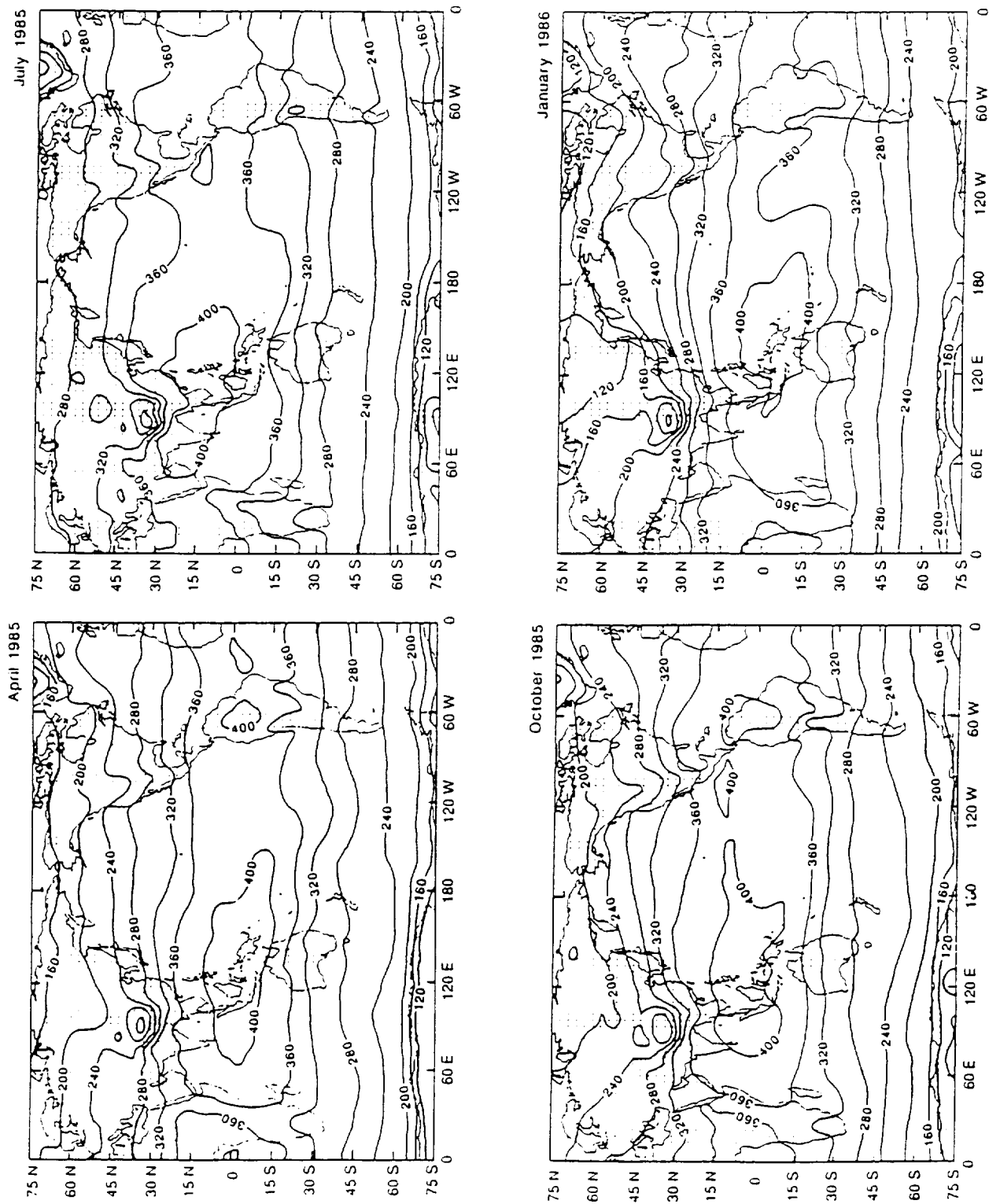


Figure 3

Atmospheric Downward Longwave Flux at the Surface

(W m^{-2})

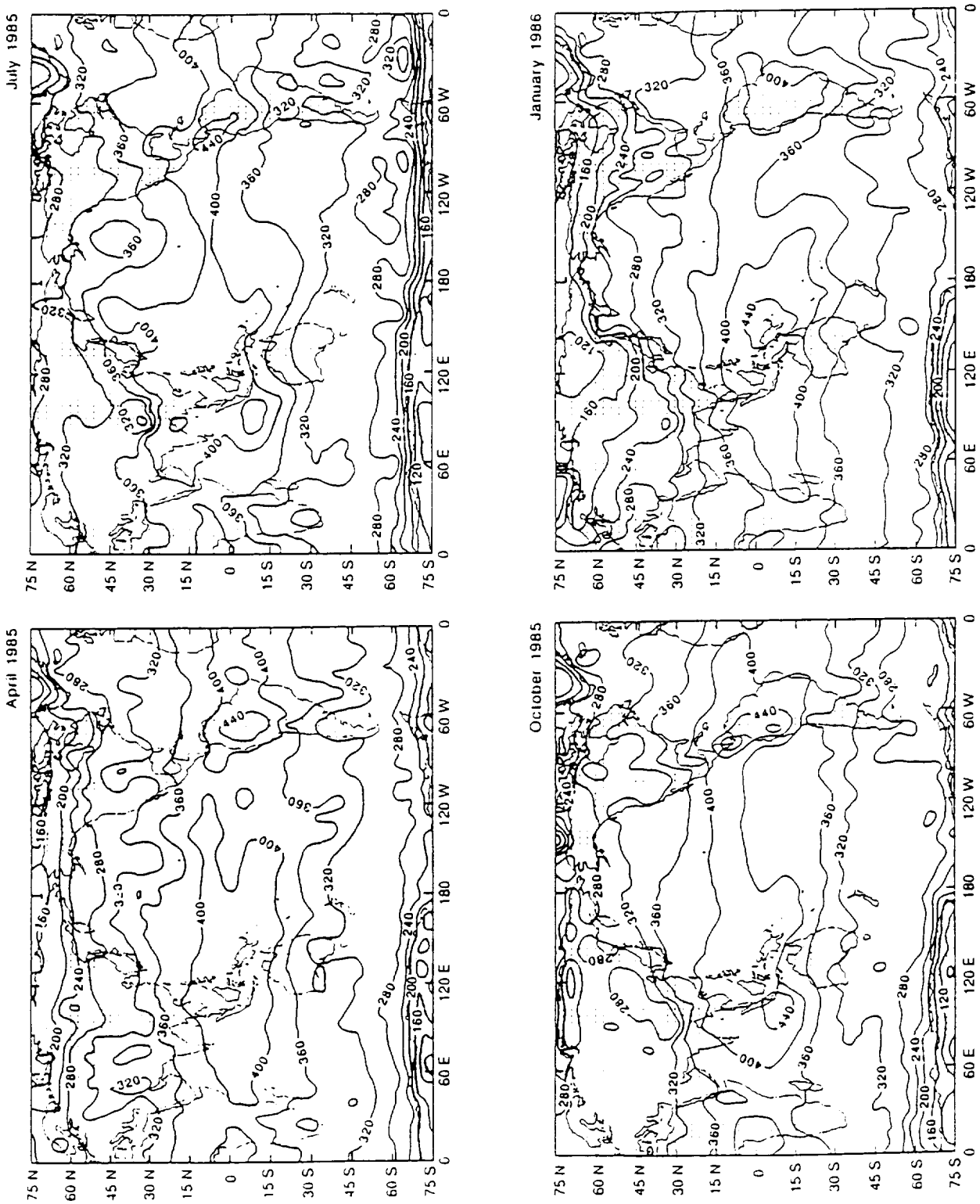


Figure 4

ZONAL MEAN SST Jan 1986

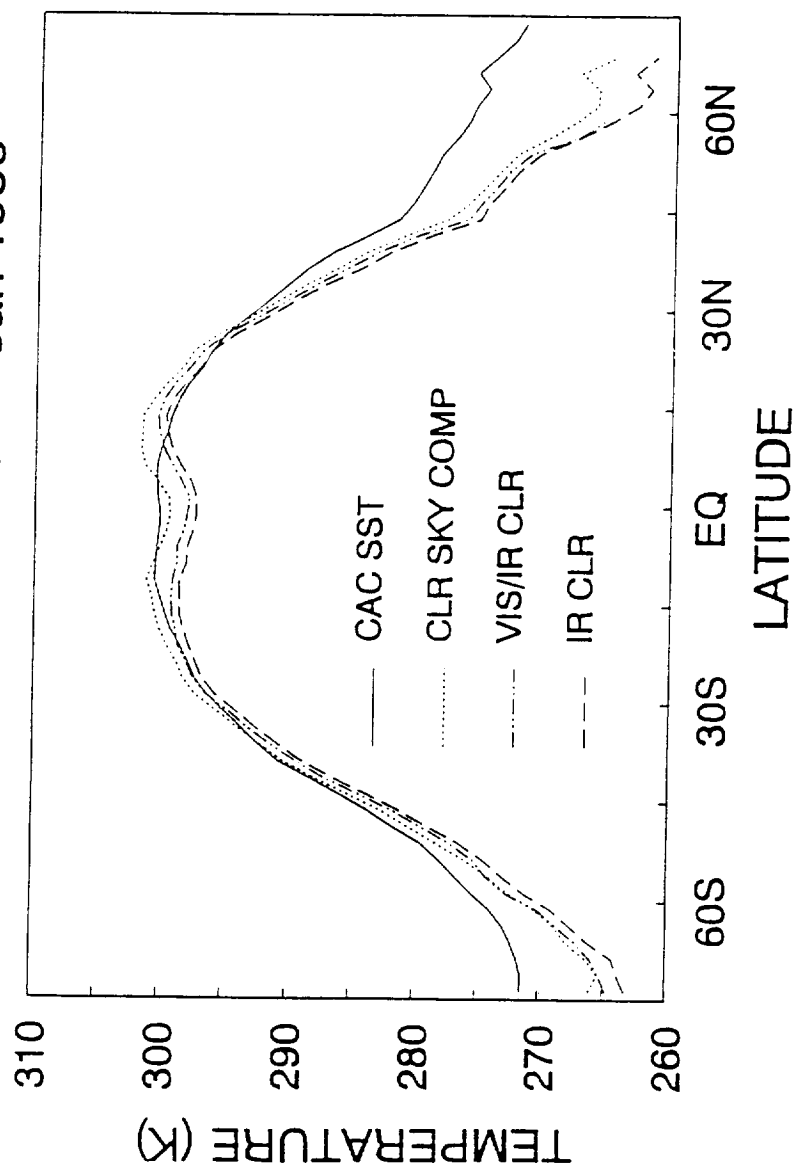


Figure 5

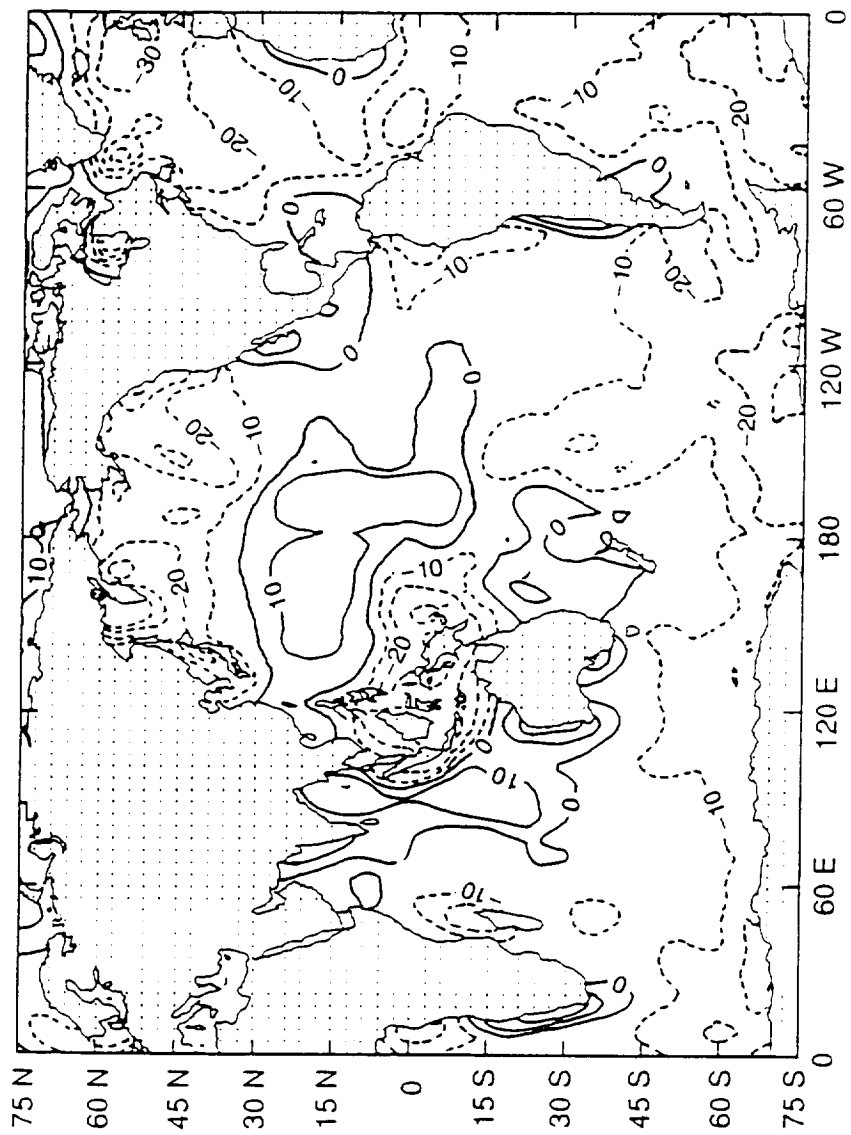


Figure 6

Clear Sky Net Upward Longwave Flux at the Surface
(W m^{-2})

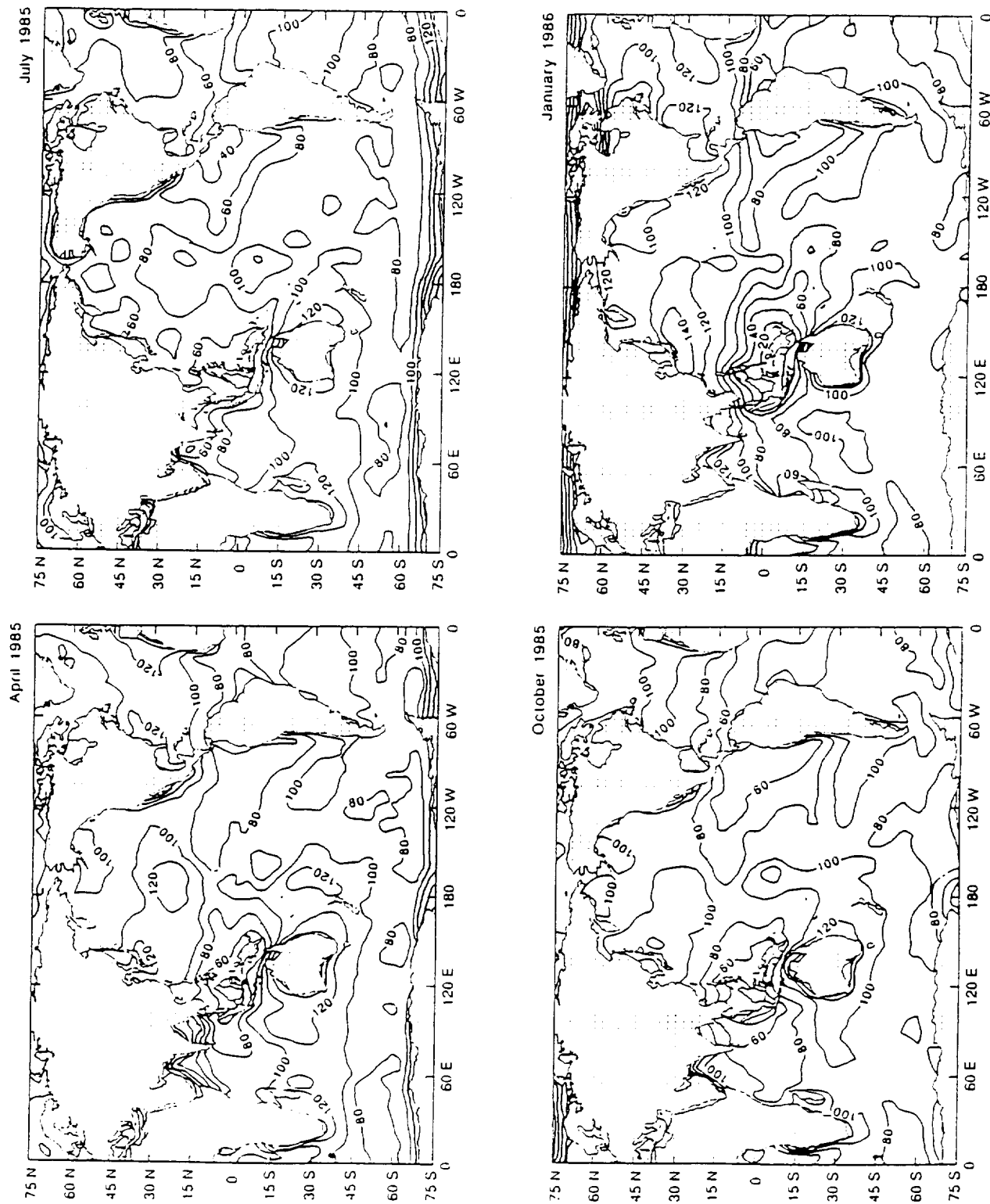


Figure 7

Atmospheric Net Upward Longwave Flux at the Surface

(W m^{-2})

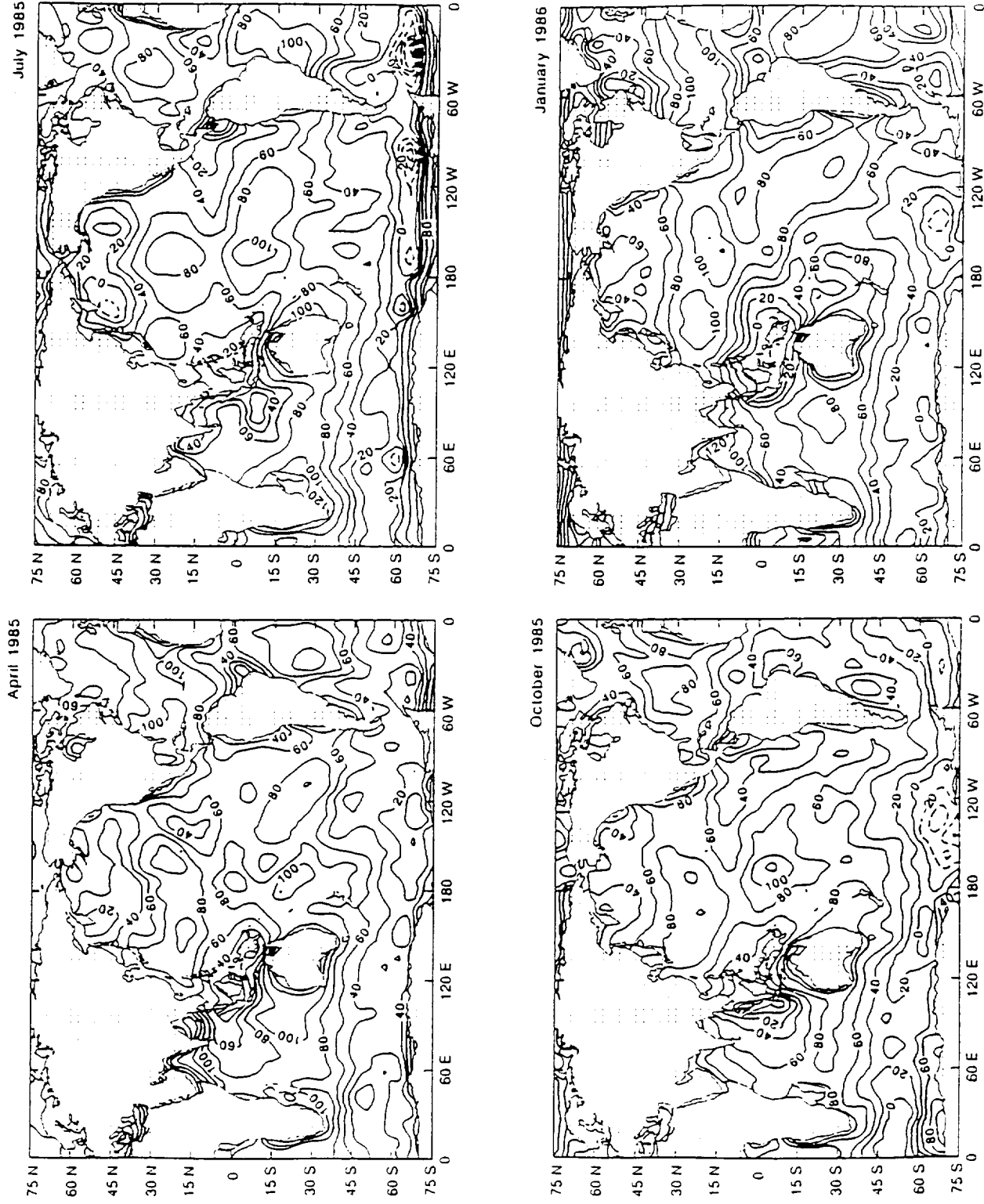
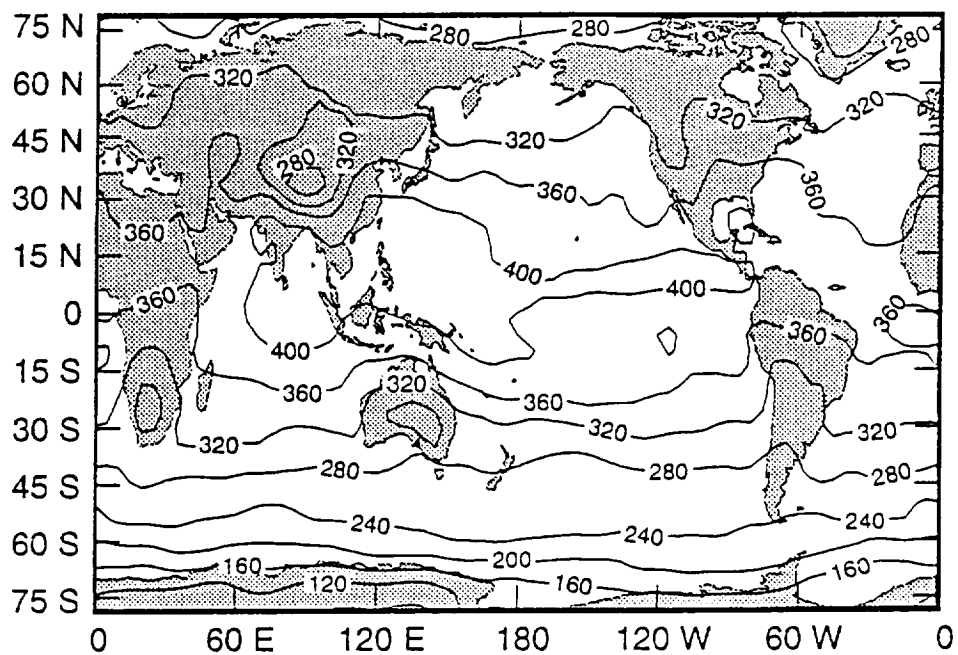


Figure 8

(a)

Wu & Cheng

July 1979



(b)

Wu & Cheng

July 1979

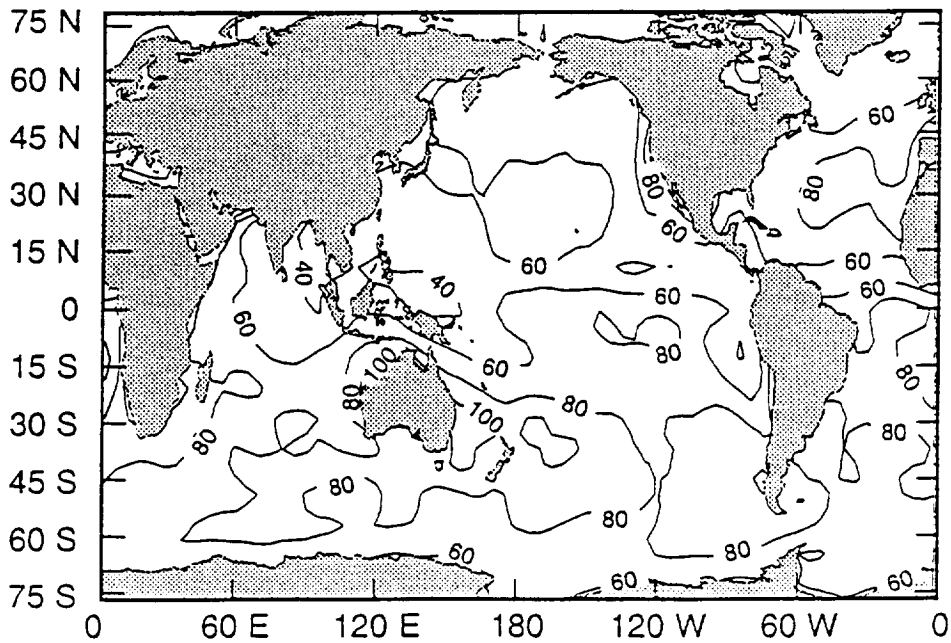


Figure 9

Technical Report

Section 3

Parameterization of atmospheric radiation transport.

Comparative Accuracy of Diffuse Radiative Properties Computed Using Selected Multiple Scattering Approximations

HARSHVARDHAN

Department of Earth and Atmospheric Sciences, Purdue University, West Lafayette, Indiana

MICHAEL D. KING

Laboratory for Atmospheres, NASA/Goddard Space Flight Center, Greenbelt, Maryland

(Manuscript received 15 November 1991, in final form 7 April 1992)

ABSTRACT

Computational results have been obtained for the spherical albedo, global transmission, and global absorption of plane-parallel layers composed of cloud droplets. These computations, obtained using the doubling method for the entire range of single scattering albedos ($0 \leq \omega_0 \leq 1$) and for optical depths between 0.1 and 100, are compared with corresponding results obtained using selected multiple scattering approximations. Both the relative and absolute accuracies of asymptotic theory for thick layers, three diffuse two-stream approximations, and two integrated two-stream approximations are presented as a function of optical thickness and single scattering albedo for a scattering phase function representative of cloud droplets at visible wavelengths. The spherical albedo and global absorption computed using asymptotic theory are found to be accurate to better than 5% for all values of the single scattering albedo, provided the optical thickness exceeds about 2. The diffuse two-stream approximations have relative accuracies that are much worse than 5% for the spherical albedo over most of the parameter space, yet are accurate to within 5% in the global absorption when the absorption is significant. The integrated delta-Eddington scheme appears to be the most suitable model over the entire range of variables, generally producing relative errors of less than 5% in both the spherical albedo and global absorption.

1. Introduction

The role of clouds in determining the earth's radiation budget has led to increased interest in the parameterization of the radiative properties of cloud layers in numerical atmospheric models. Recent work has been concerned with relating cloud microphysics to optical properties (Slingo 1989) that can then be used in radiative transfer schemes within models. Most models now use some form of approximation to compute cloud radiative properties, such as the plane albedo from a given set of optical properties (optical thickness, single scattering albedo, etc.). Whereas in the past these optical properties were generally fixed, there is now increasing use of interactive schemes in which cloud optical properties are generated internally by the model (Charlock and Ramanathan 1985; Harshvardhan et al. 1989).

As cloud fields evolve during a model integration, the optical properties of the generated clouds and models of gaseous absorption are used in a radiative-transfer scheme to provide the shortwave and longwave

radiative-energy field through the atmosphere. These computations need to be carried out at each model grid point at least every time the model cloud fields are updated. In models that resolve the diurnal cycle, this could be every three hours of simulated time, or even hourly. The computational burden is such that rapid, yet accurate, techniques are essential. In the shortwave, a common procedure is the computation of cloud-layer properties by a two-stream method and the adding of radiative fluxes through the atmosphere in an energy-conserving scheme (Lacis and Hansen 1974; Coakley et al. 1983; Charlock and Ramanathan 1985; Geleyn and Hollingsworth 1979; Harshvardhan et al. 1987), although the two-stream equations can also be solved directly for multiple layers using matrix solvers (Wiscombe 1977; Toon et al. 1989). The flux adding method is essentially a severely truncated form of the adding-doubling method (Hansen and Travis 1974), using upward and downward fluxes instead of intensities.

In order to compute radiative fluxes through several atmospheric layers by the flux adding method, the radiative properties of cloud layers for two different sources are required (Harshvardhan et al. 1987; Kiehl et al. 1987). When collimated solar radiation is incident on an isolated cloud layer at some zenith angle with respect to the vertical direction, the fluxes emergent

Corresponding author address: Dr. Harshvardhan, Purdue University, 1397 Civil Engineering Building, West Lafayette, IN 47907-1397.

from the layer in the upward and downward directions are determined by the plane albedo and total transmission of the layer, respectively. If the incident source is diffuse, the emergent flux may be obtained by an angular integration over the incident intensity field. In two-stream methods, the angular distribution of the incident intensity field is not resolved, and a common practice is to assume an isotropic diffuse source. For example, in a multilayer cloud system, the diffuse solar flux transmitted through the upper layer is the incident source for the lower layer. Also, in the case of a cloud layer overlying a reflecting ground surface, multiple reflections between the cloud and ground are considered by assuming an isotropic diffuse source at the bottom boundary of the cloud layer. These diffuse radiative properties have also been used in the past to provide estimates of global effects of aerosol layers (Chýlek and Coakley 1974). A comprehensive study of the accuracy of various multiple scattering approximations for the plane albedo, total transmission, and fractional absorption of isolated cloud layers corresponding to incident collimated radiation was presented by King and Harshvardhan (1986a,b). The present study complements the earlier one in assessing the accuracy of various approximations for calculating the radiative properties of cloud and aerosol layers for an incident isotropic diffuse source.

The presentation follows the organization of King and Harshvardhan (1986a, hereafter referred to as KH). Section 2 discusses multiple scattering calculations used to obtain the diffuse radiative properties of cloud layers of varying optical thicknesses and single scattering albedos. These computational results, obtained with the doubling method, will be considered the benchmark solutions with which various multiple scattering approximations will be compared. Section 3 introduces the asymptotic theory approximation and the general class of two-stream approximations that we will consider. Section 4 presents the results of the comparison between the approximate and exact results in terms of absolute and relative differences. A discussion of the results follows in section 5. Section 6 is a summary including recommendations for using these approximations.

2. Multiple scattering computations

To assess the accuracy of various multiple scattering approximations, radiative transfer computations were performed using the doubling method described by Hansen and Travis (1974), together with the invariant embedding initialization described by King (1983). These computations were performed for a cloud drop size distribution typical of fair weather cumulus (FWC) clouds (Hansen 1971), and were performed at a wavelength $\lambda = 0.754 \mu\text{m}$ assuming a refractive index of liquid water $m = 1.332$. A detailed description of the cloud model, together with an illustration of the single

scattering phase function, can be found in KH. The azimuth-independent terms of the reflection and transmission functions were used to obtain the plane albedo $r(\tau_i, \mu_0)$ and total transmission $t(\tau_i, \mu_0)$ as a function of τ_i , the total optical thickness of the layer, and μ_0 , the cosine of the solar zenith angle. In terms of these functions the spherical albedo, global transmission, and global absorption of the layer are given by

$$\bar{r}(\tau_i) = 2 \int_0^1 r(\tau_i, \mu_0) \mu_0 d\mu_0, \quad (1)$$

$$\bar{t}(\tau_i) = 2 \int_0^1 t(\tau_i, \mu_0) \mu_0 d\mu_0, \quad (2)$$

$$\bar{a}(\tau_i) = 1 - \bar{r}(\tau_i) - \bar{t}(\tau_i); \quad (3)$$

In order to cover a wide range of applications, these computations were performed for values of the single scattering albedo ranging from pure absorption ($\omega_0 = 0$) to conservative scattering ($\omega_0 = 1$). The single scattering phase function was left unchanged such that all computations apply to a phase function having an asymmetry factor $g = 0.843$.

Figure 1 illustrates numerical computations of the spherical albedo $[\bar{r}(\tau_i)]$, global transmission $[\bar{t}(\tau_i)]$, and global absorption $[\bar{a}(\tau_i)]$ as a function of ω_0 and τ_i . The doubling computations used to generate these results were obtained at 12 optical depths 0.0625, 0.125, ..., 128 interleaved with another set of 11 optical depths 0.0884, 0.1768, ..., 90.51. Each set of doubling computations was itself made at each of 31 values of the single scattering albedo. The single scattering albedo scale is linear in the similarity parameter s , defined by

$$s = \left(\frac{1 - \omega_0}{1 - \omega_0 g} \right)^{1/2}. \quad (4)$$

This makes it possible to expand the scale in the vicinity of conservative scattering ($\omega_0 = 1$) and still to span the full range $0 \leq \omega_0 \leq 1$. The angular computations, including the integration in (1) and (2), were performed at 80 Gaussian quadrature points. As in KH, the computed results were first interpolated to generate a 300×300 matrix prior to plotting. The interpolated arrays represent the exact results to which the radiative transfer approximations are compared in section 4.

It is perhaps pertinent to point out certain features of the radiative properties illustrated in Fig. 1. For conservative or very weakly absorbing layers, the spherical albedo increases rapidly with increasing optical thickness for small values of τ_i and then much more slowly as τ_i becomes large. This is the well-known nonlinear behavior that leads to problems in estimating area-averaged albedos for a nonhomogeneous cloud layer (Harshvardhan and Randall 1985). For moderate to strong absorption, the saturation of both the spherical

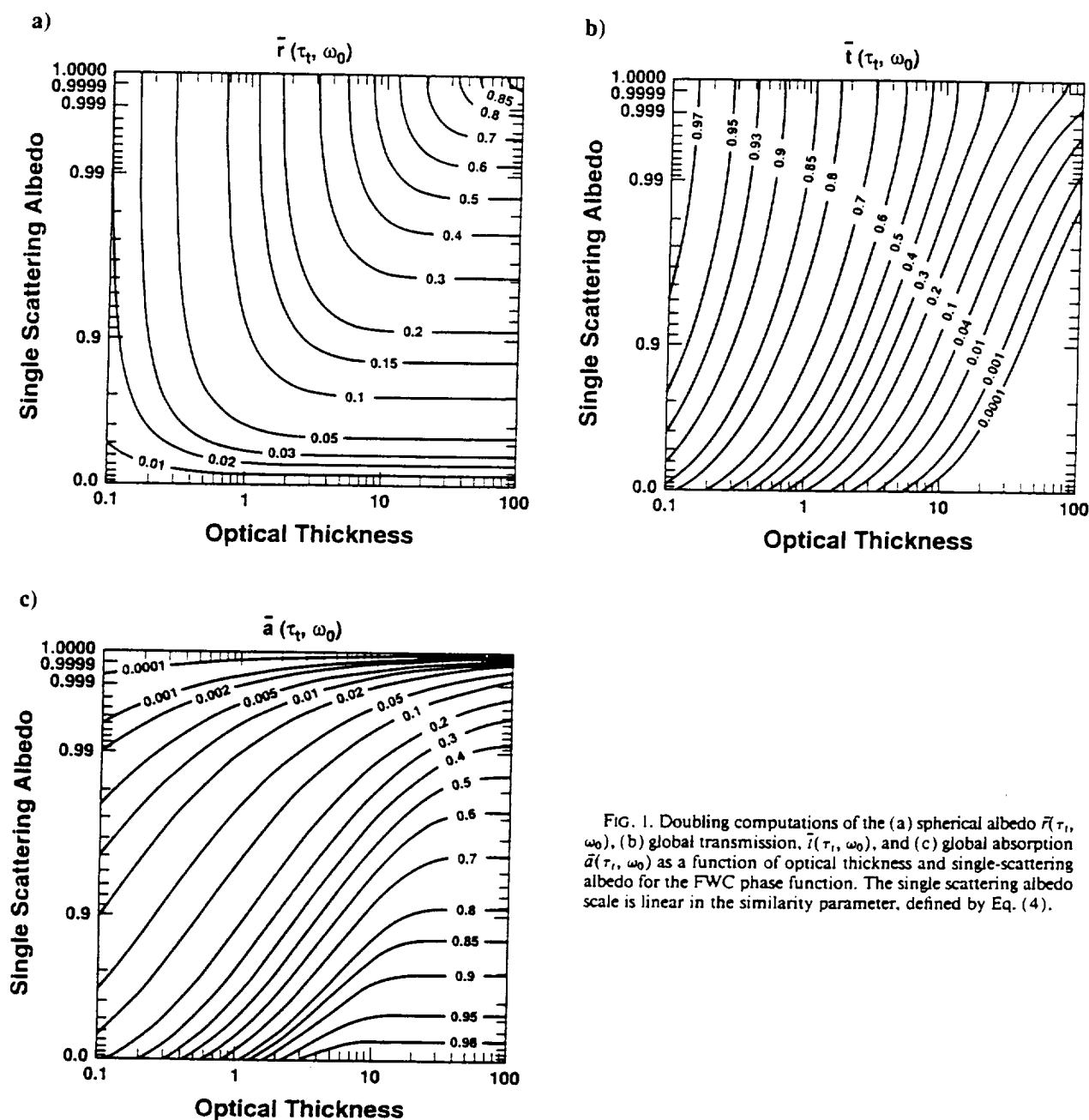


FIG. 1. Doubling computations of the (a) spherical albedo $\bar{r}(\tau_t, \omega_0)$, (b) global transmission, $\bar{t}(\tau_t, \omega_0)$, and (c) global absorption $\bar{a}(\tau_t, \omega_0)$ as a function of optical thickness and single-scattering albedo for the FWC phase function. The single scattering albedo scale is linear in the similarity parameter, defined by Eq. (4).

albedo and global absorption at optical thicknesses of about 10 or even less is the most striking feature of Fig. 1. In the near-infrared, this implies that cloud absorption is primarily a function of the single scattering albedo and not the optical thickness once the cloud layer is several hundred meters thick (Twomey 1976). The importance of determining the spectral dependence of ω_0 for cloud layers and the development of accurate parameterizations for inclusion in radiative transfer models follows from this observation (King et al. 1990; Fouquart et al. 1991).

3. Radiative-transfer approximations

Three classes of approximations will be considered here for comparison with the multiple scattering results presented above. In all cases, analytic or easily integrable functions relate the radiative properties to the optical properties. The three approximations we will consider are asymptotic theory for thick layers, diffuse two-stream approximations, and integrated two-stream approximations. Although there are several variations of two-stream approximations, only a few common and representative models will be considered.

a. Asymptotic theory

Asymptotic theory is a rigorous solution to the equation of transfer in optically thick layers, and as such, makes no assumption about the angular distribution of scattered radiation within the medium. Expressions for the plane albedo and total transmission of an optically thick layer under collimated illumination conditions can be found in KH and will not be repeated here. From these expressions, it can be shown that the asymptotic theory approximations for the spherical albedo $[\hat{r}(\tau_i)]$, global transmission $[\hat{i}(\tau_i)]$, and global absorption $[\hat{a}(\tau_i)]$ are given by

$$\hat{r}(\tau_i) = \bar{r}_\infty - \frac{mn^2 e^{-2k\tau_i}}{1 - l^2 e^{-2k\tau_i}}, \quad (5)$$

$$\hat{i}(\tau_i) = \frac{mn^2 e^{-k\tau_i}}{1 - l^2 e^{-2k\tau_i}}, \quad (6)$$

$$\hat{a}(\tau_i) = 1 - \hat{r}(\tau_i) - \hat{i}(\tau_i), \quad (7)$$

for nonconservative scattering ($\omega_0 < 1$). In these expressions, \bar{r}_∞ is the spherical albedo of a semi-infinite atmosphere and m , n , l , and k are constants (coefficients) that depend primarily on the similarity parameter given by (4). All of the functions and constants that appear in these expressions can be computed by equating asymptotic formulas and doubling results at three values of the optical thickness for which asymptotic theory is valid (viz., $\tau_i = 8, 16$, and 32), as first pointed out by van de Hulst (1968). Similarity relations for calculating \bar{r}_∞ (denoted A^* by van de Hulst 1968), m , n , l , and k as a function of s for the full range $0 \leq s \leq 1$ can be found in Table 1 of King et al. (1990). Once these coefficients have been computed, expressions for all of the radiative properties are analytic functions that can be computed rapidly within a radiative transfer code.

For the special case of conservative scattering ($\omega_0 = 1$), Eqs. (5) and (6) reduce to

$$\hat{r}(\tau_i) = 1 - \frac{4}{3(1-g)(\tau_i + 2q_0)}, \quad (8)$$

$$\hat{i}(\tau_i) = \frac{4}{3(1-g)(\tau_i + 2q_0)}, \quad (9)$$

where q_0 is the extrapolation length. The reduced extrapolation length $q' = (1-g)q_0$ is known to range between 0.709 and 0.715 for all possible phase functions (van de Hulst 1980), and has the value $q' = 0.715$ for the phase function used here. Again, one is left with simple analytic functions describing the variation of $\hat{r}(\tau_i)$ and $\hat{i}(\tau_i)$ as a function of τ_i for a given asymmetry factor g . The set of equations (5)–(9) forms the approximations for the diffuse radiative properties of a medium based on asymptotic theory.

b. Diffuse two-stream approximations

In the absence of any direct collimated beam, the two-stream equations of radiative transfer result in a

set of differential equations for the upward and downward diffuse fluxes $F^\pm(\tau)$ (Coakley and Chýlek 1975; Meador and Weaver 1980)

$$\frac{dF^-(\tau)}{d\tau} = \gamma_1 F^-(\tau) - \gamma_2 F^+(\tau), \quad (10)$$

$$\frac{dF^+(\tau)}{d\tau} = \gamma_2 F^-(\tau) - \gamma_1 F^+(\tau), \quad (11)$$

where $F^-(\tau)$ represents the upward flux and $F^+(\tau)$ the downward flux at optical depth τ . The equations can easily be solved subject to the boundary conditions

$$F^+(0) = F_0, \quad (12)$$

$$F^-(\tau_i) = 0, \quad (13)$$

for a diffuse isotropic source incident at the top boundary of the layer (or cloud) and for which no illumination is incident from below. The spherical albedo is thus obtained from the expression

$$\hat{r}(\tau_i) = F^-(0)/F_0, \quad (14)$$

and the global transmission from

$$\hat{i}(\tau_i) = F^+(\tau_i)/F_0. \quad (15)$$

For nonconservative scattering ($\omega_0 < 1$), the solution may be obtained in the form (Coakley and Chýlek 1975; Meador and Weaver 1980)

$$\hat{r}(\tau_i) = \frac{\gamma_2(1 - e^{-2k\tau_i})}{k + \gamma_1 + (k - \gamma_1)e^{-2k\tau_i}}, \quad (16)$$

$$\hat{i}(\tau_i) = \frac{2ke^{-k\tau_i}}{k + \gamma_1 + (k - \gamma_1)e^{-2k\tau_i}}, \quad (17)$$

and for conservative scattering ($\omega_0 = 1$)

$$\hat{r}(\tau_i) = \frac{\gamma_1 \tau_i}{1 + \gamma_1 \tau_i}, \quad (18)$$

$$\hat{i}(\tau_i) = 1 - \hat{r}(\tau_i). \quad (19)$$

In (16)–(19), the coefficients γ_1 and γ_2 depend on the particular two-stream approximation, with the diffusion exponent k defined as

$$k = (\gamma_1^2 - \gamma_2^2)^{1/2}. \quad (20)$$

Table 1 lists three diffuse two-stream models used for this study and the corresponding values of γ_1 and γ_2 . The discrete ordinates model is identified as the quadrature scheme by Meador and Weaver (1980) and Toon et al. (1989). The hemispheric-mean model defined by Toon et al. (1989) is similar to the Coakley–Chýlek model II referred to by KH and first introduced by Chýlek and Coakley (1974). The two-stream model used by Sagan and Pollack (1967) has coefficients similar to those of both of the aforementioned models. Instead of the asymmetry parameter g , some two-stream models use the average backscatter fraction $\bar{\beta}$, which is defined in KH and readily computed from the backscatter fraction $\beta(\mu_0)$, introduced by Coakley

and Chýlek (1975) and Zdunkowski et al. (1980) to compute the radiative properties of layers for collimated incident sources. The Eddington model has, of course, been used widely (Shettle and Weinman 1970). The set of equations (16)–(20) is used to compute the diffuse radiative properties for the two-stream approximations. It should be noted that these expressions have fairly simple analytic forms that favor rapid computation.

c. Integrated two-stream approximations

Extensive discussion of two-stream approximations for a collimated source can be found in KH as well as in earlier work, in particular the comprehensive treatment by Meador and Weaver (1980). Expressions for the approximate plane albedo [$\hat{r}(\tau_i, \mu_0)$], total transmission [$\hat{t}(\tau_i, \mu_0)$], and fractional absorption [$\hat{a}(\tau_i, \mu_0)$] are the set of equations (21)–(29) in KH. These expressions include the transformations that are required in the case of delta scaling (Joseph et al. 1976). To obtain comparable expressions for the diffuse radiative properties, $\hat{r}(\tau_i, \mu_0)$ and $\hat{t}(\tau_i, \mu_0)$ must be integrated according to Eqs. (1) and (2). These expressions, however, are quite complicated, and thus integration in a closed form is not generally practical.

An analytic expression for the spherical albedo in the Eddington and delta-Eddington approximations has been obtained by Wiscombe and Warren (1980) and involves exponential integrals that are not conducive to rapid computation within a model. For this study, $\hat{r}(\tau_i, \mu_0)$ and $\hat{t}(\tau_i, \mu_0)$ obtained by the delta-Eddington approximation were numerically integrated to provide $\bar{r}(\tau_i)$ and $\bar{t}(\tau_i)$. King and Harshvardhan found that the delta-Eddington approximation for collimated illumination conditions is quite accurate over a wide range of τ_i and μ_0 , especially when ω_0 is near unity. A model that performs well for optically thin layers over the limited range of ω_0 studied by KH is the plane albedo scheme of Coakley and Chýlek (1975), designated Coakley–Chýlek model I by KH. Two-stream methods for collimated sources require a third coefficient, γ_3 , which appears with the source term and is thus not included in Eqs. (10) and (11). The

expressions for γ_3 used by the two integrated models presented here are given in Table 1.

The integrations in Eqs. (1) and (2) required to obtain the diffuse properties are performed using 80-point Gaussian quadrature, and the results should be considered identical to an analytic solution for all practical purposes. The general form of the quadrature summation is

$$\bar{f}(\tau_i) = 2 \sum_{i=1}^N r(\tau_i, \mu_i) \mu_i w_i, \quad (21)$$

where μ_i are the Gaussian quadrature points on the half space and w_i are the corresponding Gaussian weights. This detailed integration, however, is of no practical value because the computational burden is onerous when applied to a global climate model. We have, therefore, also included results for the delta-Eddington and Coakley–Chýlek (I) models integrated using two-point and four-point quadrature, respectively. The diffuse radiative properties can then be obtained with a computational effort comparable to that required to compute properties for collimated radiation.

4. Results

We have examined both the absolute and relative accuracies of the spherical albedo, global transmission, and global absorption as a function of τ_i and ω_0 for the asymptotic approximation, as well as the Eddington, discrete ordinates, and hemispheric-mean diffuse two-stream approximations. Other diffuse two-stream approximations that we have examined generally yield somewhat poorer results when compared to our doubling benchmark calculations. In addition, we have considered the integrated delta-Eddington and Coakley–Chýlek (I) approximations computed using both 80 points and a limited number of Gaussian quadrature points for integration over the solar zenith angle.

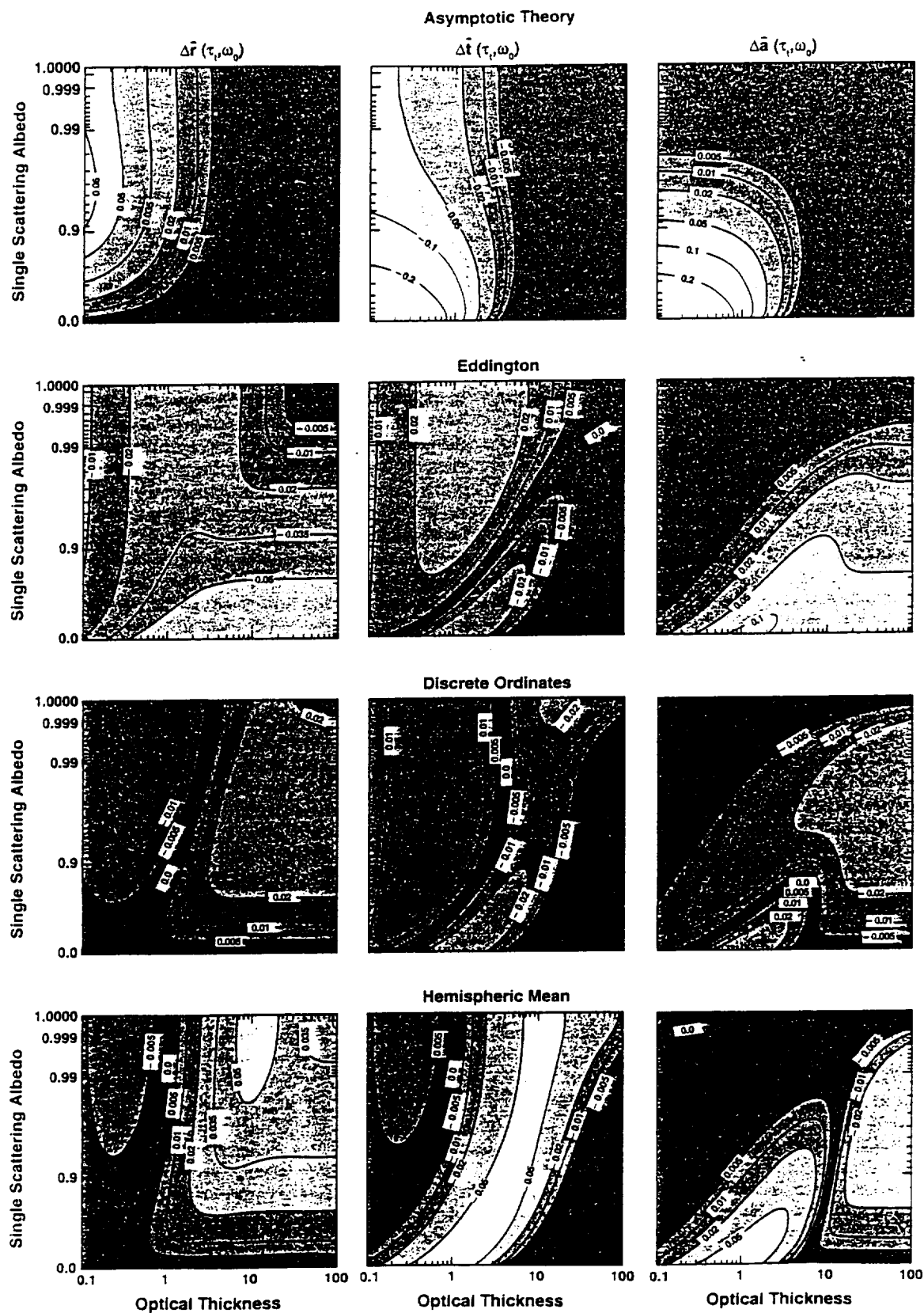
Figure 2 illustrates a 4×3 plot composite of results for the absolute difference in the spherical albedo, global transmission, and global absorption for four of these models, where the first row applies to asymptotic theory and succeeding rows to the Eddington, discrete

TABLE 1. Summary of γ_i coefficients in selected two-stream approximations.

Method	γ_1	γ_2	γ_3
<i>Diffuse</i>			
Eddington	$1/4[7 - \omega_0(4 + 3g)]$	$-1/4[1 - \omega_0(4 - 3g)]$	—
Discrete ordinates	$\sqrt{3}/2[2 - \omega_0(1 + g)]$	$\sqrt{3}/2[\omega_0(1 - g)]$	—
Hemispheric mean	$2 - \omega_0(1 + g)$	$\omega_0(1 - g)$	—
<i>Integrated</i>			
Delta-Eddington	$1/4[7 - \omega'_0(4 + 3g')]$	$-1/4[1 - \omega'_0(4 - 3g')]$	$1/4(2 - 3g'\mu_0)$
Coakley–Chýlek (I)	$\{1 - \omega_0[1 - \beta(\mu_0)]\}/\mu_0$	$\omega_0\beta(\mu_0)/\mu_0$	$\beta(\mu_0)$

$$\omega'_0 = (1 - g^2)\omega_0/(1 - \omega_0g^2)$$

$$g' = g/(1 + g)$$



ordinates, and hemispheric-mean approximations. Individual plots in the first column of Fig. 1 represent absolute errors in the spherical albedo, defined as

$$\Delta \bar{F}(\tau_i, \omega_0) = \bar{F}(\tau_i, \omega_0) - \bar{F}(\tau_i, \omega_0), \quad (22)$$

with succeeding columns representing corresponding errors in global transmission [$\Delta \bar{I}(\tau_i, \omega_0)$] and global absorption [$\Delta \bar{a}(\tau_i, \omega_0)$]. With these definitions, positive (negative) errors indicate that the radiative transfer approximation overestimates (underestimates) the exact solution, taken as the computational results presented in Fig. 1. The relative errors in the spherical albedo, global transmission, and global absorption are presented in Fig. 3, and are given in percent. It is necessary to consider the performance of a particular model in both a relative and an absolute sense in order to delineate a range of acceptability.

Individual contour plots in Figs. 2 and 3 have been shaded to draw attention to those regions of greatest accuracy. For example, asymptotic theory is seen to be accurate to within 5% in reflection and absorption for $\tau_i \geq 2$ and for all values of ω_0 . In transmission, relative errors exceed 5% for $\omega_0 < 0.90$ and $2 \leq \tau_i < 8$, but the absolute errors are so small (< 0.03) that the approximation could probably still be used without serious adverse results. It is evident from Figs. 2 and 3 that the asymptotic approximation provides accurate results for all three diffuse radiative properties over the entire range of ω_0 as long as $\tau_i \geq 2$.

The three diffuse two-stream models considered here are seen to yield unacceptable errors in one or more of the radiative properties over regions that would normally be encountered in modeling applications. Although the range of acceptability will depend on the particular application, one can consider a 5% error in the spherical albedo as a standard for comparison. The spherical albedo is usually the parameter of choice in estimating the sensitivity of any radiative perturbation. When the value itself is small, however, an absolute error criterion is more useful. For optically thin layers, the absolute errors in spherical albedo are generally less than 0.01 for the discrete ordinates and hemispheric-mean approximations. Errors in global transmission are similar for all three models, while the Eddington and hemispheric-mean models are successful in estimating the global absorption of a layer when $\omega_0 \geq 0.99$ and $\tau_i \leq 10$ with errors of less than 1%. If the range of acceptability is relaxed to 5%, then the Eddington and hemispheric-mean models can be used for absorption when ω_0 is as low as 0.95 except for optically thick layers. This covers the range of single scattering albedo encountered in water clouds throughout the visible and near-infrared spectrum (King et al. 1990).

The two integrated two-stream methods studied in this investigation provide more accurate results for all three diffuse radiative properties as shown in Figs. 4 and 5. The delta-Eddington model was shown by KH to be highly successful in estimating the plane albedo for conservative scattering. There was a marked degradation of performance when nonconservative cases were considered. The present study shows that this model, when integrated over an isotropic diffuse incident source, provides excellent results for the spherical albedo and global transmission over most of the range of τ_i and ω_0 . Errors in excess of 10% in global absorption are present for moderate optical depths ($0.5 \leq \tau_i \leq 5$) when ω_0 exceeds about 0.95. It may be seen from Fig. 4, however, that the absolute errors in global absorption are less than 0.02 throughout this region. In addition, the large relative error in global transmission for optically thick absorbing layers is irrelevant since the global transmission is itself close to zero, as is the absolute error. The Coakley-Chýlek (I) model provides results of comparable accuracy for optically thin layers. This is not surprising since KH showed that it was the most accurate of the two-stream models for this case. The delta-Eddington model, however, when integrated over all incident angles, is nearly as accurate as the Coakley-Chýlek (I) model for optically thin layers. Moreover, the accuracy of the integrated delta-Eddington model does not degrade as rapidly at higher optical depths.

As mentioned previously, these two models would only be of academic interest if a rigorous numerical integration were required for every computation of the diffuse radiative properties. We have, therefore, also presented results obtained using a limited number of quadrature points in the integration over solar zenith angle [cf. Eq. (21)]. As can be seen from the second panel of Figs. 4 and 5, a two-point integration of the delta-Eddington models yields accuracies that are comparable to the accuracy obtained using an 80-point integration. For the Coakley-Chýlek (I) model, however, it is necessary to use a four-point integration to obtain results that are of comparable accuracy.

5. Discussion

Although the results presented here are not exhaustive in the sense that all possible approximations have not been tested, we feel they are representative of what one might expect for any class of model. All the schemes are computationally efficient, and it is not necessary to perform a rigorous integration for the models based on incident collimated sources. The approximations presented here can be incorporated into

FIG. 2. Absolute accuracy of asymptotic theory, Eddington, discrete ordinates and hemispheric-mean approximations to the spherical albedo, global transmission and global absorption as a function of optical thickness and single scattering albedo. The FWC phase function is assumed throughout.

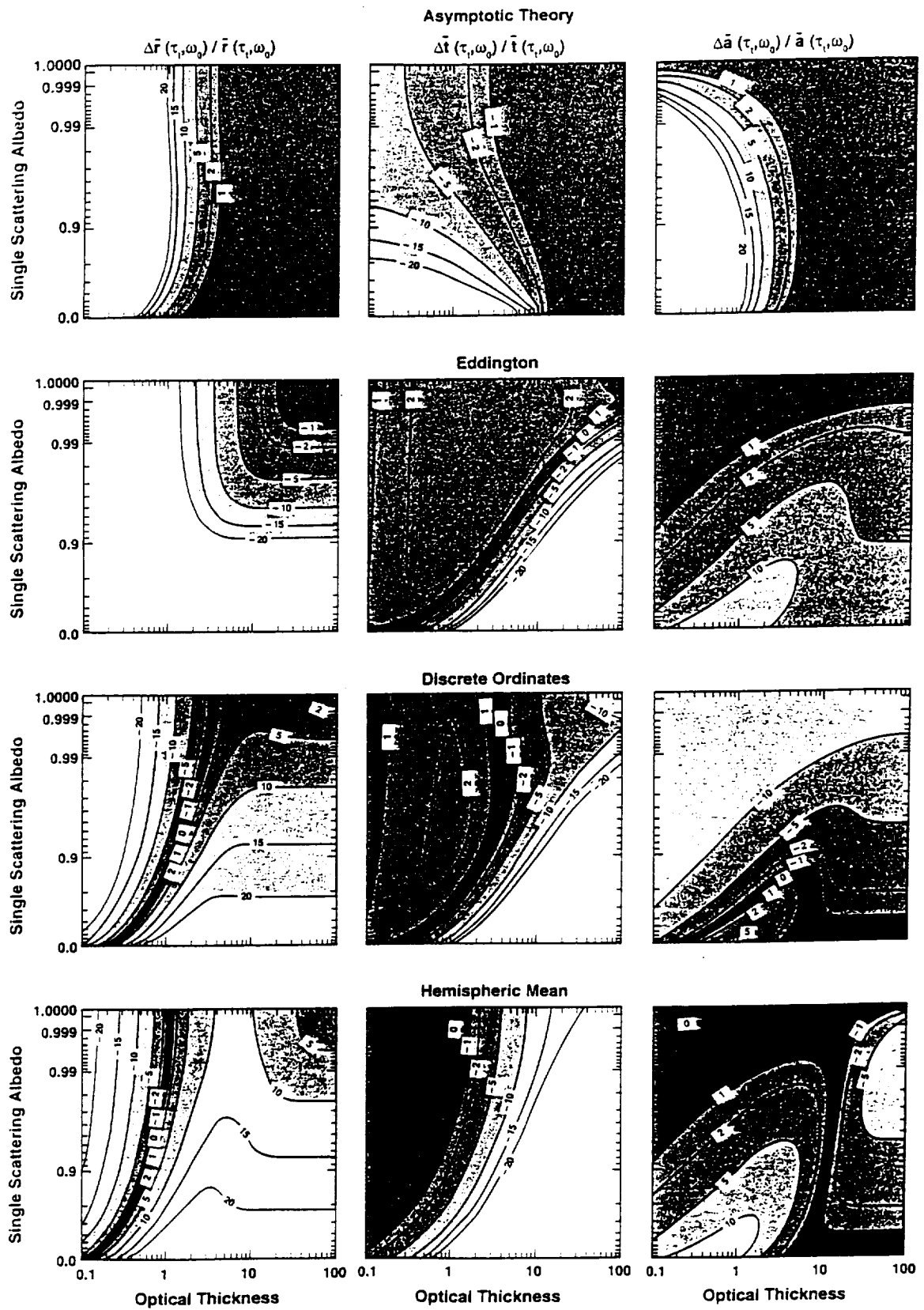


FIG. 3. As in Fig. 2 except for relative accuracies (in percent).

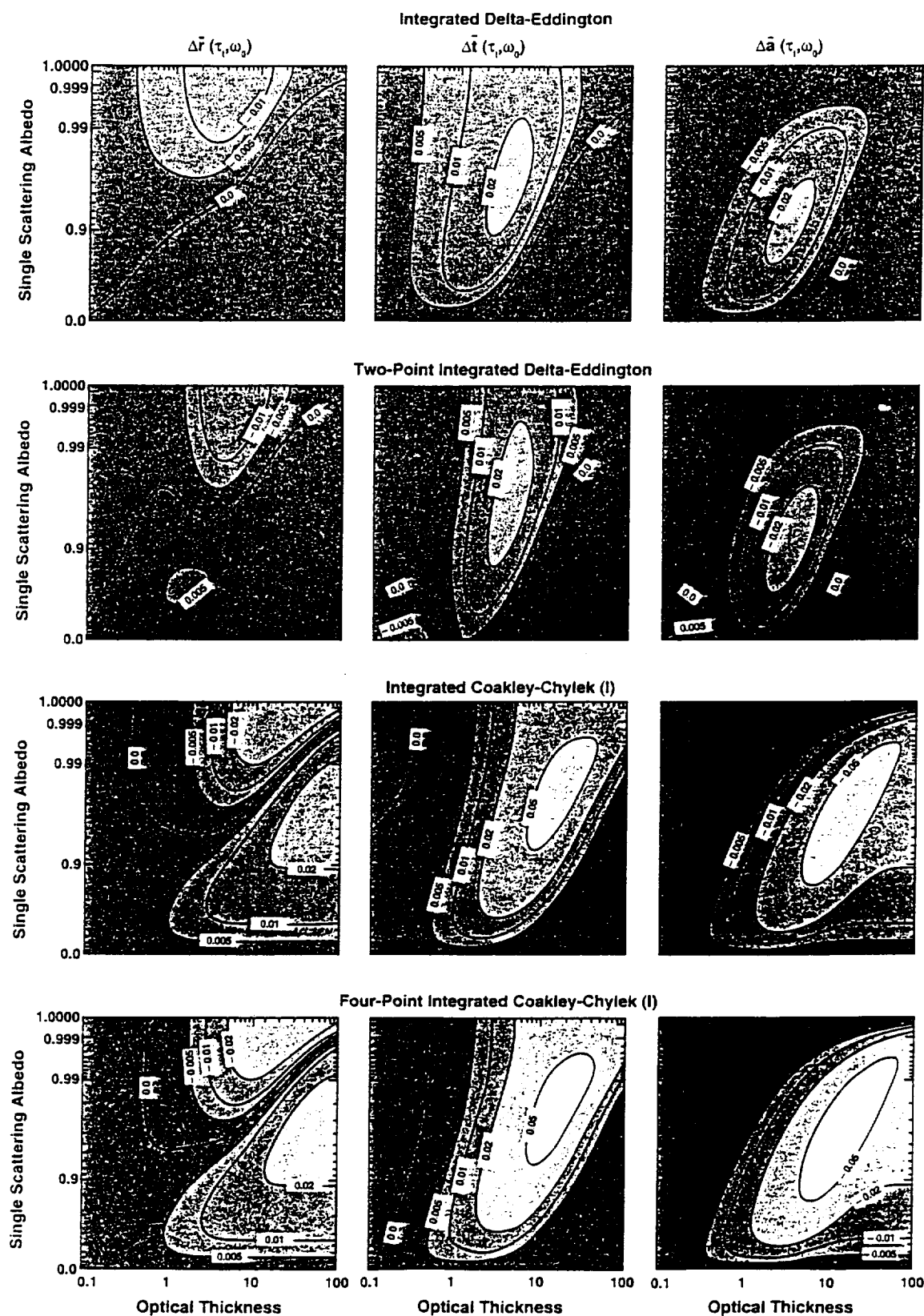


FIG. 4. As in Fig. 2 but for the integrated delta-Eddington, two-point-integrated delta-Eddington, integrated Coakley-Chylek (I), and four-point integrated Coakley-Chylek (I) approximations.

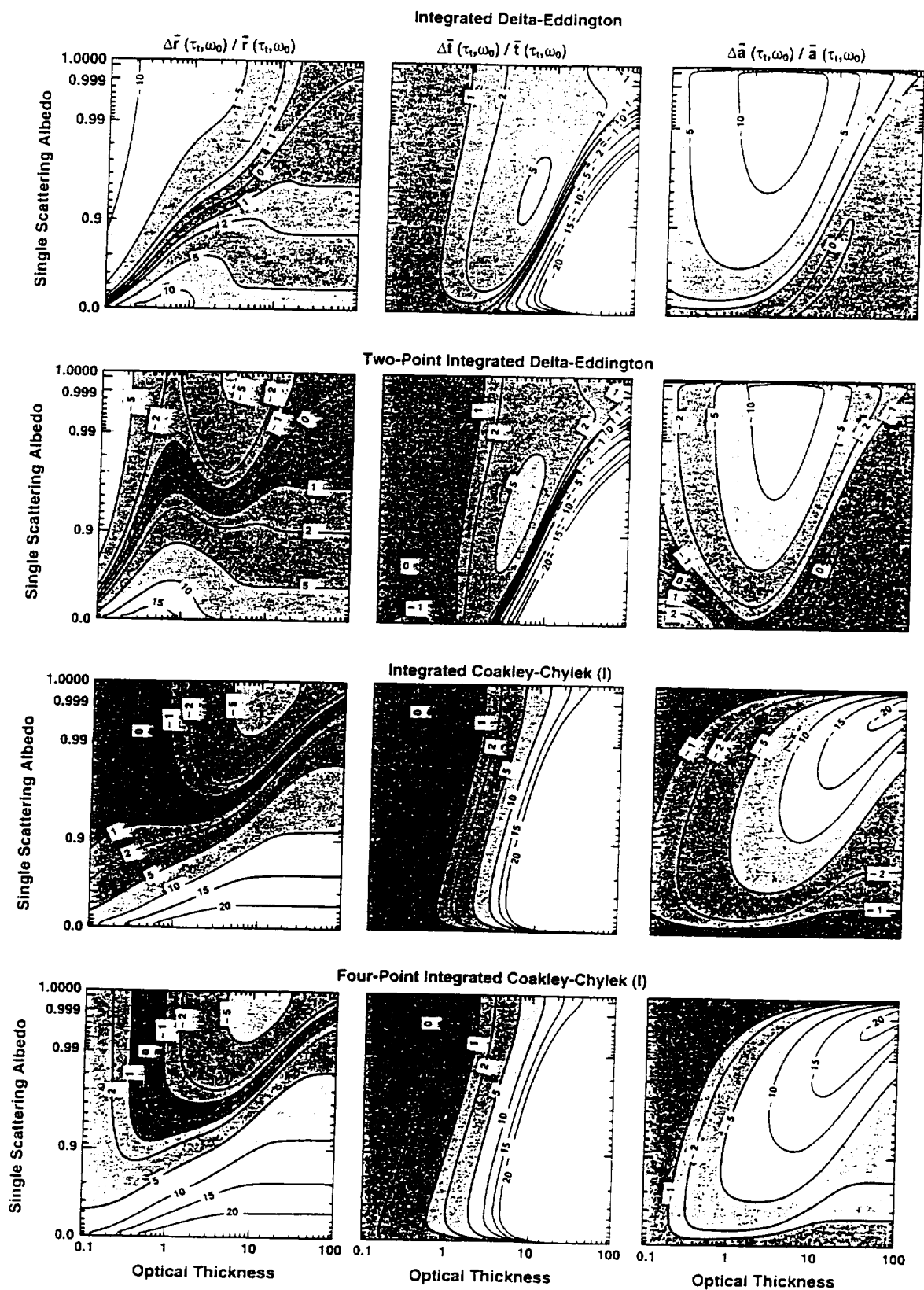


FIG. 5. As in Fig. 4 except for relative accuracies (in percent).

a multilayer radiative transfer module that may be added to the radiation code in a numerical model.

All computations presented here were obtained for a FWC drop size distribution having an asymmetry factor $g = 0.843$. Variations along the ω_0 axis can therefore be viewed as representing the effect of altering the gaseous absorption in the layer at a particular wavelength, or to some extent, variations in the wavelength if g does not vary too greatly. This would cover the solar near-infrared spectrum over which $(1 - \omega_0)$ varies by several orders of magnitude, while g generally lies between 0.80 and 0.90 (cf. King et al. 1990).

As found by KH for collimated radiative properties, the asymptotic approximation yields consistently excellent results for optically thick layers, regardless of single scattering albedo and solar zenith angle. Figures 2 and 3 show that the same is true for the diffuse radiative properties as long as $\tau_i \geq 2$. In a numerical model with internally generated cloud optical properties, this requirement will not always be met. Errors become unacceptably large when $\tau_i < 1$. For this reason, the asymptotic approximation should only be used when it is known a priori that $\tau_i \geq 2$ at all times. This is the one serious shortcoming of an otherwise simple and accurate model. The method also requires a pre-computed table of coefficients m , n , k , l , and \bar{r}_∞ , or analytic forms that compute these quantities within the program. Analytic expressions for these coefficients in terms of the similarity parameter can be found in King et al. (1990), which further discusses a remote sensing application of asymptotic theory.

The three diffuse two-stream models presented here are the simplest to implement in a numerical atmospheric model and are the most computationally efficient, but their accuracy is limited to certain regions of the parameter space. They are also not uniformly accurate for all three radiative properties. This is especially true in the Eddington approximation, where the spherical albedo is frequently too inaccurate to be of any value in a numerical model. In addition, the Eddington model yields unphysical values of the spherical albedo and global absorption when absorption is very large (King and Harshvardhan 1986b). This situation arises occasionally in the water vapor bands of the near-infrared and frequently in the thermal infrared. The problem can be rectified in a computer code with the addition of a check for unphysical values that could then be forced to the condition of zero reflection. The discrete ordinates model does not suffer from this limitation and generally yields better results for the spherical albedo than does the Eddington approximation. The somewhat poorer results for global absorption are not too important since the absolute errors are small in this case. The hemispheric-mean model yields results very similar to the discrete ordinates model, except for global absorption. The smaller relative errors for weak absorption are an especially attractive feature of the hemispheric-mean model,

which otherwise suffers from the fact that it tends to overestimate the spherical albedo by more than 5% for the very important case of nearly conservative optically thick layers.

The integrated delta-Eddington model yields excellent results for all three radiative properties over the entire range of optical properties that are encountered in the radiation code of a numerical atmospheric model. In fact, errors in the diffuse radiative properties are generally smaller than the errors found by KH for collimated radiative properties, with no unphysical results anywhere in the parameter space. There has obviously been some cancellation of errors in the angular integration. As mentioned earlier, the one error-prone region is moderate optical thickness and weak absorption. This was also true for the errors in fractional absorption for a collimated source. Since the direct beam is usually handled by a delta-Eddington or similar approximation, the coefficients and functions used for this model are usually already present in a numerical model. There is, however, an extra computational overhead in the angular integration, in that planar properties need to be computed at several angles and then numerically integrated. As seen in Figs. 4 and 5, however, these computations need be carried out at only two points to yield results comparable to a detailed numerical integration.

The integrated Coakley-Chýlek (I) model is of limited value, except perhaps for optically thin, weakly absorbing layers. There is also an added computational burden since at least four angular computations are required for the phase function used here. For collimated radiative properties and for optically thin layers, KH found that this model was superior to the delta-Eddington model. For diffuse radiative properties, on the other hand, we find that there is little advantage in using the Coakley-Chýlek (I) model, even for optically thin layers.

6. Summary and recommendations

In the present study the spherical albedo, global transmission, and global absorption computed by various radiative transfer approximations have been compared with doubling computations as a function of optical thickness and single scattering albedo. Since the entire range of ω_0 has been considered for optical depths from 0.1 to 100, the results presented here can be utilized to decide which approximate method is the most accurate for a particular application. The results presented here should be considered in parallel with the findings of KH regarding the plane albedo, total transmission, and fractional absorption for a collimated incident source.

In order to summarize the results of this study, it is useful to present composite figures extracted from the individual figures to highlight regions of highest accuracy. Following van de Hulst (1980), we show in

Fig. 6 the regions for which a particular model is accurate to within 1% and 5%. Only those models that are reasonably accurate in the particular radiative property have been included. These models include asymptotic theory, the two-point delta-Eddington method, and the four-point Coakley-Chýlek (I) method. Although the hemispheric-mean model yields acceptable results for the global absorption, it is not included here because results for the spherical albedo are generally poor.

At the 1% (5%) level, asymptotic theory can be used for all ω_0 as long as $\tau_i \geq 3.5$ (2). For smaller optical depths, there is a choice that can be made between the delta-Eddington and Coakley-Chýlek (I) models, but our recommendation is to use the delta-Eddington method. Many general circulation models are already using this method to compute collimated radiative

properties, and the additional overhead incurred in the two-point integration should be minimal. If a scheme is needed to span the entire domain, the asymptotic method should not be used since its performance deteriorates very rapidly for $\tau_i \leq 3$. For this situation, typical of GCM applications, the integrated delta-Eddington scheme should yield acceptable results.

The overall errors for a multilayer cloud system over a reflecting surface will depend on the optical thickness and single scattering albedo of the individual layers. At present, it is felt that errors in parameterizing the band-averaged single scattering albedo of cloud layers in the near-infrared will dominate errors in approximating the radiative properties of individual layers (Fouquart et al. 1991). For example, the use of a single value of ω_0 to represent the entire solar near infrared can result in errors in the layer absorption of several

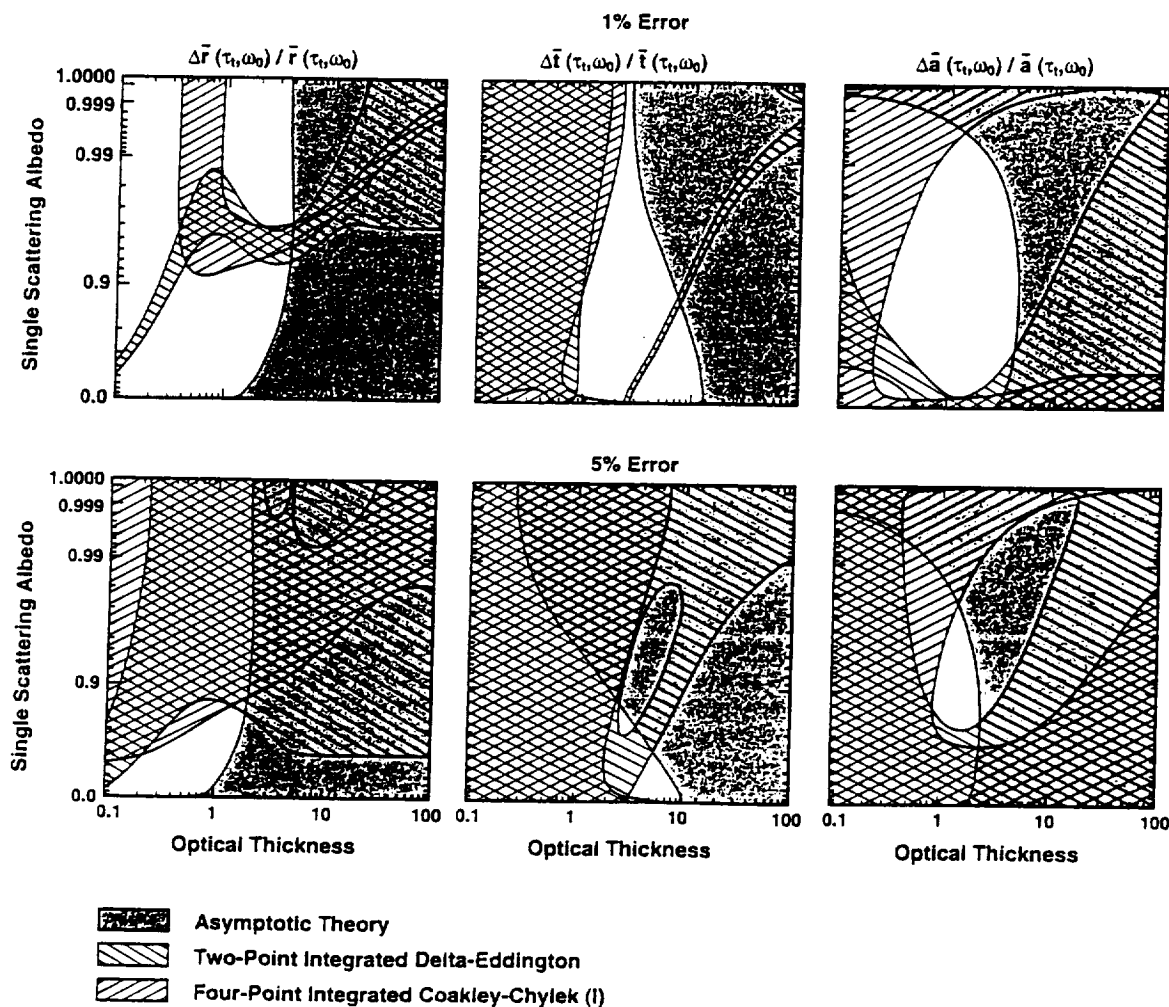


FIG. 6. The domain of validity of selected approximations to the diffuse radiative properties of cloud layers as a function of optical thickness (τ_i) and single scattering albedo (ω_0). The upper panels correspond to a relative accuracy of 1% and the lower panels to 5%. The single scattering albedo scale is linear in the similarity parameter. The FWC phase function is assumed throughout.

hundred percent (Slingo 1989). The sensitivity of all radiative properties to ω_0 can be appreciated by inspection of Fig. 1. Since any scheme has to limit the number of bands for computational efficiency, the selection of these bands and the average absorbing properties used could determine the overall accuracy. For a given set of τ_i and ω_0 , however, the results presented in this study could act as a guide for choosing an appropriate model. Finally, it is pertinent to mention that these accuracies refer to an idealized plane parallel model. There is, of course, the additional problem of representing inhomogeneous cloud systems including geometric effects (Harshvardhan and Thomas 1984; Stephens 1988), a problem not considered in this study.

Acknowledgments. The authors are grateful to Howard G. Meyer for aid in performing the computations, Tim Gilbert for the graphics, and Wanda Curtis for typing the manuscript. This study was supported by NSF Grant ATM-8909870, NASA Grant NAG 5-1125, and the NASA Radiation Processes Research Program.

REFERENCES

- Charlock, T. P., and V. Ramanathan, 1985: The albedo field and cloud radiative forcing produced by a general circulation model with internally generated cloud optics. *J. Atmos. Sci.*, **42**, 1408–1429.
- Chýlek, P., and J. A. Coakley, Jr., 1974: Aerosols and climate. *Science*, **183**, 75–77.
- Coakley, J. A., Jr., and P. Chýlek, 1975: The two-stream approximation in radiative transfer: Including the angle of the incident radiation. *J. Atmos. Sci.*, **32**, 409–418.
- , R. D. Cess, and F. B. Yurevich, 1983: The effect of tropospheric aerosols on the Earth's radiation budget: A parameterization for climate models. *J. Atmos. Sci.*, **40**, 116–138.
- Fouquart, Y., B. Bonnel, and V. Ramaswamy, 1991: Intercomparing shortwave radiation codes for climate studies. *J. Geophys. Res.*, **96**, 8955–8968.
- Geleyn, J. F., and A. Hollingsworth, 1979: An economical analytical method for the computation of the interaction between scattering and line absorption of radiation. *Contrib. Atmos. Phys.*, **52**, 1–16.
- Hansen, J. E., 1971: Multiple scattering of polarized light in planetary atmospheres. Part I: The doubling method. *J. Atmos. Sci.*, **36**, 508–518.
- , and L. D. Travis, 1974: Light scattering in planetary atmospheres. *Space Sci. Rev.*, **93**, 527–610.
- Harshvardhan, and R. W. L. Thomas, 1984: Solar reflection from interacting and shadowing cloud elements. *J. Geophys. Res.*, **89**, 7179–7185.
- , and D. A. Randall, 1985: Comments on "The parameterization of radiation for numerical weather prediction and climate models." *Mon. Wea. Rev.*, **113**, 1832–1833.
- , R. Davies, D. A. Randall, and T. G. Corsetti, 1987: A fast radiation parameterization for general circulation models. *J. Geophys. Res.*, **92**, 1009–1016.
- , D. A. Randall, T. G. Corsetti, and D. A. Dazlich, 1989: Earth radiation budget and cloudiness simulations with a general circulation model. *J. Atmos. Sci.*, **46**, 1922–1942.
- Joseph, J. H., W. J. Wiscombe, and J. A. Weinman, 1976: The delta-Eddington approximation for radiative flux transfer. *J. Atmos. Sci.*, **33**, 2452–2459.
- Kiehl, J. T., R. J. Wolski, B. P. Briegleb, and V. Ramanathan, 1987: Documentation of radiation and cloud routines in the NCAR Community Climate Model (CCM1). NCAR Tech. Note, NCAR/TN-228 + 1A, 109 pp.
- King, M. D., 1983: Number of terms required in the Fourier expansion of the reflection function for optically thick atmospheres. *J. Quant. Spectrosc. Radiat. Transfer*, **30**, 143–161.
- , and Harshvardhan, 1986a: Comparative accuracy of selected multiple scattering approximations. *J. Atmos. Sci.*, **43**, 784–801.
- , and —, 1986b: Comparative accuracy of the albedo, transmission and absorption for selected radiative transfer approximations. NASA Reference Publication, 1160, 41 pp.
- , L. F. Radke, and P. V. Hobbs, 1990: Determination of the spectral absorption of solar radiation by marine stratocumulus clouds from airborne measurements within clouds. *J. Atmos. Sci.*, **47**, 894–907.
- Lacis, A. A., and J. E. Hansen, 1974: A parameterization for the absorption of solar radiation in the Earth's atmosphere. *J. Atmos. Sci.*, **31**, 118–133.
- Meador, W. E., and W. R. Weaver, 1980: Two-stream approximations to radiative transfer in planetary atmospheres: A unified description of existing methods and a new improvement. *J. Atmos. Sci.*, **37**, 630–643.
- Sagan, C., and J. B. Pollack, 1967: Anisotropic nonconservative scattering and the clouds of Venus. *J. Geophys. Res.*, **72**, 469–477.
- Shettle, E. P., and J. A. Weinman, 1970: The transfer of solar irradiance through inhomogeneous turbid atmospheres evaluated by Eddington's approximation. *J. Atmos. Sci.*, **27**, 1048–1055.
- Slingo, A., 1989: A GCM parameterization for the shortwave radiative properties of water clouds. *J. Atmos. Sci.*, **46**, 1419–1427.
- Stephens, G. L., 1988: Radiative transfer through arbitrarily shaped optical media. Parts I and II. *J. Atmos. Sci.*, **45**, 1818–1848.
- Toon, O. B., C. P. McKay, T. P. Ackerman, and K. Santhanam, 1989: Rapid calculation of radiative heating rates and photodissociation rates in inhomogeneous multiple scattering atmospheres. *J. Geophys. Res.*, **94**, 16 287–16 301.
- Twomey, S., 1976: Computations of the absorption of solar radiation by clouds. *J. Atmos. Sci.*, **33**, 1087–1091.
- van de Hulst, H. C., 1968: Asymptotic fitting, a method for solving anisotropic transfer problems in thick layers. *J. Comput. Phys.*, **3**, 291–306.
- , 1980: *Multiple Light Scattering, Tables, Formulas, and Applications*, Vols. 1 and 2. Academic Press, 739 pp.
- Wiscombe, W. J., 1977: The delta-Eddington approximation for a vertically inhomogeneous atmosphere. NCAR Tech. Note, NCAR/TN-121 + STR, 66 pp. [NTIS PB 270618].
- , and S. G. Warren, 1980: A model of the spectral albedo of snow. I: Pure snow. *J. Atmos. Sci.*, **37**, 2712–2733.
- Zdunkowski, W. G., R. M. Welch, and G. Korb, 1980: An investigation of the structure of typical two-stream-methods for the calculation of solar fluxes and heating rates in clouds. *Contrib. Atmos. Phys.*, **53**, 147–166.

Simple parameterizations of the radiative properties of cloud layers: a review

Harshvardhan and Raymond C. Espinoza, Jr.
Department of Earth and Atmospheric Sciences
Purdue University
West Lafayette, Indiana 47907, USA

Atmospheric Research, 1993

ABSTRACT

Current atmospheric general circulation models parameterize cloud-radiation effects through relationships that are based on the assumption that a model grid is partly clear and the remaining area is filled with a homogeneous cloud layer. The optical properties of this homogeneous layer are related to cloud microphysical quantities such as the liquid water path and effective drop radius which in turn are diagnosed from model variables. In the future it will be necessary to consider distributions of liquid water paths within a grid and relate the effective radius to the type of cloud formed since the grid mean radiative properties are very sensitive to these parameters. There is also the need for a computationally efficient technique to model overlapping liquid and vapor absorption in the solar near infrared.

INTRODUCTION

The role of clouds has been identified as the area of research of the highest priority in many global change programs (e.g. Committee on Earth Sciences, 1989). One reason is the dramatic radiative effect of clouds in both the solar and thermal regions of the electromagnetic spectrum. In general, clouds have opposite effects in these two spectral regions and the net effect for the earth-atmosphere column is the difference between these two large forcings. The global distribution of the individual and combined forcing at the top of the atmosphere has been studied extensively during the Earth Radiation Budget Experiment (ERBE). The ERBE results (Harrison et al., 1990) indicate that in the global annual mean, clouds have a cooling effect, i.e. the reflection of solar radiation dominates the thermal trapping effect. However, in areas such as the tropics, the two effects nearly cancel, but of course, the vertical profile of the forcing is quite different in the solar and in the thermal.

In order to include the radiative effect of clouds in a numerical climate model it is essential to consider all the important processes that could change cloud cover and cloud radiative properties during a climate simulation. These are examples of interactive feedback processes that when included in climate models can alter their response to a given forcing such as doubling atmospheric carbon dioxide. Figure 1 shows schematically some possible feedback paths involving cloud microphysics.

The most comprehensive tool for the simulation and analysis of climatic change is a general circulation model (GCM) of the atmosphere. Often, GCMs are coupled to simple ocean and sea ice models. The manner in which cloud-radiation effects are parameterized differs from model to model. This review will deal with the rationale behind these parameterizations and discuss possibilities for future improvements.

RADIATIVE PROPERTIES OF HOMOGENEOUS CLOUDS

All current GCMs have interactive cloud generation schemes and parameterizations for computing the radiative properties of cloudy layers. Earlier models fixed cloud radiative properties (Wetherald and Manabe, 1980) which limited the ability of changes in cloud properties to

feed back to the climate system. An exhaustive list of cloud parameterizations is given in Cess et al. (1990) which reports on an intercomparison of 19 atmospheric GCMs that were subjected to a reverse climate experiment. The models were run twice in a perpetual July mode for prescribed sea surface temperatures (SST) that were uniformly 2 K above and 2 K below the climatological mean SSTs for July. All models showed decreased cloud cover for the warm simulation relative to the colder one but the climate sensitivity parameter (Cess et al., 1990), λ , whose magnitude depends on the various feedbacks in the models ranged over a factor of 3. This is because changes in the vertical distribution of clouds were different from model to model and the optical (hence, radiative) properties of clouds changed with the change in mean climate in a manner that was unique to each model.

Cloud Microphysics

The parameterization of cloud optical properties in terms of GCM resolved variables is a fairly recent trend and is based on first principles applied to homogeneous cloud layers. It may be shown that the extinction coefficient of a volume of cloud drops is related simply to various moments of cloud microphysical parameters in two limiting cases (Stephens, 1984). At solar wavelengths, the characteristic dimension of cloud drops is much larger ($> 4 \mu\text{m}$) than the wavelength and in this case the droplet extinction coefficient, $\sigma \text{ (km}^{-1}\text{)}$, is proportional to L/r_e where $L \text{ (g m}^{-3}\text{)}$ is the liquid water content and $r_e \text{ (}\mu\text{m)}$ is the effective radius which is defined as the ratio of the third to the second moments of the drop size distribution (DSD). It is this inverse relationship to drop size that results in an increase in the extinction coefficient (and cloud albedo) when the DSD is shifted to smaller sizes (Twomey, 1977).

The radiative properties of a homogeneous cloud layer are computed using the column integrated extinction coefficient which is a non-dimensional parameter called the optical depth. For example, the optical depth at visible wavelengths is

$$\tau_{\text{vis}} = \int_{\text{base}}^{\text{top}} \sigma_{\text{vis}} dz, \quad (1)$$

where z is geometric height.

Since the column integrated liquid water path is

$$W(\text{g m}^{-2}) = \int_{\text{base}}^{\text{top}} L(\text{g m}^{-3}) dz, \quad (2)$$

then for visible wavelengths

$$\tau_{\text{vis}} \propto W/r_e, \quad (3)$$

if r_e is uniform through the cloud. Furthermore, τ_{vis} can be parameterized solely in terms of W if one assumes further that there is a systematic relationship between r_e and W (e.g. the model of Stephens, 1978). If τ_{vis} can be related to W , cloud optical properties at other wavelengths follow immediately. For instance, the thermal flux emittance of a cloud layer is approximated by

$$\varepsilon_{\text{ir}} \equiv 1 - \exp(-\beta \tau_{\text{ir}}), \quad (4)$$

where cloud optical depth at thermal wavelengths is $\tau_{\text{ir}} \equiv 0.5 \tau_{\text{vis}}$ (Platt and Harshvardhan, 1988). The diffusivity factor, β , which accounts for the angular distribution of thermal emission is roughly 1.5 so that the thermal flux emittance of a cloud layer may be written as

$$\varepsilon_{\text{ir}} \equiv 1 - \exp(-0.75 \tau_{\text{vis}}). \quad (5)$$

The above development can be extended to ice clouds with some modifications (Platt and Harshvardhan, 1988).

Application to GCMs

Equations (3) and (5) form the basis of most parameterizations of cloud optical properties in GCMs. The radiative properties of a cloud layer (reflectance, transmittance and absorptance)

are computed using a two-stream technique (King and Harshvardhan, 1986) which requires as input the droplet single scattering albedo, ω , and asymmetry parameter, g , of the scattering phase function in addition to τ . Models generally prescribe these as wavelength dependent constants. The radiative properties of isolated cloud layers have to be integrated into the column model and this is usually accomplished through a flux adding (Harshvardhan et al., 1987) or matrix inversion (Toon et al., 1989) technique. Application of the above procedure is possible only if a GCM provides information on the cloud water content and related microphysics. However, this aspect of modeling is in its infancy and many GCMs use the layer mean temperature as a surrogate for cloud microphysics (see Tables 4 and 5 of Cess et al., 1990).

The validity of using temperature to parameterize cloud microphysics has not been thoroughly examined over the entire range of global conditions. However, there is empirical and theoretical evidence that optical properties can be related to temperature for cold clouds (Petukhov, et al., 1975; Feigelson, 1978; Heymsfield and Platt, 1984; Somerville and Remer, 1984; Betts and Harshvardhan, 1987; Platt and Harshvardhan, 1988; Stephens et al., 1990). At the very least, the sharp change in effective radius accompanying phase change can be used to distinguish between water and ice clouds in a GCM (Charlock and Ramanathan, 1985). However, a direct relationship with temperature invariably breaks down if extended to convective anvils which are optically thick (Harshvardhan et al., 1989). The studies cited above also show that the optical properties of warm clouds cannot be parameterized in terms of temperature alone. In principle, it is possible to incorporate cloud formation and dissipation mechanisms into larger scale models (Heymsfield and Donner, 1990).

MEAN PROPERTIES OF CLOUD FIELDS

The horizontal grid increment of GCMs is of the order of 200 - 500 km within which one generally finds mesoscale structure as well as detailed structure at much smaller scales. There is need for subgrid scale parameterization of cloudiness in GCMs because of the stark contrast between clear and cloudy radiation fields as well as the non-linear behavior of radiative properties with respect to cloud optical properties. Most current GCM radiation routines

distinguish between clear and cloudy portions of the horizontal grid in each layer and they also include some scheme for overlapping fractional cloud cover in the vertical (Tian and Curry, 1989). Tables 4 and 5 of Cess et al. (1990) list the cloud fraction generation schemes in several current GCMs.

In principle, if there is some means of determining the cloud water (or ice) content in a grid volume, the application of the relationships given by eqs. (3) - (5) to a partially filled area can provide the overall grid box mean radiative properties of the layer. However, the *distribution* of the liquid water in the cloudy portion could affect the grid mean properties substantially. This was demonstrated by Harshvardhan and Randall (1985) for very simple, yet plausible, variations in the liquid water content of a spatial grid. Their results are reproduced in Figure 2 and show quite clearly that mean radiative properties of a cloudy layer can not be uniquely related to the mean liquid water column amount in the grid.

There is also observational evidence of this non-unique dependence. Stephens and Greenwald (1991) have correlated the microwave derived liquid water path and albedo of clouds from an analysis of Nimbus 7 data. Figure 3 summarizes their study which shows that the albedo-liquid water relationships for homogeneous clouds derived from eq. (3) are applicable to clouds in midlatitudes but can not be applied in the tropics. In fact, the relationship in the tropics is much like Case C shown in Figure 2. There is obviously considerable structure in tropical clouds within the field of view analyzed in the study. In addition, there are cloud geometry effects which have not been considered in Figure 2.

The current practice of separating a horizontal area into clear and cloudy fractions is a particular, though extreme, example of a subgrid scale liquid water distribution parameterization. Observational and modeling studies currently being conducted should lead to more general parameterizations. A possible source of information on subgrid scale variability is data from the International Satellite Cloud Climatology Project (ISCCP) which has cataloged cloud properties inferred from visible and infrared window radiances measured by instruments on geostationary and polar orbiting satellites (Rossow and Schiffer, 1991). The data coverage is nearly global

with a time resolution of three hours for the period July 1983 to the present. A parallel campaign of field observations under the FIRE (First ISCCP Regional Experiment) program (Cox et al., 1987; Albrecht et al., 1988) has also yielded a wealth of information on the horizontal variability of cloud microphysical properties in stratocumulus (Nakajima et al., 1991) and cirrus clouds (Spinhirne and Hart, 1990).

The three dimensional structure of cloud fields is currently being simulated by cloud scale models (Moeng, 1986; Tao et al., 1987; Xu and Krueger, 1991). Computational constraints have prevented extended time integrations but in the near future, model realizations could be used to construct parameterizations for coarser resolution GCMs. The mean radiative properties of the cloudy portion of the field can then be computed from the distribution of model microphysical and macrophysical quantities and parameterized in terms of the mean and higher moments of, for example, liquid water and effective radius distributions. The model envisaged is shown schematically in Figure 4 for liquid water path.

SPECTRAL RADIATIVE PROPERTIES

The above discussion focused on computations of cloud radiative properties at visible wavelengths but of course is applicable for all radiative properties throughout the spectrum. At thermal wavelengths, the emittance of water clouds saturates at fairly modest thicknesses (see eq. 5) but a subgrid scale model as in Figure 4b would be useful for thin cirrus and even marine stratocumulus. One of the most pressing problems in cloud radiation modeling is the parameterization of cloud optical properties in the solar near infrared which contains almost fifty percent of the extra-terrestrial solar energy. At wavelengths greater than $0.7\ \mu\text{m}$, water in the vapor and condensed phases exhibits strong absorption features that overlap somewhat. Furthermore, cloud layer absorptance depends critically on the single scattering albedo, ω , which varies through the near infrared and, more importantly, depends on the DSD (King et al., 1990). The recent study of Intercomparison of Radiation Codes in Climate Models (ICRCCM) showed that low resolution models produced large errors because of the spectral averaging of ω (Fouquart et al., 1991).

It is for the above reasons that solar radiation computations are made for several bands and the single-scattering properties are parameterized in terms of cloud microphysical quantities for each band separately. Slingo (1989) has proposed a four band model for which the optical properties, τ , ω , and g , are in the form

$$\tau_i = (a_i + b_i/r_e) W \quad (6)$$

$$1 - \omega_i = c_i + d_i r_e \quad (7)$$

$$g_i = e_i + f_i r_e \quad (8)$$

where $a_i - f_i$ are band dependent coefficients that are obtained by fitting the parameterized results to more exact calculations and W and r_e are assumed to be given. Since models do not diagnose r_e , the above relationships have been extended by Ritter and Geleyn (1992) to include a relationship of the form

$$r_e = c_1 + c_2 L \quad (9)$$

where c_1 and c_2 are coefficients. Ebert and Curry (1992) have obtained coefficients for eqs. (6) - (8) that are appropriate for ice clouds. Again, it is necessary to make some diagnosis of cloud microphysical properties in order to apply the relationships.

The absorptive properties of condensed phase water in the near infrared cannot be considered in isolation but must be integrated with water vapor absorption. This is usually accomplished by modeling vapor absorption with the k-distribution technique (Lacis and Hansen, 1974) which approximates the solution to the spectrally varying problem with an equivalent set of pseudo-monochromatic computations. Accuracy generally increases with the number of bands used and the number of k-values within bands. However, computation time rapidly

becomes prohibitive. Since liquid and vapor absorb at similar wavelengths, the spectrally integrated radiative properties of a cloud layer depend on the column amount of vapor above the cloud because the solar flux impinging on the layer does not contain energy that has already been depleted by the vapor above (Davies et al., 1984). Methods of incorporating this into a parameterization have been suggested by Fouquart and Bonnel (1980), Ramaswamy and Freidenreich (1992) and others.

A suggestion by Briegleb (1992) that involves the identification of vapor absorption with different liquid absorption bands can reduce computation time significantly. Figure 5(a) shows the solar spectral column absorption by water vapor and a thick cloud of liquid droplets separately in the absence of the other constituent for a solar zenith angle of 30° and a standard midlatitude summer water vapor profile. The liquid DSD is from King et al. (1990) and has an effective radius of $8\text{ }\mu\text{m}$. The cloud is assumed to be thick enough such that radiative properties have attained their asymptotic values. It may be seen that there is a tendency for vapor and liquid absorption to increase in lockstep with increasing wavelength (decreasing wavenumber). This feature motivated Briegleb (1992) to assign the different k-values from Lacis and Hansen (1974) to distinct droplet absorption properties based on the Slingo (1989) parameterization.

There is, however, a flaw in this argument that can be appreciated by inspection of Figure 5(b) which is a scatter plot of the two separate absorptions shown in Figure 5(a) sampled at 100 cm^{-1} intervals. Whereas it is true that high vapor absorption is associated with high liquid absorption, there is fairly strong liquid absorption even when vapor absorption is low. In fact, if there is a substantial column of vapor above the cloud, all the solar absorption in the cloud layer will occur in these window regions. The general idea of relating vapor and liquid absorption can still be applied by deriving a more quantitative relationship based on k-distributions at higher resolution.

An example of such a relationship made using the k-distribution given in Table 1 of Chou (1986) is shown in Figure 6. The k-distribution is solar flux-weighted and computed for $p = 300$ mb and $T = 240$ K. Cloud layer absorption is linearly proportional to the single scattering albedo, ω , in the thin limit and is primarily a function of the similarity parameter, s , where

$$s = [(1 - \omega)/(1 - \omega_g)]^{1/2}, \quad (10)$$

for very thick clouds (King and Harshvardhan, 1986). By assigning the appropriate broad band liquid properties to each of the k-values in the particular band and computing the weighted sum, two separate relationships are obtained for the limiting cases of exceedingly thin and thick layers. The relationships shown in Figure 6 are unique to the cloud drop size distribution considered but a more flexible model could perhaps be a useful alternative to current techniques. If computation time is not a constraint, then a multi-band model is probably preferable.

SUMMARY

Since the early climate models of the 1960s there has been a gradual progression of increasingly interactive cloud radiation parameterizations. This has allowed the various cloud radiation feedbacks to operate in models. One result has been the wide range in climate sensitivity displayed by models having different parameterizations. The intercomparison study of Cess et al. (1990) has clearly demonstrated the divergence in the treatment of clouds in current models.

Future thrusts will probably be in the areas of modeling and parameterizing cloud microstructure and also cloud field macrostructure. Climate models will continue to get more interactive and the role of clouds in model simulations will become increasingly important when oceanic coupling is included. Studies with cloud scale and mesoscale models are already influencing GCM parameterizations (Xu and Krueger, 1991). This trend will accelerate as the various groups cooperate in the study of the role of clouds in maintaining the current climate and

modifying the climatic response to anthropogenic forcings.

ACKNOWLEDGEMENTS

This study was supported by NSF Grants ATM-8909870 and ATM-9002936 and NASA Grant NAG 5-1125. I wish to thank Wanda Curtis and Tim Gilbert for assistance with manuscript preparation and an anonymous reviewer for editorial assistance.

REFERENCES

- Albrecht, B.A., Randall, D.A. and Nicholls, S., 1988. Observations of marine stratocumulus clouds during FIRE. *Bull. Amer. Meteor. Soc.*, 69: 618-626.
- Betts, A.K. and Harshvardhan, 1987. Thermodynamic constraint on the cloud liquid water feedback in climate models. *J. Geophys. Res.*, 92: 8483-8485.
- Briegleb, B.P., 1992. Delta-Eddington approximation for solar radiation in the NCAR community climate model. *J. Geophys. Res.*, 97: 7603-7612.
- Cess, R.D., Potter, G.L., Blanchet, J.P., Boer, G.J., DelGenio, A.D., Deque, M., Dymnikov, V., Galin, V., Gates, W.L., Ghan, S.J., Kiehl, J.T., Lacis, A.A., Le Treut, H., Li, Z.-X., Liang, X.-Z., McAvaney, B.J., Meleshko, V.P., Mitchell, J.F.B., Morcrette, J.-J., Randall, D.A., Rikus, L., Roeckner, E., Royer, J.F., Schlese, U., Sheinin, D.A., Slingo, A., Sokolov, A.P., Taylor, K.E., Washington, W.M., Wetherald, R.T., Yagai, I. and Zhang, M.-H. 1990. Intercomparison and interpretation of climate feedback processes in 19 atmospheric general circulation models. *J. Geophys. Res.*, 95: 16,601-16,615.
- Charlock, T.P. and Ramanathan, V., 1985. The albedo field and cloud radiative forcing produced by a general circulation model with internally generated cloud optics. *J. Atmos. Sci.*, 42: 1408-1429.
- Chou, M.-D., 1986. Atmospheric solar heating rate in the water vapor bands. *J. Climate Appl. Meteor.*, 25: 1532-1542.
- Committee on Earth Sciences, 1989. *Our Changing Planet: The FY 1990 Research Plan. The U.S. Global Change Research Program.* Washington, D.C., 118 pp. plus three appendices.
- Cox, S.K., McDougal, D.S., Randall, D.A. and Schiffer, R.A., 1987. FIRE - The First ISCCP Regional Experiment. *Bull. Amer. Meteor. Soc.*, 68: 116-118.
- Davies, R., Ridgway, W.L. and Kim, K.-E., 1984. Spectral absorption of solar radiation in cloudy atmospheres: a 20 wavenumber model. *J. Atmos. Sci.*, 41: 2126-2137.
- Ebert, E.E. and Curry, J.A., 1992. A parameterization of ice cloud optical properties for climate models. *J. Geophys. Res.*, 97: 3831-3836.
- Feigelson, E.M., 1978. Preliminary radiation model of a cloudy atmosphere. Part I - structure of clouds and solar radiation. *Contrib. Atmos. Phys.*, 51: 203-229.
- Fouquart, Y. and Bonnel, B., 1980. Computations of solar heating of the Earth's atmosphere: A new parameterization. *Contrib. Atmos. Phys.*, 53: 35-62.
- Fouquart, Y., Bonnel, B. and Ramaswamy, V., 1991. Intercomparing shortwave radiation codes for climate studies. *J. Geophys. Res.*, 96: 8955-8968.

- Harrison, E.F., Minnis, P., Barkstrom, B.R., Ramanathan, V., Cess, R.D. and Gibson, G.G., 1990. Seasonal variation of cloud radiative forcing derived from the Earth Radiation Budget Experiment. *J. Geophys. Res.*, 95: 18,687- 18,703.
- Harshvardhan and Randall, D.A., 1985. Comments on "The parameterization of radiation for numerical weather prediction and climate models." *Mon. Wea. Rev.*, 113: 1832-1833.
- Harshvardhan, Davies, R., Randall, D.A. and Corsetti, T.G., 1987. A fast radiation parameterization for atmospheric circulation models. *J. Geophys. Res.*, 92: 1009-1016.
- Harshvardhan, Randall, D.A., Corsetti, T.G. and Dazlich, D.A., 1989. Earth radiation budget and cloudiness simulations with a general circulation model. *J. Atmos. Sci.*, 46: 1922-1942.
- Heymsfield, A.J. and Platt, C.M.R., 1984. A parameterization of the particle size spectrum of ice clouds in terms of the ambient temperature and the ice water content. *J. Atmos. Sci.*, 41: 846-855.
- Heymsfield, A.J. and Donner, L.J., 1990. A scheme for parameterizing ice-cloud water content in general circulation models. *J. Atmos. Sci.*, 47: 1865-1877.
- King, M.D. and Harshvardhan, 1986. Comparative accuracy of selected multiple scattering approximations. *J. Atmos. Sci.*, 43: 784-801.
- King, M.D., Radke, L.F. and Hobbs, P.V., 1990. Determination of the spectral absorption of solar radiation by marine stratocumulus clouds from airborne measurements within clouds. *J. Atmos. Sci.*, 47: 894-907.
- Lacis, A.A. and Hansen, J.E., 1974. A parameterization for the absorption of solar radiation in the earth's atmosphere. *J. Atmos. Sci.*, 31: 118-133.
- Moeng, C.-H., 1986. Large-eddy simulation of a stratus-topped boundary layer. Part I: Structure and budgets. *J. Atmos. Sci.*, 43: 2886-2900.
- Nakajima, T., King, M.D., Spinhirne, J.D. and Radke, L.F., 1991. Determination of the optical thickness and effective particle radius of clouds from reflected solar radiation measurements. Part II: Marine stratocumulus observations. *J. Atmos. Sci.*, 48: 728-750.
- Petukhov, V.K., Feigelson, E.M. and Manuylova, N.I., 1975. The regulating role of clouds in the heat effects of anthropogenic aerosols and carbon dioxide. *Izv. Acad. Sci. USSR Atmos. Oceanic Phys.*, 11: 802-808.
- Platt, C.M.R. and Harshvardhan, 1988. Temperature dependence of cirrus extinction: Implications for climate feedback. *J. Geophys. Res.*, 93: 11,051-11,058.
- Ramaswamy, V. and Freidenreich, S.M., 1992. A study of broadband parameterizations of the solar radiative interactions with water vapor and water drops. *J. Geophys. Res.*, 97: 11,487-11,512.

- Ritter, B. and Geleyn, J.-F., 1992. A comprehensive radiation scheme for numerical weather prediction models with potential applications in climate simulations. *Mon. Wea. Rev.*, 120: 303-325.
- Rossow, W.B. and Schiffer, R.A., 1991. ISCCP cloud data products. *Bull. Amer. Meteor. Soc.*, 72: 2-20.
- Slingo, A., 1989. A GCM parameterization for the shortwave radiative properties of water clouds. *J. Atmos. Sci.*, 46: 1419-1427.
- Somerville, R.C.J. and Remer, L.A., 1984. Cloud optical thickness feedbacks in the carbon dioxide climate problem. *J. Geophys. Res.* 89: 9668-9672.
- Spinhirne, J.D. and Hart, W.D., 1990. Cirrus structure and radiative parameters from airborne lidar and spectral radiometer observations: The 28 October 1986 FIRE study. *Mon. Wea. Rev.*, 118: 2329-2343.
- Stephens, G.L., 1978. Radiation profiles in extended water clouds. II: parameterization schemes. *J. Atmos. Sci.*, 35: 2123-2132.
- Stephens, G.L., 1984. The parameterization of radiation for numerical weather prediction and climate models. *Mon. Wea. Rev.*, 112: 826-867.
- Stephens, G.L. and Greenwald, T.J., 1991. The earth's radiation budget and its relations to atmospheric hydrology. 2. Observations of cloud effects. *J. Geophys. Res.*, 96: 15,325-15340.
- Stephens, G.L., Tsay, S.C., Stackhouse, P.W., Jr. and Flatau, P.J., 1990. The relevance of the microphysical and radiative properties of cirrus clouds to climate and climate feedback. *J. Atmos. Sci.*, 47: 1742-1753.
- Tao, W.-K., Simpson, J.S. and Soong, S.-T., 1987. Statistical properties of a cloud ensemble: a numerical study. *J. Atmos. Sci.*, 44: 3175-3187.
- Tian, L., and Curry, J.A., 1989. Cloud overlap statistics. *J. Geophys. Res.*, 94: 9925-9935.
- Toon, O.B., McKay, C.P., Ackerman, T.P. and Santhanam, K., 1989. Rapid calculation of radiative heating rates and photodissociation rates in inhomogeneous multiple scattering atmospheres. *J. Geophys. Res.*, 94: 16,287-16,301.
- Twomey, S., 1977. The influence of pollution on the short wave albedo of clouds. *J. Atmos. Sci.*, 34: 1149-1152.
- Wetherald, R.T. and Manabe, S., 1980. Cloud cover and climate sensitivity. *J. Atmos. Sci.*, 37: 1485-1510.
- Xu, K.-M. and Krueger, S.K., 1991. Evaluation of cloudiness parameterizations using a cumulus ensemble model. *Mon. Wea. Rev.*, 119: 342-367.

Figure Captions

- Fig. 1. Some plausible cloud feedback processes.
- Fig. 2. (a) Schematic illustration of three liquid water path (W , g m^{-2}) probability distributions considered as examples; (b) and (c) show the diffuse albedo and emittance, respectively, for the three cases illustrated in (a), after Harshvardhan and Randall (1985).
- Fig. 3. Ellipses containing 97% of the annual composite cloud albedo-liquid water path relationship data for the tropics and midlatitudes. Also shown are the results of theoretical calculations (solid curves) for plane-parallel clouds with various effective radii r_e (μm), after Stephens and Greenwald (1991).
- Fig. 4. Schematic diagram of the liquid water path distribution in (a) current GCMs and (b) future models.
- Fig. 5. (a) Solar near infrared absorption by water vapor (thin line) and cloud droplets (thick line) separately in the absence of the other constituent for a midlatitude summer water vapor profile. The effective radius of the droplets is $8 \mu\text{m}$ and the cloud is assumed to be optically thick. Solar zenith angle is 30° . The outer envelope shown by the dashed line is the extraterrestrial solar flux. All fluxes have been averaged over 100 cm^{-1} ; (b) scatter plot of vapor and liquid absorption shown in (a).
- Fig. 6. Relationship between droplet single scattering albedo and vapor absorption for the limiting cases of thin and thick cloud layers.

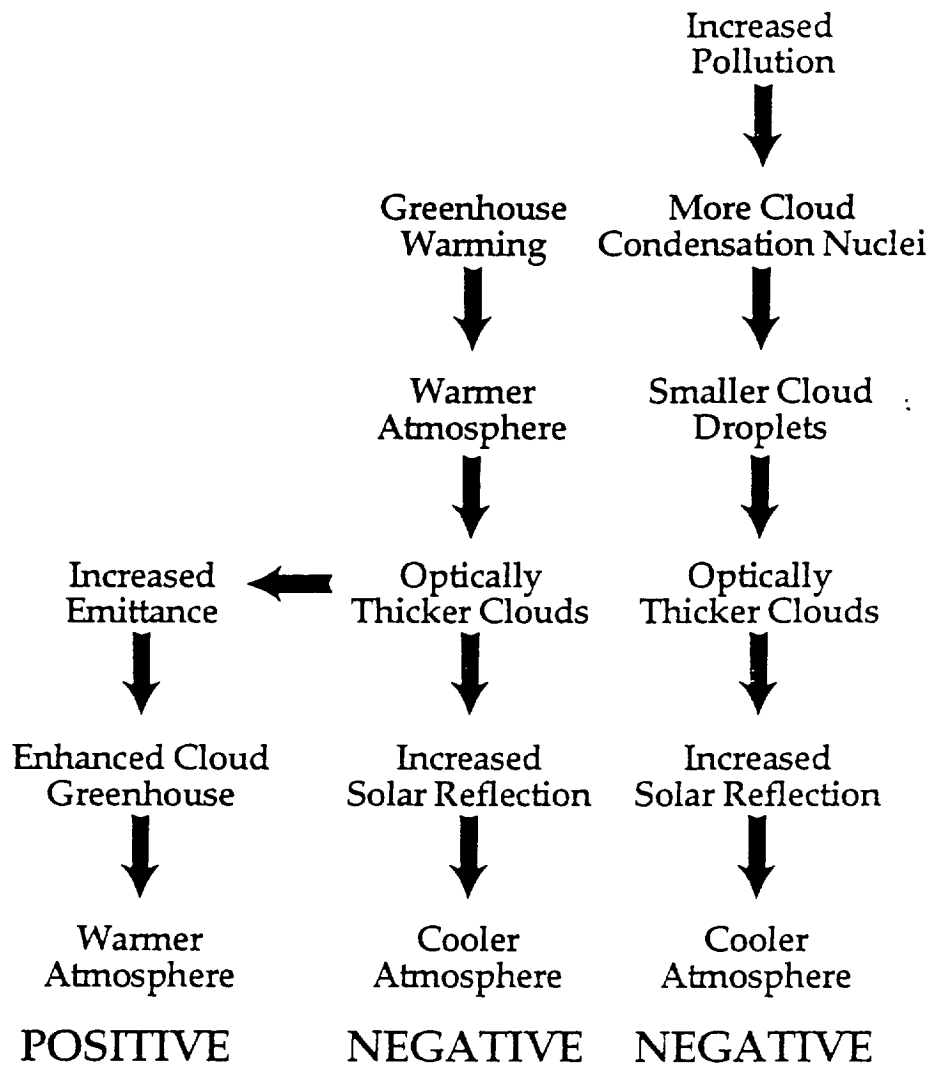
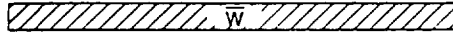


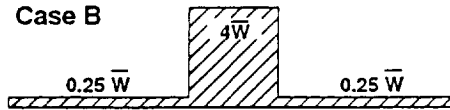
Figure 1

a)

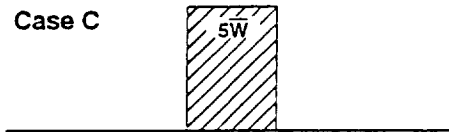
Case A



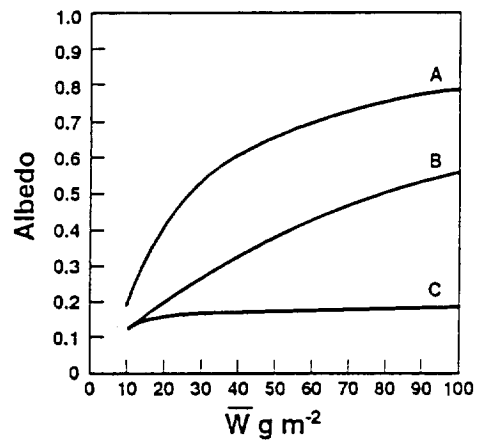
Case B



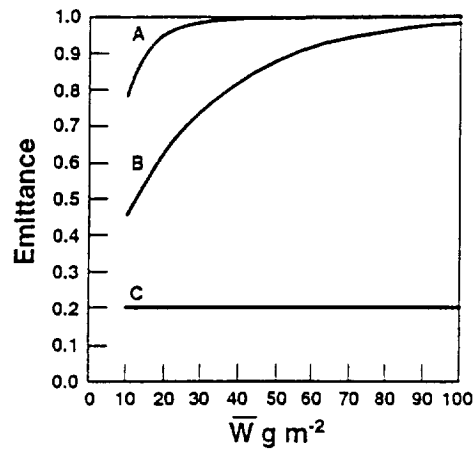
Case C



b)



c)



Figures 2a, 2b and 2c

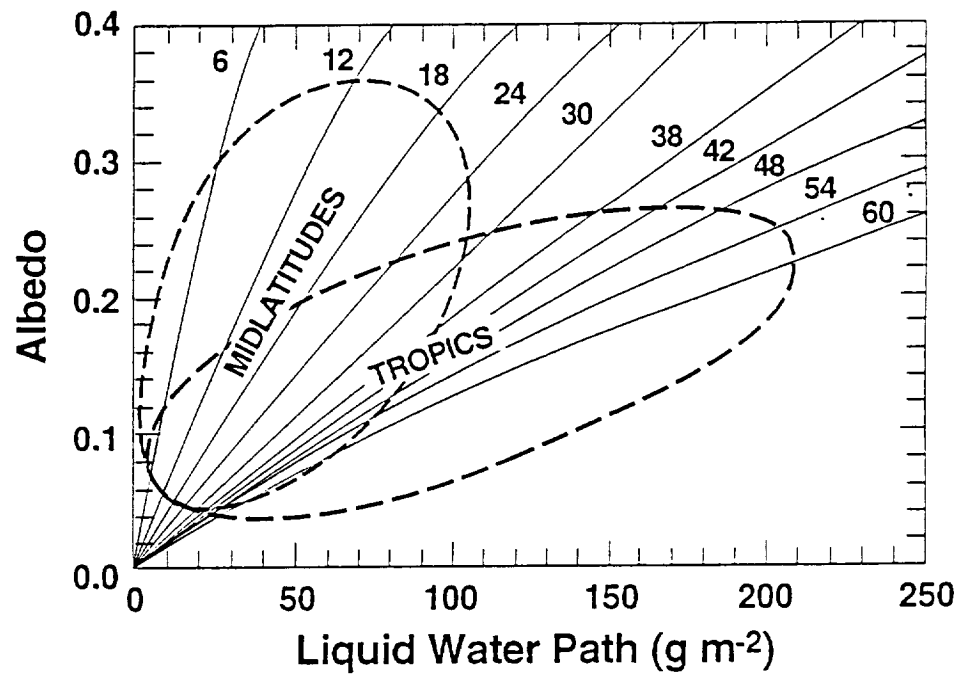
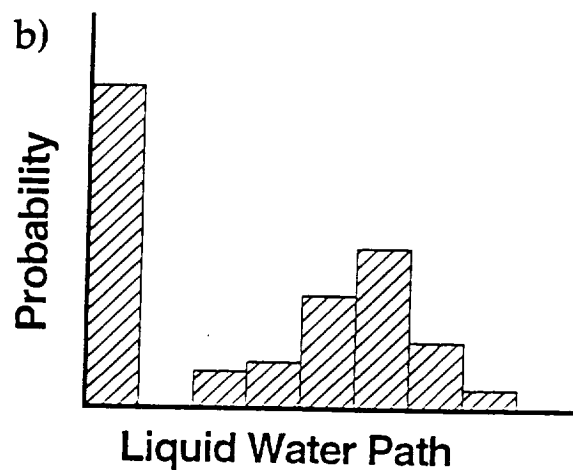
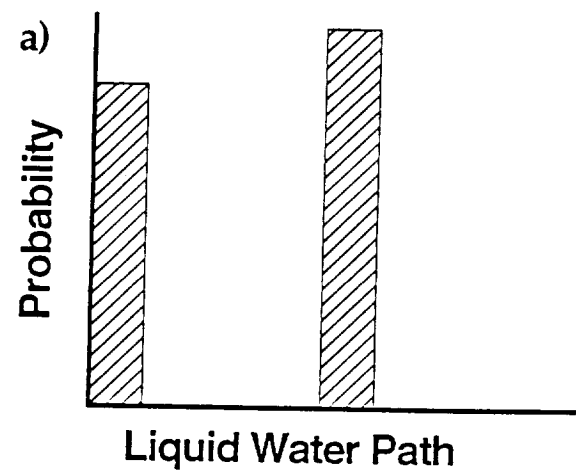
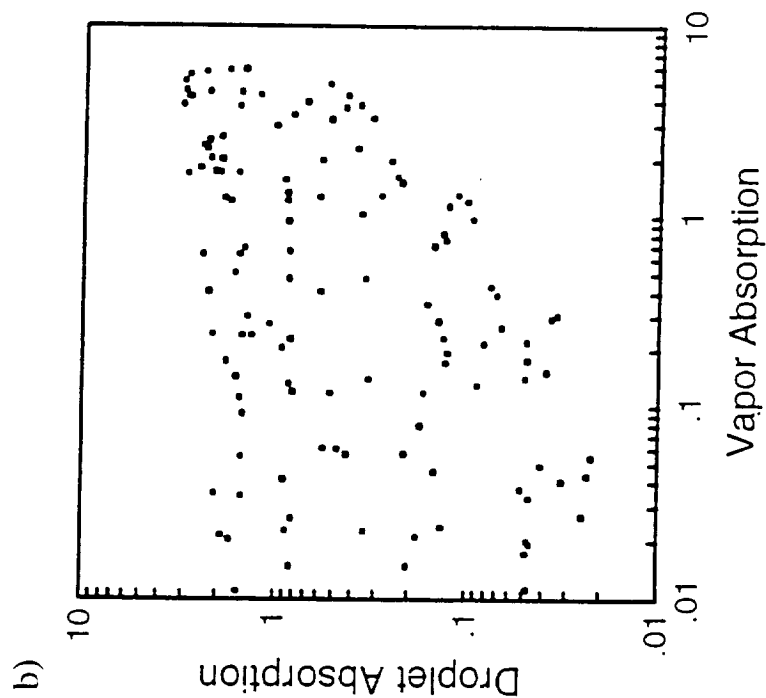
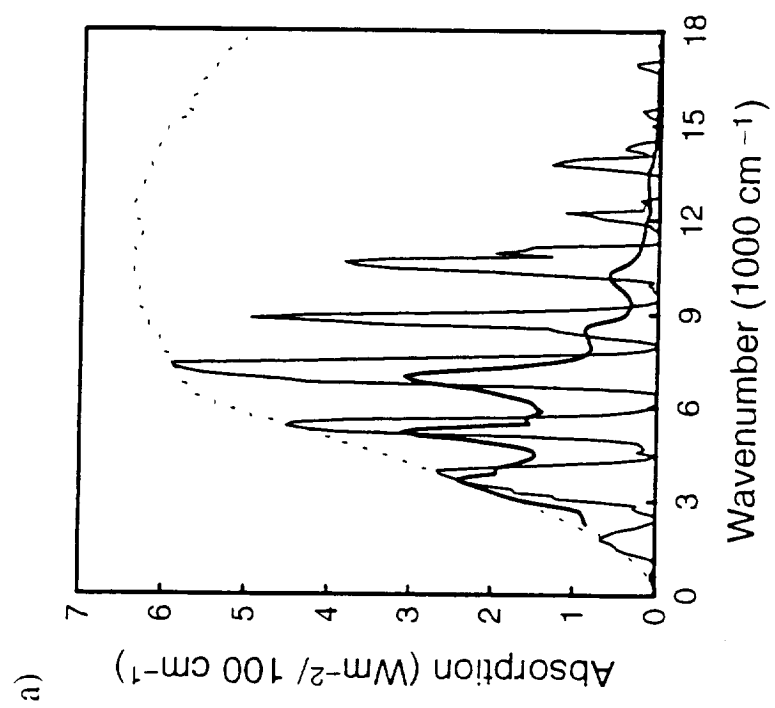


Figure 3



Figures 4a and 4b



Figures 5a and 5b

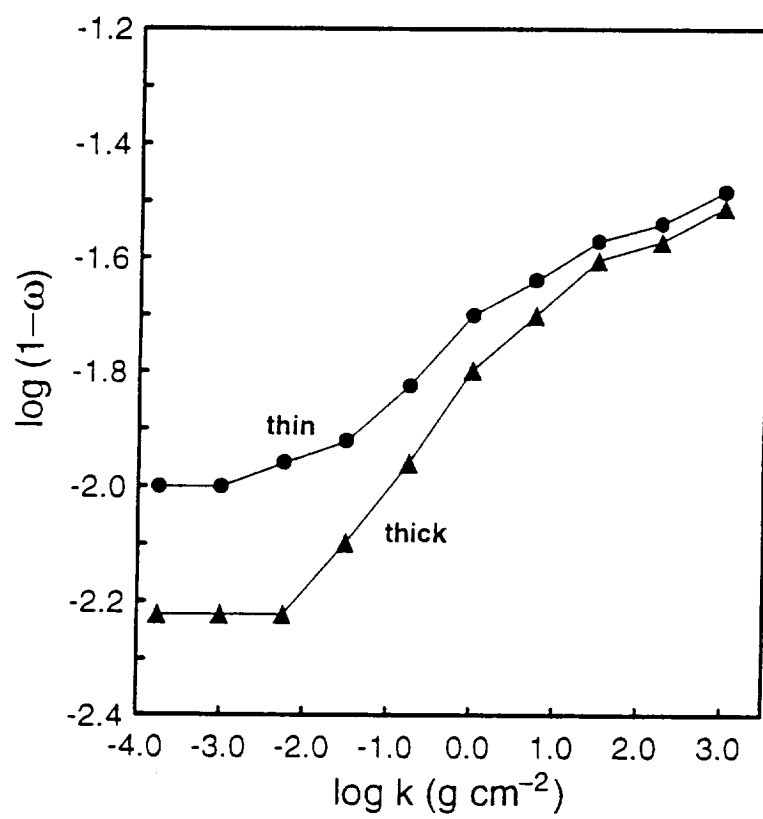


Figure 6